

https://dspace.org/

Mechatronic design of a quadrotor test rig for system identification

Beharie, Milan.

2014-01-16
http://hdl.handle.net10539/13491

Downloaded from a DSpace repository. https://dspace.org/

UNIVERSITY OF THE WITWATERSRAND, JOHANNESBURG
SCHOOL OF MECHANICAL, INDUSTRIAL, AND AERONAUTICAL ENGINEERING

Mechatronic Design of a Quadrotor Test Rig for System Identification

Name: Milan Beharie
Student No: 0502037D

A dissertation submitted to the Faculty of Engineering and the Built Environment, University of the Witwatersrand Johannesburg, in fulfilment of the requirements for the degree of Master of Science in Engineering.

Johannesburg, March 2013

Declaration

I, Milan Beharie, (0502037D) am registered for Course No. MECN 8001, (RESEARCH) in the year 2013.

I herewith submit the following research project report titled: "Mechatronic Design of a Quadrotor Rig for System Identification" in partial fulfilment of the requirements of the above course.

I hereby declare the following:

- I am aware that plagiarism (the use of someone else's work without their permission and/or without acknowledging the original source) is wrong;
- I confirm that the work submitted herewith for assessment in the above course is my own unaided work except where I have explicitly indicated otherwise;
- This task has not been submitted before, either individually or jointly, for any course requirement, examination or degree at this or any other tertiary educational institution;
- I understand that the University of the Witwatersrand may take disciplinary action against me if it can be shown that this task is not my own unaided work or that I have failed to acknowledge the source of the ideas or words in my writing in this task.

Signature: _____

Date: 27th March 2013

Abstract

This research study presents the design, development and construction of a mechatronic test stand for the evaluation of powerplant parameters on a quadrotor. As opposed to alternate forms of UAV, the power plant serves a dual purpose of control and propulsion emphasising the importance of the identification process. Since control and propulsion are coupled, the power plant (motor coupled with propeller) was studied in detail using a black box structure (establishing relationships between the inputs and outputs). Extractions of motor parameters in previous studies used traditional Brushless Direct Current Motor (BLDC) equations and propeller theory, however the accuracy achievable and confidence in the extracted parameters remained questionable. The constructed apparatus set and data acquisition process developed for this project served to satisfy this need by allowing for the extraction of the unknown parameters instilling confidence in the modeling process. An in-depth analysis of the thrust stand from conception to construction was performed with an ideal parameter selection for optimum data resolution during collection. Additionally four RPM sensors were constructed each relying on an alternate means of sensing. The sensors when benchmarked against one another showed a variation of less than 1% in RPM. In order to optimise the powerplant selection, 36 sets of data had been acquired consisting of 6 motors with 6 propeller combinations. A data acquisition Graphical User Interface (GUI) was created in Labview utilising the National Instruments(NI) programming structure establishing communication between the powerplant and sensors. Post processing of the data involved the development of an algorithm that isolated each steady state plateau, establishing the average value in that vicinity using a pre-defined user confidence offset. The algorithm, due to the target pattern implementation, performed as designed on all data sets except those that exhibited corrupt data patterns brought on by resonance. The algorithm establishes relationships between thrust, torque, RPM and the pulse width modulated input signal. The established relationships are then used as inputs into a developed six degree of freedom mathematical model. A mission profile was constructed with distinct phases of which the mathematical model was used to simulate. Each phase in the mission profile excited different modes of the quadrotor dynamics creating an ideal simulation environment in which changes can be implemented and studied.

Acknowledgements

The author would like to thank his family and girlfriend for providing guidance and financial support throughout. He would also like to thank his supervisors Prof J.O. Pedro and Prof L. Dala and additionally his work colleagues at Cash2digital for the priceless assistance and moral support offered during the project duration. Without the contribution of the above people this project would never have been possible.

List of Contents

Declaration ..... **ii**

Abstract ..... **iii**

Acknowledgements ..... **iv**

List of Contents ..... **v**

List of Figures ..... **x**

List of Tables ..... **xix**

Nomenclature ..... **xx**

1. Introduction **1**

1.1 Research Background 1

1.2 Research Rationale and Motivation 2

1.3 Problem Statement 3

1.4 Literature Review 3

1.4.1 Quadrotor Operation 3

1.4.2 Existing Quadrotor Designs 5
1.4.3 Basic Quadrotor Mechanical Design/ Hardware 8
1.4.4 Motors, Propellers and Testing 9
1.5 System Identification 12
1.6 Identified Gaps in the Literature 13
1.7 Research Objectives 14
1.8 Research Scope and Limitations 14
1.9 Research Strategy and Methodology 15
1.10 Research Contributions 16
1.11 Dissertation Outline 16

2. Physical and Mathematical Model of the System 18
2.1 The need for an Aerodynamic Model 18
2.2 Frames of Reference 18
2.2.1 Inertial Frame 18
2.2.2 Body-Fixed Axes 19
2.2.3 Stability Axes 20
2.3 Modelling Assumptions 20
2.4 Modelling Overview 22
2.5 Mass, Geometry and Inertia 23
2.6 Quadrotor Dynamics 25
2.6.1 Equations of Motion 25
2.6.2 Rolling and Pitching Moments 27
2.6.3 Yawing Moments 28
2.6.4 Forces 32
2.7 Coordinate System Transformation 38
2.7.1 Compound Rotations and Transformations 39
2.8 Non- Linear Model 40
2.8.1 Angular Rate and Acceleration 40
2.8.2 Translational Velocity and Acceleration 42
2.8.3 Displacement and Angular Position 43
2.9 Flight Mission Planning 44
2.9.1 Vertical Ascent 45

2.9.2 Equilibrium Analysis 46
3. Hardware and Software Integration 52
3.1 Hardware Communication Protocol 52
3.1.1 I2C Software Communication Protocol 53
3.1.2 SPI Communication Protocol 54
3.1.3 Serial Communication Parameters 57
3.2 Labview System Design Software 58
3.2.1 State-Machine Architecture 58
3.2.2 Field Programmable Gate Array (FPGA) 59
3.2.3 Pulse Position Modulation (PPM) 62
3.2.4 Sensor Data Acquisition 62
3.2.5 Speed Controller Calibration and Start-Up 63
3.2.6 Throttle Timing 66
3.2.7 User Motor Testing Interface 67

4. Attitude Heading and Reference System 70
4.1 Function and Definition 70
4.2 Electronic Hardware Architecture 70
4.2.1 Triple Axis Gyroscope 71
4.2.2 Triple-Axis Accelerometer 75
4.2.3 Triple Axis Magnetometer 81
4.2.4 Accelerometer Gyroscope Combination 84
4.2.5 Accelerometer Test Sensor 85
4.2.6 Razor IMU sensor 87
4.2.7 Direction Cosine Matrix Algorithm (DCM) 90
4.2.8 AHRS Software Architecture 96
4.3 IMU and AHRS Implementation 96

5. Data Acquisition 99
5.1 Overview 99
5.2 Data Acquisition Process and Design 100
5.3 Propeller Testing 101
5.3.1 Propellers Loadings and Safety 103

5.4 Brushless Motor 104
5.4.1 Brushless DC Motor Construction and Operation 104
5.4.2 Brushless DC Outrunner vs Inrunner 105
5.4.3 Brushless Motor Control 106
5.4.4 Electronic Speed Controllers 106
5.4.5 Non-Contact RPM Sensors 109
5.4.6 Infrared-Reflective Sensor 113
5.4.7 Sensorless Motor RPM Detection via BEMF 115
5.4.8 Incremental Encoder 116
5.4.9 Hall Sensors 120
5.5 Thrust Measurements 121
5.5.1 Strain Gage 122
5.5.2 Cantilever Beam Defining Equations 131
5.5.3 Motor Torque 138
5.5.4 Current Monitoring and Power Supply 140
5.6 Controller for Data Acquisition 141
5.6.1 C-Series Modules 142
5.6.2 SBrio-9602 Main Controller 142
5.6.3 Labview FPGA and Real time 143
5.7 Complete Setup 144
5.7.1 Precautionary Measures 145
5.7.2 Verification Results 150
5.7.3 Data Processing and Parameter Estimation 156
5.7.4 Problematic Data Patterns 167

6. Identification Results 171
6.1 Motor Performance Results 171

7. Simulation Model 178
7.1 Mathematical Model Overview 179
7.2 Quadrotor Plant 179
7.3 Quadrotor Control Input 182
7.4 Simulink Results 183

7.4.1 Take-off/ Ascent Phase 184
7.4.2 Hover Phase 187
7.4.3 Mode Excitation Phase 190
7.4.4 Landing/ Descent Phase 194

8. Summary, Conclusion and Future Work 198
8.1 Summary 198
8.1.1 Test Rig Implementation 198
8.1.2 Data Acquisition Results 199
8.1.3 Inertial Measurement Unit and AHRS 199
8.1.4 Mathematical Modelling 199
8.2 Conclusion 200
8.3 Future Work 201
8.3.1 Quadrotor Construction 201
8.3.2 Sensors 202
8.3.3 Control Systems 202
8.3.4 Wind Tunnel Test Data 203

9. References 204

Appendix A – Raw Data 208
Appendix B – Strain Gauge 224
Appendix C – Encoder and ESC 226
Appendix D – Transformations and Moment of Inertia 231
D.1 Transformation in 2 dimensions 232
D.2 Transformation in 3 dimensions: 236
D.3 Moment of Inertia: 238
Appendix E- IMU Flow and Coding structure 239
E.1 IMU User Command Setup 240
E.2 Coding structure 242

List of Figures

Figure 1.1: Raven B Mini UAV being deployed by a soldier for reconnaissance 2
Figure 1.2: Yaw, pitch and roll rotations of a quadrotor 4
Figure 1.3: Variation in motor speed to create control, the front denoted by a green circle (Raza & Gueaieb, 2010). 4
Figure 1.4: Draganflyer X4 UAV (Innovations, n.d.) 5
Figure 1.5: Cyber Quad mini (Cybertechnology, n.d.) 6
Figure 1.6: Ascending Technologies Hummingbird UAV's (Ascending Technologies, n.d.) 7
Figure 1.7: Microdrone Quadrotor UAV (Microdrone, n.d.) 7
Figure 1.8: Parrot AR Drone 8
Figure 1.9: A custom built cage for the JAviator (Craciunas, et al., 2008) 9
Figure 1.10: Quadrotor Construction 9
Figure 1.11: ANUX2 developed by Pounds (Pounds, et al., 2004) 10
Figure 1.12: Pivot type apparatus set for thrust calculation (DiCesare, et al., 2008) 11
Figure 1.13: STARMAC Thrust rig (Hoffmann, et al., 2007) 11
Figure 1.14: Setup for rotor torque identification experiment (Oliveira, 2011) 12
Figure 1.15: Process of System identification 13
Figure 1.16: Flow of research activities 15
Figure 1.17: Dissertation Outline 17
Figure 2.1: Body-fixed axes attached to the quadrotor 19
Figure 2.2: Sideslip angle illustrated using the stability and body-fixed axis. 21
Figure 2.3: Flowchart of the mathematical modelling process. 23
Figure 2.4: Quadrotor being modelled as a 6-DOF system 24

Figure 2.5: Simplified point mass model after a pitch and roll....24
Figure 2.6: Simplified point mass model after a –ve pitch and roll....28
Figure 2.7: Moments acting about the propeller hub of rotor 1 and 3....29
Figure 2.8: Plan view of the quadrotor with action/reaction torque pairs....29
Figure 2.9: Forces experienced by the quadrotor during cruise in the +ve $\boldsymbol{XE}$ direction....34
Figure 2.10: Forces experienced by the quadrotor during cruise the -ve $\boldsymbol{XE}$ direction....35
Figure 2.11: Forces experienced by the quadcopter during the take-off/ascent phase....35
Figure 2.12: Forces experienced by the quadcopter during the landing/descent phase....35
Figure 2.13: Wetted Area as view from each plane....36
Figure 2.14: An "If" statement used for the devised drag equation....38
Figure 2.15: Importance of maintaining the sequence of rotation....39
Figure 2.16: Mission profile for the quadrotor to be performed for mathematical analysis. 45
Figure 2.17: Resultant force acting on the quadrotor during ascent....46
Figure 2.18: Relationship between Thrust and RPM used in the simulation environment ...51
Figure 2.19: Relationship between PWM and thrust used in the simulation environment ...51
Figure 3.1: I2C Communication Start-Stop sequence (Devantech, n.d.)....53
Figure 3.2: SPI master-slave daisy chain architecture....54
Figure 3.3: SPI data transmission for CPOL=0, CPHA=1....56
Figure 3.4: Polarity and phase on the SPI communication bus....56
Figure 3.5: Simple state machine architecture....59
Figure 3.6: FPGA parallel loops in the data acquisition process for RPM sensors....61
Figure 3.7: Labview BLDC motor commutation....62
Figure 3.8: RPM data acquisition in the FPGA....63
Figure 3.9: Oscilloscope reading for pulse analysis....63
Figure 3.10: Flow process of the ESC arming and motor start-up....65
Figure 3.11: Throttle timing nested cases....66
Figure 3.12: Nested loop structure in Labview....67
Figure 3.13: Thrust rig motor testing interface....68
Figure 3.14: Thrust rig simulation outputs....68
Figure 3.15: User decision case structure....69
Figure 4.1: Sparkfun 9DOF AHRS solution....71
Figure 4.2: ITG-3200 Gyroscope 6DOF solution....72
Figure 4.3: Rotation order 1 for finite rotations....73

Figure 4.4: Rotation order 2 for rotations. 73
Figure 4.5: Using vector cross and dot products. 74
Figure 4.6: ITG-3200 (Invensense, n.d.). 74
Figure 4.7: Acceleration vector at used to decipher orientation. 76
Figure 4.8: Accelerometer analogy 77
Figure 4.9: Calibration technique used on the accelerometer 79
Figure 4.10: Interpretation of angles 81
Figure 4.11: A graph of ideal distortion free magnetometer data centred around (0,0) (Konvalin, n.d.) 82
Figure 4.12: The effects of hard-iron distortion on a hard (Konvalin, n.d.) 83
Figure 4.13: Soft iron distortion of a circle into an ellipse 84
Figure 4.14: LIS3DH mounted using perforated board and comparative sizing with pin mapping 85
Figure 4.15: Wiring schematic of the LIS3DH sensor (ST Electronics, 2010) 87
Figure 4.16: LIS3DH accelerometer coupled to the Arduino used for testing 87
Figure 4.17: Atmega-328 pin out specifications 88
Figure 4.18: Arduino Hardware Development Board f or ATMEGA-328 88
Figure 4.19: 9-dof IMU pin mapping 89
Figure 4.20: Interfacing of the sensors with the main processor using I2C communication. 89
Figure 4.21: Master (Atmega328-AU) Pin mapping on the Razor IMU unit 90
Figure 4.22: Operation of the DCM algorithm 93
Figure 4.23: Rotation of a coordinate system in 3-D 94
Figure 4.24: Mounting of the IMU on the rotating rig 97
Figure 4.25: Positive IMU roll with yaw and pitch held constant 98
Figure 4.26: Negative IMU roll with yaw and pitch held constant 98
Figure 5.1: Black box structure of the powerplant 99
Figure 5.2: Thrust stand concept built using strain gauges 100
Figure 5.3: Propeller pitch 102
Figure 5.4: Propeller sizes used for testing 102
Figure 5.5: Simplified BLDC Motor Diagram (Brown, 2002) 104
Figure 5.6: 3-phase 22 pole (11 pair) Brushless "Outrunner", top and bottom views 105
Figure 5.7: PWM Signal 106
Figure 5.8: Duty cycle of waves 107

Figure 5.9: Duty cycle of wave monitoring on the oscilloscope at 5% and 10% Duty cycle 108
Figure 5.10: The electromagnetic light spectrum 109
Figure 5.11: Beam encoder for propeller rpm detection. 110
Figure 5.12: Simple IR transmitter and NPN Phototransistor setup 111
Figure 5.13: IR absorbing marking applied to the blade tips 111
Figure 5.14: Schmitt trigger switching scheme and hysteresis zone. 112
Figure 5.15: Schmitt trigger using LM358P. 113
Figure 5.16: Schematic for the logic board IR transmitter and receiver. 113
Figure 5.17: IR receiver transmitter pair 114
Figure 5.18: Thrust rig supporting structure for the opto-reflective sensor 114
Figure 5.19: K1 RPM Meter 116
Figure 5.20: RS 291-4226 Incremental encoder with custom coupling. 116
Figure 5.21: Encoding phase A and B offset by 90 degrees 117
Figure 5.22: RPM comparison for uncoupled and couple encoder simulations with no blade. 118
Figure 5.23: Current draw for uncoupled and coupled encoder simulations with no blade. 118
Figure 5.24: RPM for uncoupled and couple encoder simulations with 11x4.7 blade. 119
Figure 5.25: Current draw for the 11x4.7 blade. 119
Figure 5.26: Custom built hall sensor rig. 120
Figure 5.27: Effect of the incorrect orientation of the magnet poles. 120
Figure 5.28: Overview of apparatus for thrust measurement. 121
Figure 5.29: KFG series strain gauge. 122
Figure 5.30: 2 and 4 gauge setup. 123
Figure 5.31: Active dummy-bridge 124
Figure 5.32: 4- gauge system with potentiometer(trim) adjustment. 127
Figure 5.33: Single strain gauge (half- bridge, Top side). 127
Figure 5.34: Half-Dummy-bridge circuit board. 128
Figure 5.35: Full –Bridge circuit board with and without trim correction 128
Figure 5.36: Double gauges (4-active strain gage setup, Top side). 129
Figure 5.37: PJ Dynamic strain amplifier rear panel 129
Figure 5.38: Strain gauge calibration curve 131
Figure 5.39: Thrust rig with gauges. 132

Figure 5.40: Variation in amplifier voltage output as a function of gain and beam height.. 136
Figure 5.41: Variation in beam length with yield strength 137
Figure 5.42: Variation in yield strengths with end tip mass..... 137
Figure 5.43: Coupling of the torque to thrust rig..... 139
Figure 5.44: Constructed torque tower..... 139
Figure 5.45: Current monitoring using a shunt resistor. 140
Figure 5.46: Battery and charge. 141
Figure 5.47: Hardware flow diagram. 141
Figure 5.48: NI Controller Setup with C-series modules and PSU..... 143
Figure 5.49: Anatomy of the FPGA (NI, n.d.). 144
Figure 5.50: Complete setup with propeller mount, IR beam and tachometer. 145
Figure 5.51: Beam deflection under resonance. 146
Figure 5.52: Graph of beam resonance. 147
Figure 5.53: Marked and unmarked 10x4.5” blades. 147
Figure 5.54: Noise on the IR beam sensor for a 9x4.7” propeller. 149
Figure 5.55: The effect of blade twist on RPM values. 149
Figure 5.56: RPM detection using the RS encoder (Aeolian 1000KV). 151
Figure 5.57: RPM detection using the IR-Beam apparatus (Aeolian 1000KV). 151
Figure 5.58: RPM detection using the Hall sensor (Aeolian 1000KV). 152
Figure 5.59: Variation in the sensor rpm's with respect to the Encoder rpm (Aeolian 1000KV). 152
Figure 5.60: Thrust variation with PWM signal (Aeolian 1000KVA). 153
Figure 5.61: Variation in the sensor rpm's with current draw (Aeolian 1000KV)..... 153
Figure 5.62: Beam IR encoder and photo-reflective encoder for 12x4.5” blade. 154
Figure 5.63: Difference in IR beam and opto-RPM apparatus for 12X4.5” blade..... 154
Figure 5.64: Variation in the motor torque with PWM input (11x4.7” blade). 155
Figure 5.65: RPM difference filter applied to the RPM time curve 157
Figure 5.66: Binary filter 2 applied to the RPM difference curve. 158
Figure 5.67: Binary filter 3 and 4 applied post difference filters..... 159
Figure 5.68: Binary filters 3 and 4 combined into a binary 5 filter..... 160
Figure 5.69: Binary Filter 6 for the isolation values (570KV-11X4.7” Prop). 160
Figure 5.70: Average RPM data points for constant throttle plateau’s (570KV-11X4.7” Prop). 161

Figure 5.71: Average thrust data points for constant throttle plateau's (570KV-11X4.7" Prop)..... 161
Figure 5.72: Average torque data points for constant throttle plateau's (570KV-11X4.7" Prop)..... 162
Figure 5.73: Average RPM values as a function of experimental time (570KV-11X4.7" Prop). 162
Figure 5.74: Average thrust values as a function of experimental time (570KV-11X4.7" Prop)..... 163
Figure 5.75: Average torque values as a function of experimental time (570KV-11X4.7" Prop)..... 163
Figure 5.76: Thrust as a function of RPM for 570KV with an 11X4.7" prop. 164
Figure 5.77: Second order polynomial for RPM vs torque for 570KV-11X4.7" prop. 164
Figure 5.78: PWM vs Average Thrust for 570KV-11X4.7" prop. 165
Figure 5.79: Third order polynomial for PWM vs RPM for 570KV-11X4.7" prop. 165
Figure 5.80: An overview of the created Binary Shift algorithm. 166
Figure 5.81: A problematic RPM difference curve data set. 167
Figure 5.82: Plot of thrust vs RPM for a threshold value=0.2. 168
Figure 5.83: Plot of thrust vs RPM for a threshold value=1.2. 169
Figure 5.84: Plot of thrust vs RPM for a threshold value =0.7. 169
Figure 5.85 Plot of thrust vs RPM representing a data set that cannot be processed..... 170
Figure 6.1: Overview the data processing and presentation process. 172
Figure 6.2: Thrust variation for all test runs. 173
Figure 6.3: Current variation for all test runs. 173
Figure 6.4: Comparative analysis of all tested motors. 175
Figure 7.1: Simplified Simulink quadrotor motor representation. 180
Figure 7.2: Expanded view of the plant model. 181
Figure 7.3: Decision blocks for the drag terms in the SIMULINK model. 182
Figure 7.4: PWM actuator control as a step input (Matlab). 183
Figure 7.5: PWM signal for all motors during the ascent phase. 184
Figure 7.6: Variation in displacement with time during the ascent phase. 185
Figure 7.7: Variation in translational velocity with time during the ascent phase. 185
Figure 7.8: Variation in angular displacements with time during the ascent phase. 186
Figure 7.9: Variation in angular velocity with time during the ascent phase. 186

Figure 7.10: Trajectory plot during the ascent phase from base. 187
Figure 7.11: PWM signal for all motors during the hover phase. 188
Figure 7.12: Variation in displacement with time during the hover phase. 188
Figure 7.13: Variation in the translational velocity with time in the hover phase. 189
Figure 7.14: Variation in angular displacements with time during the hover phase. 189
Figure 7.15: Variation in angular velocity with time during the hover phase. 190
Figure 7.16: PWM signal for all motors during a signal perturbation on motor 4. 191
Figure 7.17: Variation in the displacement with time in the excitation phase. 191
Figure 7.18: Variation in the linear velocity with time in the excitation phase. 192
Figure 7.19: Variation in the angular displacement with time in the excitation phase. 192
Figure 7.20: Variation in the linear velocity with time in the excitation phase. 193
Figure 7.21: Trajectory plot during the excitation phase. 193
Figure 7.22: PWM input for the landing phase of the mission. 194
Figure 7.23: Variation in displacement with time during the descent phase. 195
Figure 7.24: Variation in translational velocity with time during the descent phase. 195
Figure 7.25: Variation in angular displacements with time during the descent phase. 196
Figure 7.26: Variation in angular velocity with time during the descent phase. 196
Figure 7.27: Trajectory plot during the descent phase. 197
Figure 8.1: Quadrotor UAV preliminary design. 201
Figure 8.2: Avionics integration into proposed chassis. 202
Figure A.1: Propeller raw data curves for a 390KV motor. 209
Figure A.2: Popeller raw data curves for a 490KV motor. 209
Figure A.3: Propeller raw data curves for a 570KV motor. 210
Figure A.4: Propeller raw data curves for a 690KV motor. 210
Figure A.5: Propeller raw data curves for a 1000KV motor. 211
Figure A.6: Propeller raw data curves for a 1200KV motor. 211
Figure A.7: Variation in RPM for 9x4.7” propeller with different motor combinations. 212
Figure A.8: Variation in RPM for 10x4.5” propeller with different motor combinations. 212
Figure A.9: Variation in RPM for 11x4.5” propeller with different motor combinations. 213
Figure A.10: Variation in RPM for 11x4.7” propeller with different motor combinations. 213
Figure A.11: Variation in RPM for 12x4.5” propeller with different motor combinations. 214
Figure A.12: Variation in RPM for 9x4.5” tri-blade propeller with different motor combinations 214

Figure A.13: Flight time and efficiency vs. resultant force for 390KV with a single battery. 215
Figure A.14: Flight time and efficiency vs. resultant force for 490KV with a single battery. 215
Figure A.15: Flight time and efficiency vs. resultant force for 570KV with a single battery. 216
Figure A.16: Flight time and efficiency vs. resultant force for 690KV with a single battery. 216
Figure A.17: Flight time and efficiency vs. resultant force for 1000KV with a single battery. 217
Figure A.18: Flight time and efficiency vs. resultant force for 1200KV with a single battery. 217
Figure A.19: Flight time and efficiency vs. resultant force for 390KV with a dual battery.. 218
Figure A.20: Flight time and efficiency vs. resultant force for 490KV with a dual battery.. 218
Figure A.21: Flight time and efficiency vs. resultant force for 570KV with a dual battery.. 219
Figure A.22: Flight time and efficiency vs. resultant force for 690KV with a dual battery.. 219
Figure A.23: Flight time and efficiency vs. resultant force for 1000KV with a dual battery. 220
Figure A.24: Flight time and efficiency vs. resultant force for 1200KV with a dual battery. 220
Figure A.25: Flight time and efficiency vs. resultant force for 390KV with a tri-battery..... 221
Figure A.26: Flight time and efficiency vs. resultant force for 490KV with a tri-battery..... 221
Figure A.27: Flight time and efficiency vs. resultant force for 570KV with a tri-battery..... 222
Figure A.28: Flight time and efficiency vs. resultant force for 690KV with a tri-battery..... 222
Figure A.29: Flight time and efficiency vs. resultant force for 1000KV with a tri-battery... 223
Figure A.30: Flight time and efficiency vs. resultant force for 1200KV with a tri-battery... 223
Figure B.1: Strain Gauge Technical specifications 225
Figure C.1: Mechanical Data of Incremental Shaft encoder 227
Figure C.2: Electical Data of Incremental Shaft encoder 227
Figure C.3: Connection Diagram of Incremental Shaft encoder 228
Figure C.4: Ordering Data of Incremental Shaft encoder 228
Figure C.5: Start-up and throttle range procedures for ESC arming 229
Figure C.6: Programming ESC with the transmitter..... 230

Figure D.1: Plan view of the vehicle during a clockwise (+ve) yaw rotation 232
Figure D.2: A +ve pitch rotation of a coordinate system in 3-D 234
Figure D.3: A +ve roll rotation of a coordinate system in 3-D 235
Figure D.4: A +ve yaw rotation of a coordinate system in 3-D 236
Figure E.1: Main Setup Flow chart 240
Figure E.2: Control messages from the user 241

List of Tables

Table 1: ACK bit table....53
Table 2: CPOL and CPHA summary combination table....55
Table 3: ITG-3200 3-Axiz gyroscope specifications (Invensense, n.d.)....75
Table 4: Table of Rotation for accelerometer calibration....78
Table 5: Pin mapping for LIS3DH accelerometer (ST Electronics, 2010)....86
Table 6: KFG-3-120-C1-11L1M2R gage mechanical properties....122
Table 7: Fixed geometrical parameters for the thrust apparatus....135
Table 8: Quadrotor total mass variation with battery capacity....176
Table 9: Variation in performance parameters with propeller and battery combinations. 177

Nomenclature

Symbol	Description
B_a	Frictional force coefficient
C_D	Coefficient of drag
$\overrightarrow{F_{D_E}}$	Drag force vector along the earth-fixed axes
F_{Dx}, F_{Dy}, F_{Dz}	Components of the drag force along the earth-fixed *x, y* and *z*-axes respectively
F_{BX}, F_{BY}, F_{BZ}	Forces along the body-fixed *x, y* and *z* axes respectively
$\overrightarrow{F_{W_z}}$	Weight vector in the earth-fixed axes
$F_{W_{Bx}}, F_{W_{By}}, F_{W_{Bz}}$	Weight components along the *x, y* and *z*-axes of the body-fixed axes respectively
g	Earth's gravitational acceleration

I_B	Tensor of inertia matrix in the body-fixed axes
$I_{xx}, I_{yy,} I_{zz}$	Moment of inertia about x_b , y_b and z_b respectively
I_{xy}, I_{yz}, I_{xz}	Moment of inertia about $x_b y_b$, $y_b z_b$ and $x_b z_b$ planes respectively
l_{arm}	Quadrotor arm length
M_A	Moments calculated about the propeller hub centre point
m_{hub}	Mass of central hub
m_{rotor}	Mass of propeller and rotor combination
$M_{xb}, M_{yb}\ M_{zb}$	Net moment generated about x_B, y_B and z_B axes respectively
M_{XT_b}	Pitching moment generated by the thrust force in the body-fixed axes
M_{YT_b}	Rolling moment generated by the thrust force in the body-fixed axes
M_{Drag}	Moment due to the drag force
$M_{Electromotive}$	Electromotive moment

$M_{Friction}$	Frictional moment
$M_{inertia}$	Inertial moment
$M_{Gx_B}, M_{Gy_B}, M_{Gz_B}$	Gyroscopic moment about the body-fixed *x, y* and *z*-axes respectively
m_{TOTAL}	Quadrotor mass
m_{sphere}	Central sphere mass
$m_{battery}$	Battery mass
R_{hub}	Radius of propeller hub
R	Propeller blade radius
$\mathbb{T}_{BE}$	Matrix of transformation from the earth-fixed to body-fixed axes
$\mathbb{T}_{EB}$	Matrix of transformation from the body-fixed to earth-fixed axes
T_{rotor1}	Thrust produced by motor 1
T_{rotor2}	Thrust produced by motor 2
T_{rotor3}	Thrust produced by motor 3
T_{rotor4}	Thrust produced by motor 4
T_{Rt1}	Frame torque reaction for motor 1

T_{Rt2}	Frame torque reaction for motor 2
T_{Rt3}	Frame torque reaction for motor 3
T_{Rt4}	Frame torque reaction for motor 4
$\mathbb{T}_{Eb_\psi}$	Yaw transformation
$\mathbb{T}_{Eb_\theta}$	Pitch transformation
$\mathbb{T}_{Eb_\phi}$	Roll transformation
T_{total}	Total thrust
T_{min}	Minimum thrust

Symbol	**Description**
ρ	Air density
$\vec{\Omega}$	Angular velocity vector
$\omega_{1,2,3,4}$	Angular velocity of rotors 1, 2, 3 and 4 respectively
$\dot{p}, \dot{q}, \dot{r}$	Rate of change of the roll, pitch and yaw rates respectively
p_0, q_0, r_0	Roll, pitch and yaw accelerations respectively

ϕ, θ, ψ	Roll, pitch and yaw angles respectively
$\dot{\phi}, \dot{\theta}, \dot{\psi}$	Rate of change roll, pich and yaw angles respectively.
ϕ_0, θ_0, ψ_0	Initial roll, pitch and yaw angles at t=0

Acronym	**Description**
A	Amp
AOA	Angle of Attack
ASIC	Application-specific integrated circuit,
AHRS	Attitude and heading reference system
BLDC	Brushless Direct Current
BLDCM	Brushless Direct Current
CS	Chip select
CTS	Clear to send
CPHA	Clock phase
CPOL	Clock polarity
DSR	Data set ready

DTR	Data terminal ready
DOF	Degree of freedom
DIO	Digital input output
ESC	Electronic speed controller
FPGA	Field programmable gate array
GUI	Graphical user interface
IR	Infrared
I2C	Inter-Integrated Circuit
MISO	Master in slave out
MOSI	Master out slave in
MSB	Most significant bit
PPM	Pulse position modulation
PWM	Pulse width modulation
RC	Radio control
RGB	Red-Green-Blue
RTS	Request to send

RPM	Revolutions per a minute
SCL	Serial clock line
SCLK	Serial clock
SDA	Serial data line
SPI	Serial Peripheral Interface
SS	Slave select
UAV	Unmanned aerial vehicle
VTOL	Vertical take-off and landing
VHSIC	Very-high-speed integrated circuits
VHDL	VHSIC hardware description language

1. Introduction

1.1 Research Background

The Unmanned Aerial Vehicle (UAV) is an aircraft with no pilot on board. They can be controlled remotely by an operator, or can be controlled autonomously via pre-programmed flight paths. Complex and risky missions without any on-board human involvement are the biggest advantage of UAV' s. UAV's have attracted considerable interest for a variety of applications. Such aircraft have already been implemented by the military for reconnaissance flights, convoy protection, search and rescue operations and military attack missions. Future combat operations will continue to place unmanned aircraft in challenging conditions such as the urban warfare environment. However, the poor reliability, reduced autonomy and operator workload requirements of current unmanned vehicles present a roadblock to their success. It is anticipated that future operations will require multiple UAVs performing in a cooperative mode, sharing resources and complementing other air or ground assets. Surveillance and reconnaissance tasks that rely on UAVs require sophisticated modelling, planning and control technologies (Vachtsevano, et al., 2007). Civilian applications range from fire fighting, site surveying, non-military security work, such as surveillance of pipelines, photography to meteorological work.

While fixed-wing vehicles are suited for certain application due to their range, speed and flight duration, rotorcraft or Vertical Take-Off and Landing (VTOL) vehicles are considered to be more preferable for surveillance, precise delivery and for missions requiring agility

and accuracy. Rotorcraft agility can be attributed to it having very few constraints on motion and require less launching and landing support compared to alternate fixed-wing.



Figure 1.1: Raven B Mini UAV being deployed by a soldier for reconnaissance

Control of the quadrotor is accomplished by varying the speeds of the four motors relative to each other. The four rotors present dual purposes as they are the sole sources of lift and the only form of control. Quadrotors naturally demand a sophisticated control system in order to allow for balanced flight. Controlled flight of a quad-rotor would be virtually impossible by one operator, as the dynamics of such a system demand constant adjustment of four motors simultaneously. This inherent instability allows for complex stability controllers and algorithms to be implemented and tested (DiCesare, et al., 2008).

1.2 Research Rationale and Motivation

The low cost and simplicity of the quadrotor design provides an excellent testing ground for application of advanced system identification and control techniques which are ideally suited for research institutes and universities with small budgets. Prior to the design and build of the quadrotor, it is essential that a form of system identification is performed in order to ascertain the correct powerplant parameters. Identified powerplant parameters allow for simulations to be carried out, analysed and improved prior to costly construction.

1.3 Problem Statement

A quadrotor has apparent advantages over other rotary wing UAVs. It is mechanically simple and is controlled by only changing the speed of rotation for the four motors. The low cost and simplicity means the quadrotor provides an excellent testing ground for the application of advanced control techniques on UAV's. However, the technical challenges for small rotary-wing UAV systems are numerous. High thrust-to-weight ratios are necessary for the propulsion system. An endurance long enough to perform a meaningful mission is the highest priority. In order to achieve this goal a careful matching of aircraft mass, batteries, electric motors, and rotors is imperative. The absence of a method to measure the parameters of interest that allow for a careful pairing of hardware is a problem that needs to be addressed. This is an essential pre-requisite for optimal simulation and cost effective testing.

1.4 Literature Review

It is pertinent that the function, construction and existing designs of the quadrotor be explored. This allows for the overall function of the quadrotor to be understood whilst setting the foundation for the rig design in terms of the present and future implementation.

1.4.1 Quadrotor Operation

Each rotor in a quadrotor is responsible for a certain amount of thrust and torque about its centre of rotation, as well as for a drag force opposite to the rotorcraft's direction of flight. The quadrotor's propellers are not all alike. They are divided in two pairs, two pusher and two puller blades, which work in contra-rotation (Rawashdeh, et al., 2009). As a consequence, the resulting net torque can be null if all propellers turn with the same angular velocity, thus allowing for the aircraft to remain still around its centre of gravity. Aircraft orientation (or attitude) around its center of mass is described by the angles of yaw, pitch and roll. This is very useful because the forces used to control the aircraft act around its center of mass, causing it to pitch, roll or yaw.

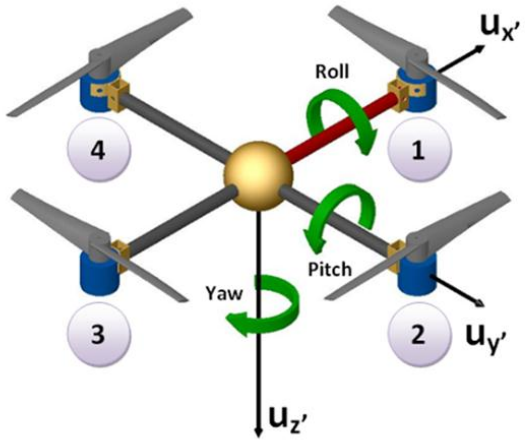

Figure 1.2: Yaw, pitch and roll rotations of a quadrotor

Changes in the pitch angle are induced by contrary variation of speeds in propellers 1 and 3 (see Figure 1.2), resulting in forward or backwards translation. If we do this same action for propellers 2 and 4, we can produce a change in the roll angle and we will get lateral translation. Yaw is induced by mismatching the balance in aerodynamic torques (i.e. by offsetting the cumulative thrust between the counter-rotating blade pairs). By changing these three angles in a quadrotor we are able to make it manoeuvre in any direction as illustrated in Figure 1.3 (DiCesare, et al., 2008) (Rimestad, et al., 2008) (Finkpetersen, 2008).

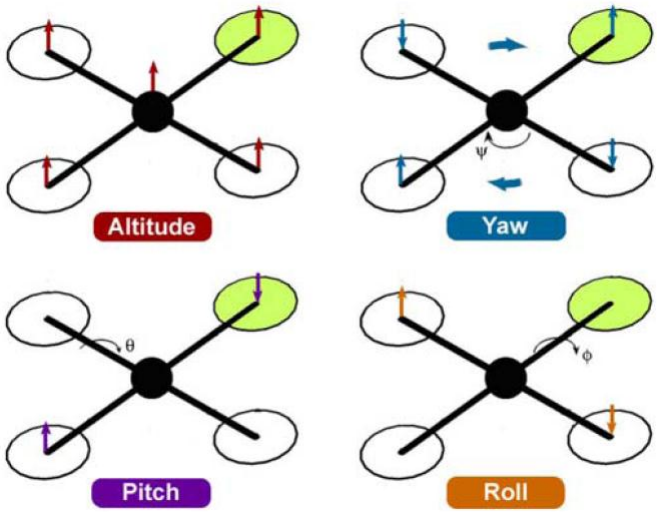

Figure 1.3: Variation in motor speed to create control, the front denoted by a green circle (Raza & Gueaieb, 2010).

1.4.2 Existing Quadrotor Designs

Quadrotor implementations and studies do not limit themselves to the academic environment. In the last decade, several commercially available models have appeared in the market, with a variety of models available from entertainment specific to custom built units intended for use in research and development facilities and private organisations. The following sections highlight features of the respective brands.

1.4.2.1 Draganflyer X4 and E4

The Draganflyer X4 UAV (shown in Figure 1.4) is commercially available and used for aerial photography and video. It was designed to minimize the cost of aerial photography and decrease the overall time in obtaining high-quality images from inaccessible locations. Self-stabilization of the UAV is achieved via the use of magnetometers, accelerometers, barometric pressure sensors and an advanced flight computer allowing for the user to focus on the photography aspect. The direct drive four brushless motors and carbon fibre rotor blades are the only moving parts in the assembly. It can also be easily assembled and disassembled for easy transit (Innovations, n.d.).



Figure 1.4: Draganflyer X4 UAV (Innovations, n.d.)

1.4.2.2 CyberQuad Mini

CyberQuads are electric ducted quadrotor VTOL UAV. A unique amalgamation of state-of-the-art VTOL UAV technologies, CyberQuads combine the mechanical simplicity, low noise, stability and agility of a quadrotor with the compactness, safety and efficiency of ducted fans. Figure 1.5 illustrates the shrouded design which provides added safety from the rotor blades. The CyberQuads are low maintenance, easily transportable and rapidly deployable. The ducted rotor design produces more lift in forward flight, enabling efficient cruise and higher forward velocity. Autonomous navigation is achieved through way point navigation, auto-take-off and the Ground Control Station (with its aerial map interface) (Cybertechnology, n.d.).



Figure 1.5: Cyber Quad mini (Cybertechnology, n.d.)

1.4.2.3 Asctec Hummingbird

The Asctec Hummingbird series as shown in Figure 1.6 are manufactured in Germany by Ascending Technologies. They offer a range of multi-rotor systems, which can carry payloads up to 500 grams. Beginning with sizes from small and compact to the very large they can customize the structure to the required on-board hardware. The modular structure enables fast component changes in case of a crash or modification during integration and testing. Various derivatives are available depending on the research task at hand. The hardware can be expanded to the following options: an Atom Processor board, different cameras, laser scanners and other accessories. These are mainly purchased for research purposes and up until recently have branched into aerial photography (Ascending Technologies, n.d.).

1.4.2.4 Microdrone

Microdrone is a German company specialising in the development of aerial vehicles such as the MD4-1000 illustrated in Figure 1.7 which are based on the principle of quadcopters. The two most popular derivatives are the MD4-200 and the MD4-1000. The MD4-200 has a peak thrust output of 15.5 N with a max take-off weight (MTOW) of 1100g using 4S Lithuim polymers rated at 2300Mah. The bigger MD4-1000 has a peak thrust of 118N with a MTOW of 5550g using 6S2P Lipo's rated at 22V and 13000mAh. A modular payload concept allows us, to flexibly adapt the equipment to the intended mission. The availability of a high resolution digital still camera, several video solutions adapted to very different lighting conditions and also a high-end thermography heat imaging systems ensures the capability to carry out miscellaneous tasks of image recording and image broadcasting (Microdrone, n.d.).



Figure 1.6: Ascending Technologies Hummingbird UAV's (Ascending Technologies, n.d.)



Figure 1.7: Microdrone Quadrotor UAV (Microdrone, n.d.)

1.4.2.5 Parrot AR Drone

The Parrot AR Drone has a strong footing in the toy market (shown in Figure 1.8). Its foam outer shell maintains a low take-off weight and provides improved aerodynamics via the ducted/shrouded fan design. It is controlled via an iPhone/iPod Touch using the built in accelerometers to deliver pitch and roll commands wirelessly. Two cameras feed-back to the controller, allowing the user to navigate remotely. The low weight of the craft does not make it suitable for a medium or high disturbance environment, and the weight reductions mean a smaller battery capacity which directly affects the flight time of the platform (David Schmidt, 2011).



Figure 1.8: Parrot AR Drone

1.4.3 Basic Quadrotor Mechanical Design/ Hardware

A benefit of electric quad-rotor robots is their mechanical simplicity. With few moving parts and brushless motors, the quadrotor remains simple and cost effective. Figure 1.9 and Figure 1.10 illustrates the basic quadrotor components. Quadrotors consist of four arms and a central hub which house all the avionics. The central hub is shaped like a cage to protect the flight system from collision during a crash and is constructed from a carbon fibre sandwich ensuring a high integrity and a relatively low weight. The sandwiched plates are joined using custom built connecting rods. Parts are done in pair ensuring a symmetrical frame design that does not need to be trimmed constantly during flight (Craciunas, et al., 2008). The cage housing the avionics is a structural member and is

required to sustain large loads in event of a crash preventing costly damage as shown in Figure 1.9. The sensors form the feedback system allowing for the controller to compensate for any changes or disturbances to the state.



Figure 1.9: A custom built cage for the JAviator (Craciunas, et al., 2008)

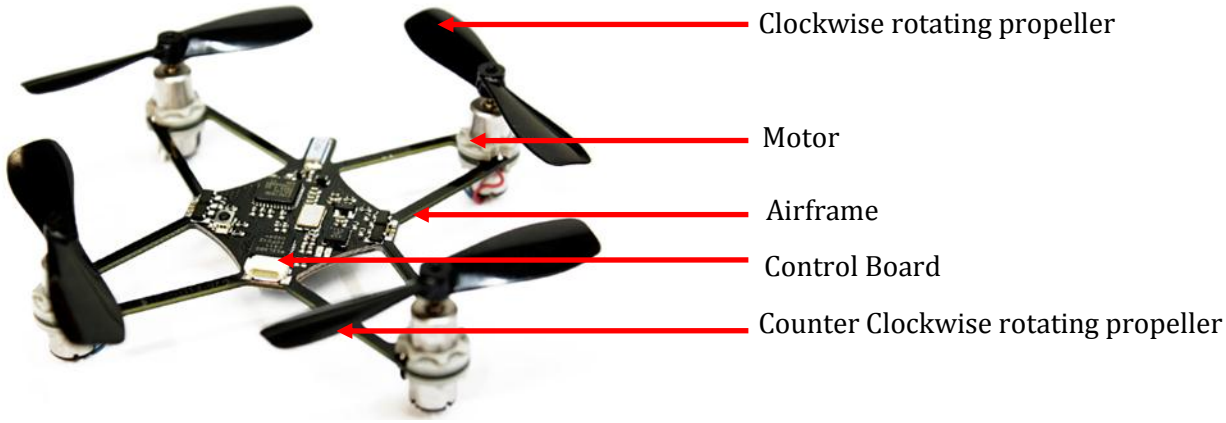

Figure 1.10: Quadrotor Construction

1.4.4 Motors, Propellers and Testing

The rotors, motor and battery determine the flight time of the Quadrotor. The rotors, especially, influence the natural dynamics and power efficiency. Pounds (Pounds, et al., 2004) used momentum theory to provide a relationship between thrust, induced velocity and power. A further study was then commissioned on the modelling of blade flapping and aeroelasticity. The simulations on the propeller were conducted using a Matlab iterative simulator finding the steady-states. This generated a custom-built propeller airfoil called

the ANUX2 (Figure 1.11) with ideal chord and twist. The powerplant current drawn was recorded at a total of 22 amps at 12V constituting a flight time of 8mins.



Figure 1.11: ANUX2 developed by Pounds (Pounds, et al., 2004)

Bristeau (Bristeau, et al., 2009) studied the aerodynamic effects of the propeller and its interaction with the motion of the rigid body of the UAV. He concluded that the flexibility of the propeller blades play a vital role in the dynamics of the UAV in a low frequency domain and should be compensated for in a closed-loop system.

Di Cesare (DiCesare, et al., 2008) constructed a pivot type apparatus as seen in Figure 1.12 for the testing of the thrust produced by different rotor blades versus power input. The test was conducted by placing the motor and the blade on one side of the balance and as the thrust increased, it had the opposite effect on the opposing side of the balance and pressed down on a scale to demonstrate the downward force. Five different blade designs were tested with various airfoils, diameters, pitch, and number of blades. The APC 9x6" propellers were selected due to the high thrust to current ratio.

Hoffman (Hoffmann, et al., 2007) evaluated the motor and rotor characteristics using a thrust test stand as shown in Figure 1.13. It measures the forces and torques using a load cell with adjustable lever allowing for load sensitivity to be varied. An Atmel microprocessor board was programmed to perform motor control through its pulse width modulation (PWM) outputs, and to acquire analog inputs from the load cell, current sensor, and battery voltage. The microprocessor board interfaces with a data acquisition program on the PC to perform automated tests, making measurements at 400 samples per second, well faster than the Nyquist frequency of the rotor rotation effects being measured. To perform some experiments, external wind was applied using a fan. Wind speeds were measured using a Kestral 1000 wind meter, with a rated accuracy of ±3%.



Figure 1.12: Pivot type apparatus set for thrust calculation (DiCesare, et al., 2008)

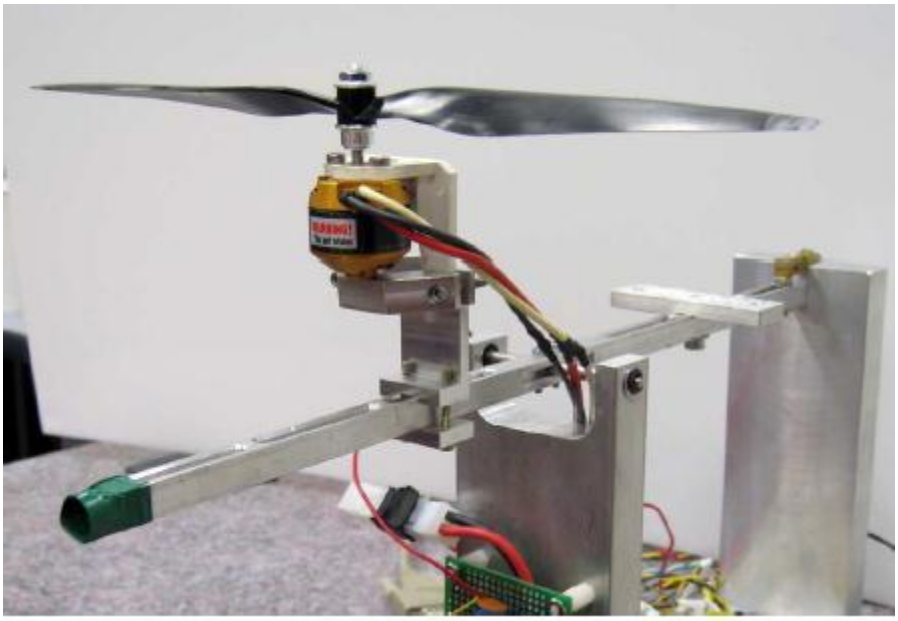

Figure 1.13: STARMAC Thrust rig (Hoffmann, et al., 2007)

Oliveira (Oliveira, 2011) measured the torque generated by the motor of the quadrotor by placing its Z-axis perpendicular to the gravity vector effectively blocking the DOFs around the other axes. As seen in Figure 1.14, a rigid lever was attached to the aircraft's center of

mass and its other end applied to the scale, so that the torque(M) caused on the quadrotor's airframe due to the rotation of a rotor.

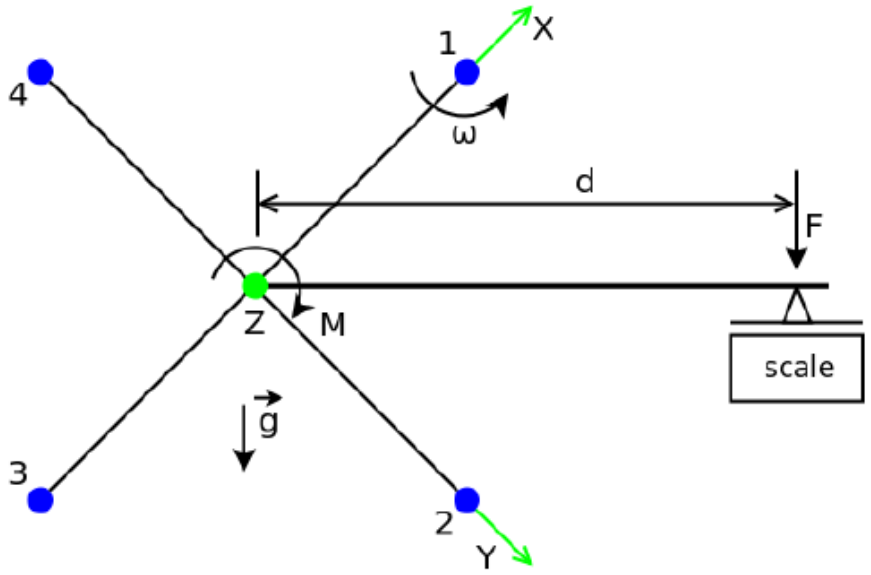

Figure 1.14: Setup for rotor torque identification experiment (Oliveira, 2011)

1.5 System Identification

System identification deals with finding the system model *f* and *g* given the measured input *u* and corresponding output *y* as illustrated in Figure 1.15. This form of identification is in essence identifying the mathematical model which may consist of differential equation with unknown parameters which are determined implicitly from experimental data including inputs related to a specified response. In modelling terms it may be interpreted as determining the equations and unknown modelling parameters Θ such that the model output *y* is matched by the system response *z*.

System identification can be identified as the inverse problem with the basic function of determining the mathematical model structure representative of a dynamic system, however if the developed structure does not satisfy target convergence then the model has to be recreated. The identification process amounts to repeatedly selecting a model structure, computing the best model in the structure, and evaluating this model's properties to see if they are satisfactory. Pounds (Pounds, et al., 2007) performed system identification

of a brushless on a hobby motor driving a custom rotor. The system plant was then identified using a step excitation experiment. Experiments were used to characterise the expected load disturbances culminating in a proportional controller design which reduced the rise times and propagation of disturbances.

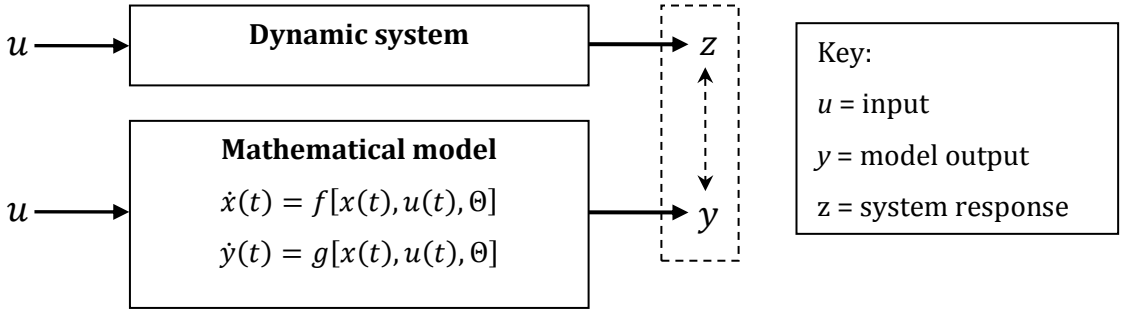

Figure 1.15: Process of System identification

Stanculeanu and Boranglu (Stanculeanu & Borangiu, 2011) presented a new approach in the identification of the quadrotor dynamic model using a black-box system for identification. The predication error method allowed for identification of the closed-loop system to be performed with Proportional-Integral-Derivative (PID) based flight stabilization regulators.

1.6 Identified Gaps in the Literature

In the development of quadrotor UAV's, modelling, simulation and control have played a vital role (Domingues, 2009) (Salih, et al., 2010). While there has been a lot of research done on the modelling of such a system with motor equations and blade aerodynamics (Pounds, et al., 2004) (Huang, et al., 2008), none have considered the development of an apparatus set and data sorting algorithm that has the capability of capturing the physical variation of the thrust vector with motor rating, blade pitch, blade diameter a high level of repeatability. In contrast, Christiaan et al. (Finkpeterson, et al., 2008) used the technique of system identification to quantify the variation in thrust with RPM and through a analytical solver and ascertained the relationship for a single setup. However, if we are to argue that there is no existing research on an apparatus set along with a data processing algorithm that is

capable of adequately capturing the relationships with a high level of repeatability, then this remains a gap to be filled. This report will suggest key issues which need to be addressed when considering the development of such an apparatus set along with the coupled data sorting algorithm, additionally it will verify the functioning of the identified trends via a custom built mathematical model.

1.7 Research Objectives

It remains the aim of this project that the following outcomes are achieved:

- The powerplant of the quadrotor to be defined in terms of the relationship between the inputs and outputs.
- Rigs for RPM, thrust and torque need to be constructed in order to extract the parameters with as greater accuracy as possible.
- The collected data will then be used as input parameters into the mathematical model allowing for an increased realism during simulation.
- A constructed mathematical model allowing for the quadrotor model to be perturbed and the output parameters to be studied.
- The effects of changes in geometry and power plant on the mathematical model will be studied, in order to create a cost effective testing and simulation environment.

1.8 Research Scope and Limitations

This thesis will specifically look at an isolated method of extracting the relationships between the input and output parameters of the powerplant using a constructed rig with coupled data sorting algorithm. The data sets will be limited to the availability of propeller and motor combinations. The available motors varied in 6 increasing ratings mainly the 390KV, 490KV, 570KV, 690KV, 1000KV and 1200KV. The available propellers varied in 3 increasing diameters mainly the 9”x4.7, 10”x4.5, 10”x4.7, 11”x4.7, 12”x4.5 respectively. This allows for 30 unique data sets to be generated emphasising the need for repeatability in the data sorting phase. The development of the algorithm along with manipulation techniques employed will be explored. Mathematical modelling will be limited to the designed mission profile due to the absence of a developed controller catering for dynamic conditions.

1.9 Research Strategy and Methodology

The presented strategy is to find solutions to the problem statement and satisfy the research objectives presented in the aforementioned sections. Compared to earlier studies this work suggests the quadrotor design cycle be composed of a pre-development phase which avoids costly hardware implementation (DiCesare, et al., 2008). The system can be implemented with accuracy and consistency in terms of data collection and processing. Figure 1.16 illustrates the research flow of activities which are segmented into two main parts, the real time testing, data collection, simulation and analysis.

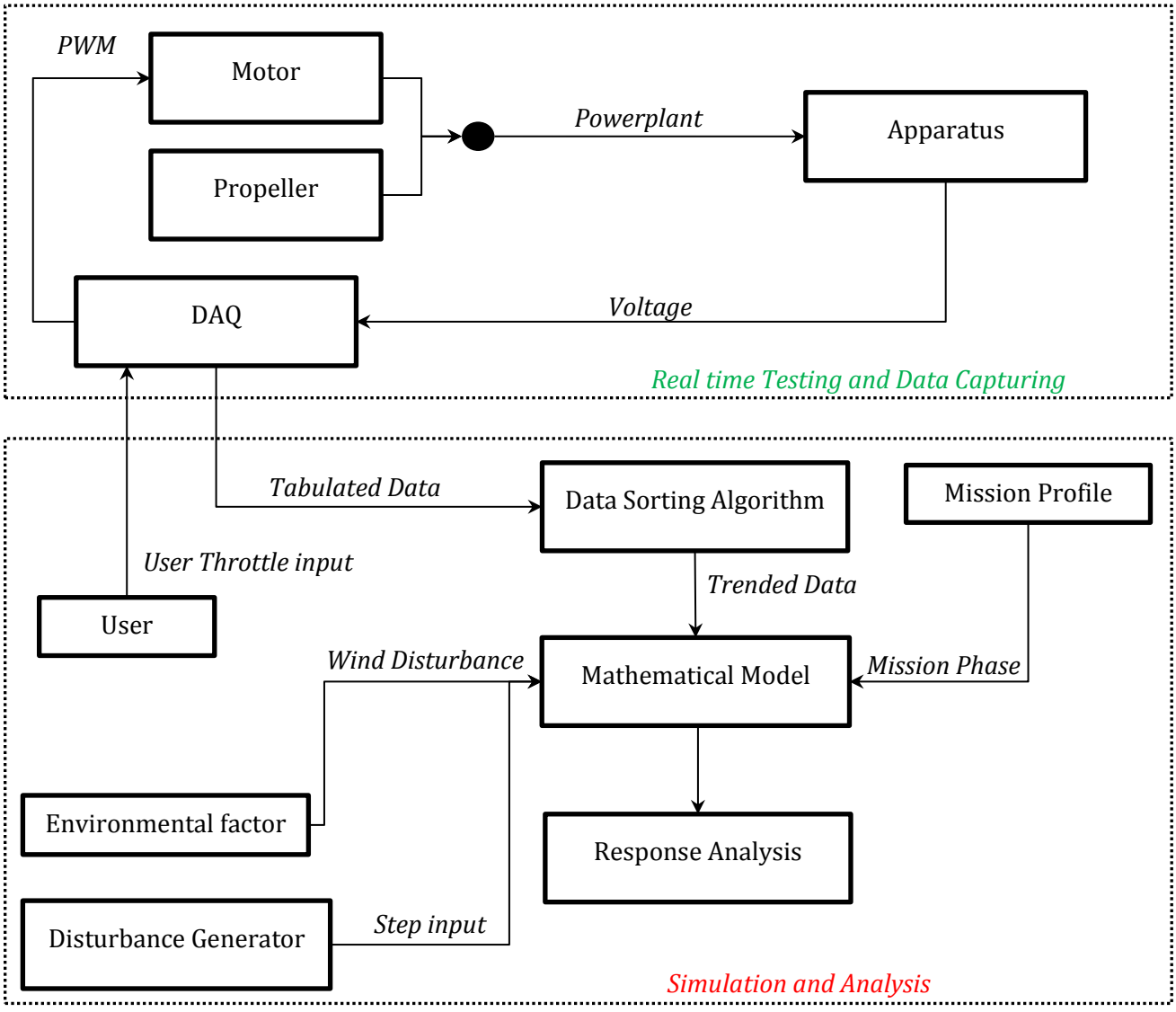

Figure 1.16: Flow of research activities

The real time testing and data collection is associated with the setup of the powerplant and propeller combination, voltage configuration and data formatting. Data acquisition will be performed using the SBRIO-9602 controller with add-on modules purchased from the National Instruments group. A data acquisition and processing strategy will have to be devised and implemented to allow for fast yet accurate data analysis. Post data acquisition, the parameters of interest will need to be identified and trended allowing for a variation in input, to condition the output. The quadrotor attitude is required to be simulated via a custom built 6-DOF mathematical model which caters for atmospheric input and allows for the insertion of the trended and identified powerplant parameters. The quadrotor performance can then simulated and evaluated using a variation in control input.

1.10 Research Contributions

Provided the research objectives are satisfied this thesis will outlay the process and procedures to adequately identify the parameters necessary for accurate modelling of a quadrotor power-plant. In achieving the outlined objectives the adopted process and procedures will contribute the following to research:

- Relationship between the power-plants inputs and outputs have been identified using a set of constructed test rigs dedicated to data acquisition.
- A data sorting algorithm was developed capable of sorting data quickly and effectively using a newly developed technique.
- Identified power-plant parameters allowing for effective and accurate simulation.
- A cost effective and efficient testing environment for parameter sensitivity analysis.
- An effective tool for Quadrotor design prior to a physical build.

1.11 Dissertation Outline

Figure 1.17 outlines the research conducted for this thesis. The left hand column highlights the major research sections covered and the right hand side further segments these categories.

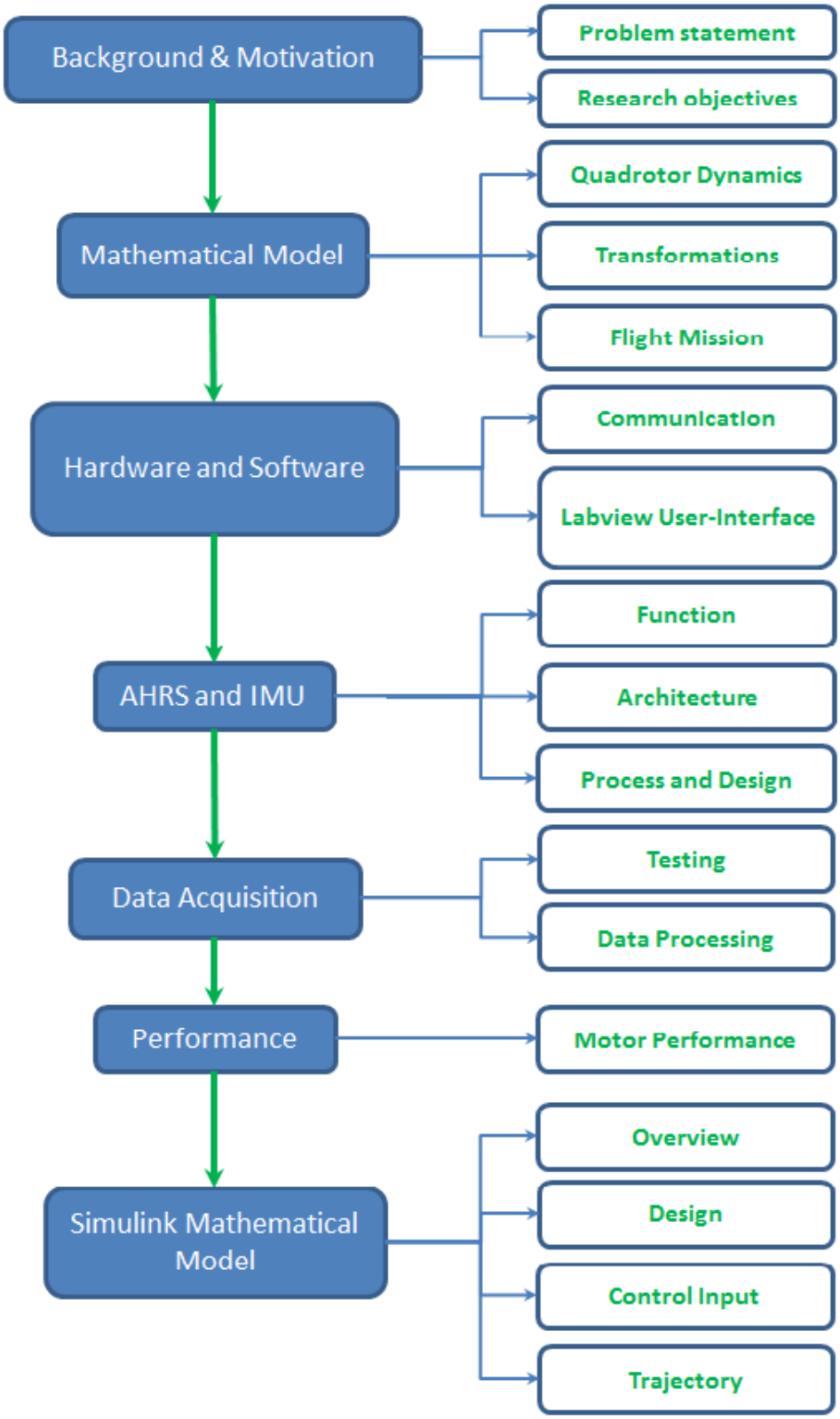

Figure 1.17: Dissertation Outline

2. Physical and Mathematical Model of the System

2.1 The need for an Aerodynamic Model

It is a necessary first step to conceive a mathematical model for the appropriate description of the physics of the system in order to address the estimation of aerodynamic parameters using the proposed computational techniques. This develops a further understanding of the mathematical procedures used and their relevant implication on the dynamics of the system whilst giving insight into the effects of simplifications used. Simplifications to the model outlined in section 2.3 are presented in order to avoid complexity but still maintain a fair degree of precision. The model used is based on a 6 degree of freedom system (6DOF) used to model aircraft.

2.2 Frames of Reference

The following frames of reference will be used in the present study.

2.2.1 Inertial Frame

Earth is regarded as a flat and stationary inertial space. Any coordinate system or frame of reference attached to the Earth is an inertial system. An inertial frame of reference can

described as a frame in which all of Newton laws are obeyed. This frame is needed to formulate the equations of motion of the quadrotor (Etkin & Duff Reid, 1996).

2.2.2 Body-Fixed Axes

Body-fixed axes as shown in
, are defined and fixed relative to the body of the vehicle (Etkin & Duff Reid, 1996):

- X_B axis is aligned along the vehicle body and is usually positive toward the normal direction of motion.

- Y_B axis is at a right angle to the x body axis and is oriented along the wings of the vehicle. If there are no wings (as with a missile), a "horizontal" direction is defined in a way that is useful. The Y_B axis is usually taken to be positive to right side of the vehicle.

- Z_B axis is perpendicular to wing-body (X_BY_B) plane and usually points downward.

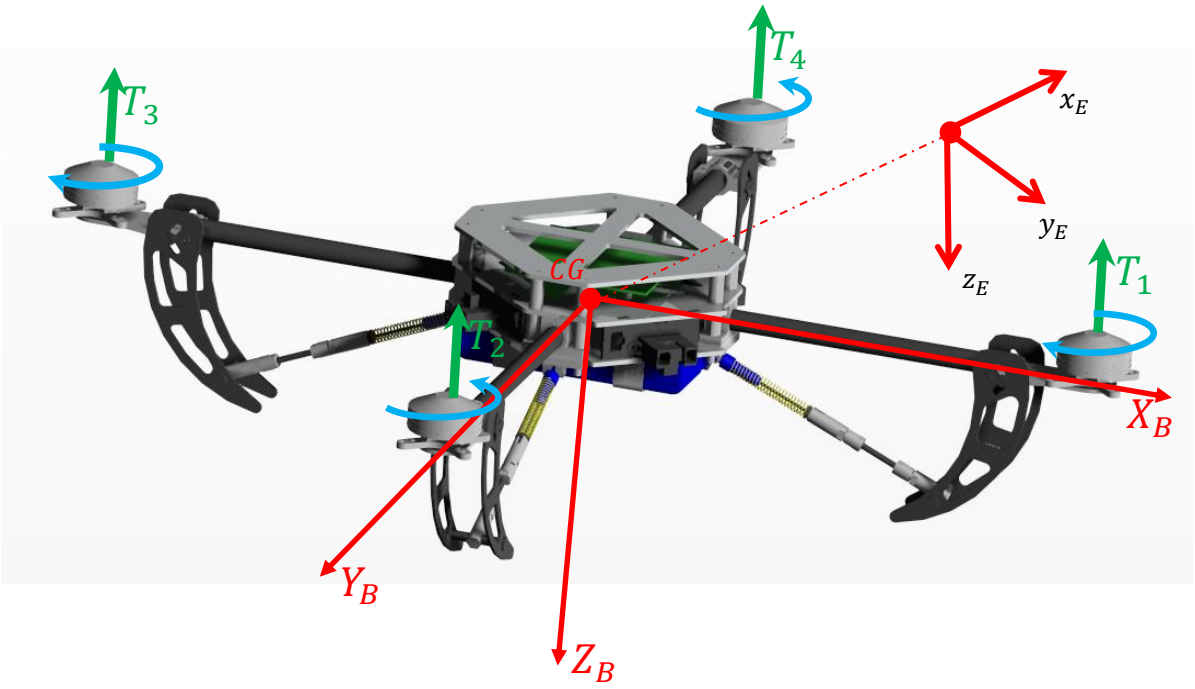

Figure 2.1: Body-fixed axes attached to the quadrotor.

2.2.3 Stability Axes

During flight the angle of the nose (the X_B Axis) may not align with the direction of the oncoming air. The difference in these directions is the angle of attack. If the quadrotor is in a sideslip, the velocity vector rotates by a sideslip angle β (shown in Figure 2.2). Parameters are defined in terms of a modified axis system called "stability axes". The stability axes system is used to get the X_S axis aligned with the oncoming flow direction. Essentially, the body axes system is rotated about the Y_B axis by the trim angle of attack and then "re-fixed" to the body of the aircraft:

- X_s stability axis is aligned into the direction of the oncoming air in steady flight. (It is projected into the plane made by the X_B and Z_B axes if there is sideslip).

- Y_s stability axis is the same as the Y_B.

- Z_s stability axis is perpendicular to the plane made by the X stability axis and the Y_B axis.

The velocity vector is projected onto the $X-Z$ plane of symmetry for measuring α, and onto the $X-Y$ plane for measuring β. Thus it contains both α and β.

2.3 Modelling Assumptions

As described in sections above it is essential that a mathematical model of the developed quadrotor is created. The mathematical model is created using Newton-Euler equations which require body and earth-fixed axes. The body-fixed axes allow for the inertias of the quadrotor to remain constant as opposed to variable inertias in an earth-fixed sense. The velocities and acceleration must be relative to an inertial frame of reference which is the earth fixed frame. The quadrotor motion represents a complex system of highly nonlinear factors which can be simplified by making the following assumptions: (Mary, et al., 2010)

- The earth is stationary and therefore an approximate inertial reference frame

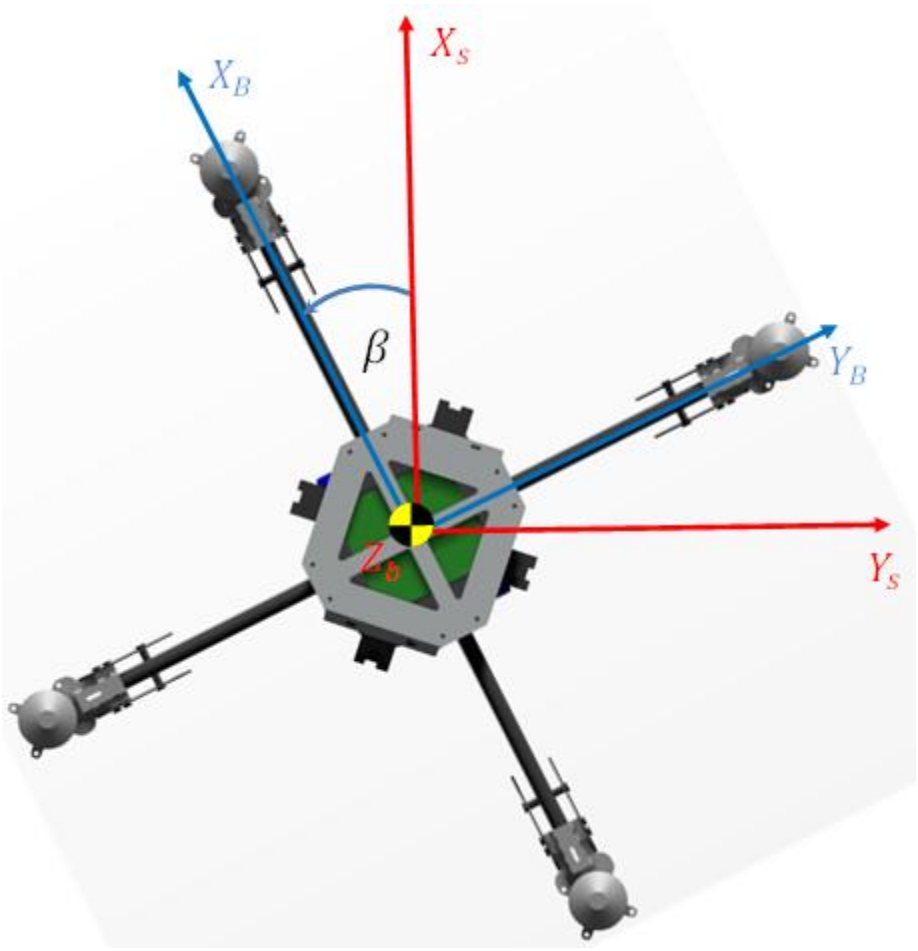

Figure 2.2: Sideslip angle illustrated using the stability and body-fixed axis.

- The centre of mass and the body-fixed frame origin coincide.
- The body is rigid and symmetrical.
- The quadrotor's arms will be approximated by 2 pairs of rods each pair parallel to the X_B and Y_B axes. The rotor mass is represented by a single point-mass on the edge of each arm and the central hub by an additional point mass.
- The variation in gravitational force with change in altitude can be neglected.
- The rotor blades are rigid, neglecting blade flapping and twist.
- The quadrotor has 6 degrees-of-freedom.

- The quadrotor's mass and the gravitational center coincide, no moment is generated by the weight force.
- All motors and blades are equal in mass.
- Components of the airframe are non- lifting surfaces.
- Environmental disturbance are neglected due to the absence of wind tunnel data.
- Relationships between torque, thrust and RPM are relevant to a specific motor data set and varies from motor to motor.
- Simulation mass inclusive of a single battery cell.
- Ground effects are assumed to be minute.

The above assumptions set the foundation on which the mathematical model can be developed.

2.4 Modelling Overview

The flowchart illustrates the coupling of the moments and forces and is essential for debugging of the constructed mathematical model (see Figure 2.3). The relationship between torque, thrust, RPM and PWM were identified using a system identification technique and remain coupled. Any change in rotor RPM is induced by a user defined input of PWM. The aforementioned quantities are utilised as input into the plant.

The plant model is constructed by initially evaluating the moments of inertia followed by the derivation of the equations of motion. The hub, gyroscopic rolling and pitching moments as seen in Figure 2.4 are then evaluated. Forces acting on the body in the form of thrust, drag and gravity are evaluated. Details of the transformation from the earth-fixed to body-fixed axes are shown in Appendix E. The final equations of motion are then developed with a flight mission profile for real time analysis.

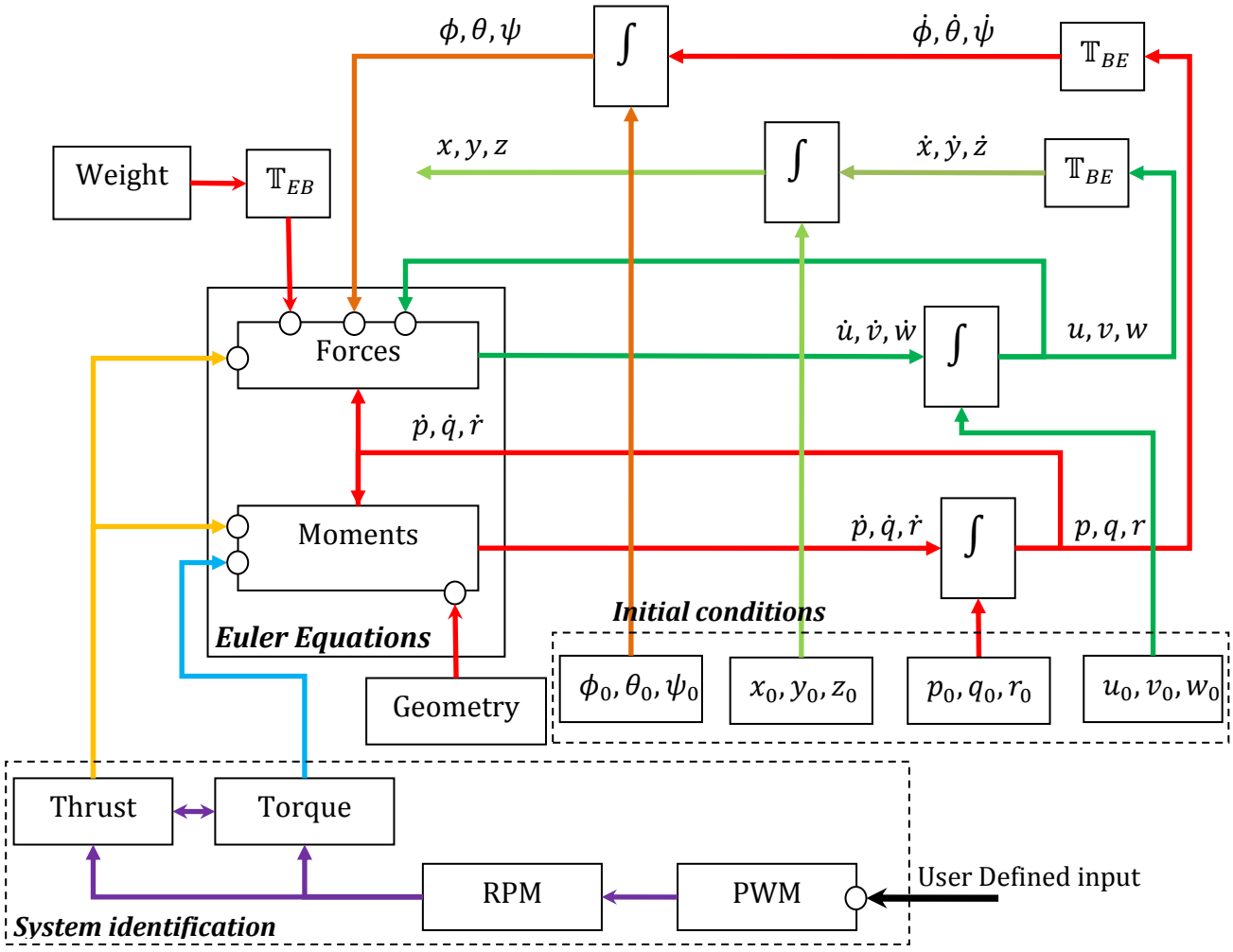

Figure 2.3: Flowchart of the mathematical modelling process.

2.5 Mass, Geometry and Inertia

The underlined structure as in Figure 2.5 allows for the calculation of the moment of inertia. The values obtained from this section will allow for Newton's second law of motion to be employed. The physical model has the following 3 components as per the mechanical construction outlined in section 1.4.3:

- 4 support arms
- 4 rotors and propellers
- A central hub housing the avionics and power source

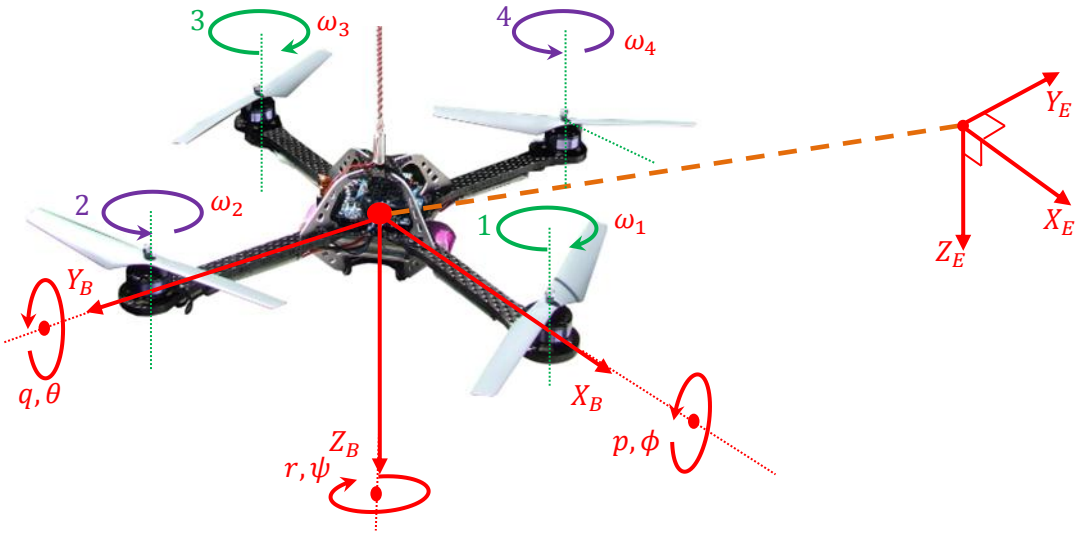

Figure 2.4: Quadrotor being modelled as a 6-DOF system

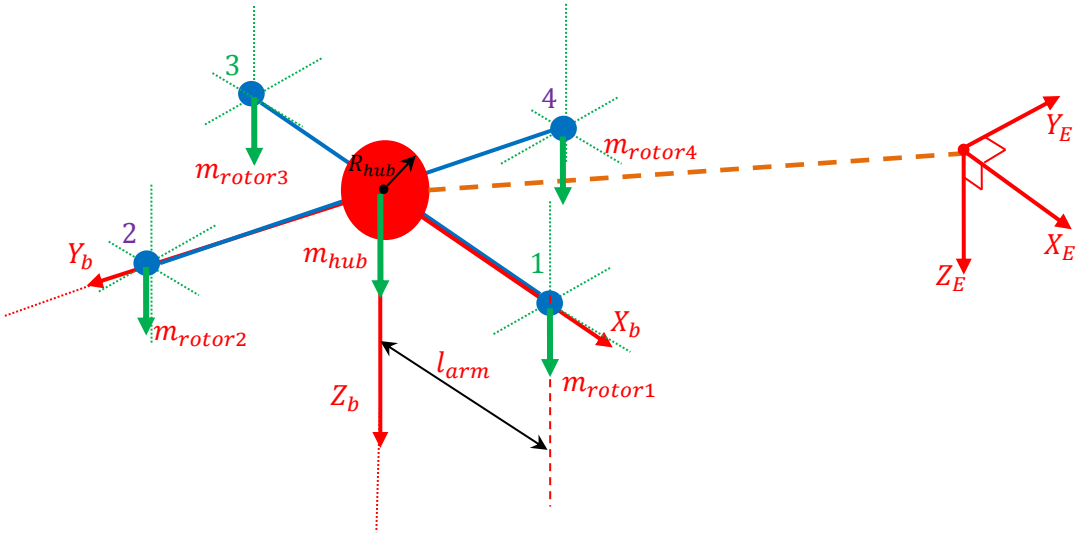

Figure 2.5: Simplified point mass model after a pitch and roll

A general body inertia tensor is given by:

$$\overrightarrow{I_B} = \begin{bmatrix} I_x & I_{xy} & I_{xz} \\ I_{yx} & I_y & I_{yz} \\ I_{zx} & I_{zy} & I_z \end{bmatrix} \tag{2.1}$$

Due to the symmetrical nature of the quadrotor about $X_B Z_B$ and $Y_B Z_B$ planes of symmetry, the inertial matrix is given by:

$$\overrightarrow{I_B} = \begin{bmatrix} I_x & 0 & 0 \\ 0 & I_y & 0 \\ 0 & 0 & I_z \end{bmatrix} \tag{2.2}$$

The moment of inertia about the X_B and Y_B axis in alignment with the assumption made is given by: (See Appendix D.3)

$$I_{Y_B} = I_{X_B} = 2\left(m_{rotor} {l_{arm}}^2\right) + \frac{2}{5}\left(m_{hub} {R_{hub}}^2\right) \tag{2.3}$$

The moment of inertia about the Z_B-axis in alignment with the assumption made is given by:

$$I_{Z_B} = 4\left(m_{rotor} {l_{arm}}^2\right) + \frac{2}{5}\left(m_{hub} {R_{hub}}^2\right) \tag{2.4}$$

2.6 Quadrotor Dynamics

2.6.1 Equations of Motion

Application of Newton's second law for the translational dynamic gives:

$$\vec{F} = \frac{d}{dt}\left(m.\vec{\mathrm{V}}\right) \tag{2.5}$$

Eq. (2.5) can be expanded to:

$$\vec{F} = \left(m.\vec{\mathrm{V}}\right)_{rot} + \vec{\Omega} \times \left(m.\vec{\mathrm{V}}\right) \tag{2.6}$$

The scalar form of Eq. (2.6) is given by:

$$F_{X_B} = M_{TOTAL}(\dot{u} + qw - vr) \tag{2.7}$$

$$F_{Y_B} = M_{TOTAL}(\dot{v} + ru - wp) \tag{2.8}$$

$$F_{Z_B} = M_{TOTAL}(\dot{w} + pv - qu) \tag{2.9}$$

The attitude of the quadrotor is assessed by means of successive rotations around each one of the inertial axes, expressed in terms of the Euler roll, pitch and yaw angles. The moments exerted on the quadrotor's airframe directly in the body-fixed rotating frame are considered.

Application of Euler equations for the rotational dynamics gives:

$$\vec{M} = \frac{d}{dt}\left(\vec{I}.\vec{\Omega}\right) \tag{2.10}$$

The Coriollis effect appears as the second term added to Eq. (2.5):

$$\vec{M} = \left(\frac{\overrightarrow{dL}}{dt}\right)_{rot} + \vec{\Omega} \times \left(\vec{I}.\vec{\Omega}\right) \tag{2.11}$$

where:

$L = Angular\ Momentum$

The scalar form of Eq. (2.11) is given as:

$$M_{X_B} = I_x\dot{p} + \left(I_x - I_y\right)qr \tag{2.12}$$

$$M_{Y_B} = I_y\dot{q} + (I_x - I_z)rp \tag{2.13}$$

$$M_{Z_B} = I_z\dot{r} + \left(I_y - I_x\right)pq \tag{2.14}$$

The following sections will investigate the moments and forces present which act on quadrotor.

2.6.2 Rolling and Pitching Moments

Each motor when combined with a propeller generates a thrust as seen in Figure 2.6. Thrust is generated by the rotation of a propeller through viscous air. Contrary to the weight vector, a transformation for the thrust vector in the body-fixed axes is not needed as it remains aligned with the body-fixed z-axis.

Summing moment about the X_B(roll) axis:

$$\sum M_{XT_B} = (T_{rotor1} - T_{rotor3})l_{arm} \tag{2.15}$$

Similarly summing moment about the Y_B (pitch) axis:

$$\sum M_{YT_B} = (T_{rotor4} - T_{rotor2})l_{arm} \tag{2.16}$$

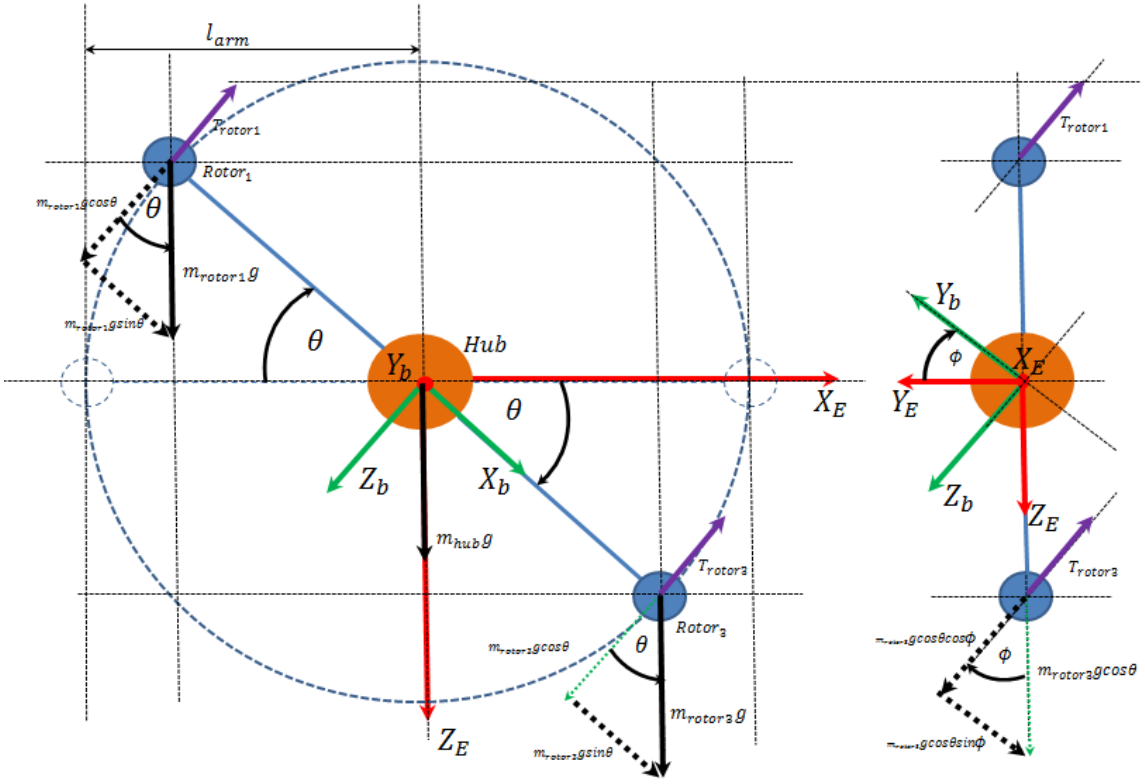

Figure 2.6: Simplified point mass model after a –ve pitch and roll

It may be noted in both cases as per Figure 2.6 that the moments generated by the components of the weight of rotors 1 and 3, 2 and 4, perpendicular to the length of the arms are opposing. It is for this reason that they have been neglected from the summation about the roll and pitch axes respectively. The rotor moments acting on the frame about the Z_B (yaw) axis will be calculated in the following section.

2.6.3 Yawing Moments

All torques acting on the rotor are transferred to the aircraft's airframe by means of the reaction to the electromagnetic torque generated by the brushless motor (shown in Figure 2.7 and Figure 2.8).

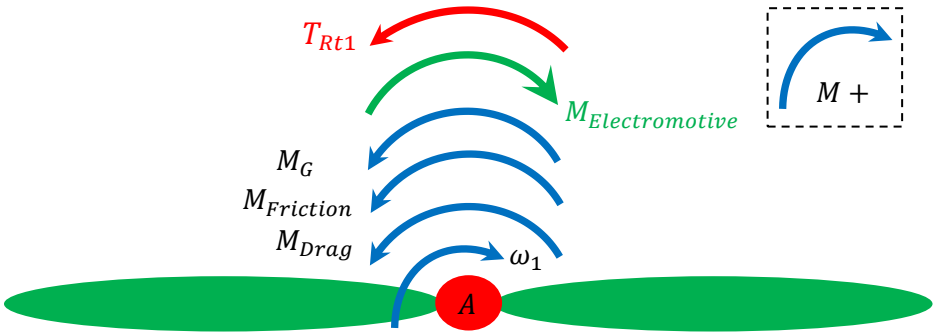

Figure 2.7: Moments acting about the propeller hub of rotor 1 and 3

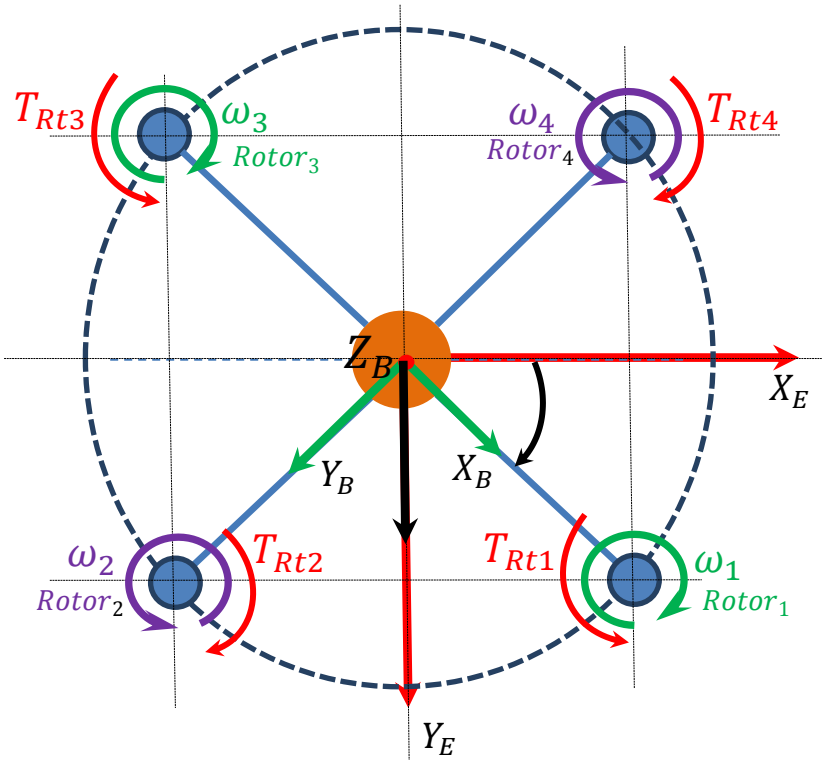

Figure 2.8: Plan view of the quadrotor with action/reaction torque pairs

2.6.3.1 Drag Moment

Figure 2.7 illustrates the moments acting about the rotor hub. M_{Drag} represents the propeller drag torque associated with the generation of lift and opposes the direction of angular rotation.

$$M_{Drag} = C_D \rho \pi R^5 \omega^2 \tag{2.17}$$

where:
$\omega = Angular\ velcocity$

2.6.3.2 Frictional Moment

The brushless motor during commutation has a frictional force to overcome which can be evaluated as:

$$M_{Friction} = B_a \omega \tag{2.18}$$

2.6.3.3 Gyroscopic Moment

The motor being a rotating object generates a gyroscopic torque about each axis. The gyroscopic moment generated about the X_B-axis (Clockwise rotations are +ve) for motors 1-4 is given by:

$$M_{GX_B} = I_G q \begin{bmatrix} \omega_1 \\ -\omega_2 \\ \omega_3 \\ -\omega_4 \end{bmatrix} \tag{2.19}$$

Similarly the gyroscopic moment generated about the Y_B axis is given by:

$$M_{GY_B} = I_G p \begin{bmatrix} -\omega_1 \\ \omega_2 \\ -\omega_3 \\ \omega_4 \end{bmatrix} \tag{2.20}$$

The gyroscopic moment generated about the Z_B axis for motors 1-4 can be stated as:

$$M_{GZ_B} = I_G \begin{bmatrix} \dot{\omega_1} \\ -\dot{\omega_2} \\ \dot{\omega_3} \\ -\dot{\omega_4} \end{bmatrix} \tag{2.21}$$

2.6.3.4 Rotor Hub Moments

The combined moment about the rotor hub as illustrated in Figure 2.7 and is given by:

$$\sum M_A = M_{Electromotive} - M_G - M_{Friction} - M_{Drag} = 0 \tag{2.22}$$

$$\therefore M_{Electromotive} = M_{inertia} + M_{Friction} + M_{Drag} \tag{2.23}$$

As illustrated in Figure 2.8 the electromotive force is transferred to the frame by means of the motor mount. The reaction moment to the electromotive force is given by T_{RT1} where:

$$T_{RT1} = -M_{Electromotive} \tag{2.24}$$

The variation in magnitude of Eq. (2.23) will be later identified using the constructed apparatus (see section 5.5.3).

Using Figure 2.8 we can ascertain the reaction moments of each rotor:

$$\sum M_{Gz_B} = (T_{Rt4} + T_{Rt2}) - (T_{Rt3} + T_{Rt1}) \tag{2.25}$$

$T_{Rt1,2,3,4}$ represents the reaction torques generated about the yaw axis due to angular rotations of the BLDC motors. The complete moment equation about the x- axis is given by combining Eq. (2.15) with Eq. (2.19):

$$\sum M_{X_B} = M_{XT_B} + M_{Gx_B} \tag{2.26}$$

$$\therefore \sum M_{X_B} = (T_{rotor1} - T_{rotor3}) l_{arm} + I_G q \begin{bmatrix} -\omega_1 \\ +\omega_2 \\ -\omega_3 \\ +\omega_4 \end{bmatrix} \tag{2.27}$$

Similarly for the complete summation of moments about the y-axis is given by combining Eq. (2.16) with Eq. (2.20):

$$\sum M_{Y_B} = M_{YT_B} + M_{Gy_B} \tag{2.28}$$

$$\therefore \sum M_{Y_B} = (T_{rotor4} - T_{rotor2}) l_{arm} + I_G p \begin{bmatrix} +\omega_1 \\ -\omega_2 \\ +\omega_3 \\ -\omega_4 \end{bmatrix} \tag{2.29}$$

Similarly Eq. (2.30) represents the summation of the moments about the Z_B axis.

$$\sum M_{Z_B} = (T_{Rt4} + T_{Rt2}) - (T_{Rt3} + T_{Rt1}) \tag{2.30}$$

2.6.4 Forces

The quadrotor as seen in Figure 2.6 is subject to three sets of forces. The first being the thrust exerted by the motor and propeller combination on the quadrotor's frame, the second being the influence that gravity has on its mass and the last being the influence of air drag. As previously stated it is assumed that all thrust vectors remain perpendicular to the arms of the quadrotor throughout any maneuver. The implication of this is that a transformation is not needed for the thrust vectors however the same cannot be said for the weight vectors. The weight vectors as illustrated by Figure 2.5 are always parallel to the Z_E-axis of inertial frame. As per section 2.7, any position can be represented by 3 rotations hence the weight vector in the body-fixed plane will need to undergo a transformation from the earth-fixed to body-fixed frame for purposes of integration into the equations of motion in the body-fixed frame. Unlike the earth-fixed frame where the mass is represented by 1 component the body-fixed frame will have 3 component of the weight vector.

2.6.4.1 Gravity force

The interaction of the earth gravity field and the quadrotor causes its weight force to act upon its centre of mass. This is modelled in the inertial frame of reference using Newton's second law of motion:

$$\overrightarrow{F_{W_z}} = \begin{bmatrix} 0 \\ 0 \\ M_{TOTAL}g \end{bmatrix} \tag{2.33}$$

The component of the weight vector along all 3 axis can be calculated using the following equation:

$$\overrightarrow{F_{W_b}} = \mathbb{T}_{BE} \begin{bmatrix} 0 \\ 0 \\ M_{TOTAL}g \end{bmatrix} = \begin{bmatrix} F_{W_{XB}} \\ F_{W_{YB}} \\ F_{W_{ZB}} \end{bmatrix} \tag{2.34}$$

where:

M_{TOTAL} is the mass sum of the 4 motors, 4 arms and central hub and the transformation matrix and its derivation can be viewed in section 2.7.1.

Hence :

$$\begin{bmatrix} F_{W_{bx}} \\ F_{W_{by}} \\ F_{W_{bz}} \end{bmatrix} = M_{TOTAL}g \begin{bmatrix} -\sin\theta \\ \sin\phi\cos\theta \\ \cos\phi\cos\theta \end{bmatrix} \tag{2.35}$$

2.6.4.2 Drag Force

Aircraft drag can be modelled as opposing the direction of the aircraft forward velocity and in the $-X_b$ direction, however in the case of a quadrotor, the drag force can act along both the $-X_b$ and $+X_b$ directions. Additionally since the quadrotor is classified as VTOL it encounters an additional drag force along the $-Z_b$ and Z_b(see Figure 2.11 and Figure 2.12) axis during the descent and ascent phases respectively.

Figure 2.9 and Figure 2.10 are synonymous of this phenomenon along the X_E axis and Figure 2.11 and Figure 2.12 along the Z_E axis. The previously described figures are illustrative of the change in the drag force vector with the motion of the quadrotor.

The drag force experienced in the earth-fixed frame of reference is given by:

$$\overrightarrow{F_{D_E}} = \begin{bmatrix} F_{Dx} \\ F_{Dy} \\ F_{Dz} \end{bmatrix} \tag{2.36}$$

The components of the drag vectors along all 3 axis can be calculated using the following equation:

$$\begin{bmatrix} F_{D\,Bx} \\ F_{D\,By} \\ F_{D\,Bz} \end{bmatrix} = \frac{1}{2} C_D \rho S \begin{bmatrix} \dot{x}^2 \\ \dot{y}^2 \\ \dot{z}^2 \end{bmatrix} \tag{2.37}$$

Eq. (2.38)-(2.40) are functions of velocity and become null when the velocities are null.

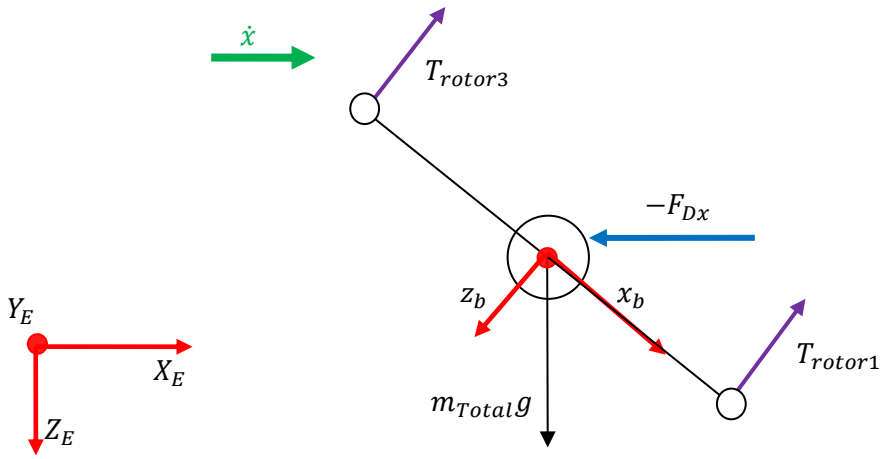

Figure 2.9: Forces experienced by the quadrotor during cruise in the +ve X_E direction.

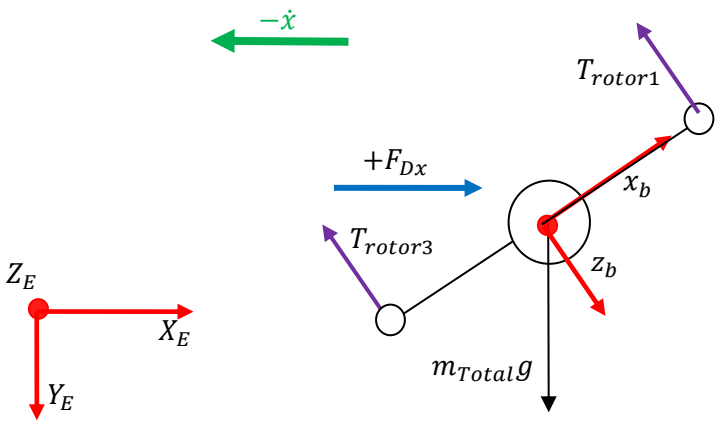

Figure 2.10: Forces experienced by the quadrotor during cruise the -ve X_E direction.

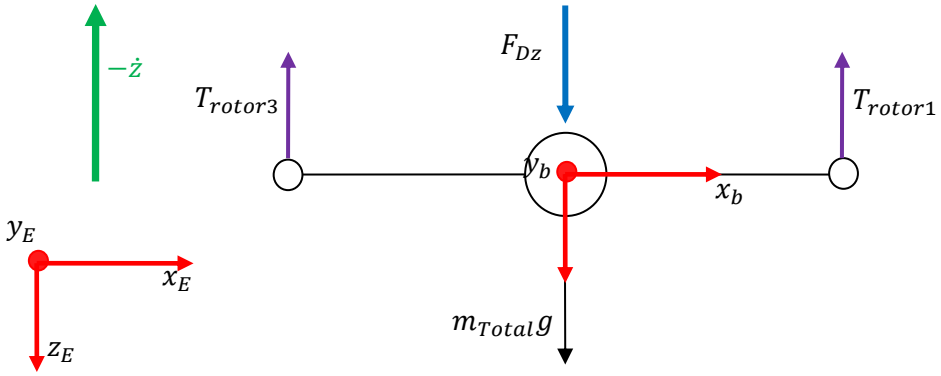

Figure 2.11: Forces experienced by the quadcopter during the take-off/ascent phase.

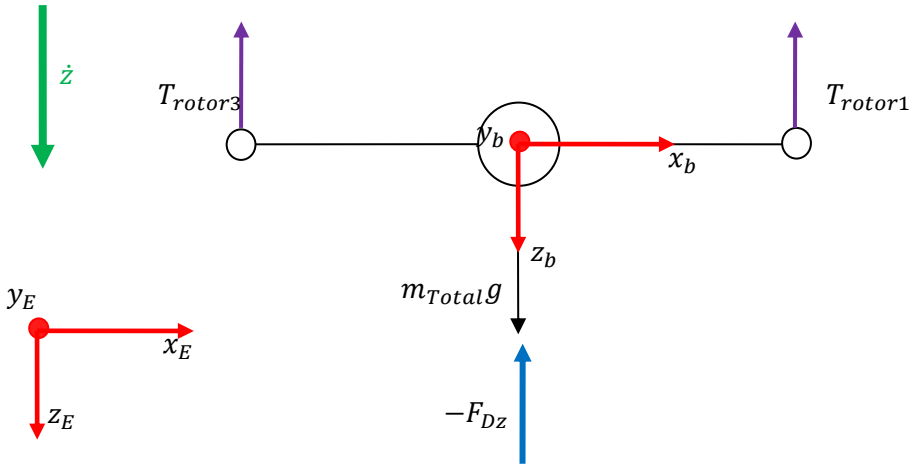

Figure 2.12: Forces experienced by the quadcopter during the landing/descent phase.

The wetted area "S" in Figure 2.13 is defined as the cross sectional area of the spherical hub used in the calculation of the drag components as seen in Eq. (2.37), the end motor masses and supporting arms are assumed to have negligible area. The wetted area in the $X_B Z_B$ and $Y_B Z_B$ planes are equal. Due to the negligible cross-sectional of the motor masses the wetted area in the $X_B Y_B$ plane is the same as in the previously stated planes.

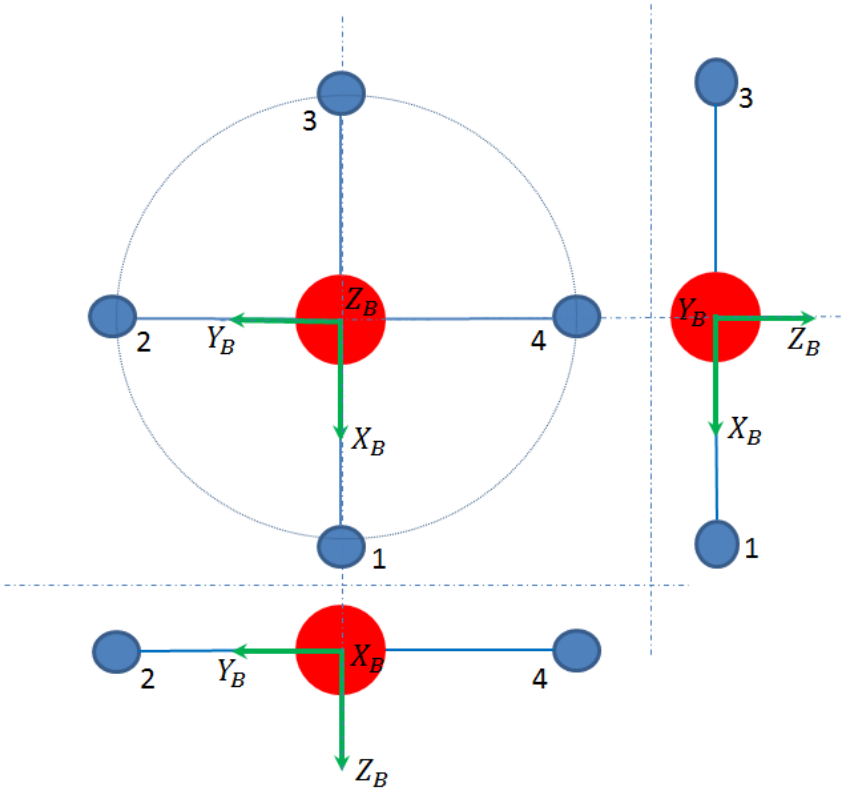

Figure 2.13: Wetted Area as view from each plane.

2.6.4.3 Force equations

Summing force along the X_b axis for translation along the +ve X_E as per Figure 2.9:

$$\sum F_{X_b} = -(m_{TOTAL} g) \sin\theta + F_{D_{Bx}} \tag{2.38}$$

Summing force along the X_b axis for translation along the -ve X_E:

$$\sum F_{X_b} = -(m_{TOTAL}g)\sin\theta - F_{D_{Bx}} \tag{2.39}$$

Since we cannot have more than one equation of motion along the x-axis:

$$\sum F_{X_b} = -(m_{TOTAL}g)\sin\theta \pm F_{D_{Bx}} \tag{2.40}$$

The $\pm$ term can be achieved through the use of "if" statement. Similarly summing forces along the Y_b axis for translation along the both the +ve, -ve Y_E axis as per Figure 2.9:

$$\sum F_{Y_B} = -(m_{TOTAL}g)\sin\phi\cos\theta \pm \left(F_{D_{By}}\right) \tag{2.41}$$

Similarly summing forces along the Z_B axis for translation along the both the +ve, -ve Z_E axis as per Figure 2.11 and Figure 2.12.

$$\sum F_{Z_B} = -(T_{rotor1} + T_{rotor2} + T_{rotor3} + T_{rotor4}) + \left(m_{TOTAL}g \pm F_{Drag}\right)\cos\phi\cos\theta \tag{2.42}$$

The construed "if" statement allows for drag along one axis to be used in both the positive and negative directions of velocity.

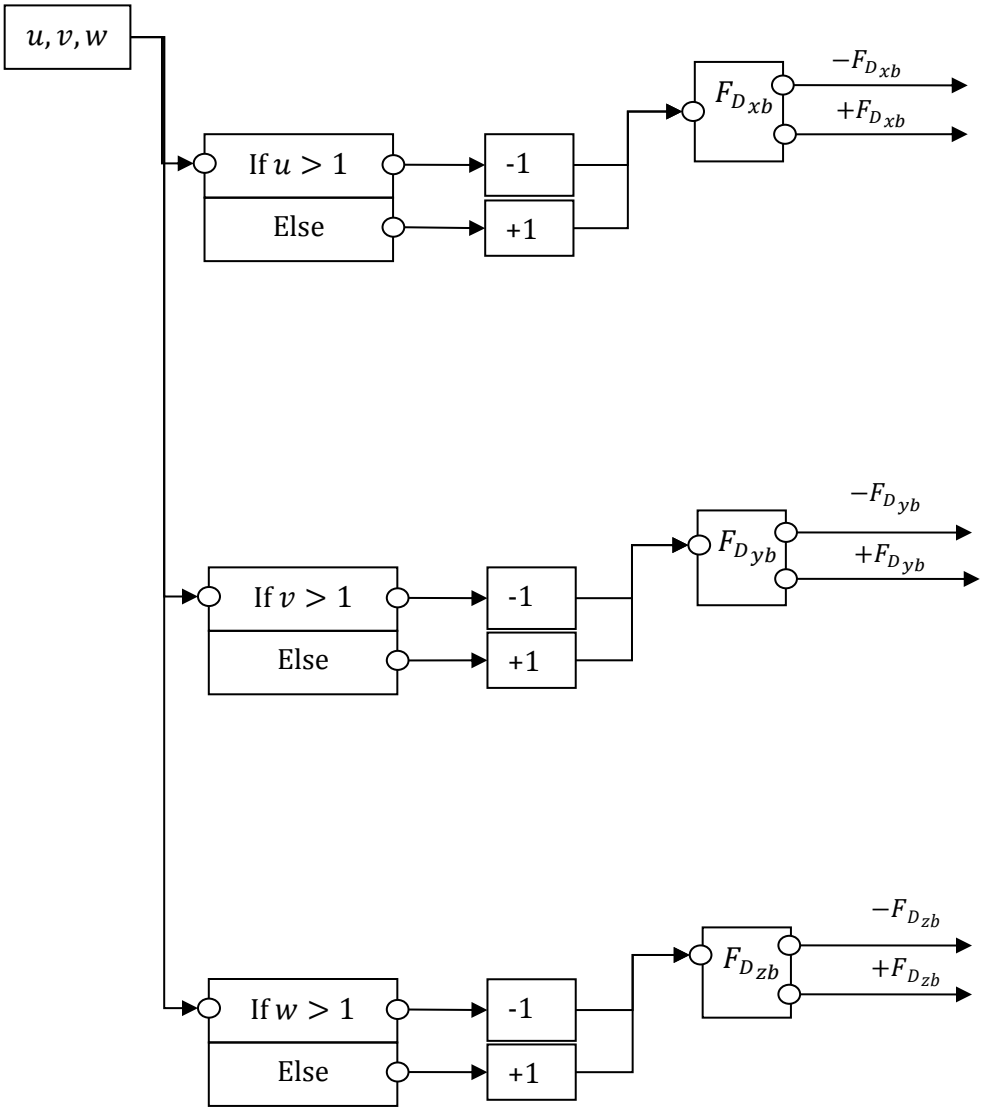

Figure 2.14: An "If" statement used for the devised drag equation.

2.7 Coordinate System Transformation

Coordinate transformation allows for a mapping of coordinates from the earth to body fixed frame. Any point in the Euclidean space can be represented by a sequence of three basic rotations. The initial sequence in which the rotations are done need to be maintained in order to correctly obtain an orientation and can be viewed in Figure 2.15

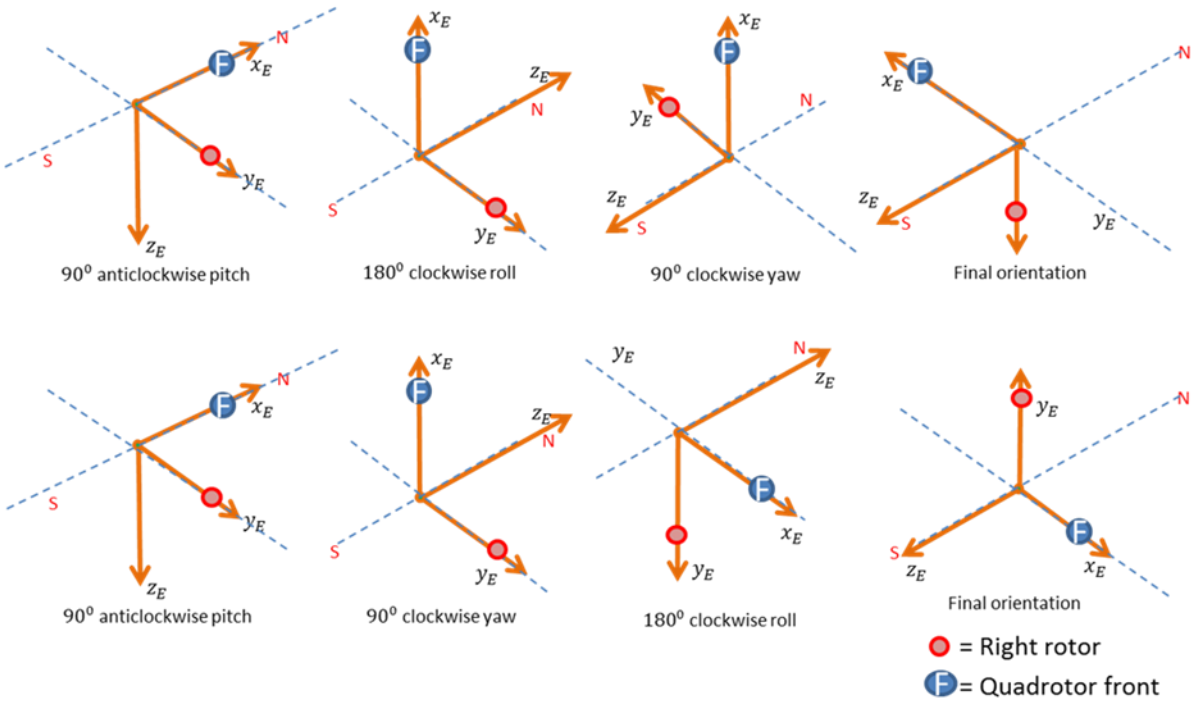

Figure 2.15: Importance of maintaining the sequence of rotation

2.7.1 Compound Rotations and Transformations

Appendix D – Transformations and Moment of Inertia outlined mapping of coordinates from the earth-fixed to body-fixed coordinate system for individual roll, pitch and yaw rotations. It is known that any point in the Euclidean 3D space can be represented by a sequence of three basic rotation around the Euler angles, and the exact sequence needs to be preserved in order to correctly obtain the rotation in 3D as discussed in the introduction of section 2.7. Any transformation performed in on the quadrotor will adhere to the following rotation order:

$$\mathbb{T}_{bE} = \left(\mathbb{T}_{EB_\phi}\right)\left(\mathbb{T}_{EB_\theta}\right)\left(\mathbb{T}_{EB_\psi}\right) \tag{2.43}$$

Further expanding Eq. (2.43) using equation D.27, D.29 and D.30:

$$\mathbb{T}_{bE} = \begin{bmatrix} 1 & 0 & 0 \\ 0 & cos(\phi) & -sin(\phi) \\ 0 & sin(\phi) & cos(\phi) \end{bmatrix} \begin{bmatrix} cos(\theta) & 0 & sin(\theta) \\ 0 & 1 & 0 \\ -sin(\theta) & 0 & cos(\theta) \end{bmatrix} \begin{bmatrix} cos(\psi) & -sin(\psi) & 0 \\ sin(\psi) & cos(\psi) & 0 \\ 0 & 0 & 1 \end{bmatrix} \tag{2.44}$$

The final form of the transformation is given by:

$$\mathbb{T}_{bE} = \begin{bmatrix} cos(\theta)cos(\psi) & -cos(\theta)sin(\psi) & sin(\theta) \\ -sin(\phi)sin(\theta)cos(\psi) + cos(\phi)sin(\psi) & sin(\phi)sin(\theta)sin(\psi) + cos(\phi)cos(\psi) & -sin(\phi)cos(\theta) \\ -sin(\theta)cos(\phi)cos(\psi) + sin(\phi)sin(\psi) & cos(\phi)sin(\theta)sin(\psi) + sin(\phi)sin(\psi) & cos(\phi)cos(\psi) \end{bmatrix} \tag{2.45}$$

2.8 Non- Linear Model

2.8.1 Angular Rate and Acceleration

Equating Eq. (2.7) to Eq. (2.27) the roll rate can be derived:

$$(T_{rotor1} - T_{rotor3})l_{arm} + I_G q \begin{bmatrix} -\omega_1 \\ +\omega_2 \\ -\omega_3 \\ +\omega_4 \end{bmatrix} = \dot{p} + (I_x - I_y)qr \tag{2.46}$$

This can be further simplified to:

$$\dot{p} = \frac{1}{I_x}\left((T_{rotor1} - T_{rotor3})l_{arm} + I_G q \begin{bmatrix} -\omega_1 \\ +\omega_2 \\ -\omega_3 \\ +\omega_4 \end{bmatrix} + (I_y - I_x)qr \right) \tag{2.47}$$

Integrating Eq. (2.50) the roll rate can be derived:

$$p = \int_{t=0}^{t=t} \left(\frac{1}{I_x}\left((T_{rotor1} - T_{rotor3})l_{arm} + I_G q \begin{bmatrix} -\omega_1 \\ +\omega_2 \\ -\omega_3 \\ +\omega_4 \end{bmatrix} + (I_y - I_x)qr \right) \right) . dt \tag{2.48}$$

Equating Eq. (2.8) to Eq. (2.29) the pitch rate can be derived:

$$(T_{rotor4} - T_{rotor2})l_{arm} + I_G p \begin{bmatrix} +\omega_1 \\ -\omega_2 \\ +\omega_3 \\ -\omega_4 \end{bmatrix} = I_x \dot{q} + (I_x - I_z) rp \tag{2.49}$$

This can be further simplified:

$$\dot{q} = \frac{1}{I_y}\left((T_{rotor4} - T_{rotor2})l_{arm} + (I_z - I_x) rp + I_G p \begin{bmatrix} +\omega_1 \\ -\omega_2 \\ +\omega_3 \\ -\omega_4 \end{bmatrix} \right) \tag{2.50}$$

Integrating Eq. (2.53) the roll rate can be derived:

$$q = \int_{t=0}^{t=t} \left(\frac{1}{I_y}\left((T_{rotor4} - T_{rotor2})l_{arm} + (I_z - I_x) rp + I_G p \begin{bmatrix} +\omega_1 \\ -\omega_2 \\ +\omega_3 \\ -\omega_4 \end{bmatrix} \right) \right). dt \tag{2.51}$$

Equating Eq. (2.9) to Eq. (2.30) the yaw rate can be derived:

$$(T_{Rt4} + T_{Rt2}) - (T_{Rt3} + T_{Rt1}) = I_x \dot{r} + \left(I_y - I_x\right) pq \tag{2.52}$$

This can be further simplified:

$$\dot{r} = \frac{1}{I_x}\Big((T_{Rt4} + T_{Rt2}) - (T_{Rt3} + T_{Rt1}) + \left(I_x - I_y\right) pq \Big) \tag{2.53}$$

The yaw rate is given by:

$$r = \int_{t=0}^{t=t} \left(\frac{1}{I_x}\Big((T_{Rt4} + T_{Rt2}) - (T_{Rt3} + T_{Rt1}) + \left(I_x - I_y\right) pq \Big) \right). dt \tag{2.54}$$

2.8.2 Translational Velocity and Acceleration

The translational velocity along the X_b-axis can be calculated by equating Eq. (2.12) to Eq. (2.35):

$$M_{TOTAL} g \sin\theta = M_{TOTAL}(\dot{u} + qw - vr) \tag{2.55}$$

Simplifying Eq. (2.55) allows for the translation acceleration along the X_B axis to be solved:

$$\dot{u} = vr - qw + g \sin\theta \tag{2.56}$$

Integrating Eq. (2.56) allows for the translational velocity to be solved:

$$u = \int_{t=0}^{t=t} (vr - qw + g \sin\theta).dt + u_0 \tag{2.57}$$

The translational velocity along the Y_b-axis can be calculated by equating Eq. (2.12) to Eq. (2.35):

$$-M_{TOTAL} g \sin\phi \cos\theta = M_{TOTAL}(\dot{v} + ru - wp) \tag{2.58}$$

Simplifying Eq. (2.58) allows for the translation acceleration to be solved:

$$\dot{v} = wp - ru - g \sin\phi \cos\theta \tag{2.59}$$

Integrating Eq. (2.59) allows for the translational velocity to be solved:

$$v = \int_{t=0}^{t=t} (wp - ru - g \sin\phi \cos\theta).dt + v_0 \tag{2.60}$$

The translational velocity along the Y_b-axis can be calculated by equating Eq. (2.14) and Eq. (2.30) to Eq. (2.36):

$$-(T_{rotor1} + T_{rotor2} + T_{rotor3} + T_{rotor4}) + M_{TOTAL} g \cos\phi \cos\theta = M_{TOTAL}(\dot{w} + pv - qu) \tag{2.61}$$

Simplifying Eq. (2.61) allows for the translation acceleration to be solved:

$$\dot{w} = g \cos\phi \cos\theta - \frac{1}{M_{TOTAL}}(T_{total}) + qu - pv \tag{2.62}$$

Where:

$$T_{total} = T_{rotor1} + T_{rotor2} + T_{rotor3} + T_{rotor4} \tag{2.63}$$

Integrating Eq. (2.62) allows for the translational velocity to be solved:

$$w = \int_{t=0}^{t=t} \left(g \cos\phi \cos\theta - \frac{1}{M_{TOTAL}}(T_{total}) + qu - pv \right) . dt + \omega_0 \tag{2.64}$$

2.8.3 Displacement and Angular Position

The translational velocity in the earth-fixed frame is derived using a transformation from the body to earth-fixed frame.

$$\begin{bmatrix} \dot{x} \\ \dot{y} \\ \dot{z} \end{bmatrix} = \mathbb{T}_{Eb} \begin{bmatrix} u \\ v \\ w \end{bmatrix} \tag{2.65}$$

The translation displacement along each axis is given by:

$$\begin{bmatrix} x \\ y \\ z \end{bmatrix} = \begin{bmatrix} x_0 \\ y_0 \\ z_0 \end{bmatrix} + \int \begin{bmatrix} \dot{x} \\ \dot{y} \\ \dot{z} \end{bmatrix} . dt \tag{2.66}$$

The angular velocity in the earth fixed frame is derived using a transformation from the body to earth fixed frame.

$$\begin{bmatrix} \dot{\phi} \\ \dot{\theta} \\ \dot{\psi} \end{bmatrix} = \begin{bmatrix} p \\ q \\ r \end{bmatrix} \mathbb{T}_{Eb} \tag{2.67}$$

where:

$$\mathbb{T}_{Eb} = (\mathbb{T}_{bE})^{-1} = \begin{bmatrix} 1 & \sin\phi \tan\theta & \cos\phi \tan\theta \\ 0 & \cos\phi & -\sin\phi \\ 0 & \sin\phi \sec\theta & \cos\phi \sec\theta \end{bmatrix} \tag{2.68}$$

The angular displacement along each axis is given by:

$$\begin{bmatrix} \phi \\ \theta \\ \psi \end{bmatrix} = \begin{bmatrix} \phi_0 \\ \theta_0 \\ \psi_0 \end{bmatrix} + \int \begin{bmatrix} \dot{\phi} \\ \dot{\theta} \\ \dot{\psi} \end{bmatrix} . dt \tag{2.69}$$

2.9 Flight Mission Planning

Mission planning is essential in that it allows for the different phases in the mission to be visualized and segmented for analysis purposes. A simple mission plan was created which consisted of three phases:

1. Takeoff/Ascent: This quadrotor accelerates off the ground along the negative Z_b axis.
2. Hover: The quadrotor attains its steady state condition maintaining it's X_B, Y_B and Z_B coordinates with time.
3. Cruise: This quadrotor travels along the earth fixed X-axis.
4. Takeoff/Ascent: The quadrotor accelerates off the ground along the negative earth-fixed Y axis.

The ascent and descent phase will be analysed together whilst the hover and cruise phase analysed separately. The three phase profile can be viewed in Figure 2.16.

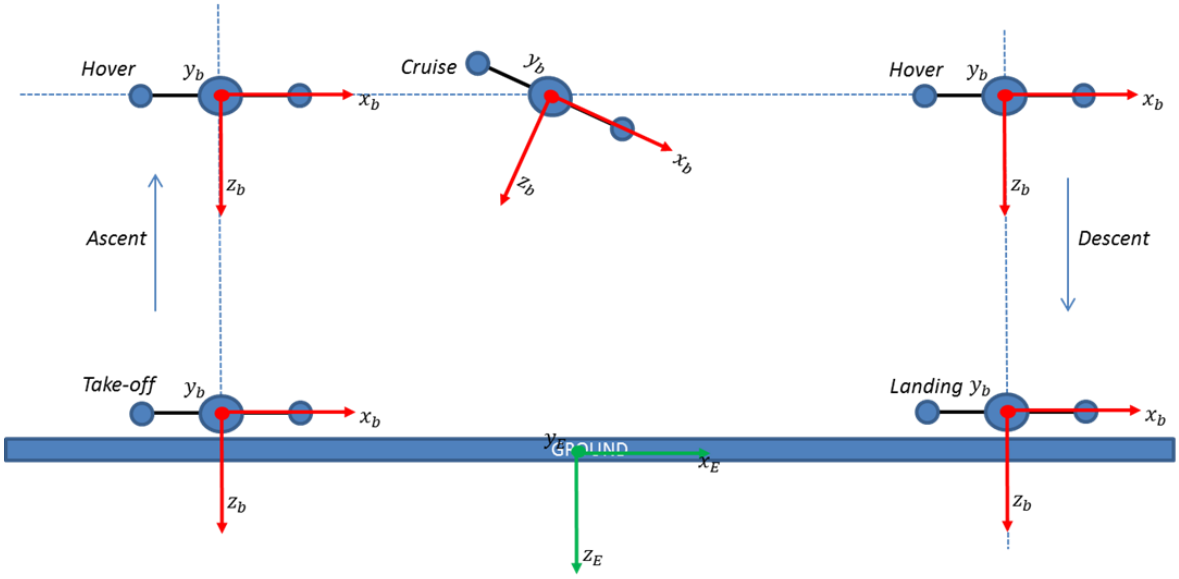

Figure 2.16: Mission profile for the quadrotor to be performed for mathematical analysis.

2.9.1 Vertical Ascent

Vertical ascent occurs on the take-off phase of the mission, during which the angular rates are zero to maximise on the resultant force in the direction -z_b.

During vertical ascent Eq. (2.70) and Eq. (2.71) hold true:

$$\sum M_{X_B,Y_B,Z_B} = 0 \tag{2.70}$$

$$\sum F_{X_B,Y_B} = 0 \tag{2.71}$$

Solving Eqs. (2.70) and (2.71) the following can be concluded:

$$\theta, \phi, \psi, p, q, r, u, v = 0 \tag{2.72}$$

Hence Eq. (2.62) is simplified to:

$$\dot{w}M_{TOTAL} = g - (T_{total}) - F_{Drag} \tag{2.73}$$

Eq. (2.73) is referred to as the resultant force.

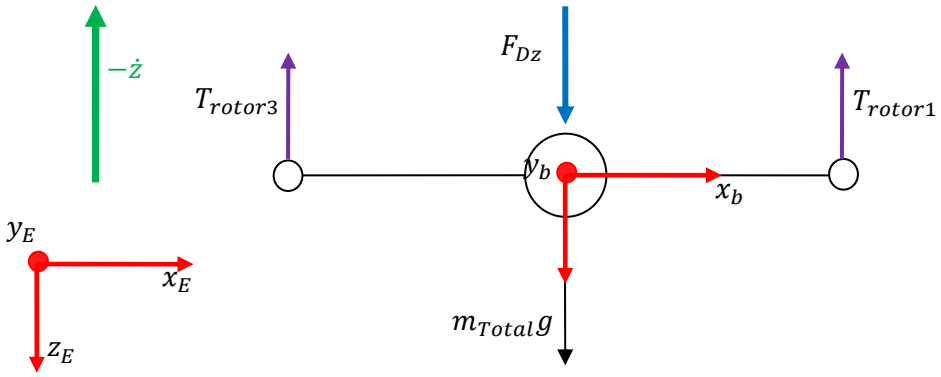

Figure 2.17: Resultant force acting on the quadrotor during ascent.

2.9.2 Equilibrium Analysis

The hover phase constitutes an equilibrium analysis since the quadrotor maintains its altitude with no angular displacement. In this case the axis of the body is aligned with that of the earth. An equilibrium analysis was performed in order to verify the equation of motion. During hover equilibrium (Steady state) exists and the quadrotor airframe is subject to the following conditions:

$$\sum F_{X_b,Y_b,Z_b} = 0 \tag{2.74}$$

$$\sum M_{X_b,Y_b,Z_b} = 0 \tag{2.75}$$

An implication of the above is the angular and translation velocities are zero.

$$\begin{bmatrix} p \\ q \\ r \end{bmatrix} = \begin{bmatrix} 0 \\ 0 \\ 0 \end{bmatrix} \tag{2.76}$$

The translational velocity is given by:

$$\begin{bmatrix} u \\ v \\ w \end{bmatrix} = \begin{bmatrix} 0 \\ 0 \\ 0 \end{bmatrix} \tag{2.77}$$

Therefore, Eq. (2.15) simplifies to the following:

$$\frac{1}{I_x}\left((T_{rotor1} - T_{rotor3})l_{arm}\right) = 0 \tag{2.78}$$

Since the arm lengths and inertia quantities are constant Eq. (2.78) can be satisfied only if the difference in thrust values are zero:

$$\therefore T_{rotor1} - T_{rotor3} = 0 \tag{2.79}$$

Hence for Eq. (2.79) to be satisfied the thrust values must be equal:

$$\therefore T_{rotor1} = T_{rotor3} \tag{2.80}$$

A similar process can be followed for Eq. (2.16) and simplifies to:

$$\frac{1}{I_y}\left((T_{rotor4} - T_{rotor2})l_{arm}\right) = 0 \tag{2.81}$$

Hence for Eq. (2.81) to be satisfied the thrust values must be equal:

$$T_{rotor4} = T_{rotor2} \tag{2.82}$$

An implication of the equilibrium conditions on Eq. (2.25) implies:

$$\frac{1}{I_x}\left((T_{Rt4} + T_{Rt2}) - (T_{Rt3} + T_{Rt1})\right) = 0 \tag{2.83}$$

which further simplifies to:

$$(T_{Rt4} + T_{Rt2}) = (T_{Rt3} + T_{Rt1}) \tag{2.84}$$

Eq. (2.84) illustrates that the torques generated by each pair of motors must be opposing. This ascertains that each pair of motors must be rotating in opposing directions and the torque generated equal in magnitude but opposite in direction. In order to satisfy Eqs. (2.80), (2.82) and (2.84) the thrust generated by each motor must be equal as thrust is a function of RPM and torque. Therefore the following remains true:

$$\therefore T_{rotor1} = T_{rotor3} = T_{rotor4} = T_{rotor2} \tag{2.85}$$

The steady-state angles are resolved by equating Eq. (2.50) and (2.54) to zero. The implications of this are shown in Eqs. (2.86) and (2.87):

$$g \sin\theta = 0 \tag{2.86}$$

The implication of Eq. (2.72) being the pitch angle must be 0:

$$\therefore \theta = 0 \tag{2.87}$$

Similarly using Eq. (2.83):

$$-g \sin\phi \cos\theta = 0 \tag{2.88}$$

Substituting for the pitch angle into Eq. (2.88) reveals:

$$-g \sin\phi = 0 \tag{2.89}$$

Hence for Eq. (2.89) to be satisfied:

$$\phi = 0 \tag{2.90}$$

Eq. (2.86) reveals the following to be true:

$$g\cos\phi\cos\theta - \frac{1}{M_{TOTAL}}(T_{total}) = 0 \tag{2.91}$$

Further simplifying by using Eq. (2.90) and (2.91):

$$M_{TOTAL}g = T_{total} \tag{2.92}$$

Eq. (2.92) is a very important milestone in derivation as it instils confidence in the derived equation. It implies that the weight of the quadrotor in hover must be balanced by the thrust force generated by the rotors. Eq. (2.92) implies that the hover state can only be maintained if the thrust generated by each motor is the same. The combination of the deductions convey that each motor must be able to generate at minimum a thrust force(T_{min}) illustrated by Eq. (2.93).

$$T_{min} = \frac{M_{TOTAL}g}{4} \tag{2.93}$$

The mass of the Quadrotor is broken up into the following:

$$M_{TOTAL} = M_{battery} + M_{sphere} + 4(M_{rotor}) + 4(M_{arm}) \tag{2.94}$$

where:

$$M_{TOTAL} = 0.4kg,\ M_{sphere} = 0.394kg,\quad M_{rotor} = 0.075kg,\quad M_{arm} = 0.02$$

Hence the total mass is given by:

$$M_{total} = 1.18kg \tag{2.95}$$

Eq. (2.93) can be resolved using Eq. (2.95):

$$\therefore T_{min} = (0.295)g = 2.89N \tag{2.96}$$

Hence each motor must produce 2.89N to sustain hover

Figure 2.18 and Figure 2.19 illustrates the relationship between the thrust produced by the motor in grams, the input signal and RPM which was found in the identification phase as per section 5.7.3.

Substituting equation 2.96 into the equation stipulated by Figure 2.18 and Figure 2.19 allows for the minimum RPM and PWM value to be identified:

$$\therefore PWM_{min} = 8.36 \tag{2.98}$$

$$\therefore RPM_{min} = 4100rev/m \tag{2.97}$$

Hence for a hover maneuver to be performed a PWM signal of 8.36 must be supplied which will rotate the propeller blades at 4100rev/m. PWM values less than 8.36 will result in a lower thrust value which will affect equilibrium resulting in the decent of the quadrotor.

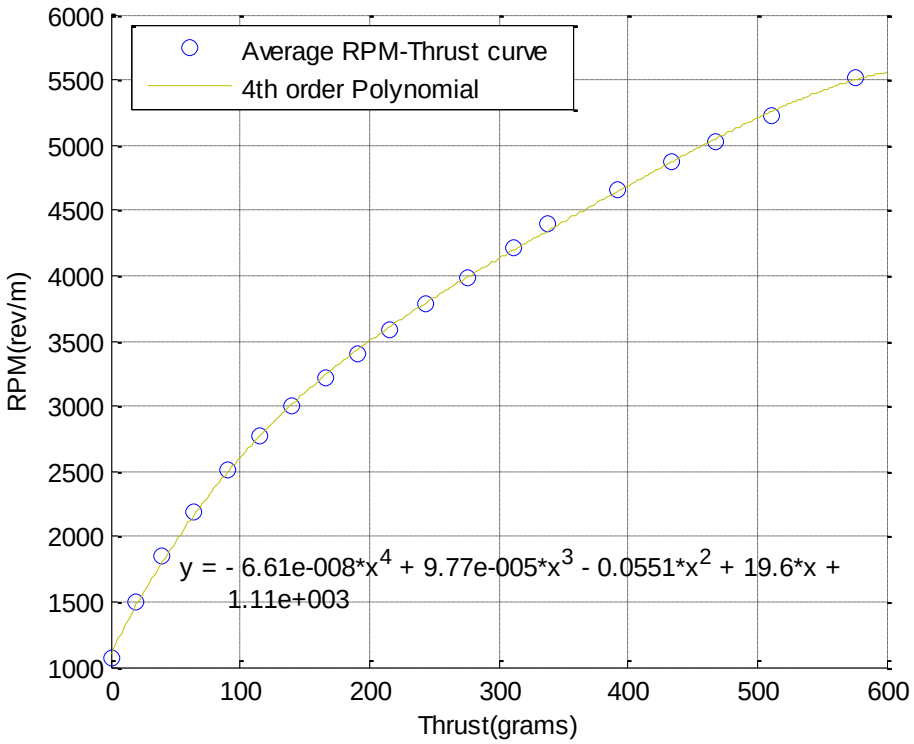

Figure 2.18: Relationship between Thrust and RPM used in the simulation environment

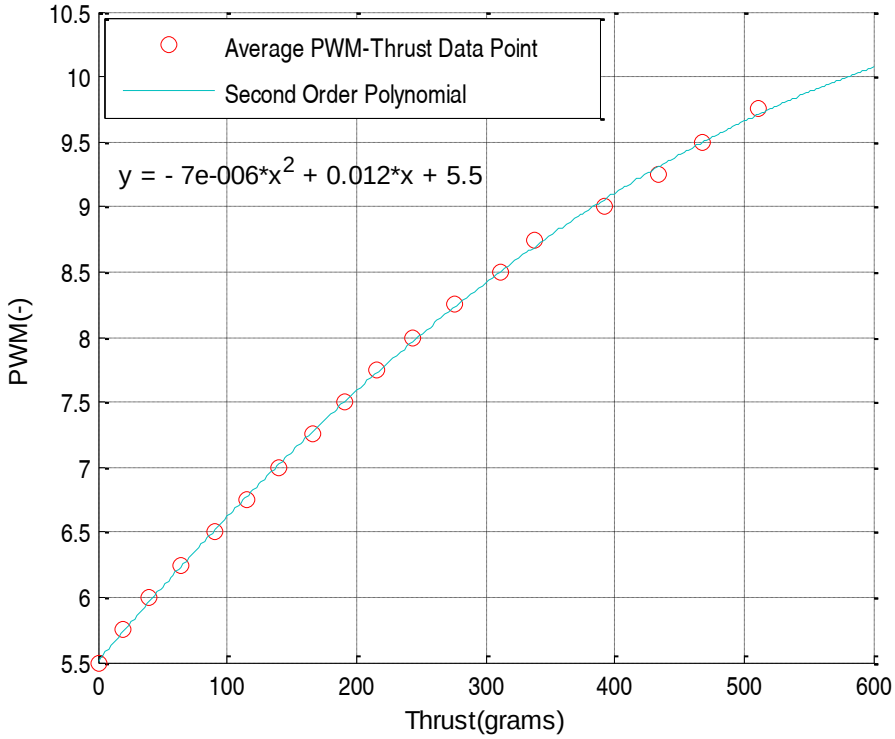

Figure 2.19: Relationship between PWM and thrust used in the simulation environment

3. Hardware and Software Integration

The quadrotor plant is a closed-loop system. The closed loop is achieved through the use of sensors in the form of inertial measurement units (IMU), proximity sensors, altimeters and various other avionics. The micro-controller serves as the central processing unit which interacts with the sensors. A decisive action is taken through pre-saved commands or predictive algorithms which compare the actual response to that which is desired, referred to as the set-point. This interaction can only take place through the use of hardware specific communication protocols which allow for devices produced by different manufacturers to communicate. Software provides the commands necessary for communication via the shared protocol. This chapter is dedicated to exposing the necessary protocols that have been employed.

3.1 Hardware Communication Protocol

The ATMEGA-328 aboard the IMU is responsible for all onboard processing and outputs data via SPI, I2C and serial communication protocols. It provides the flexibility of more than one protocol making interaction between hardware with limited protocols easier.

3.1.1 I2C Software Communication Protocol

Devices on the Inter-Integrated protocol (I2C) buses are either master or slaves. The master will initiate communication over the I2C bus to which slaves will respond. Multiple slaves can exist on an I2C bus. As opposed to a master, slaves cannot initiate a data transfer however can transfer data over this bus. The master initiates communication with a slave by issuing a start sequence on the I2C bus. A start sequence as shown in Figure 3.1 occurs when the SDA (Data line) is driven low whilst the SCL (Clock line) is kept high. The stop sequence occurs when the SDA line tends to its natural state whilst the SCL line is high. The beginning of a transaction between the master and slave is marked by the stop and start sequence. During data transfer it is important that the SDA line does not oscillate (Devantech, n.d.).

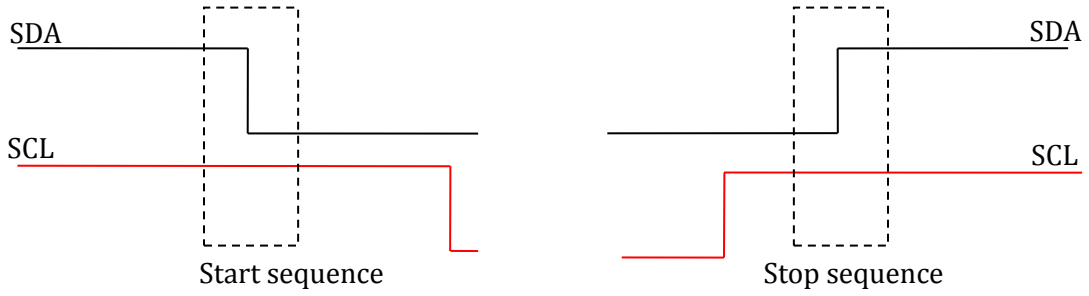

Figure 3.1: I2C Communication Start-Stop sequence (Devantech, n.d.)

Data is transferred in sequences of 8 bits. The bits are placed on the SDA line starting with the Most Significant Bit (MSB). The SCL line is then pulsed high, then low. For every 8 bits transferred, the chosen slave device replies with an acknowledge bit, there are 9 SCL clock pulses required to transfer each 8 bits of data (one byte). The standard clock (SCL) speed for I2C is 100KHz or 400KHz. The ACK byte has the following two states:

Table 1: ACK bit table

ACK bit state	Description
LOW	Data received ready to receive another byte
HIGH	Cannot accept more data, master must terminate with a stop sequence

3.1.2 SPI Communication Protocol

The Serial Peripheral Interface Bus (SPI) is a synchronous data link allowing for communications in both directions often referred to as full duplex. The SPI bus operates with one master (single- master communication protocol) and many slaves. The number of slaves available to one master is limited by the bit addressing system.

SPI is also known as a 4 wire serial bus due to the following 4 logic signals as seen in Figure 3.2:

- SCLK: Serial clock line from the master
- MOSI: Master out slave in (output from the master into the slave)
- MISO: Master in slave out (output from the slave into the master)
- SS: Slave select line

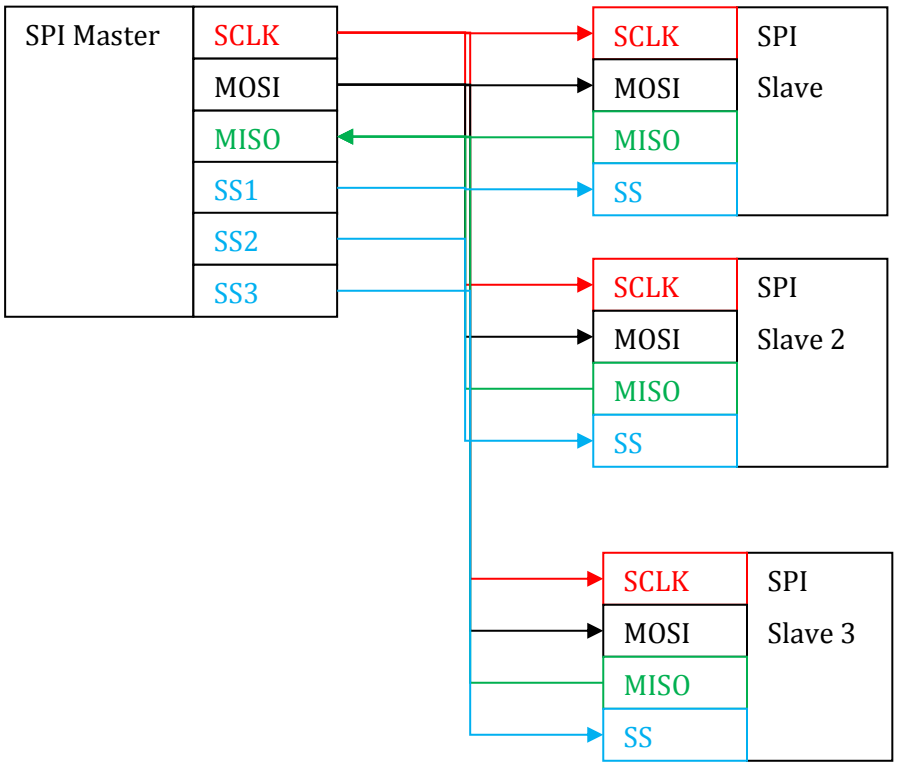

Figure 3.2: SPI master-slave daisy chain architecture

3.1.2.1 SPI Data Transmission

It is important to understand the functions of the SPI protocol in order to implement it effectively. The master must select one slave at a time. A master and slave device will follow the procedures outlined below: (Refer to Figure 3.3)

1. The master selects a slave by transmitting the appropriate chip select bit and setting it to a logic low (1= off state, 0=on state)
2. A wait period is then initiated to ensure the designated chip is selected.
3. Master starts to issue clock cycles. On each clock cycle:
   3.1 The Master sends a bit on the MOSI, data is shifted out with the MSB(most significant bit) first.
   3.2 The Slave receives a bit and sends a bit on the MISO line and the Master reads it going back to step 3.1. This cycles until the complete register has been shifted out and there is no more data to exchange. Register are generally 8-bit words.
4. Master stops toggling the clock ending transmission
5. Master deselects the slave

3.1.2.2 Clock polarity and phase

One of the pertinent functions of the master is the configuration of the clock polarity (CPOL) and phase (CPHA) as shown in Figure 3.4. Table 2 outlines 4 clock configurations with regard to phase and polarity. A clock polarity of unity implies the clock value beginning at a unity baseline whereas that of zero implies a 0 baseline value. Mode pairs 1 and 4, 2 and 3 are identical in the ways the data is captured and propagated. Data is sampled or captured on the MISO line and is propagated on the MOSI line (Paradigm, n.d.).

Table 2: CPOL and CPHA summary combination table

Mode	CPOL	CPHA	Data captured(MISO)	Data propagated(MOSI)
1	0	0	Clocks rising edge	Clock falling edge
2	0	1	Clock falling edge	Clocks rising edge
3	1	0	Clock falling edge	Clocks rising edge
4	1	1	Clocks rising edge	Clock falling edge

If multiple slaves are used, that are fixed in different configuration modes, the master will have to reconfigure itself each time it needs to communicate with a different slave.

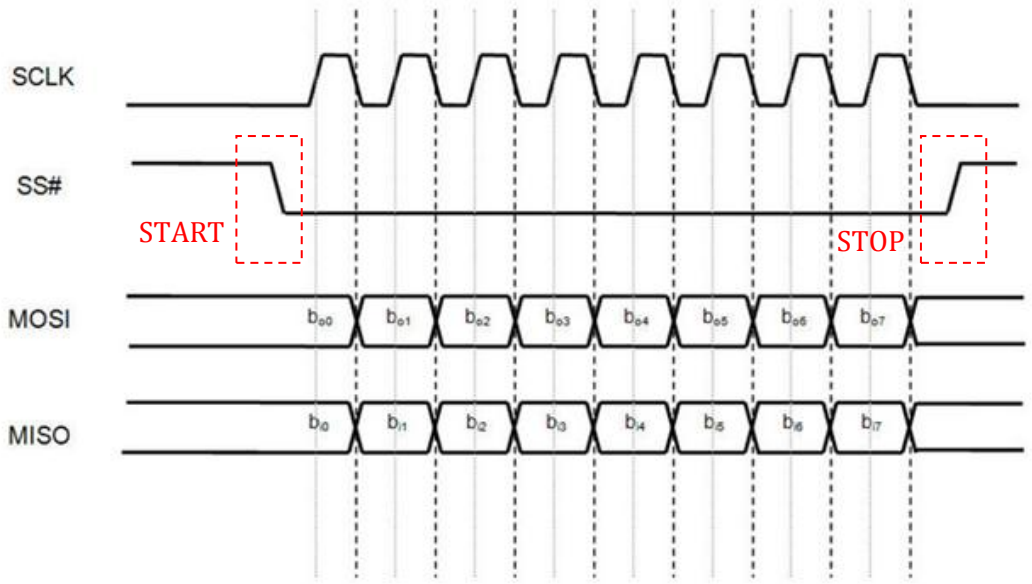

Figure 3.3: SPI data transmission for CPOL=0, CPHA=1.

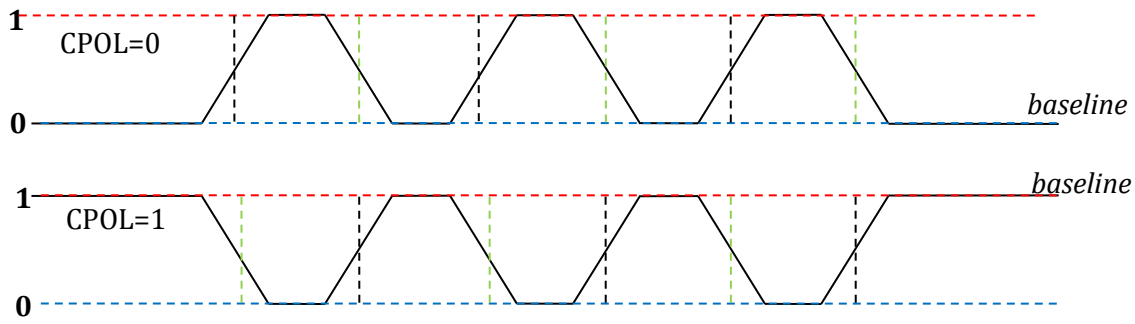

Figure 3.4: Polarity and phase on the SPI communication bus.

3.1.2.3 SPI Communication Downfalls

SPI by protocol does not define a maximum data rate and addressing scheme. It mainly has no acknowledgement of receipt of data and does not have any flow control. The existence of the slave device is unknown to the master unless an alternate identification routine is created outside the protocol.

3.1.3 Serial Communication Parameters

The important serial characteristics are baud rate, data bits, stop bits, and parity. It is essential that these parameters match. A description of these will be briefly outlined

- **Baud rate**: a speed measurement for communication. It indicates the number of bit transfers per second. 300 baud is equivalent to 300 bits per second or a sampling rate of 300Hz. High baud rates are used for device communication which are in close communication proximity.
- **Data bits**: a measurement of the actual data bits in a transmission. When the computer sends a packet of information, the amount of actual data may not be a full 8 bits. Standard values for the data packets are 5, 7, and 8 bits depending on the type of data being sent, standard ASCII has values from 0 to 127 (7 bits) whilst extended ASCII uses 0 to 255 (8 bits). A packet refers to a single byte transfer, including start/stop bits, data bits, and parity.
- **Stop bits**: used to signal the end of communication for a single packet. Typical values are 1, 1.5, and 2 bits. Since the data is clocked across the lines and each device has its own clock, it is possible for the two devices to become slightly out of sync. Therefore, the stop bits not only indicate the end of transmission but also give the computers some room for error in the clock speeds. The more bits that are used for stop bits, the greater the lenience in synchronizing the different clocks, but the slower the data transmission rate.
- **Parity**: a simple form of error checking that is used in serial communication. There are four types of parity: even, odd, marked, and spaced. Of course, the option of using no parity is also available. For even and odd parity, the serial port will set the parity bit (the last bit after the data bits) to a value to ensure that the transmission has an even or odd number of logic high bits. For example, if the data was 011, then for even parity, the parity bit would be 0 to keep the number of logic high bits even. If the parity was odd, then the parity bit would be 1, resulting in 3 logic high bits. Marked and spaced parity does not actually check the data bits, but simply sets the parity bit high for marked parity or low for spaced parity. This allows the receiving device to know the state of a bit so as to enable the device to determine if noise is corrupting the data or if the transmitting and receiving devices' clocks are out of sync.

3.1.3.1 Software Handshaking

This form of handshaking style uses actual data bytes as control characters. The lines necessary are still the simple three line set of Data Transmit (TX), Data Received (RX), and round since the control characters are sent over the transmission line like regular data.

3.1.3.2 Hardware Handshaking

The second method of handshaking is to use actual hardware lines. Like the TX and RX lines, the RTS/CTS and DTR/DSR lines work together with one being the output and the other the input. The first set of lines are RTS (Request to Send) and CTS (Clear to Send). When a receiver is ready for data, it will assert the RTS line indicating it is ready to receive data. This is then read by the sender at the CTS input, indicating it is clear to send the data. The next set of lines are DTR (Data Terminal Ready) and DSR (Data Set Ready). These lines are used mainly for modem communication. They allow the serial port and the modem to communicate their status.

3.2 Labview System Design Software

Labview system design software provides the user with the tools needed to create and deploy measurement and control systems through hardware integration. Integration of the SBRIO-9602 hardware controller is achieved via the Labview 2011 SP1 graphical system design software. Software implementation and hardware integration was easily achieved via the control blocks.

3.2.1 State-Machine Architecture

State machines are one of the essential tools used in situations where distinguishable states exist. Each state can lead to one or multiple states and can end the process flow. A state machine relies on user input or in-state calculation to determine which state to proceed. Prior to the use of a state machine, a flow chart for each process was drafted establishing all the possible decisions and that which requires user input to proceed to the next state. The drafting of the flow process is formally referred to as state diagram. Effective use of the state machine requires knowledge of the various states of the application and how one

loops relate to one another. Visualizing this improves the overall design of the application and is the fundamental approach of the state diagram. Figure 3.5 illustrates the basic state machine and can be created with a while loop, shift register, case statement and case selector.

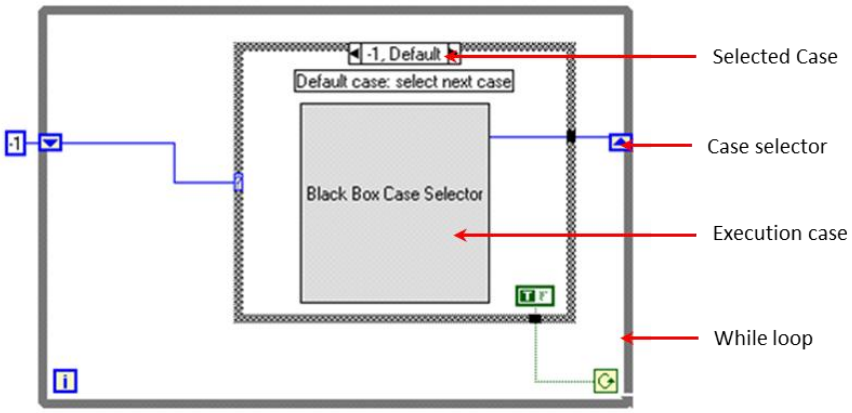

Figure 3.5: Simple state machine architecture.

The while loop is the main program loop, which executes until the conditions for exiting the program is met. The while loop's main responsibility is to call the case selector and then execute the appropriate case. The shift register keeps track of which case should execute next. Finally, each case of the case statement contains the action for one specific use action. Often the default case is used as the place to check the case selector (in other words, if the user did nothing, check again to see if he has done something yet).

3.2.2 Field Programmable Gate Array (FPGA)

The FPGA is a reprogrammable hardware logic unit and its architecture can be referred to in section 5.6.3. It's easy re-configurability eliminates the expense of ASIC re-design and maintenance. This allows for software to be designed to a hardware specific function. Prior to Labview the use of FPGA technology required a deep understanding of digital hardware design. The NI software platform converts the graphical block diagrams to hardware circuitry using standard Labview programming techniques. When an FPGA-enabled device is targeted, the programming interface is simplified to contain only FPGA-defined functions. FPGA hardware is designed to work with integer math as opposed to floating point math.

Most importantly is the parallelism (see Figure 3.6) that exists whereby tasks do not need to be prioritised as software loops can run independently. The Labview FPGA module translates the graphical code to a text-based VHDL code. The Xilinx ISE compiler tools are invoked and the VHDL code is optimized, reduced, and synthesized into a hardware circuit realization of the created software. This process also applies timing constraints to the design and tries to achieve an efficient use of FPGA. Further optimisation is performed during the FPGA compilation process to reduce digital logic creation. The end result is a bit stream file that contains the gate array configuration information. When an application is initiated, the bit stream is loaded into the FPGA chip and used to reconfigure the gate array logic. The bit stream can also be loaded into non-volatile Flash memory and loaded when power is applied to the target. There is no operating system on the FPGA chip, however execution can be started and stopped using enable-chain logic that is built into the FPGA application (NI, n.d.).

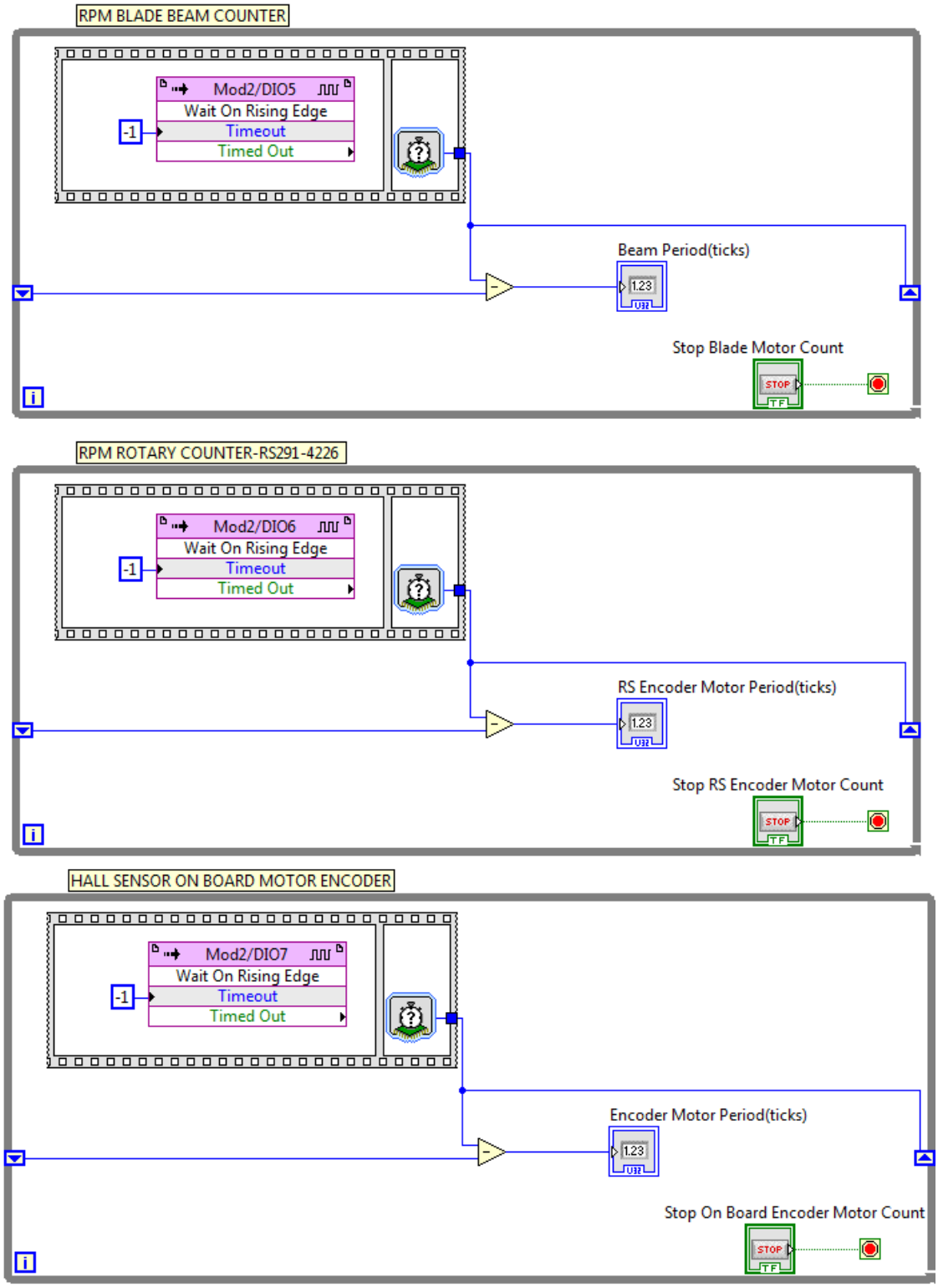

Figure 3.6: FPGA parallel loops in the data acquisition process for RPM sensors.

3.2.3 Pulse Position Modulation (PPM)

A PPM signal generator was created in the FPGA to supply a pulse train on the digital output line to the digital input line of the electronic speed controller (see Figure 3.7). To create a PPM signal in Labview FPGA, a digital pulse high is set for a predetermined time (Delay 2) and then pulled down low for a predetermined time (Delay 1). Ticks are used as finite time denominations. The outer loop or "While loop" constantly cycles through the coding in the internal loop. The code inside the "Stacked Sequence" forces the code to execute left to right when all data values wires to the frame are available. Data leaves the frames provided they have finished executing. The SBRIO has a processor rated at a 400 MHz processing speed. The period of this is equivalent to 2.5ns denoted by 1 Tick. Ticks provide an accurate timing value and achieve a larger resolution as opposed to milliseconds. Assuming the delay of 1.5 milliseconds is required; however as we need integer values this can be only be achieved through a 6×10^5 Tick value.

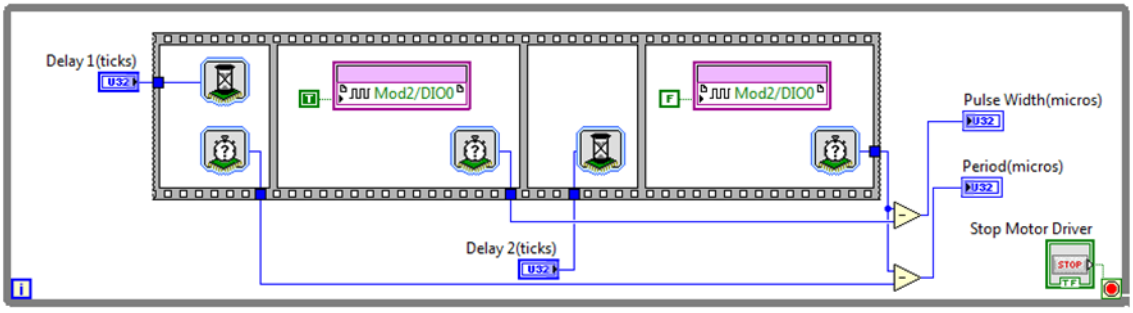

Figure 3.7: Labview BLDC motor commutation.

3.2.4 Sensor Data Acquisition

A data acquisition while loop was created for RPM sensing using the RS encoder, hall sensor and IR beam apparatus set. The loops were constructed in the FPGA allowing for parallel data collection from multiple sensors simultaneously. The parallel nature of the PFGA process can be seen in Figure 3.6. The data acquisition loops use a similar structure to the PPM signal described in section 3.2.5. A "While loop" is combined with a "Flat sequence". As per Figure 3.8 the rotary encoder is connected to the DIO line 6. The controller waits for the digital line to rise and then initiates the counter as per stacked sequence. A digital high is

registered when the blade crosses the optical path. The difference in time between the two rising edges is the period that is needed as seen in Figure 3.9.

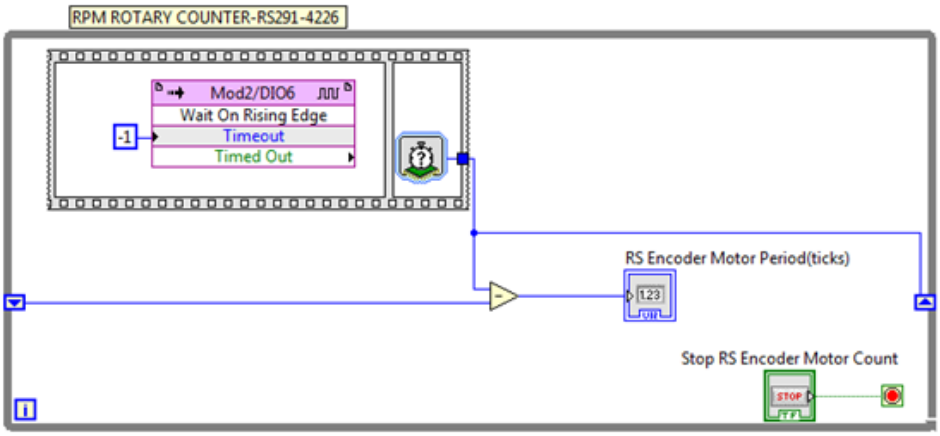

Figure 3.8: RPM data acquisition in the FPGA.

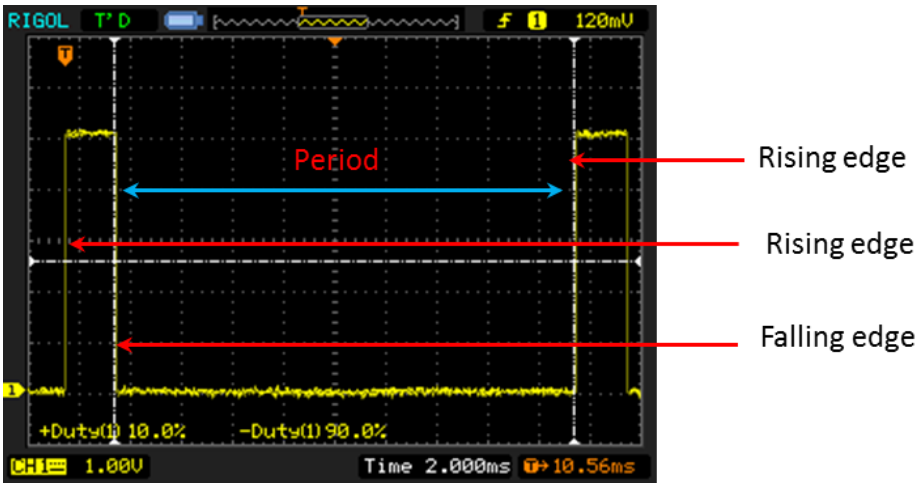

Figure 3.9: Oscilloscope reading for pulse analysis.

3.2.5 Speed Controller Calibration and Start-Up

Due to the vast number of calibration parameters and the inconvenience presented to the user on each motor run, an automated motor testing process was created. State machine architecture with user input was implemented to drive the motor testing process allowing for a single button click for motor calibration and commutation. An electronic speed

controller is needed to regulate the BLDC motor RPM. A hobby electronic speed controller utilizes user inputs prior to motor commutation. In radio controlled (RC) helicopters user inputs are through the movement of the throttle stick of a RC transmitter. The supplied user manual stipulates a startup and throttle calibration procedure (see appendix C). Calibration involves battery cell and voltage detection, minimum and maximum throttle settings, commutation direction and throttle curve settings.

Figure 3.10 illustrates the state diagram for the calibration and start up process. User input is denoted by the solid line rectangular block set, decision making processes are denoted by the blue outlined diamond block set and all errors denoted by the red outlined triangular block set. Continuous beeping of the ESC is symptom of either a loss in communication between the controller and the ESC, a loss of power to controller or incorrect PWM value used on the GUI. The beeping of the ESC is the only feedback the user has as to the state of the process.

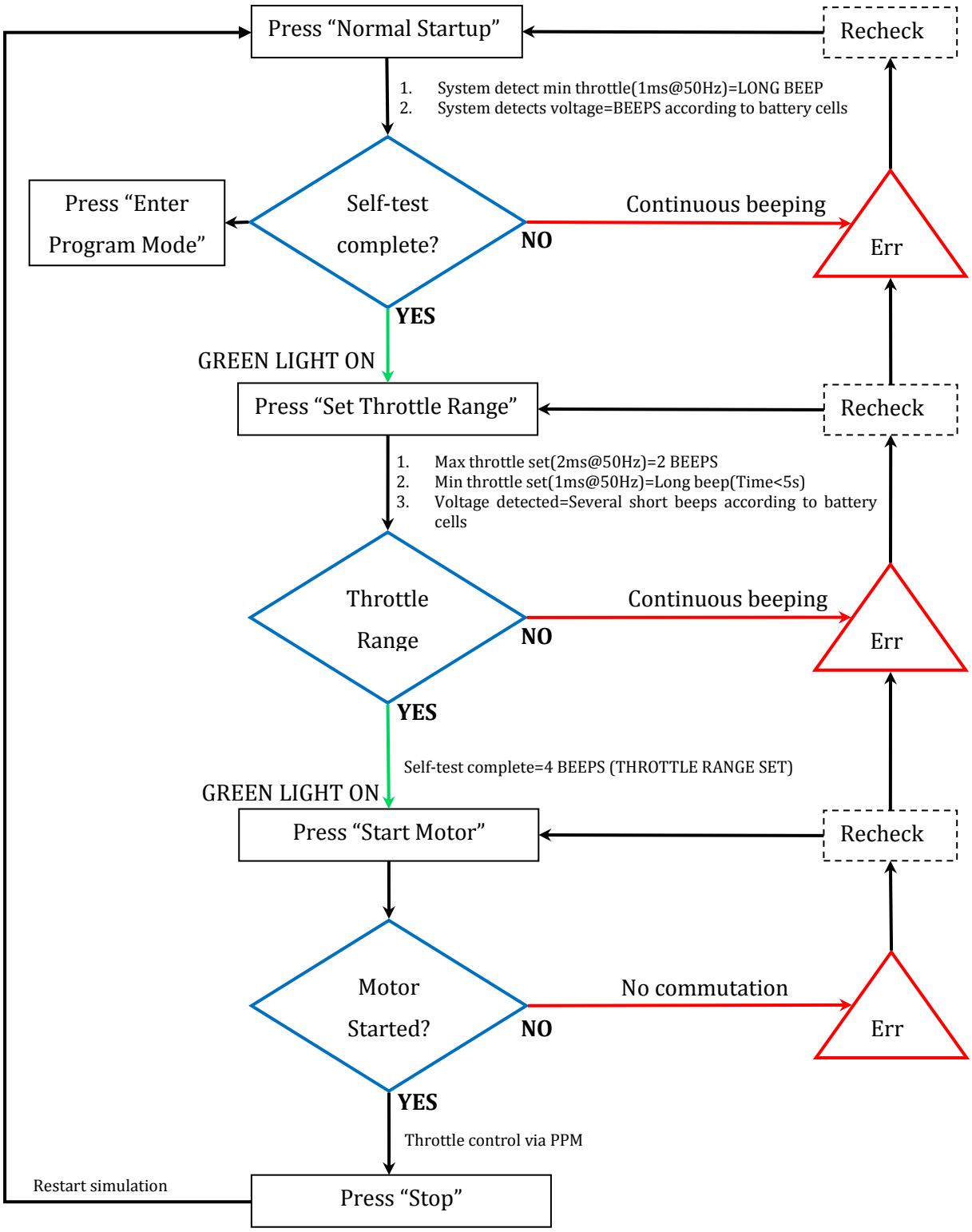

Figure 3.10: Flow process of the ESC arming and motor start-up.

3.2.6 Throttle Timing

A constant throttle timing procedure was needed in order to maintain a specified PWM signal for a predefined time. The timing was essential as it allowed a constant RPM and thrust reading at a set PWM value. The PWM value was then varied in a range of 5% to 10% in increments of 0.25% (see Figure 3.11) maintaining the 50Hz excitation frequency. Variation in the PWM signal implies a set PWM/time period over a span of 5% PWM signal. This was done in Labview by incorporating a series of nested loops which are initiated as soon as the time criteria are met (see Figure 3.12). In total 20 nested cases were used corresponding to time increments from 5% PWM to 10% PWM at 0.25% PWM. A 30 second time interval was used in order to allow for the RPM value to stabilise increasing the accuracy of the average recorded value.

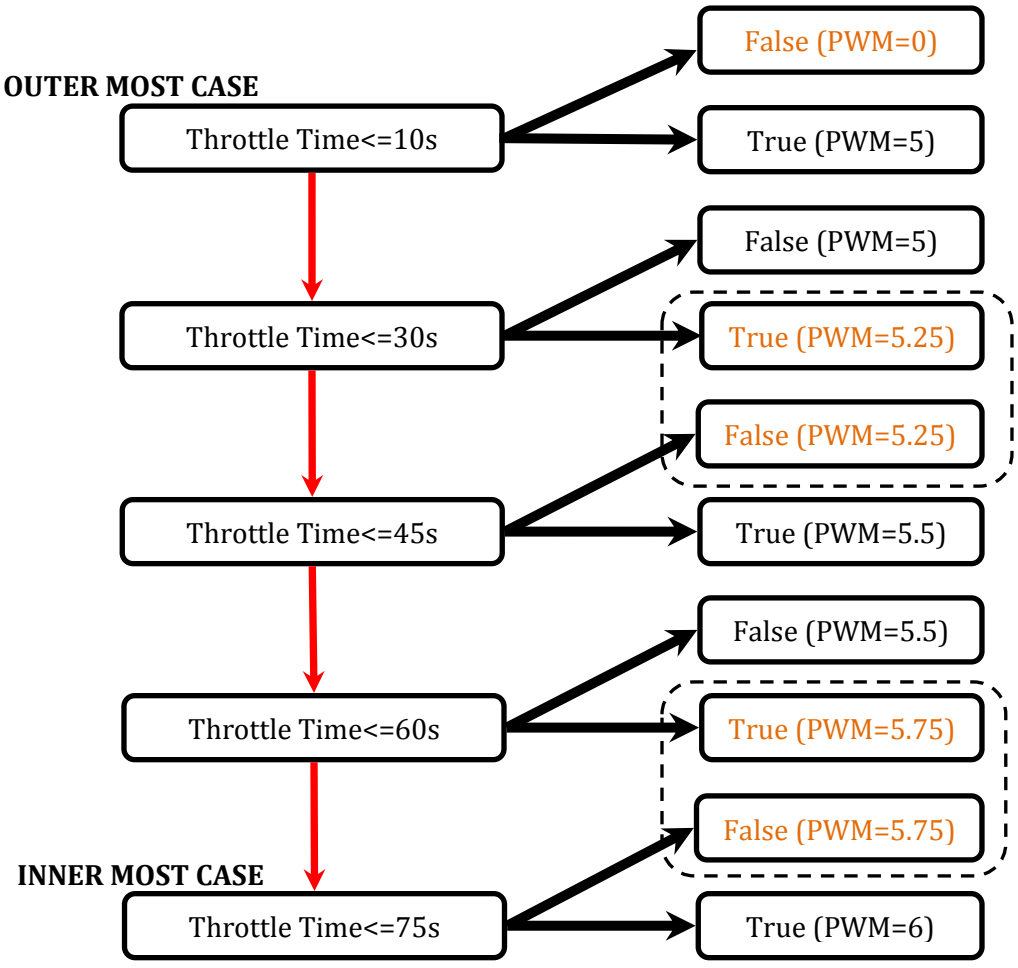

Figure 3.11: Throttle timing nested cases.

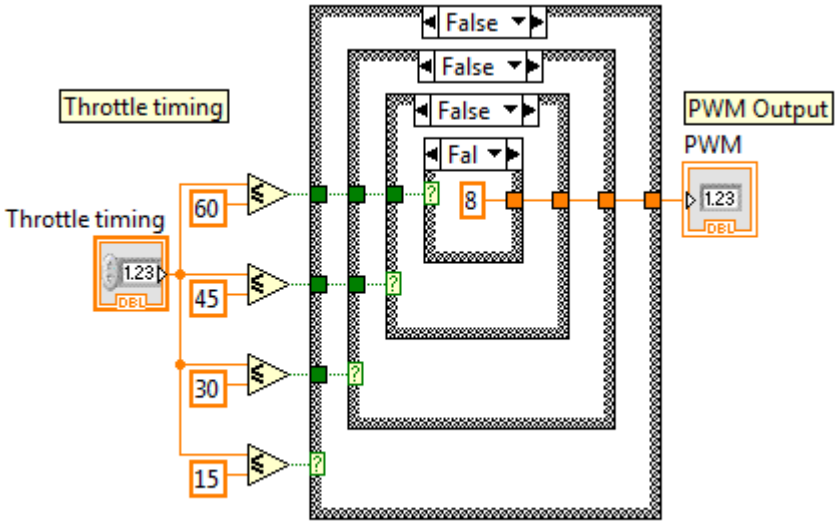

Figure 3.12: Nested loop structure in Labview.

3.2.7 User Motor Testing Interface

The motor testing interface allows for the user to specify the pulse width of the motor signal and initiate the simulation from the GUI. Once initiated Labview cycles through the sequence of events defined in Figure 3.10 and together with the Figure 3.12 allows for a totally automated process. The "Ready for Start" LED when green notifies the user that the conditioning sequence for the motor as define in Figure 3.10 has been complete and the rig is ready for testing of the motor. The "Set Throttle" button allows for different RPM throttle curves to be selected and has a linear throttle curve per the default setting. The "Duty Cycle" slider allows for manual override of the throttle step function. The indicators allow for the RPM and thrust values to be monitored. Figure 3.14 illustrates the outputs of the testing interface which notifies the user of changes in RPM with throttle and also variations in thrust. When the "Start motor" button is de-pressed the user decision case structure as seen in Figure 3.15 configures the ramp function for throttle ramping. The three identical RPM reading are indicative of three sensors being read simultaneously which are calculated on spate channels on the FPGA and cannot be mistaken as duplicated values but instil a higher level of confidence in acquired data. It may be noted that the data processing does not occur during a test run but after the data is acquired. Once acquired the data is imported directly to a CSV format for ease of processing.

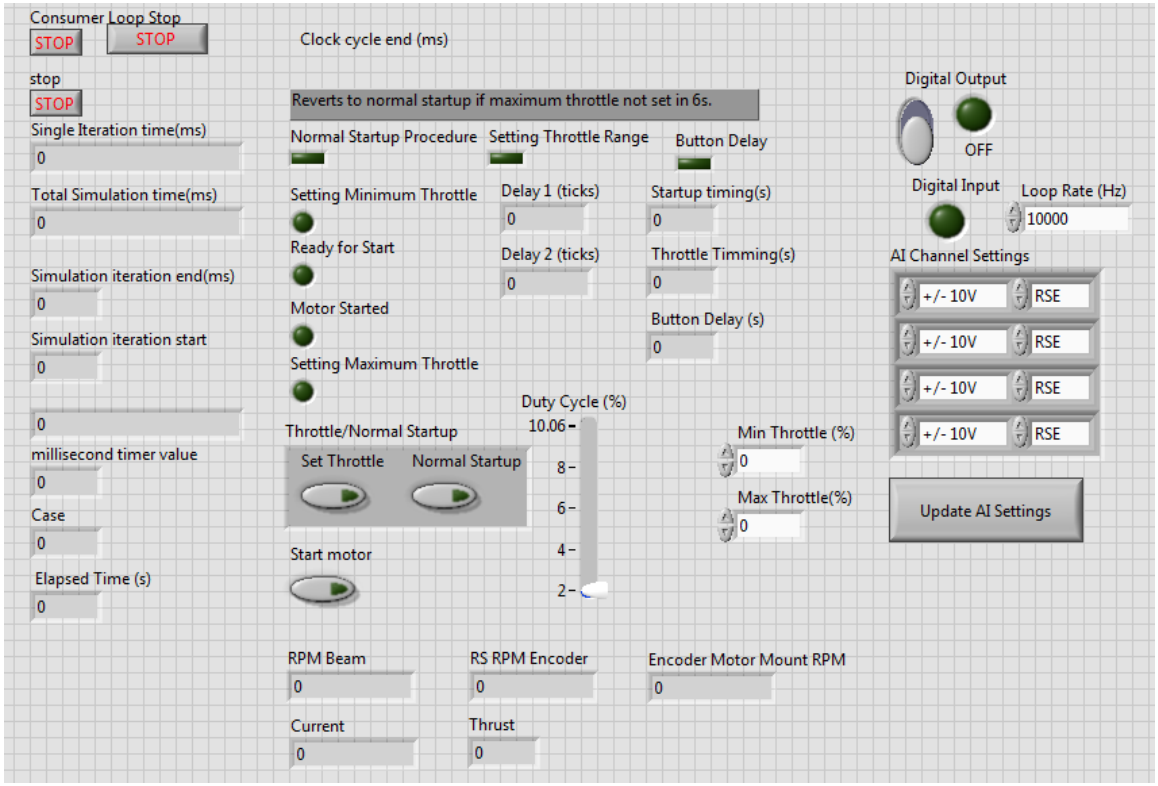

Figure 3.13: Thrust rig motor testing interface.

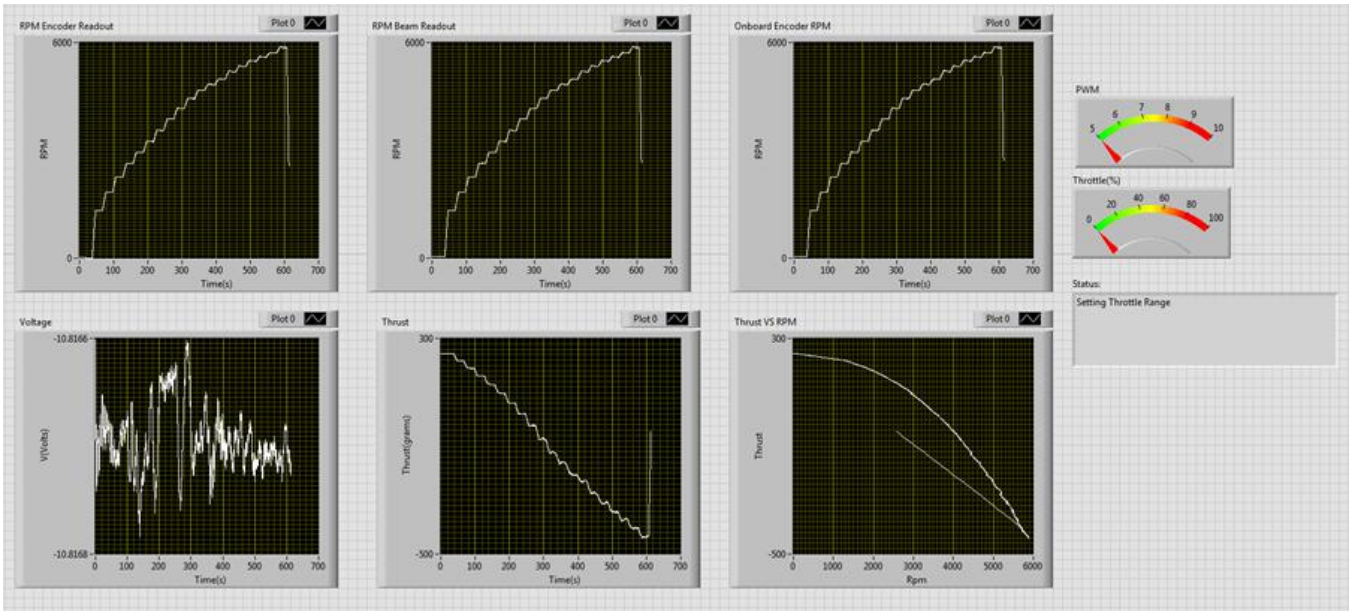

Figure 3.14: Thrust rig simulation outputs.

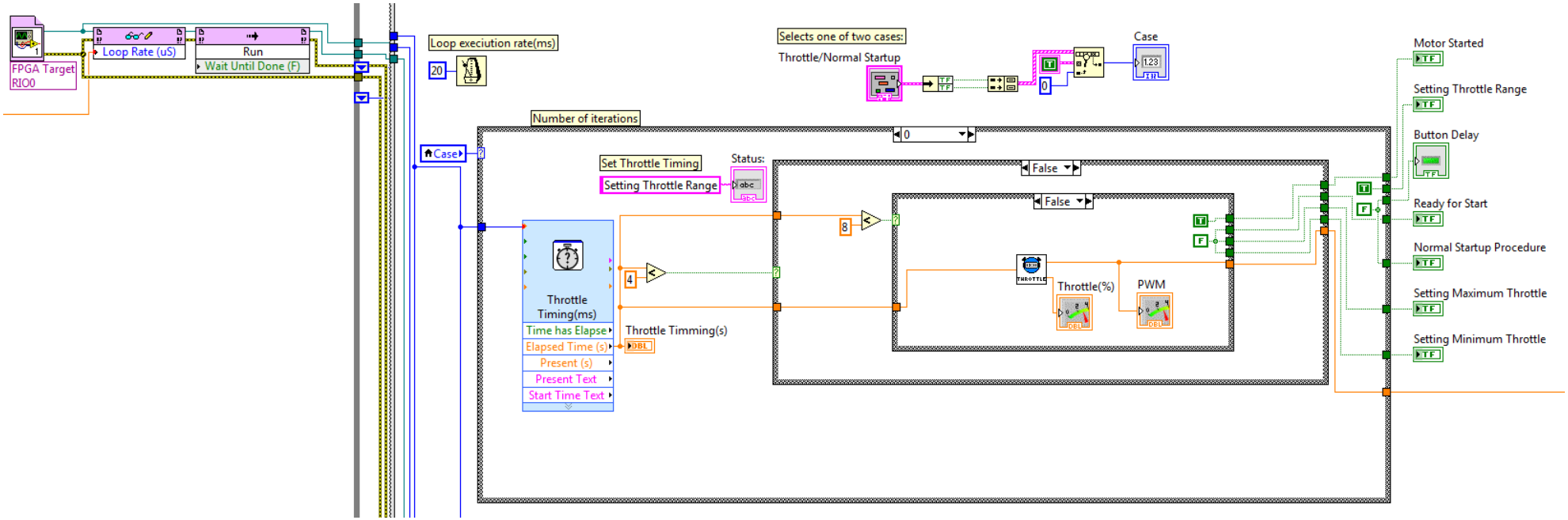

Figure 3.15: User decision case structure.

4. Attitude Heading and Reference System

This chapter will highlight the structure, behaviours and performance of the feedback sensors.

4.1 Function and Definition

The function of an altitude and heading reference system (AHRS) and its ability to provide heading, attitude and yaw information for the quadrotor is an essential part of the control system. AHRS consists of either solid-state or micro-electro-mechanical system (MEMS) gyroscopes, accelerometers and magnetometers on all three axes. The key difference between an inertial-measurement unit (IMU) and AHRS is the addition of an on-board processing system. The added processing ability of AHRS allows for solved attitude and heading solutions versus an IMU which delivers sensor data to a processor. For testing purposes a 9 DOF AHRS unit (Sparkfun) was utilised which contained all the necessary electronic hardware.

4.2 Electronic Hardware Architecture

The 9DOF IMU unit (seen in Figure 4.1) incorporates three sensors, a triple-axis gyro (ITG-3200), triple-axis accelerometer (ADXL345), and a triple-axis magnetometer (HMC5883L) to provide nine degrees of inertial measurement. Additionally it has an onboard processor (ATMEGA-328) for all onboard processing and outputs data via SPI or I2C communication protocol. The 9DOF operates at 3.3VDC via any power supplied to the white connector (JST) which will be regulated down to this operating voltage.

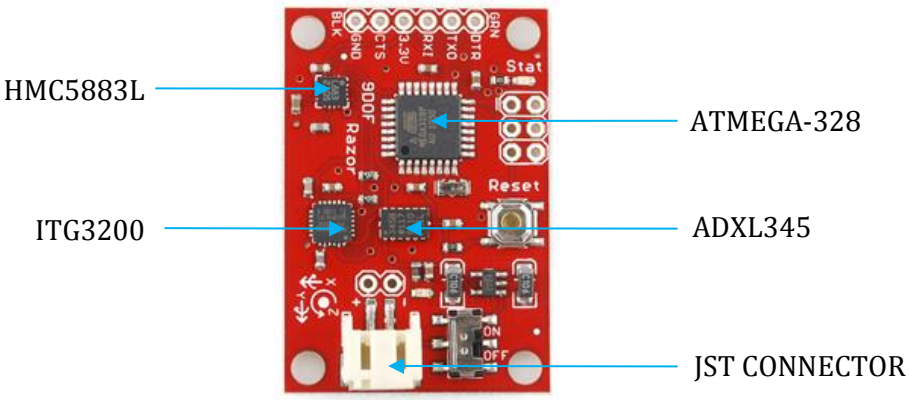

Figure 4.1: Sparkfun 9DOF AHRS solution

Translating MEMS behaviours into predictable performance at the system level requires cultivating an understanding of the transducer's performance and behaviours, and assists in establishing the impact that the sensor's behaviours will have on critical system performance criteria. It is essential to develop a strategy and process for characterising and correcting behaviours that can limit the transducer's error in the system. The following sections assist in understanding the behaviour of each sensor allowing for the impact on performance to be assessed.

4.2.1 Triple Axis Gyroscope

4.2.1.1 Gyroscope Function

Unlike mechanical gyros which stay fixed in space while the aircraft rotates around them, the electronic rate gyroscope rotates with the aircraft (in the aircraft frame of reference) producing signals proportional to the rotational rate. The rotation cannot be achieved through the integration of the gyro rate signal as numerical integration introduces numerical errors and does not produce the same result as symbolic integration. Small rotations are completely decoupled; their order does not matter. Only for the case of infinitesimal Euler angles is it true that the time rate of change of the Euler angles equal the body-referenced rotation rate.

4.2.1.2 Gyroscopic Model and IMU theory

The orientation of the quadrotor is described by three consecutive rotations, whose order is important. The angular rotations are called the Euler angles. The orientation of the body frame with respect to the earth-fixed frame can be determined in the following manner. Imagine the airplane to be positioned so that the body-axis system is parallel to the fixed frame and then apply the following rotations (see Figure 4.2):

1. Rotation about its Z_b axis through the yaw angle ψ.
2. Rotation about its Y_b axis through the pitch angle θ.
3. Rotation about its X_b axis through the roll angle ϕ.

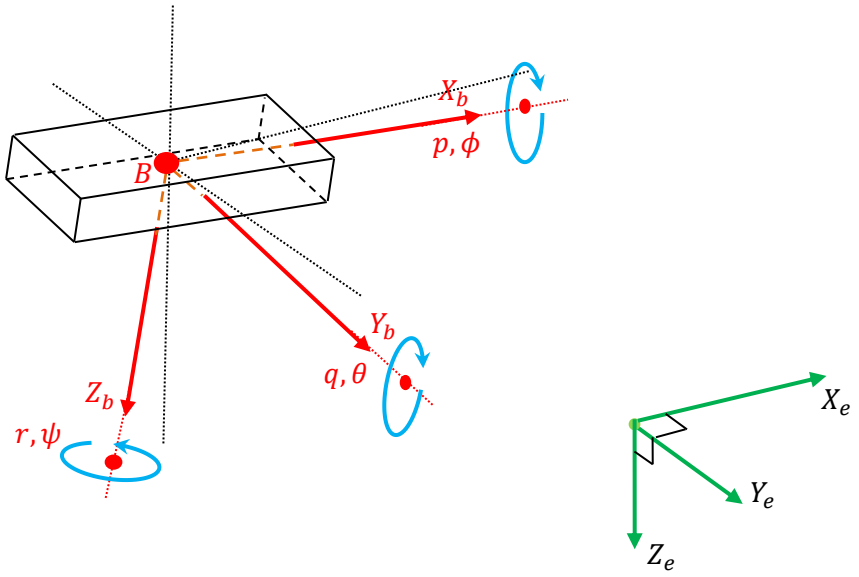

Figure 4.2: ITG-3200 Gyroscope 6DOF solution.

The order of rotation is important when using Euler angles. If component rotations used are finite, it's important that the order in which they are applied is maintained. This is because finite rotations do not obey law of vector addition, and hence cannot be classified as vector quantities. To illustrate this consider cases 1 and 2 shown in Figure 4.3 and Figure 4.4 respectively. Each rotation θ_1 and θ_2 had a magnitude of $90^o$and a direction defined by the right hand rule.

Rotation order 1:

- 90 degree clockwise rotation about the z-axis.
- 90 degree clcokwise rotation about the y-axis.

Rotation order 2:

- 90 degree clockwise rotation about the y-axis.
- 90 degree clcokwise rotation about the z-axis.

Hence the importance of rotation sequence can be seen as the final oritentation of the body axis differs by two succesive rotations as highlihted by the broken box border line in Figure 4.3 and Figure 4.4. This is known as non-commutative and are a property of finite rotations. The rotation about one axis causes a change in the angular rotation of two axes as seen in Figure 4.5.

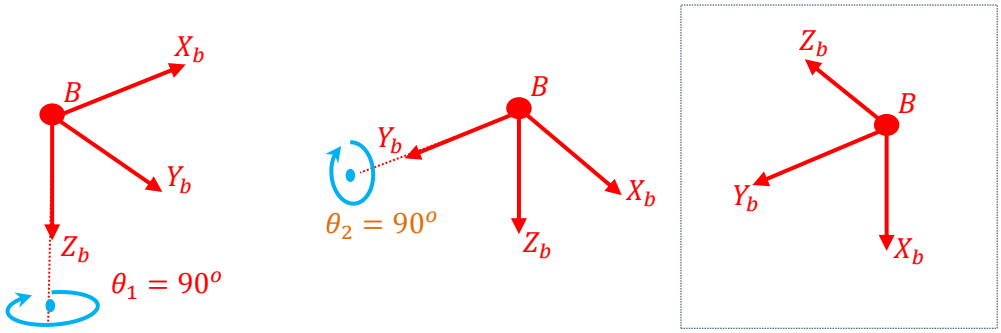

Figure 4.3: Rotation order 1 for finite rotations.

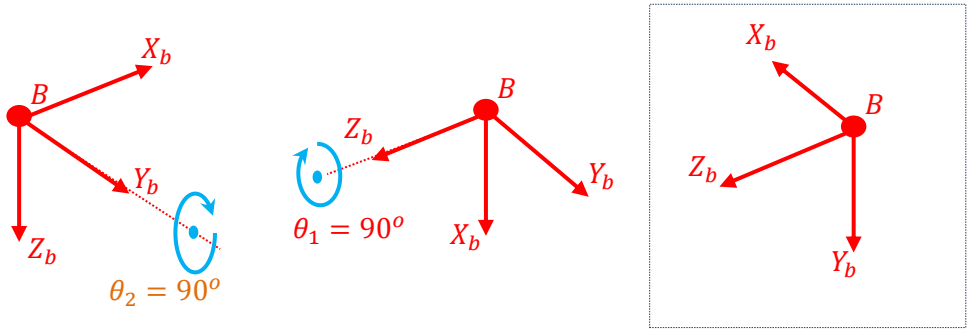

Figure 4.4: Rotation order 2 for rotations.

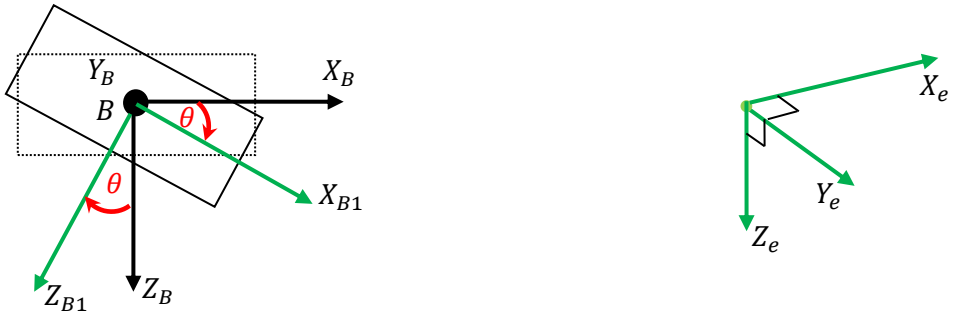

Figure 4.5: Using vector cross and dot products.

4.2.1.3 Gyroscope calibration and output processing

The gyroscope is easily calibrated by placing it on a stationary surface. Since it is subject to no rotation, the readings from the ADC on each axis must give a rotational rate of $\omega = 0^o/s$. Each axis has its own ADC as seen in Figure 4.6. If the ADC issues a value on a specific axis then this is the corresponding zero offset value on the noted axis.

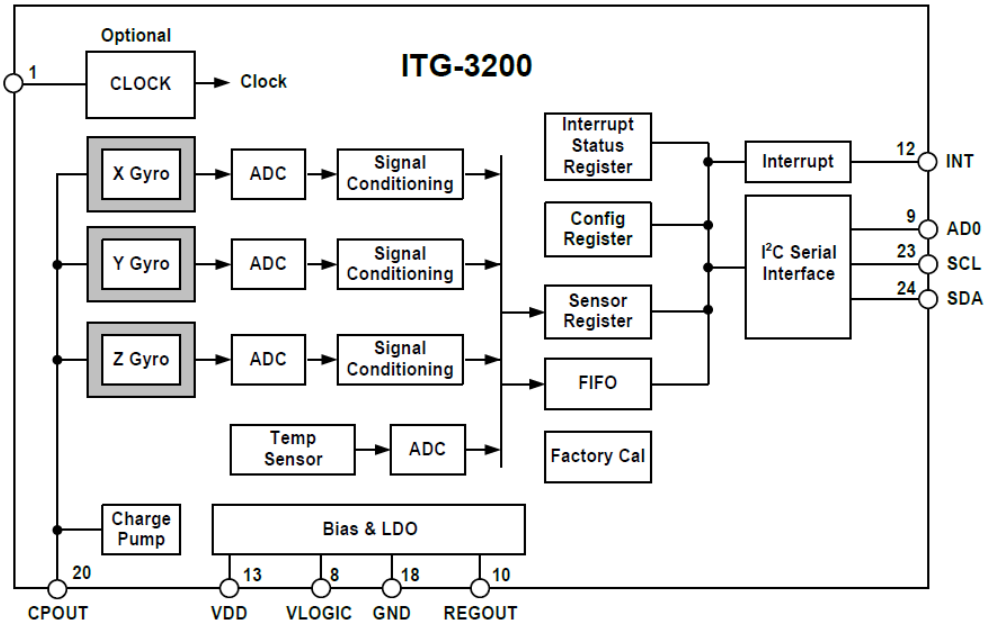

Figure 4.6: ITG-3200 (Invensense, n.d.).

4.2.1.4 Gyroscopic Performance criteria

The ITG 3200 comprises of 3 gyroscopic sensor on each axis combined with a 16 bit analog to digital converter.

The gyroscopic rate can then be computed as follows: (constant defined in Table 3)

$$Rate_{gyro} = \frac{\left(ADC_{value}\left(\frac{V_{supply}}{ADC_{Resolution}}\right) - Rate_{gyro-zero}\right)}{Sensitivity} \tag{4.1}$$

The ITG-3200 axis MEM gyroscope has the performance constants as shown in Table 3:

Table 3: ITG-3200 3-Axiz gyroscope specifications (Invensense, n.d.).

Full scale range	+-2000
$ADC_{Resolution}$	16 bit
$Sensitivity$	14.375 $LSB/^{o}/s$
V_{supply}	2.1V to 3.6V
$Rate_{gyro-zero}$	From Calibration

Assuming we have an ADC reading of 42214, and a supply voltage of 3.3V hence:

$$Rate_{gyro} = \frac{\left((42214)\left(\frac{3.3}{(2^{16}-1)}\right) - Rate_{gyro-zero}\right)}{14.375} \tag{4.2}$$

The zero rate can be achieved by calibration.

4.2.2 Triple-Axis Accelerometer

4.2.2.1 Accelerometer function

An accelerometer will measure a value of gravitational acceleration along the Z_B axis when remaining stationary on the ground, because masses on earth have weight. Such weight is

transmitted from reaction force on the ground, and is not directly caused by gravity, but rather by the mechanical force from the ground, in the same way as the push of the engine in the rocket. However, there is no change in velocity in this example, as the reaction force from the ground counteracts the acceleration of gravity, which is not felt. By contrast, an accelerometer in gravitational free fall toward the center of the Earth will measure a value of zero acceleration because, even though its velocity is increasing, it is at rest in a frame of reference in which objects are weightless. Accelerometers will read zero when gravitation provides the only acceleration that acts on the device (or the only "force" on the device thus measures all accelerations, except those accelerations due to gravity. The accelerometer measures the earth's gravitational field minus the acceleration. It can also be used to specify the orientation of the sensor by the sign of the output voltage (see Figure 4.7).

$$Acc_{reading} = g - Acc_{exerted} \tag{4.3}$$

where:

g is the gravatational acceleration.

$Acc_{exerted}$ is the acceleration exerted on the device.

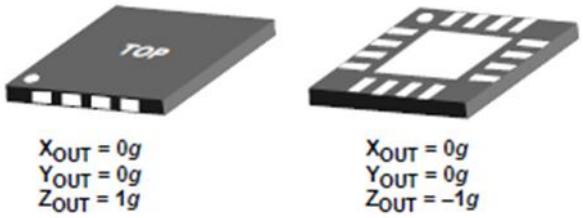

Figure 4.7: Acceleration vector at used to decipher orientation.

4.2.2.2 Accelerometer Construction

The Razor IMU unit consists of an ADXL325 accelerometer manufactured by analog devices. The accelerometer is a polysilicon surface micromachined structure built on top of a silicon wafer. Polysilicon springs suspend the structure over the surface of the wafer and provide a resistance against acceleration forces. Deflection of the structure is measured using a differential capacitor that consists of independent fixed plates and plates attached to the moving mass. The fixed plates are driven by 180° out-of-phase square waves. Acceleration

deflects the moving mass and unbalances the differential capacitor resulting in a sensor output whose amplitude is proportional to acceleration.

Phase-sensitive demodulation techniques are then used to determine the magnitude and direction of the acceleration (Analog Devices, 2009). This accelerometer concept can be viewed as a mass piece in the box suspended by springs (see Figure 4.8). The walls of the box are analogous of the walls of the accelerometer. The springs allow for the masspiece to translate back to its area of equilibrium when not put under any acceleration hence provide resistance to acceleration. The pressure exerted by the masspiece on the spring is transferred to the walls of the accelerometer measuring acceleration.

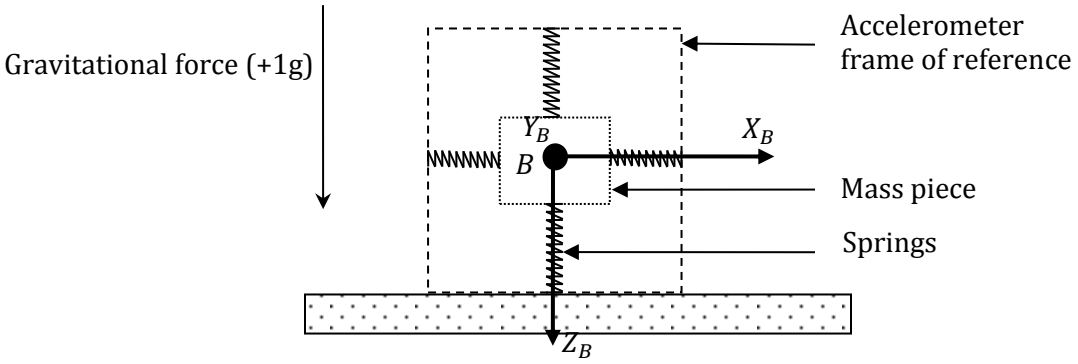

Figure 4.8: Accelerometer analogy.

4.2.2.3 Accelerometer Calibration and Output Processing

The accelerometer is easily calibrated by placing it on a surface parallel to the earth's surface. The accelerometer is rotated so that each axis has an opportunity to be parallel to the Z-Axiz of the earth (see Figure 4.9). When all three rotations are cycled through there are 2 offset values for each axis per revolution which can be averaged to obtain an average offset. The axis of the accelerometer that is aligned with gravity will always have a value as discussed in section 4.2.2.1.

The calibration offset for the body-fixed X axis (X_B) is given by:

$$Data_{offsetX} = \frac{X_{B1} - X_{B2}}{2} \tag{4.4}$$

where:

X_{B1}, X_{B2} are the calibration offsets on the body-fixed x-axis.

Similarly:

$$Data_{offsetY} = \frac{Y_{B1} - Y_{B2}}{2} \tag{4.5}$$

where:

Y_{B1}, Y_{B2} are the calibration offsets on the body-fixed y-axis.

Similarly:

$$Data_{offsetZ} = \frac{Z_{B1} - Z_{B2}}{2} \tag{4.6}$$

where:

Z_{B1}, Z_{B2} are the calibration offsets on the body-fixed z-axis

Table 4: Table of Rotation for accelerometer calibration

Rotation	Axis aligned with Z_E	Offset 1	Offset 2
1	Z_B	X_{B1}	Y_{B1}
2	Y_B	X_{B2}	Z_{B1}
3	X_B	Y_{B2}	Z_{B2}

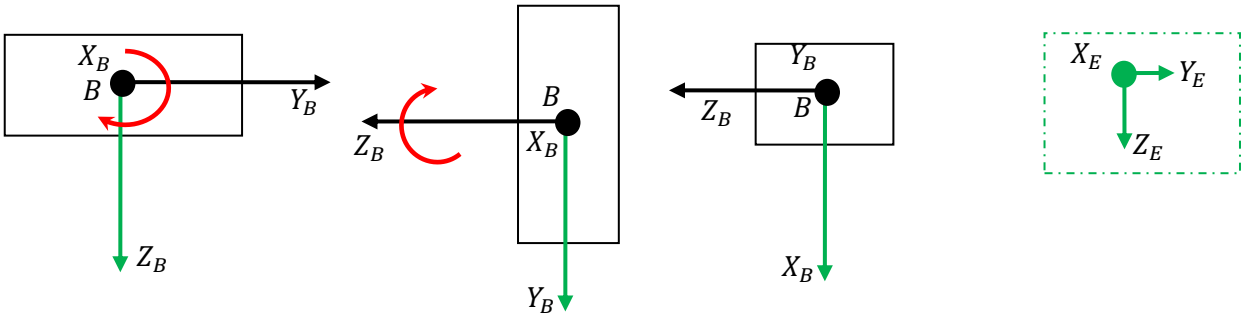

Figure 4.9: Calibration technique used on the accelerometer

The accelerometer output is a function of the ADC. The relevant properties used are highlighted in the Table 4.

Using the manufacturer specification sheet:

$$ADC_{Force-G} = \frac{\left(ADC_{read}\left(\frac{V_{supp}}{ADC_{bits}}\right) - V_{zeroG}\right)}{Sensitivity} \tag{4.7}$$

where:

ADC_{read} is the ADC value.

V_{supp} is the supply voltage.

V_{zeroG} is the zero voltage calibration value.

Assuming we use the method above to calculate 3 accelerations along the axes. Let these values be A_X, A_Y and A_z. Hence the inertial force vector can take the form of:

$$A = A_x i + A_y j + A_z k \tag{4.8}$$

where:

A_x, A_y, A_z are the accelerations along the x, y and z body-fixed axes respectively.

The magnitude of the resultant vector is given by:

$$|A| = \sqrt{(A_x)^2 + \left(A_y\right)^2 + (A_z)^2} \tag{4.9}$$

Hence the unit vector is given by:

$$\hat{A} = \frac{A_x}{|A|} i + \frac{A_y}{|A|} j + \frac{A_z}{|A|} k \tag{4.10}$$

where:

$$\left|\hat{A}\right| = 1$$

Where the angles are given b: (see Figure 4.10)

$$cos(\alpha_x) = \frac{A_X}{|A|} \tag{4.11}$$

$$cos\left(\alpha_y\right) = \frac{A_y}{|A|} \tag{4.12}$$

$$cos(\alpha_z) = \frac{A_z}{|A|} \tag{4.13}$$

$$\hat{A} = cos(\alpha_x)i + cos\left(\alpha_y\right)j + cos(\alpha_z)k \tag{4.14}$$

where:

$\alpha_x, \alpha_y, \alpha_z$ are the inclinations of the acceleration vector with respect to the corresponding the x, y and z earth-fixed axes respectively.

This can be represented graphically as:

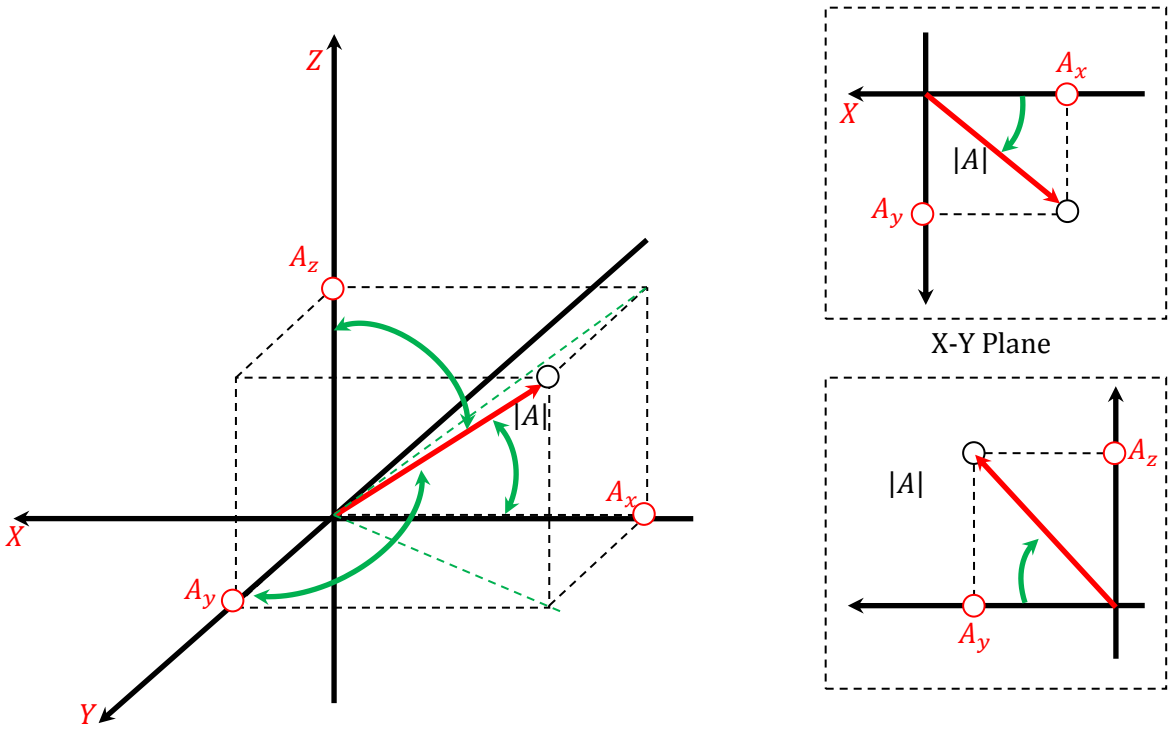

Figure 4.10: Interpretation of angles

4.2.3 Triple Axis Magnetometer

Magnetometers are used to sense magnetic field strength ascertaining magnetic declination. Good magnetometer performance is most crucial to yield a correct heading in all directions. If no distorting effects are present, rotating a magnetometer through a minimum of 360° and plotting the resulting data as y axis vs. x axis will result in a circle centered around (0, 0), as shown in Figure 4.11. Distortions of the earth's magnetic field are a result of external magnetic influences generally classified as either hard or soft-iron effects. It is important to understand the influence of these effects on the magnetic field and under which conditions is compensation applicable and effective (Konvalin, n.d.).

4.2.3.1 Soft Iron and Hard Iron Distortions

Hard iron distortion occurs when there is a material that produces a constant additive field to the earth magnetic field generating a constant additive value to the output of each magnetometer axes. The offsets will remain constant provided the orientation and position of the material generating such a field does remain constant relative to the sensor. A hard-iron distortion can be visibly identified as in Figure 4.11 by an offset of the origin of the ideal circle as seen in Figure 4.12.

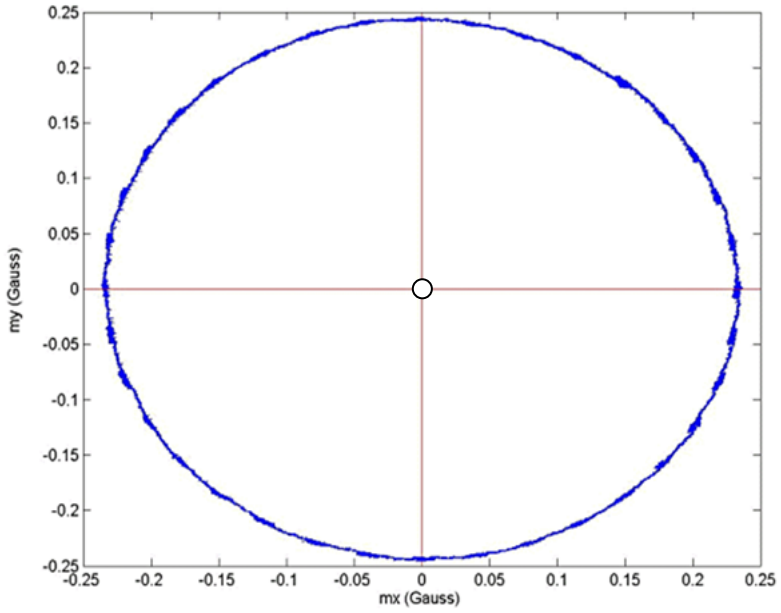

Figure 4.11: A graph of ideal distortion free magnetometer data centred around (0,0) (Konvalin, n.d.)

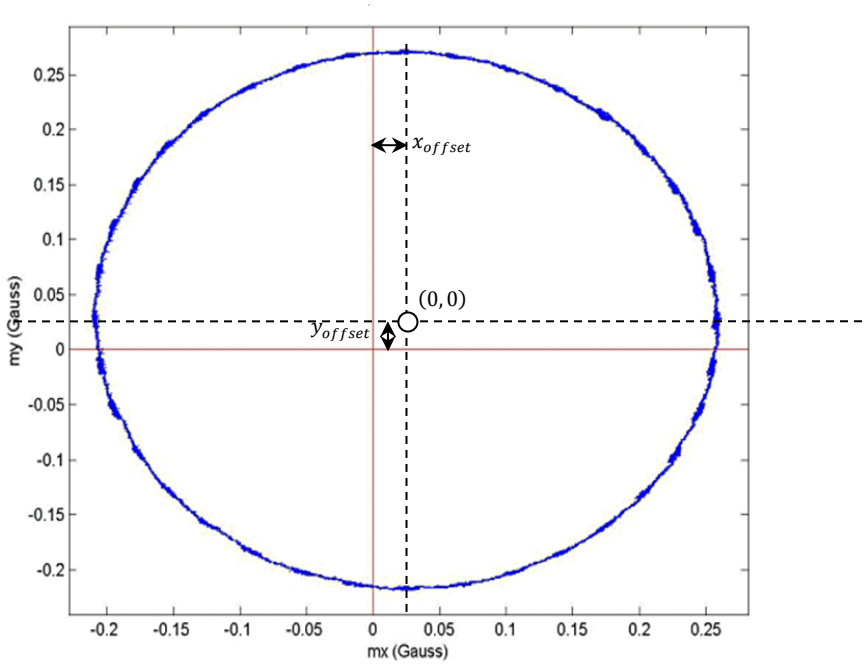

Figure 4.12: The effects of hard-iron distortion on a hard (Konvalin, n.d.)

The offsets can be calculated by:

$$x_{offset} = \frac{(x_{max} - x_{min})}{2} \tag{4.15}$$

$$y_{offset} = \frac{(y_{max} - y_{min})}{2} \tag{4.16}$$

where:

x_{max}, x_{min} are the maximum and minimum magnetic distortion values along the x-axis along the magnetometer respectively.

y_{max}, y_{min} are the maximum and minimum magnetic distortion values along the y-axis along the magnetometer respectively.

The offset values are then subtracted from the raw x and y magnetometer data eliminating majority of the hard-iron error.

Soft iron distortion unlike hard iron distortion is dependent upon the orientation of the material relative to the sensor and magnetic field hence is more complicated to compensate for than the prior. This type of compensation is computationally more intensive and may be more effective to eliminate soft iron materials from the proximity of the sensor. A soft iron distortion is generally exhibited as a perturbed circle (an ellipse) as can be viewed in Figure 4.13.

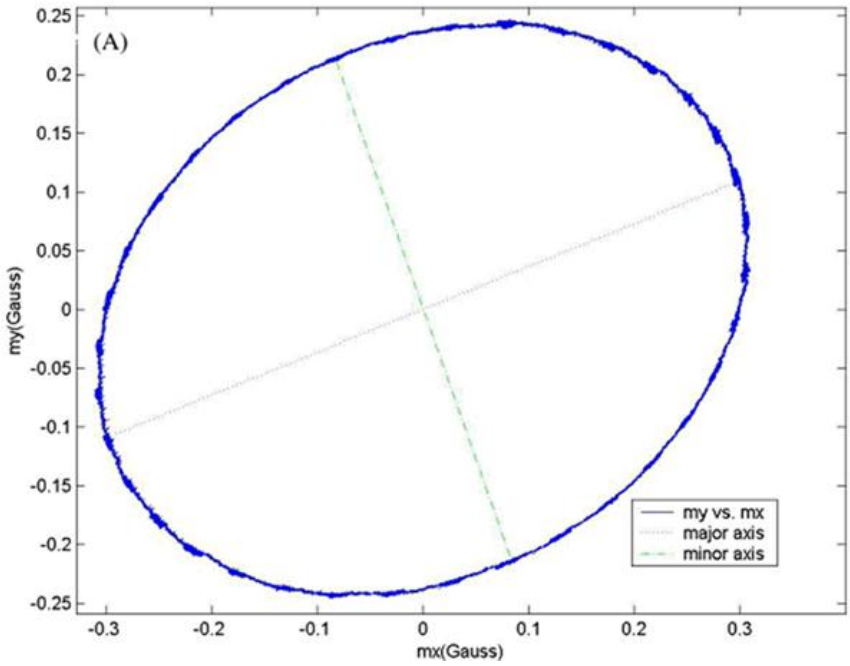

Figure 4.13: Soft iron distortion of a circle into an ellipse

4.2.4 Accelerometer Gyroscope Combination

Accelerometer's have the capability of providing inclination angles however they cannot be soley relied upon. These reasons can be attributed to the measurement of inertial forces caused by gravitation, but it might also be caused by acceleration (movement) of the device. As a result even if accelerometer is in a relatively stable state, it is still very sensitive to vibration and mechanical noise in general. This is the main reason why most IMU systems use a gyroscope to smooth out any accelerometer errors. The gyroscope is not free from noise however it measures rotation and is less sensitive to linear mechanical movements. Gyroscopes have other types of problems like drift (not coming back to zero-rate value

when rotation stops). By averaging data that comes from accelerometer and gyroscope we can obtain a relatively better estimate of the device inclination than we would obtain by using the accelerometer data alone.

4.2.5 Accelerometer Test Sensor

Prior to the implementation of the DCM algorithm, a single 3-axis accelerometer was purchased with the aim of gaining experience in software, hardware development and integration. For this purpose a LIS3DH sensor from ST electronics was purchased and the need for a cost effective surface mount board arose. This need was satisfied by the construction of a custom board which was used to embed the sensor. The sensor was embedded in a circular hole on the perforated electrical board and secured with a hardening paste setting the sensor permanently plane to the surface. Figure 4.14 illustrates the use of small gage wires were being used to create a conducting path from the copper paddings of the sensor to the pins. Mounting of the pins on the perimeter of the board allows for easy access to the outputs of the sensor. The description of the pin mapping in Figure 4.14 illustrated by the numerical indices in red is shown in Table 5. The complete setup coupled to the Arduino is shown in



Figure 4.14: LIS3DH mounted using perforated board and comparative sizing with pin mapping

Table 5: Pin mapping for LIS3DH accelerometer (ST Electronics, 2010)

Pin no	Acronym	Function
1	V_{supply}	Power Supply
4	SCL	I^2C serial clock
4	SPC	SPI serial port clock
5	GND	Ground
6	SDA	I^2C serial data
	SDI	SPI serial data input
	SDO	3 wire interface serial data output
7	SDO	SPI serial data output
	SAO	I^2C least significant bit address
8	CS	Chip select
		I^2C/SPI mode selection
9	INT2	Inertial Interrupt 2
10	RES	Ground
11	INT1	Inertial Interrupt 2
12	GND	0 V supply
13	ADC3	Analog to digital converter input 3
14	Vdd	Power supply
15	ADC2	Analog to digital converter input 2
16	ADC1	Analog to digital converter input 2

Functional validation of the MEMs accelerometer required the constructed surface mount board to be connected to the Arduino for testing (see Figure 4.16, Figure 4.15 and Figure 4.18). Per the LIS3DH data sheet, the sensor is wired on the main board, per the schematic shown in Figure 4.15.

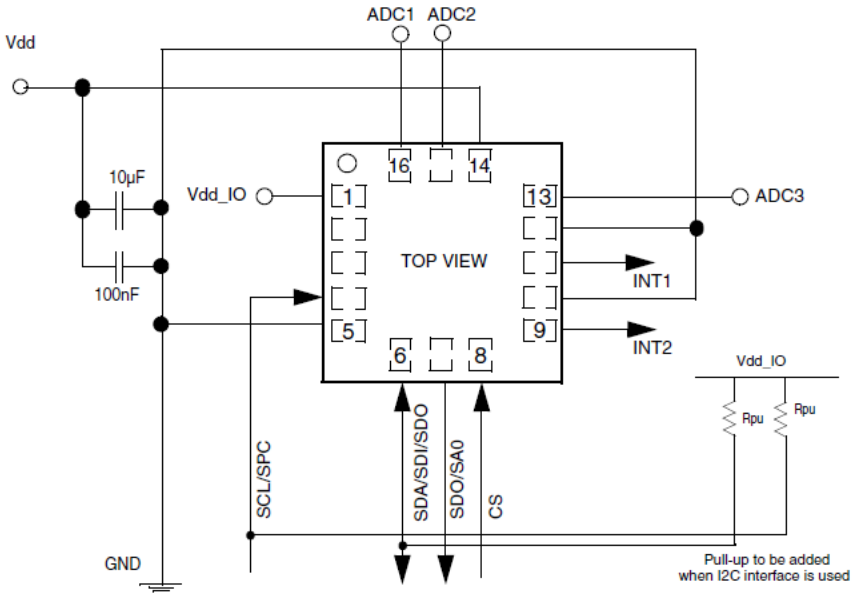

Figure 4.15: Wiring schematic of the LIS3DH sensor (ST Electronics, 2010)

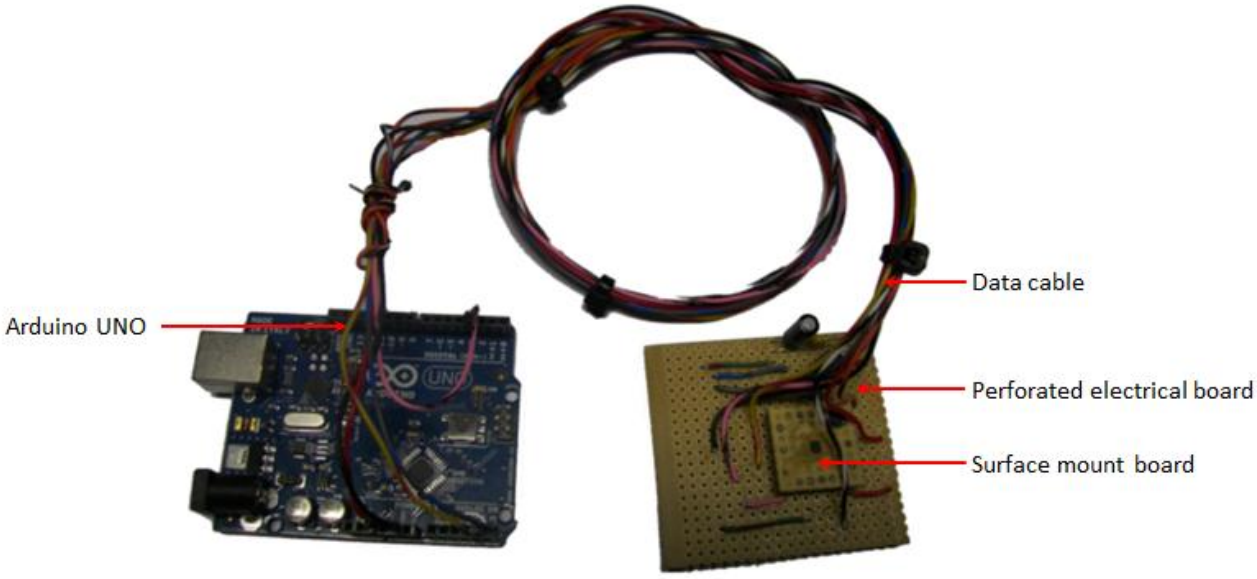

Figure 4.16: LIS3DH accelerometer coupled to the Arduino used for testing

4.2.6 Razor IMU sensor

For initial testing the Arduino Uno shield was used to programme the on-board atmega328P-AU on the Razor IMU unit. The pin mapping between the ATMEGA328P-PU onboard the Arduino and the ATMEGA328P-AU on-board the razor unit (surface mount alternative) was verified in order to assure cross compatibility. It was verified that the pin

mappings were different however the RAZOR IMU (see Figure 4.19) had the input and output labelled on the board making interfacing between the Arduino and the Razor unit simple.

RESET	(PCINT14/RESET) PC6	1	28	PC5 (ADC5/SCL/PCINT13)	Analog input 5
Digital pin 0 (RX)	(PCINT16/RXD) PD0	2	27	PC4 (ADC4/SDA/PCINT12)	Analog input 4
Digital pin 1 (TX)	(PCINT17/TXD) PD1	3	26	PC3 (ADC3/PCINT11)	Analog input 3
Digital pin 2	(PCINT18/INT0) PD2	4	25	PC2 (ADC2/PCINT10)	Analog input 2
Digital pin 3	(PCINT19/OC2B/INT1) PD3	5	24	PC1 (ADC1/PCINT9)	Analog input 1
Digital pin 4	(PCINT20/XCK/T0) PD4	6	23	PC0 (ADC0/PCINT8)	Analog input 0
VCC	VCC	7	22	GND	
Ground	GND	8	21	AREF	
-	(PCINT6/XTAL1/TOSC1) PB6	9	20	AVCC	
-	(PCINT7/XTAL2/TOSC2) PB7	10	19	PB5 (SCK/PCINT5)	Digital pin 13
Digital pin 5	(PCINT21/OC0B/T1) PD5	11	18	PB4 (MISO/PCINT4)	Digital pin 12
Digital pin 6	(PCINT22/OC0A/AIN0) PD6	12	17	PB3 (MOSI/OC2A/PCINT3)	Digital pin 11(PWM)
Digital pin 7	(PCINT23/AIN1) PD7	13	16	PB2 (SS/OC1B/PCINT2)	Digital pin 10 (PWM)
Digital pin 8	(PCINT0/CLKO/ICP1) PB0	14	15	PB1 (OC1A/PCINT1)	Digital pin 9 (PWM)

Figure 4.17: Atmega-328 pin out specifications

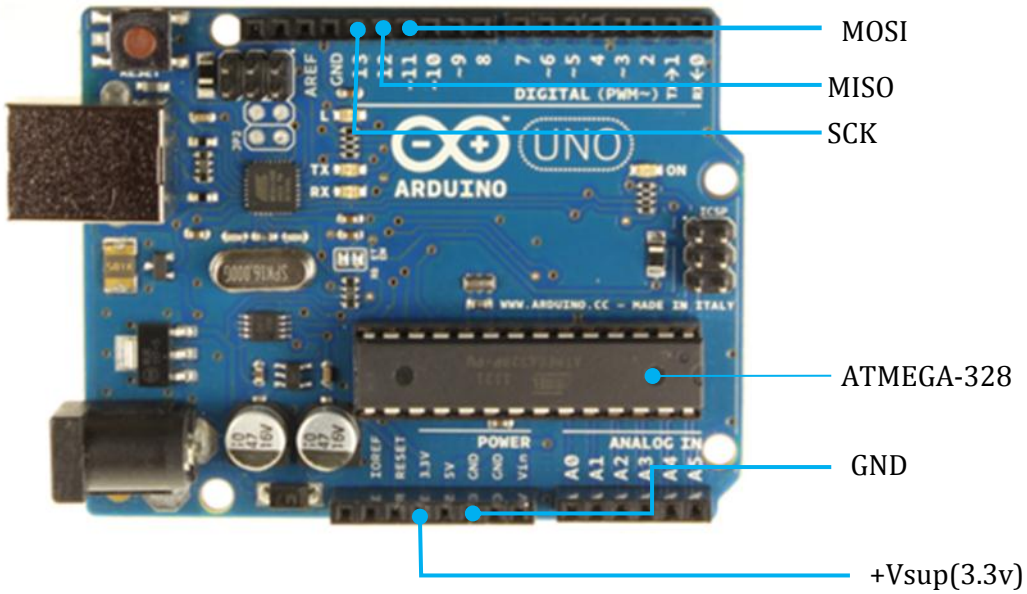

Figure 4.18: Arduino Hardware Development Board f or ATMEGA-328

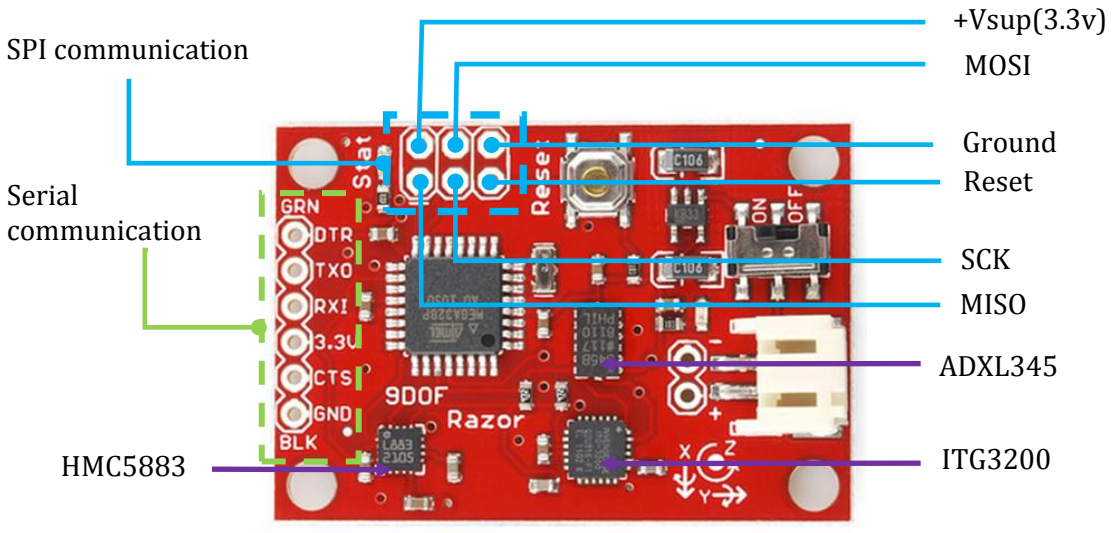

Figure 4.19: 9-dof IMU pin mapping

4.2.6.1 Hardware-BUS communication

The Razor IMU unit has the gyroscope (ITG-3200), accelerometer (ADXL-345) and magnetometer (HMC5883LSMD) sensor fused into one package communicating through the processor (ATMEGA328-AU). The sensors are all connected to the main processor via SCL (serial clock) and SDA (serial data) lines (see Figure 4.20). This ascertains that the only form of communication to the processor is via the I2C communication protocol.

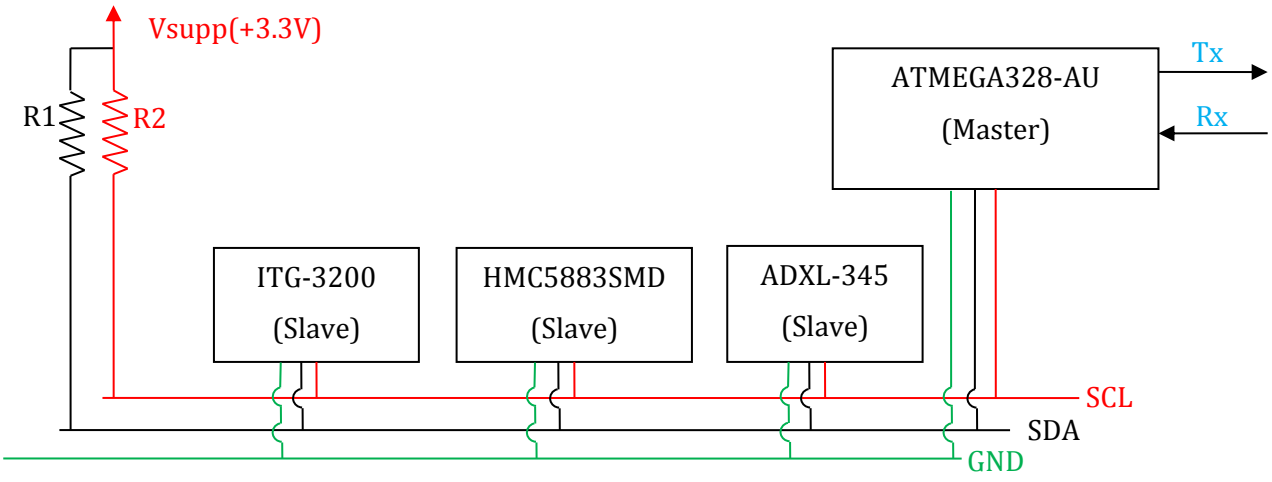

Figure 4.20: Interfacing of the sensors with the main processor using I2C communication

The master is the device that drives the SCL clock line. The slave devices in this case which are the sensors respond to the commands of the master. The communication protocol can be viewed in section 3.1.

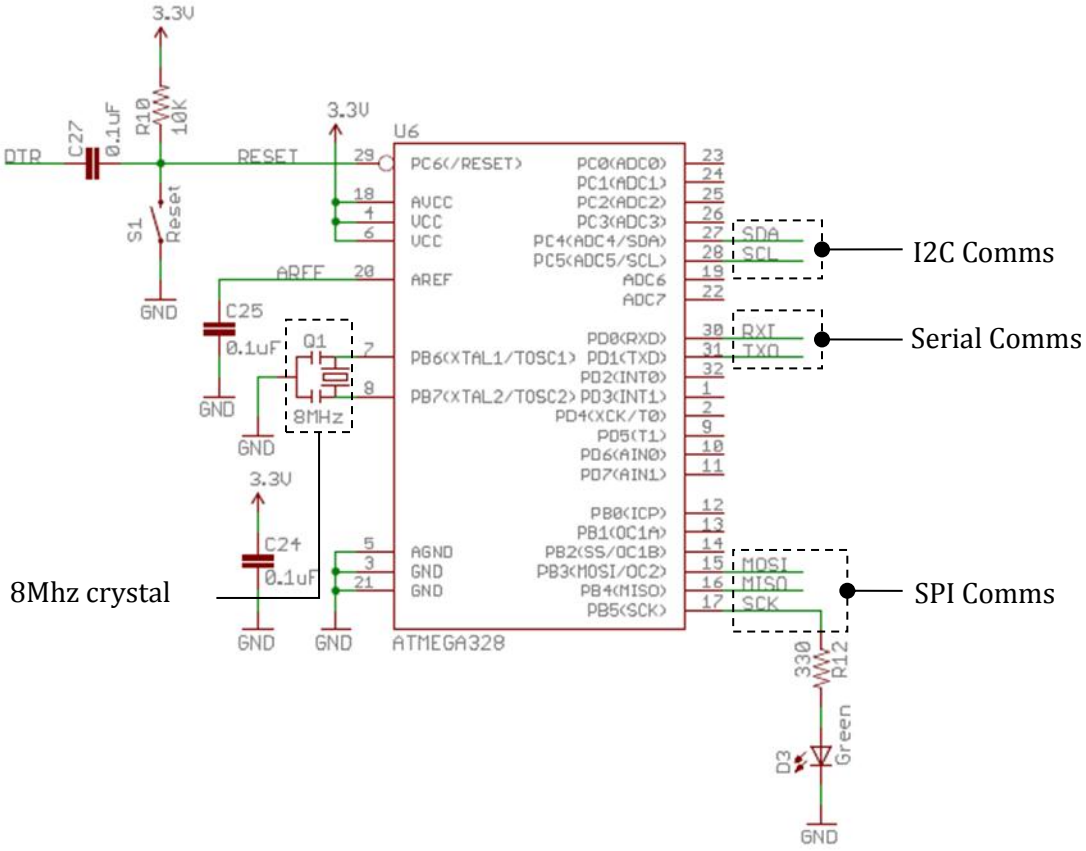

Figure 4.21: Master (Atmega328-AU) Pin mapping on the Razor IMU unit

4.2.7 Direction Cosine Matrix Algorithm (DCM)

As opposed to conventional aircraft mechanical gyros which stay fixed in space while the aircraft rotates around them the electronics gyros rotate with the aircraft producing signal proportional to the rotational rates of the aircraft. This constitutes of a situation outlined in the mathematical model where the body fixed reference frame rotates in the earth fixed reference frame. The integration of the gyroscope rates to achieve an angle will be incorrect as the body kinematics dictate the order in which the rotations occur. The incorrect order

will result in an orientation error. Kinematics of the body is essential as this will provide the necessary information in order to achieve the correct answer.

4.2.7.1 Definition and Function of DCM

The DCM algorithm also known as Magnetic, Angular Rate and Gravity sensor(MARG) calculates the orientation of a rigid body, in respect to the rotation of the earth by using rotation matrices. A visual representation of the Direction Cosine Matrix Algorithm is illustrated in Figure 4.22. The rotation matrices are related to the Euler angles, which describe the three consecutive rotations needed to describe the orientation.

4.2.7.2 Sensor Functionality within DCM

The three sensors used in the algorithm as discussed previously with a summary of its functions are:

- The accelerometer measures earth's gravity field minus acceleration, the accelerometer is not affected by drift, therefore, it can be used as an orientation reference in the X and Z axis of the rigid body to compensate the roll-pitch error (gyro's offset error). Integral drift is cause by deviation in output due the integration of readings over time. If the sensor is stationary it will measure $-g$.
- The magnetometer's readings are used to calculate the heading of the rigid body via the earth's magnetic field. The magnetometer must be three axes to be able to calculate the heading of the system in any position of the sensor platform; to compensate yaw error. The heading of the system used as the reference vector in the Y axis (yaw error).

The DCM Matrix alone can be calculated using the accelerometer and magnetometer combination. The absence of the magnetometer will cause the entire IMU to drift and magnetic north will be an unknown. The use of a gyroscope is however essential if accuracy needs to be maintained as it is not affected by external noise in the form of inertial and magnetic forces. The benefits of the gyroscope within this algorithm can be identified as:

- It is the primary sensor used to calculate the orientation of the system as it is able to measure angular velocity. Since the gyroscope is not affected by the gravitational or magnetic field, it requires the readings from the accelerometer and magnetometer to calculate a reference vector. Gyroscope readings have different offsets depending on which direction the gyroscope is facing; when these readings are integrated over time it causes the integral result to drift.
- The compensated gyroscope readings denoted as ω_{drift} are fed into the "Normalization & Kinematics" block as it can be seen in Figure 4.22. The rotation matrix's columns are unit vectors. Thus, before calculating the kinematics portion it must be normalized.

Once normalized, the gyroscope along with the previous rotation matrix is used to calculate the current rotation matrix (R Matrix) by using Equation 5.24 in the Computing Direction Cosines from Gyro Signals section. Finally, the Euler angles are calculated from the updated rotation matrix. Hence the application of the DCM algorithm is purely for the estimation regarding the device orientation in space (Premelamni & Bizard, 2009).

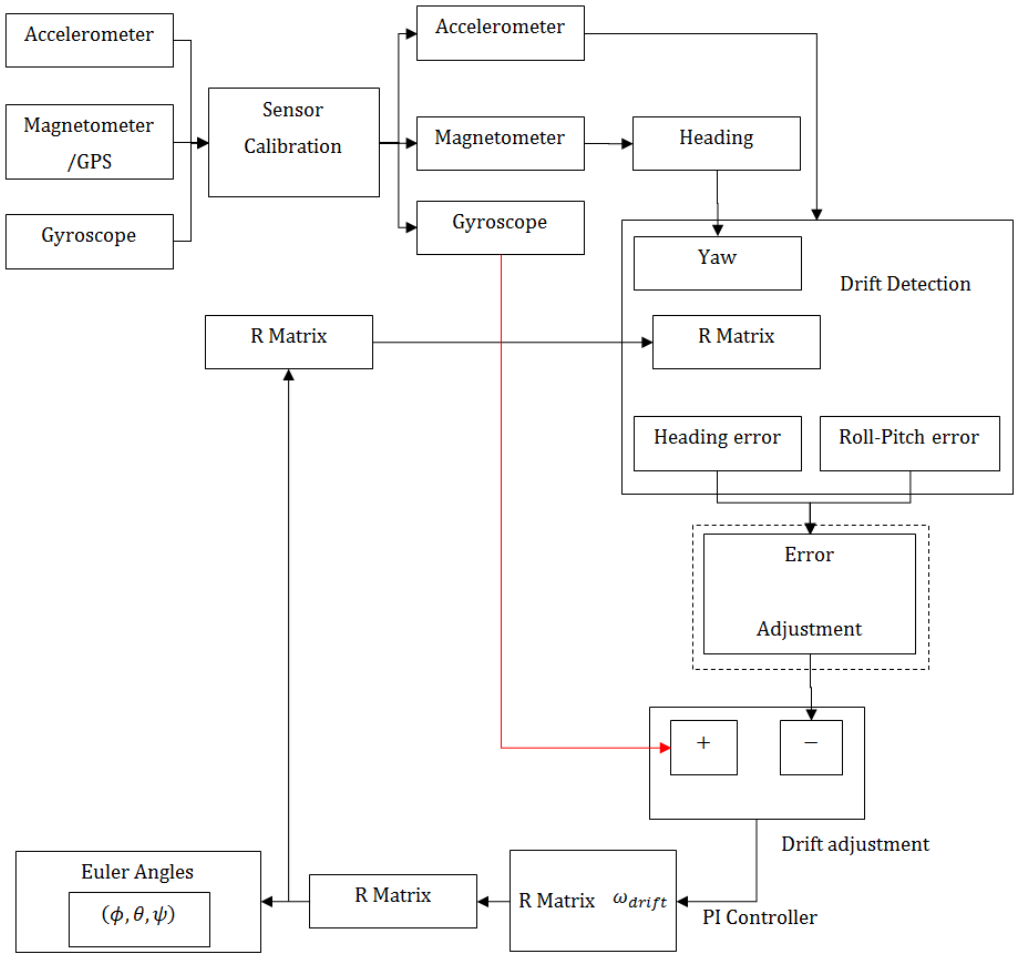

Figure 4.22: Operation of the DCM algorithm

4.2.7.3 DCM Mathematical Background

The mathematical background outlined below represents a build-up in approximation to roll, pitch and yaw values derived in 2.8.1. An approximation was needed which constitutes minimal overhead on the processor whilst still maintaining a reasonable amount of accuracy. The approximation allows for the algorithm to be run on an ATMEGA 328 available on the Arduino interface. The formal coding structure can be seen in Appendix E.2.

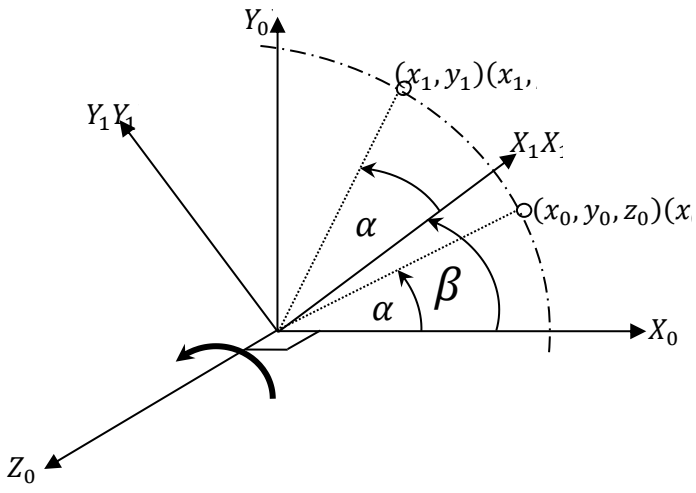

Figure 4.23: Rotation of a coordinate system in 3-D

Hence the DCM Matrix is given by:

$$DCM = R_z(\psi).R_y(\theta).R_x(\phi) \tag{4.17}$$

$$R_z(\psi) = \begin{bmatrix} \cos\psi & -\sin\psi & 0 \\ \sin\psi & \cos\psi & 0 \\ 0 & 0 & 1 \end{bmatrix}, R_y(\theta) = \begin{bmatrix} \cos\theta & 0 & \sin\theta \\ 0 & 1 & 0 \\ -\sin\theta & 0 & \cos\theta \end{bmatrix}, R_x(\phi) = \begin{bmatrix} 1 & 0 & 0 \\ 0 & \cos\phi & -\sin\phi \\ 0 & \sin\phi & \cos\phi \end{bmatrix} \tag{4.18}$$

The DCM Matrix has great importance in orientation kinematics since it defines the rotation of one frame relative to another. It can also be used to determine the global coordinates of an arbitrary vector if we know its coordinates in the body frame.

$$DCM_{Matrix} = R(\phi)R(\theta)R(\psi) = R(\phi, \theta, \psi) \tag{4.19}$$

$$DCM_{Matrix} = \begin{bmatrix} \cos\theta\cos\psi & \sin\phi\sin\theta\cos\psi - \cos\phi\sin\psi & \cos\phi\sin\theta\cos\psi - \sin\phi\sin\psi \\ \cos\theta\sin\psi & \sin\phi\sin\theta\sin\psi + \cos\phi\cos\psi & \cos\phi\sin\theta\sin\psi - \sin\phi\cos\psi \\ -\sin\theta & \sin\phi\cos\theta & \cos\phi\cos\theta \end{bmatrix} \tag{4.20}$$

Assuming we have a small perturbation in Euler angles. Using small angle approximation (small rotations):

$$DCM_{Matrix} \approx \begin{bmatrix} (1)(1) & \delta\phi\delta\theta(1) - (1)\delta\psi & (1)(\delta\theta)(1) - \delta\phi\delta\psi \\ (1)\delta\psi & \delta\phi\delta\theta\delta\psi + (1)(1) & (1)\delta\theta\delta\psi - \delta\phi(1) \\ -\delta\theta & \delta\phi(1) & (1)(1) \end{bmatrix} \tag{4.21}$$

$$DCM_{Matrix} \approx \begin{bmatrix} 1 & -\delta\psi & \delta\theta \\ \delta\psi & 1 & -\delta\phi \\ -\delta\theta & \delta\phi & 1 \end{bmatrix} = \begin{bmatrix} 0 & -\delta\psi & \delta\theta \\ \delta\psi & 0 & -\delta\phi \\ -\delta\theta & \delta\phi & 0 \end{bmatrix} + \begin{bmatrix} 1 & 0 & 0 \\ 0 & 1 & 0 \\ 0 & 0 & 1 \end{bmatrix} \tag{4.22}$$

$$DCM_{Matrix-update} = DCM_{Matrix} \begin{bmatrix} 1 & -\delta\psi & \delta\theta \\ \delta\psi & 1 & -\delta\phi \\ -\delta\theta & \delta\phi & 1 \end{bmatrix} \tag{4.23}$$

$$DCM_{Matrix-update} = DCM_{Matrix} \left[\begin{bmatrix} 0 & -\delta\psi & \delta\theta \\ \delta\psi & 0 & -\delta\phi \\ -\delta\theta & \delta\phi & 0 \end{bmatrix} + \begin{bmatrix} 1 & 0 & 0 \\ 0 & 1 & 0 \\ 0 & 0 & 1 \end{bmatrix} \right] \tag{4.24}$$

The above equation allows us to update the direction cosine matrix.

The pitch angle of the quadrotor is given by: (Rotation about the y-axis)

$$\theta = \sin^{-1}(DCM_Matrix[2][0]) \tag{4.25}$$

$$\theta = -\sin^{-1}(-\sin\theta) = \theta \tag{4.26}$$

The roll angle of the quadrotor is given by: (Rotation about the x-axis)

$$\phi = \tan^{-1}(DCM_Matrix[2][1], DCM_Matrix[2][2]) \tag{4.27}$$

$$\phi = \tan^{-1}\left(\frac{DCM_Matrix[2][1]}{DCM_Matrix[2][2]}\right) = \tan^{-1}\left(\frac{\sin\phi\cos\theta}{\cos\phi\cos\theta}\right) = \phi \tag{4.28}$$

The yaw angle of the quadrotor is given by: (Rotation about the z-axis)

$$\psi = \tan^{-1}(DCM_Matrix[1][0], DCM_Matrix[0][0]) \tag{4.29}$$

$$\psi = \tan^{-1}\left(\frac{DCM_Matrix[1][0]}{DCM_Matrix[0][0]}\right) = \tan^{-1}\left(\frac{\cos\theta \sin\psi}{\cos\theta \cos\psi}\right) = \psi \tag{4.30}$$

4.2.8 AHRS Software Architecture

The software architecture which drives the AHRS system is highlighted in Appendix E. It has been simplified for easy interpretation of the IMU process. (See Appendix E- Figure E.1)

4.2.8.1 Software interrupts

As stated previously the ATMEGA-328 is responsible for all the on-board processing and outputs data via SPI or the I2C communication protocols. The AHRS algorithm is structure with software interrupts. Interrupt flags are used to interrupt the processor from its current task. When the flag is triggered the current processor tasks are paused and the task raised by the flag is prioritised.

The benefits of an interrupt can be stated as:

- Solving of timing problems
- Economising on processor resources

It may be triggered by an external event (change in pin state) or an internal event (a timer or a software signal). Once triggered, an interrupt pauses the current activity and causes the program to execute a different function. This function is called an interrupt handler or an interrupt service routine (ISR). Once the function is completed, the program returns to what it was doing before the interrupt was triggered.

4.3 IMU and AHRS Implementation

The developed test rig was constructed for the testing of the IMU unit and in ascertaining the robustness of the control algorithm. Figure 4.24 illustrates the mounting on a custom built frame using aluminium standoffs mounted on the chassis hub. The rotation about one axis is maintained by the use of bearings which minimise friction about the role axis.

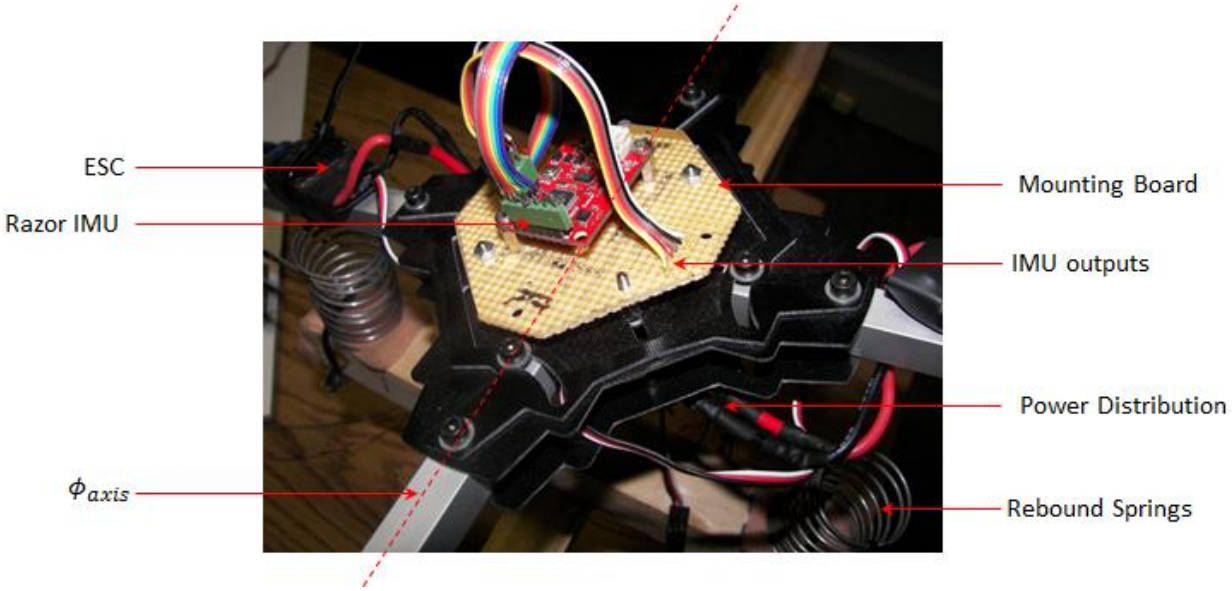

Figure 4.24: Mounting of the IMU on the rotating rig

The main function of the rig is purely to isolate a single degree of freedom making future testing of control algorithms easier. Perturbations exerted on the rotation rig must be compensated for by reaction moments generated by the change in the thrust vectors generated by the motors. This allows for the reaction rate in response to the perturbation to be calculated and if need be altered either in the developed control algorithm or the physical nature for performance improvements. As per Figure 4.25 and Figure 4.26 it can be seen that the yaw and roll axis have been isolated allowing for a pure rolling rotation. This setup will play an essential role in the construction of the feedback system which will be integrated into Labview.

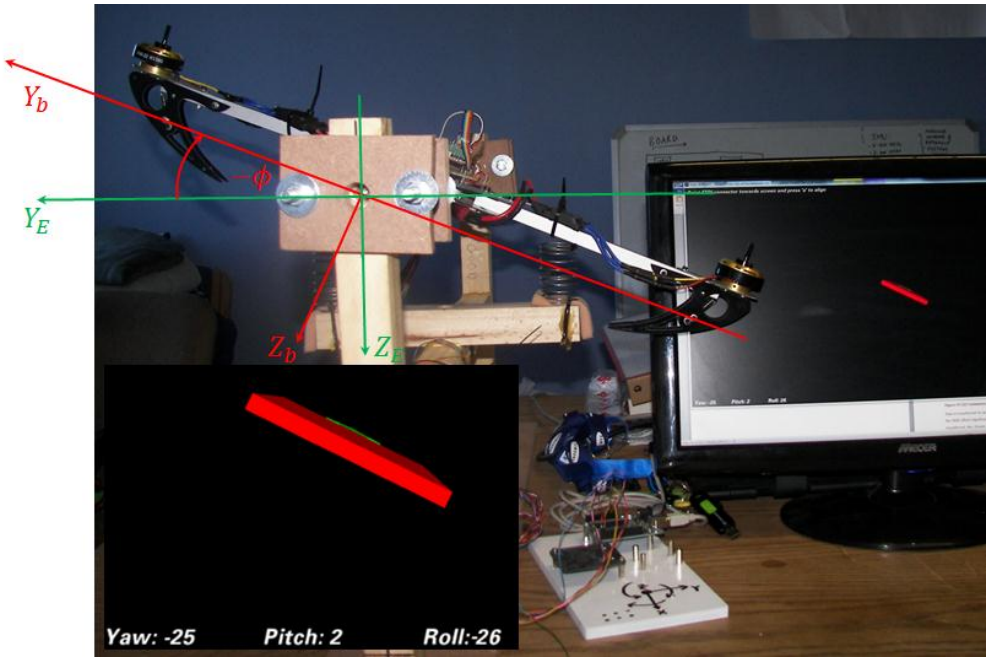

Figure 4.25: Positive IMU roll with yaw and pitch held constant

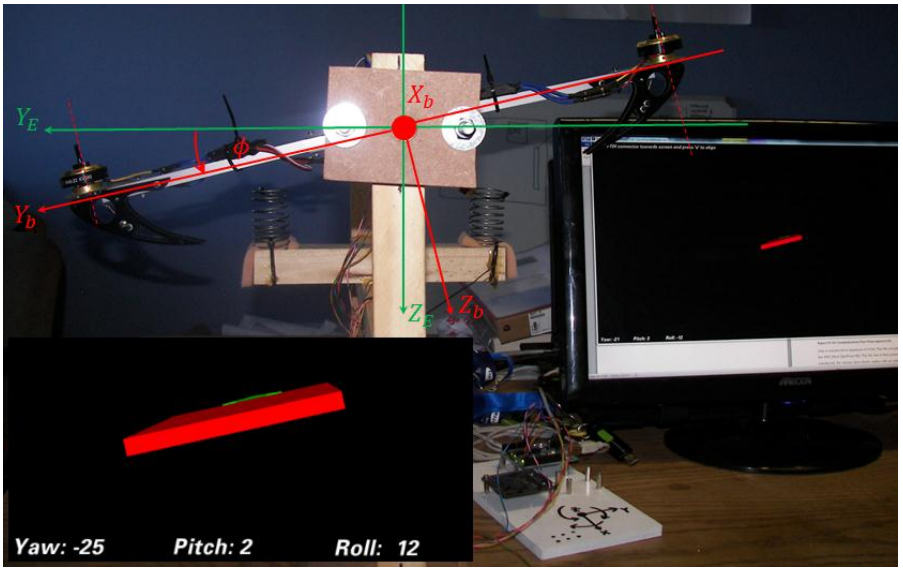

Figure 4.26: Negative IMU roll with yaw and pitch held constant

5. Data Acquisition

5.1 Overview

The data acquisition phase of this project remains an essential part of development for the Quadrotor control system. As opposed to alternative forms of UAV, the power plant in the case of the Quadrotor serves a dual purpose of control and propulsion. Since control and propulsion are coupled, it is essential that the power plant (BLDC motor coupled with propeller) is studied in detail. The data acquisition process serves to satisfy this need by the construction of apparatus that allows for the extraction of unknown parameters that define the control system. The parameters can be extracted using BLDC motor equations and propeller theory however the accuracy achievable and confidence in the data remains questionable. A black box structure was implemented on the powerplant in order to extract the necessary variables (see Figure 5.1). Relationship between these variable were then made allowing for a more realistic mathematical modelling of the system.

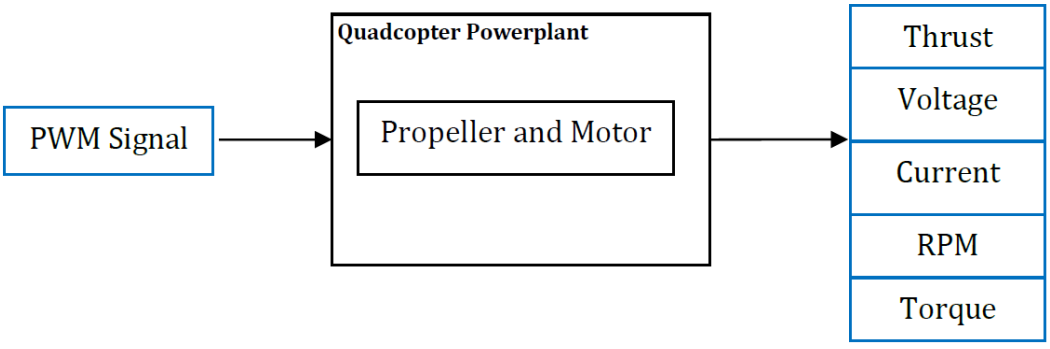

Figure 5.1: Black box structure of the powerplant

5.2 Data Acquisition Process and Design

A thrust stand was constructed using a custom built load cell. This allowed for the RPM versus thrust curves to be established for different propeller motor combinations (Figure 5.2). A mapping of motor thrust versus PWM (pulse width modulated) signals from the controller was mapped to the thrust and RPM in order for motor calibration to be done for the control system phase. The variation in propeller profiles with RPM, voltage, current and flutter can also be studied in order for an optimised propulsion system to be ascertained. A validation in RPM methods was investigated in order to ascertain a more accurate and repeatable solution. This involved the construction of three custom built stands and a purchased solution.

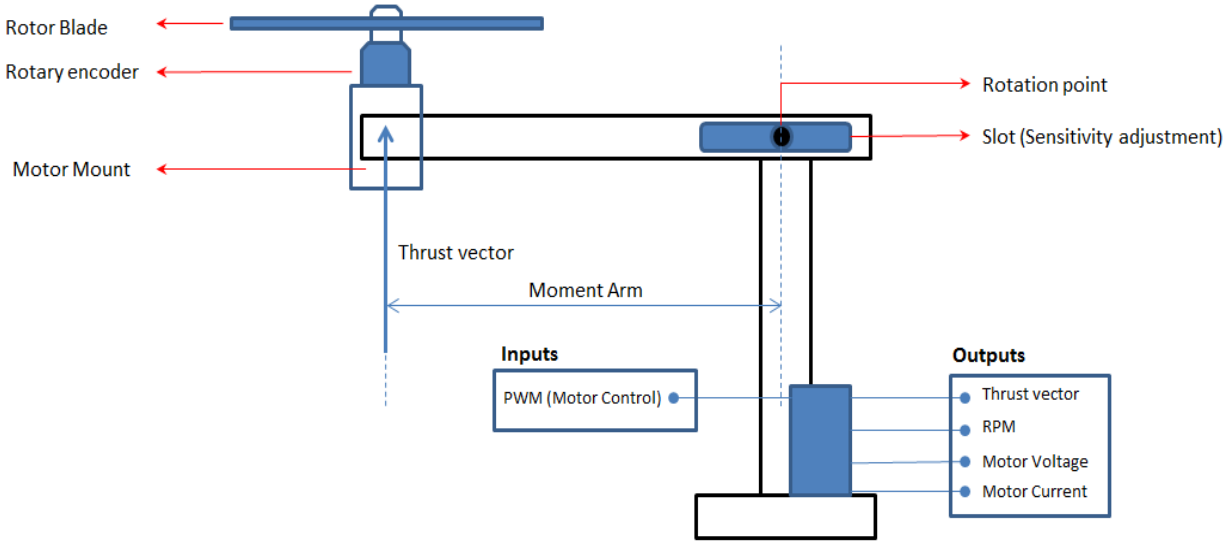

Figure 5.2: Thrust stand concept built using strain gauges

In order for a mapping to be obtained between the discussed parameters it is essential that the commutation of the brushless DC motors are understood. Motors of this nature are coupled to electronic speed controllers (ESC) which allow for the duty cycle to be altered varying the throttle. This variation in throttle represents the change in RPM of the motor. The decision to use a brushless DC motor as opposed to the conventional DC motor was made due to the higher efficiency, hardware longevity and higher torque outputs. These factors alone make this motor selection the optimal choice.

5.3 Propeller Testing

The design and optimization of the quad rotor requires parametric, scalable, physics-based models of propeller performance that can be used as a component in computational design and analysis algorithms. Propeller performance analysis at this scale is complicated by modelling uncertainties due at low Reynolds numbers at the propulsion system, lifting surfaces, large scaled surface roughness and a lack of validation data. The black box concept is dependent on the analysis and classification of propeller performance. Adequate modelling and classification allows for the most efficient setup to be achieved. The propeller through its interaction with the air converts rotary motion to propulsive force or thrust. This thrust is equal to the mass of air forced backward by the propeller per unit time multiplied by the added velocity imparted to this air (Roy & M Pradeep, n.d.).

$$Propeller\ Thrust = \dot{m}\Delta V \tag{5.1}$$

The propulsive force generated is a direct property of the type of airfoil used to extrude the blade along its length. The airfoil sections produces the aerodynamic force necessary to create lift and as a result is subject to aerodynamics penalties such as drag. As opposed to the translational flight path of a wing section, a propeller wing section undergoes a circular flight path. A propeller is geometrically characterized by a standard naming convention of two numbers as described in Eq. (5.2).

$$Propeller\ geometry = X \times Y \tag{5.2}$$

X and Y represent the diameter of the propeller and the pitch of the propeller respectively. The pitch of the propeller can be visualized as the distance the propeller moves forward in one rotation and is directly related to the angle of attack of the blade as seen in Figure 5.3. Theoretically the blade should move Y inches forward however due to inefficiencies this value is reduced. The large blade selection allowed for the influence of propeller diameter, pitch angle on thrust and current consumption to be studied (see Figure 5.4). Due to the limited number of experimental runs a larger blade selection was avoided. Blades were selected to establish the variation in blade diameter with pitch angle on current consumption, RPM and thrust.

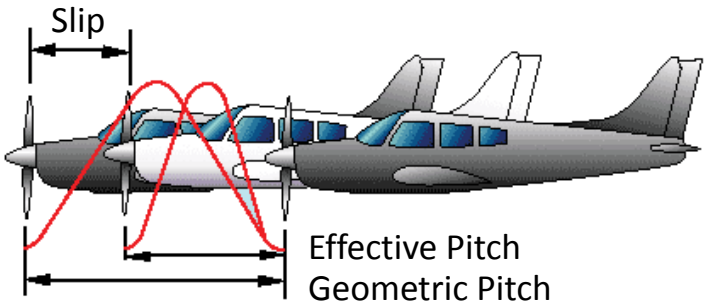

Figure 5.3: Propeller pitch



9X4.7	10X4.5	11X4.7	11X4.5	12X4.5	9X4.5

Figure 5.4: Propeller sizes used for testing

Large diameter blades have more mass distributed away from the rotation axis and constitute a higher inertia value. A higher inertia values implies that a larger starting torque would be required to initiate rotation on start-up and smaller top end accelerations will result. 6 easily acquirable blades were tested ranging from the 9" to 12" with a single variation in a 3 blade design. Due to time constraints on testing a further rage could not be tested but will be left for future work and the thesis merely outlines the functional value of the constructed apparatus

5.3.1 Propellers Loadings and Safety

The use of a non-shielded propeller blades testing area is very dangerous due to the uncertainty involved in the principle loading components. These consist of centrifugal force, thrust and drag, torsional acceleration, vibrational loading and aero elastic tip flutter. Vibration causes additional loads from cyclic motions. These motions occur when resonant frequencies are excited or when cyclic load variations exist on the blade. The magnitude of these variations depends on how close the driving frequency is to the resonant frequency and the level of damping in the propeller material. Obstructions in front of or behind the blade can cause cyclic variations in thrust load. Once a blade starts to flutter, those motions alter the flow, causing variations in loading, accelerating the onset of fatigue failure.

The interaction between variable blade loading and deflection induces a high frequency vibration with unpredictable magnitude. Thrust/drag loads are somewhat uncertain due to complexities in aerodynamic load predictions.

Efficient propeller design practice utilizes analytical/computational models to predict propeller performance and stresses. However, the uncertainty in impressed and inertial loading from complex phenomena requires testing to assure safe performance. Unfortunately, it is not possible to assure testing that convincingly replicates worst case conditions. The combinations of motor, temperature, humidity, propeller selection, aircraft performance and variation in throttle responses creates a dynamic situation. If the origins of severe loads were well understood, quantified, and measurable, structured testing might be feasible that focuses on worst case stack up of adverse conditions. The origins of severe loads are really not well understood hence it is essential to provide sufficient margins or safety factors in material properties and design to assure safe performance.

The use of composite blades has become more popular and with that the understanding of material science for amateur use is common. Composite propeller permitted to absorb moisture in high humidity environments reduce composite strength, stiffness and fatigue endurance. Reduction in stiffness typically causes resonant frequencies to move toward the driving frequency (increasing torsional loads) and, the reduction in strength reduces fatigue endurance. Composite propellers should be kept dry (Li, 2008) (Wacker, 2001). For all

purposes the use of the propeller blade must be done with the utmost of care and the understanding of where or when blades fail become very dynamic and cannot be predicted.

5.4 Brushless Motor

As stated previously the brushless DC motor was chosen due to the mechanical advantages gained from the brushless design. It is also imperative that the construction and operation of this motor is outlined.

5.4.1 Brushless DC Motor Construction and Operation

Brushless DC motors has no brushes and are electronically commutated. The high torque to weight ratio make it an ideal candidate for a Quadcopter. These motors are available in 2-phase and 3-phase configuration of which the latter is the most popular and widely used. As per this study, the 3-phase configuration will be discussed as this forms the basis of mechanical drive system employed on the Quadcopter. A brushless motor is constructed with a permanent magnet rotor and wire wound stator poles. Electrical energy is converted to mechanical energy by the magnetic attractive forces between the permanent magnet rotor and a rotating magnetic field induced in the wound stator poles. Figure 5.5 illustrates a 6 pole Brushless dc motor consisting of three electromagnetic circuits connected a t a common point. Each electromagnetic circuit is split in the center, thereby permitting the permanent magnet rotor to move in the middle of the induced magnetic field.

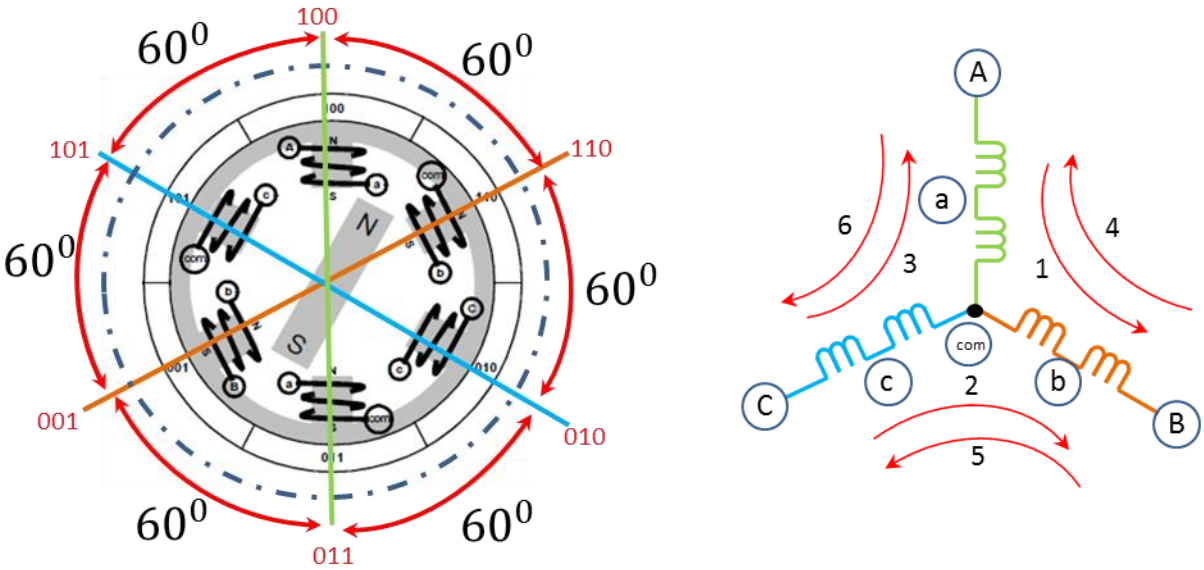

Figure 5.5: Simplified BLDC Motor Diagram (Brown, 2002)

Most BLDC motors have a three-phase winding topology with star connection. A motor with this topology is driven by energizing 2 phases at a time. The key to BLDC commutation is to sense the rotor position, then energize the phases that will produce the most amount of torque. The rotor travels 60 electrical degrees per commutation step (6 pole motor). The appropriate stator current path is activated when the rotor is 120^0 from alignment with the corresponding stator magnetic field, and then deactivated when the rotor is 60^0 from alignment, at which time the next circuit is activated and the process repeats. Commutation for the rotor position, shown in Figure 1, would be at the completion of current path 2 and the beginning of current path 3 for clockwise rotation.

5.4.2 Brushless DC Outrunner vs Inrunner

Brushless DC motors for RC are broken into outrunners and inrunners, the difference being the location of the permanent magnets in relation to the wire windings. Outrunners have the permanent magnets mounted on the outside of the windings whilst the winding are located on the armature. This allows for the permanent magnets on the casing to rotate around the armature allowing for a high torque to mass ratio (see Figure 5.6). The absence of a gearbox is another benefit of the outrunner making it silent and easy to maintain. Inrunners are suited for high RPM ranges and consist of gearboxes. The outrunner was selected due to its simplistic design, high torque in the lower rpm range and it is the most cost effective.

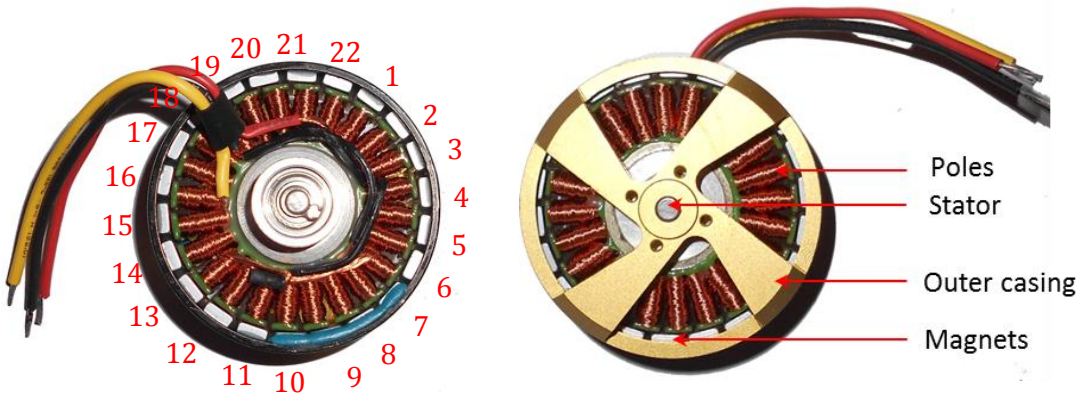

Figure 5.6: 3-phase 22 pole (11 pair) Brushless "Outrunner", top and bottom views

5.4.3 Brushless Motor Control

Pulse Width Modulation (PWM) is a modulation method which encodes a value using the width of a pulse or continuous pulse train (see Figure 5.7). Commonly a PWM signal uses a continuous square wave signal of constant frequency and variable duty cycle. The duty cycle or individual pulse widths represent the value of the signal. This value has a defined range of 0-1 or 0-100 % duty cycle. This PWM value corresponds to a defined range of an engineering value used in an application, such as the rotational speed of a wheel in RPMs.

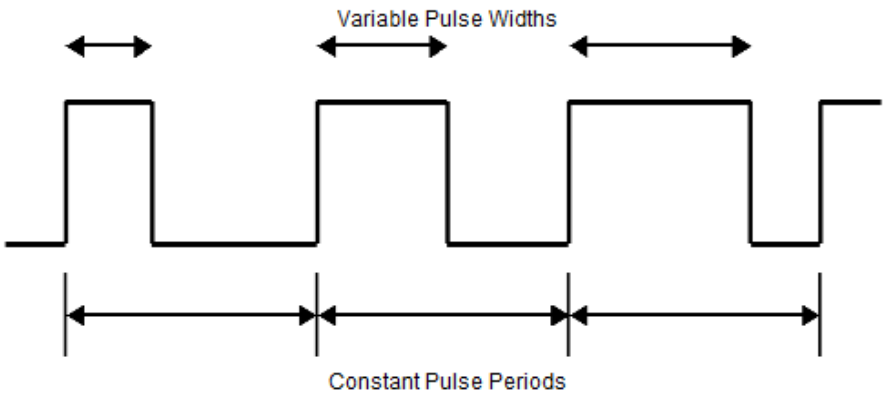

Figure 5.7: PWM Signal

5.4.4 Electronic Speed Controllers

A Brushless motor's ESC (Electronic Speed Control) uses alternating positive and negative pulses. If the receiver tells the ESC to speed up, the ESC sends pulses to the motor at a faster frequency. If the receiver tells the ESC to slow down, the ESC sends pulses to the motor at a slower frequency. Brushless motor's ESC controls the motor's RPMs (speed), by varying the timing of the alternating positive and negative pulses via the three power lines, not by varying the voltage. The timed pulses are all sent alternating from the positive side of the battery and the negative side of the battery at full battery potential.

The signal to an ESC is nominal 50Hz PWM signal, the duty cycle is adjusted for control (see Figure 5.8). When it is supplied with a 1ms width pulse at 50Hz, the ESC responds by turning off the DC motor attached to the output. A 2ms duty cycle will ramp the motor up to full throttle.

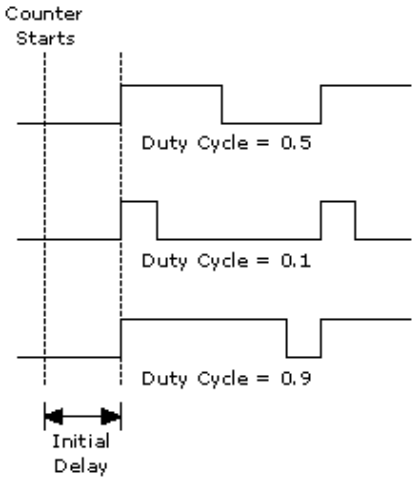

Figure 5.8: Duty cycle of waves

$$Period = \frac{1}{Frequency} \tag{5.3}$$

$$Pulse\ Period = \frac{1}{50} = 0.02s = 20mS \tag{5.4}$$

$$Duty\ Cycle = \frac{Pulse\ width}{Pulse\ Period} \times 100 \tag{5.5}$$

The ESC generally accepts a nominal 50Hz PWM servo input signal whose pulse width varies from 1ms to 2ms. When the controller supplies the ESC a 1ms width pulse at 50 Hz, the ESC responds by turning off the DC motor attached to its output. For Full throttle ESC requires pulse width of 2ms=100% throttle=10% duty cycle therefore the amount of the time the Digital pin remains low is given by:

$$Pin\ Low = Pulse\ Period - Pulse\ width \tag{5.6}$$

$$Pin\ Low = Pulse\ Period - \left(\frac{Duty\ Cycle}{100} \times Pulse\ Period\right) \tag{5.7}$$

$$Pin\ Low = Pulse\ Period\left(1 - \frac{Duty\ Cycle}{100}\right) \tag{5.8}$$

Therefore the amount of the time the Digital pin remains high is given by:

$$Pin\ High = Pulse\ Period - Pulse\ Period\left(1 - \frac{Duty\ Cycle}{100}\right) \tag{5.9}$$

$$Pin\ High = Pulse\ Period\left(1 - \left(1 - \frac{Duty\ Cycle}{100}\right)\right) \tag{5.10}$$

$$Pin\ High = Pulse\ Period\left(\frac{Duty\ Cycle}{100}\right) \tag{5.11}$$

Implementing Eq. (5.10) and (5.11) in Labview (Refer to Figure 3.7) the following pulses can be obtain using an oscilloscope. This can be verified in Figure 5.9 below for Duty cycles of 5% and 10% respectively.

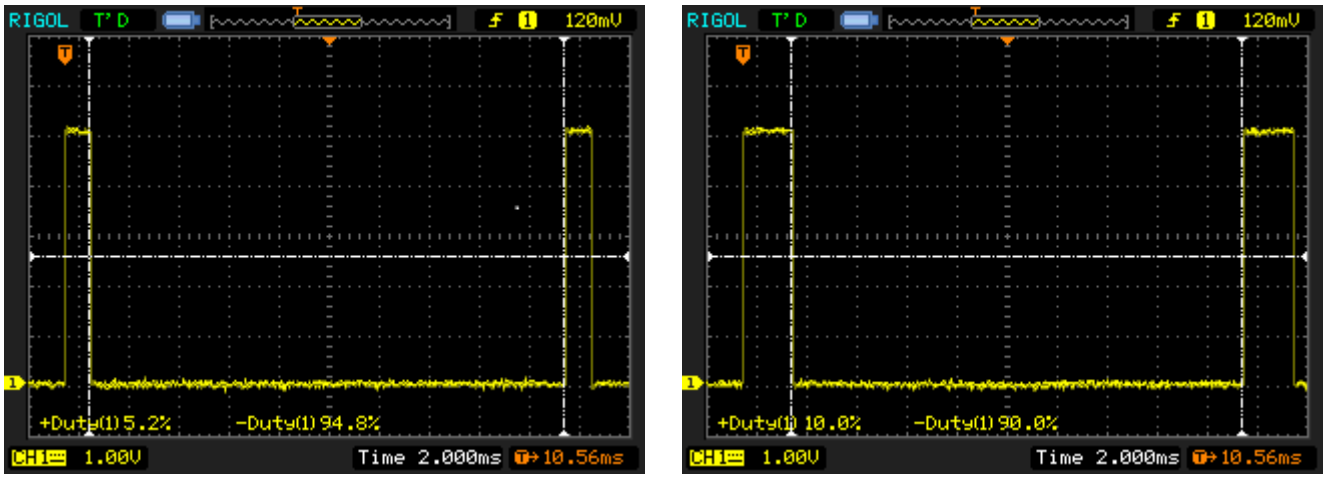

Figure 5.9: Duty cycle of wave monitoring on the oscilloscope at 5% and 10% Duty cycle

Five sets of apparatus were used for angular velocity measurements, four of the five were custom built concepts whilst the other was purchased. The first two concepts consisted of a non-contact RPM sensor using two Infrared red LED's; the second a reflective opto-

interrupter; the third used an incremental encoder, the fourth used halls sensors and the fifth a purchased K1 rpm meter. The downfall of the incremental encoder was the inherent loses associated with its direct drive coupling. The incremental encoder was used in order to ascertain the accuracy of all the constructed sensors and serve as a datum for benchmarking. If the beam encoder rpm matched that of the incremental encoder then the inherent loss in the coupling drive could be avoided by using the beam encoder.

5.4.5 Non-Contact RPM Sensors

The construction of the non-contact rpm sensors involved the understanding of the electromagnetic wave spectrum as their operation stems on the fundamental principles of the visible light and IR spectrum.

Three primary colours exist within the visible light spectrum (λ: $400nm - 700nm$); these are red, green and blue combining to form white (see Figure 5.10). An absence of either of the colours from the combination will result in black. A body appears of a particular colour because it reflects light of that wavelength. Similarly if a body appears white it means it is not absorbing any of the light and reflects all the incident wavelengths. A black body or surface in a similar manner absorbs all the wave lengths of lights incident on it and reflects none. So the absence of any wavelength in the reflected light makes it appear black. The infrared spectrum lies outside the boundaries of the visible light spectrum ($740m > \lambda > 1000nm$) and constitutes the zone in which IR optics function.

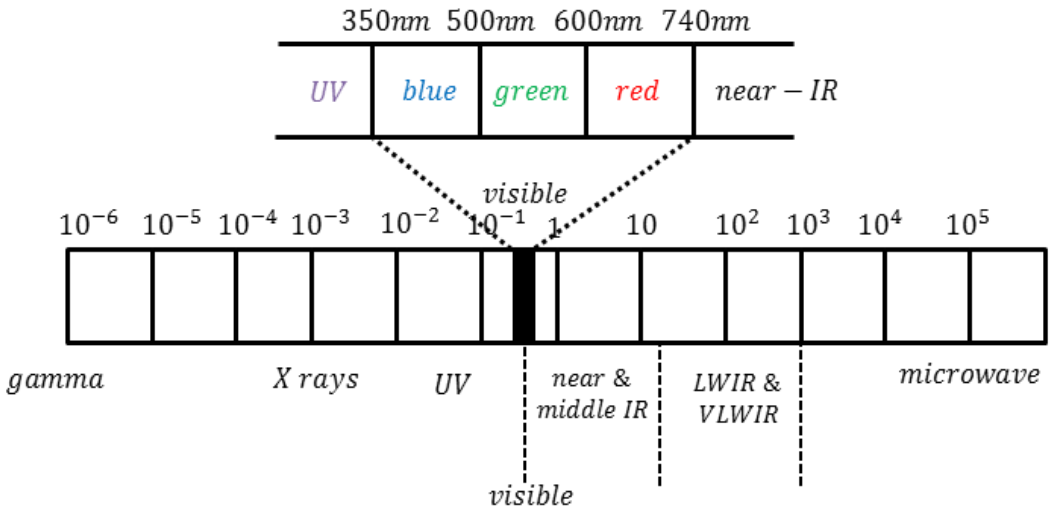

Figure 5.10: The electromagnetic light spectrum

5.4.5.1 IR-Beam Photo interrupter (Line sensor)

The beam encoder in Figure 5.11 consists of two horizontal plates which form the mounting platforms for the IR NPN Phototransistor (SFH300) and transmitter (SFH-484) on the vertical metal tubing. Two stand-off's secure the SFH300 and SFH484 to the upper and lower horizontal plates respectively. The receiver was mounted on the upper platform as to have direct contact from the source and avoid any possible IR waves from non-natural lighting (Fluorescent globes emit IR). The receiver and transmitter plates clamp to the tubing using M3 bolts allowing for the distance between the receiver and transmitter pair to be altered. This changes the interrupt distance and is an important feature as at higher RPM blade flutter become more prominent. The infrared path between the receiver and transmitter needs to be obstructed in order for a Boolean value to be registered. In the case of the tests performed, the spinning propeller provides the necessary obstruction. The non-contact RPM sensor allows for RPM to be measured without the losses associated with direct coupling to the motor drive.

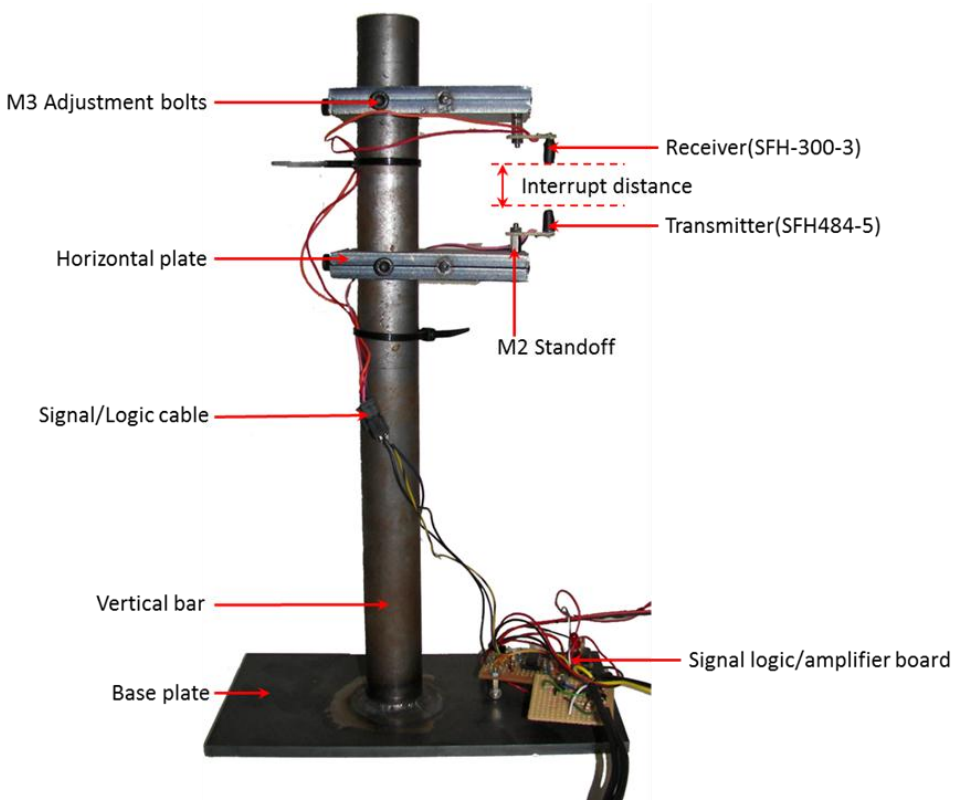

Figure 5.11: Beam encoder for propeller rpm detection.

The receiver and transmitter were paired using the peak sensitivity values. The phototransistor and transmitter have a peak sensitivity of 850nm and 880nm respectively. NPN-phototransistor with its emitter connected to ground as in Figure 5.12 will have a voltage that varies depending on the wavelength of light entering the transistor. The value of current that is output from the receiver will need to be measured post setup once the set value in this case of 850nm is set to be generated by the transmitter. This allows for a distinct point at which the Schmitt trigger can switch to a high voltage (5V) and low voltage (0V) allowing for adequate interpretation by the NI controller.

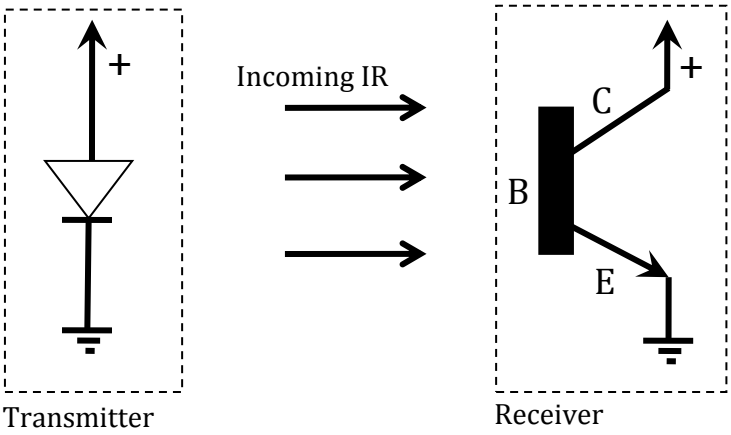

Figure 5.12: Simple IR transmitter and NPN Phototransistor setup

An LM358P operational amplifier in Figure 5.15 was used as a Schmitt trigger. The Schmitt trigger converts the sinusoidal signal from the receiver into a square wave which is conditioned for the controller. The waveform is present due to the sinusoidal variance in voltage output with wavelength. When interrupted by the blade the IR signal is shielded from the receiver outputting the lowest voltage. As the propeller blade retreats IR rays are received and the voltage value ascends to the peak value. Red blades as seen in Figure 5.13 were marked black to allow for the absorptivity of infrared light passed through the blades.



Figure 5.13: IR absorbing marking applied to the blade tips

The retreating and following of the blades as explained previously will be used to illustrate the Schmitt trigger process as in Figure 5.14. In the absence of the blade the graph maintains a high, however prior to the leading edge of the blade arriving at the sensor it will pass through a zone of switching. This zone will guarantee the circuit to switch between V_{s+max} and V_{s+min}. On the falling edge the circuit will be guaranteed to switch between V_{s-max} and V_{s-min}. The circuit however is not guaranteed not to switch between V_{s-max} and V_{s+min}. This is important for noise rejection and represents the systems hysteresis zone.

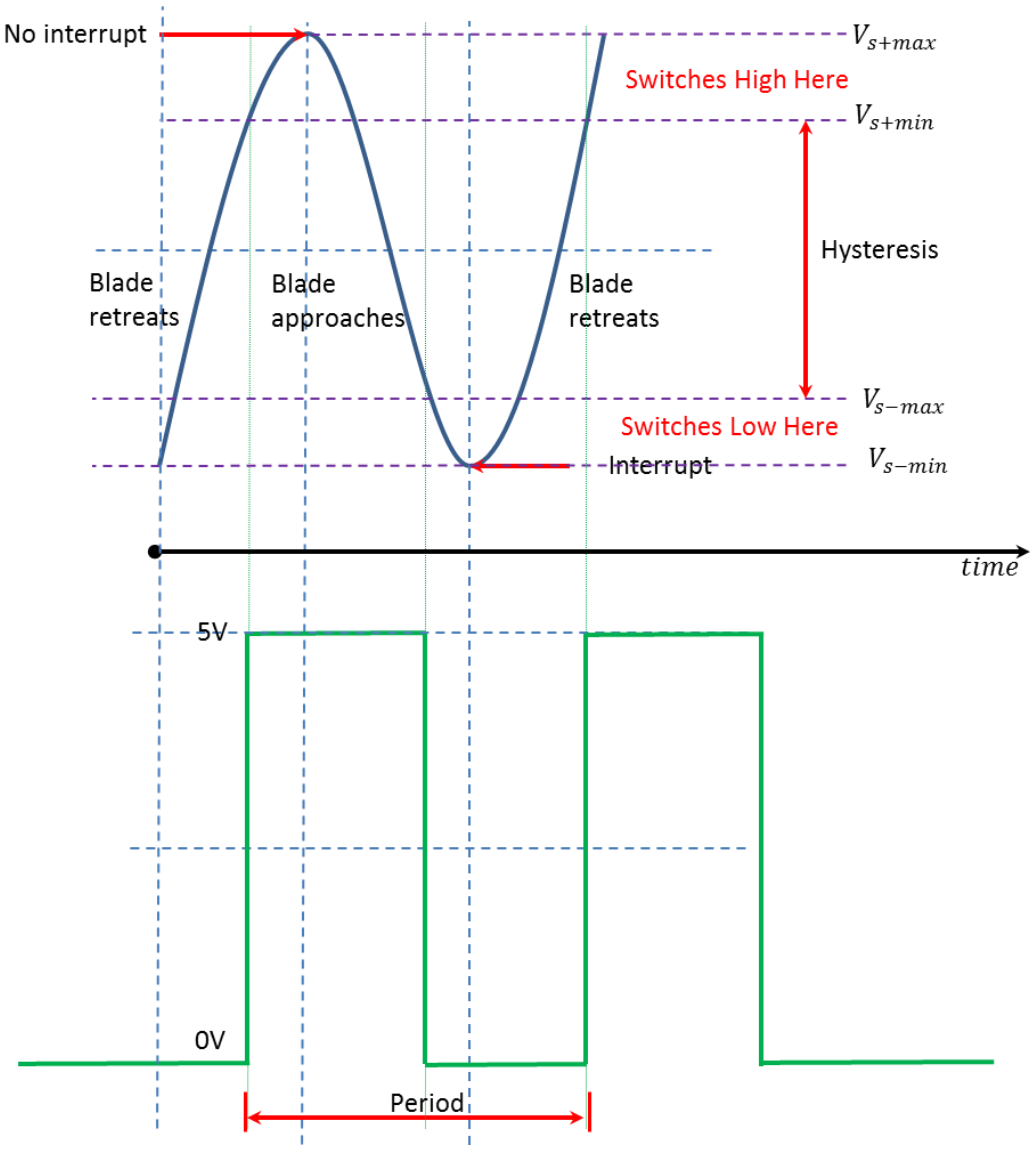

Figure 5.14: Schmitt trigger switching scheme and hysteresis zone.

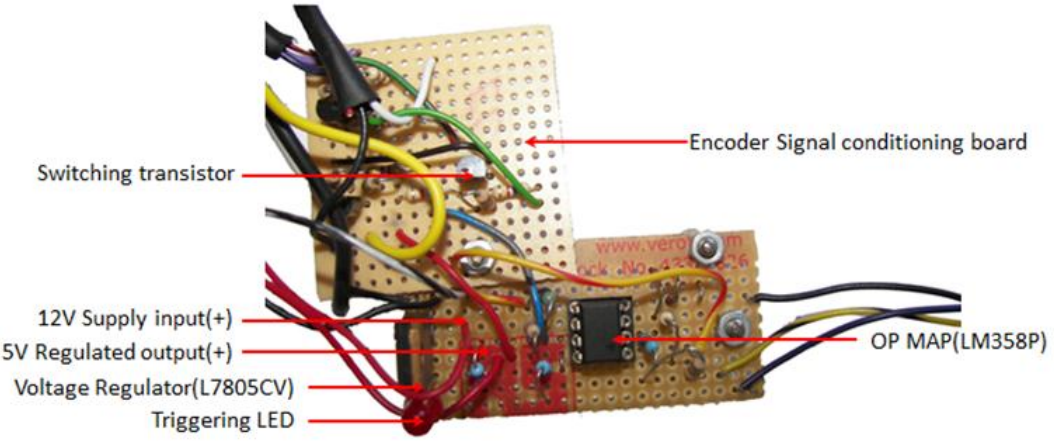

Figure 5.15: Schmitt trigger using LM358P.

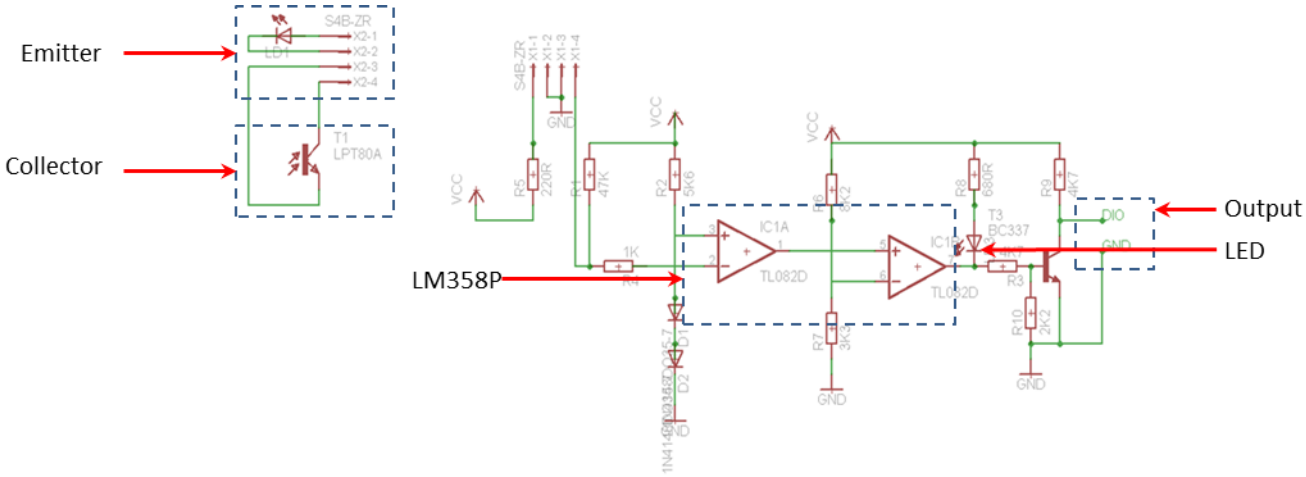

Figure 5.16: Schematic for the logic board IR transmitter and receiver.

5.4.6 Infrared-Reflective Sensor

Similar to the IR-beam encoder the infrared reflective sensors use a transmitter-receiver pair which is enclosed and positioned parallel to one another in a single enclosure. Figure 5.17 shows an OPB75 sensor with a structure similar to that described above. The sensors function by projecting IR onto an object and receiving the reflected rays. In order for this technique to be exploited the outer casing was marked black and silver tabs were used to create a reflective surface as in Figure 5.17.



Figure 5.17: IR receiver transmitter pair.

The BLDC motor is an outrunner and since the casing spins about the rotor a means of isolating the reflective sensor was needed. For this purpose sheets of expanded foam were used to build a supporting structure (depicted in Figure 5.18) allowing for mounting on the thrust rig. A circular cut-out was created in order to allow the BLDC motor to rotate independent of the supporting structure. The reflective sensor was mounted on the supporting structure using a series of holes to allow for configurability and optimization of the distance between the casing and the sensor illustrated as "d" in Figure 5.18.

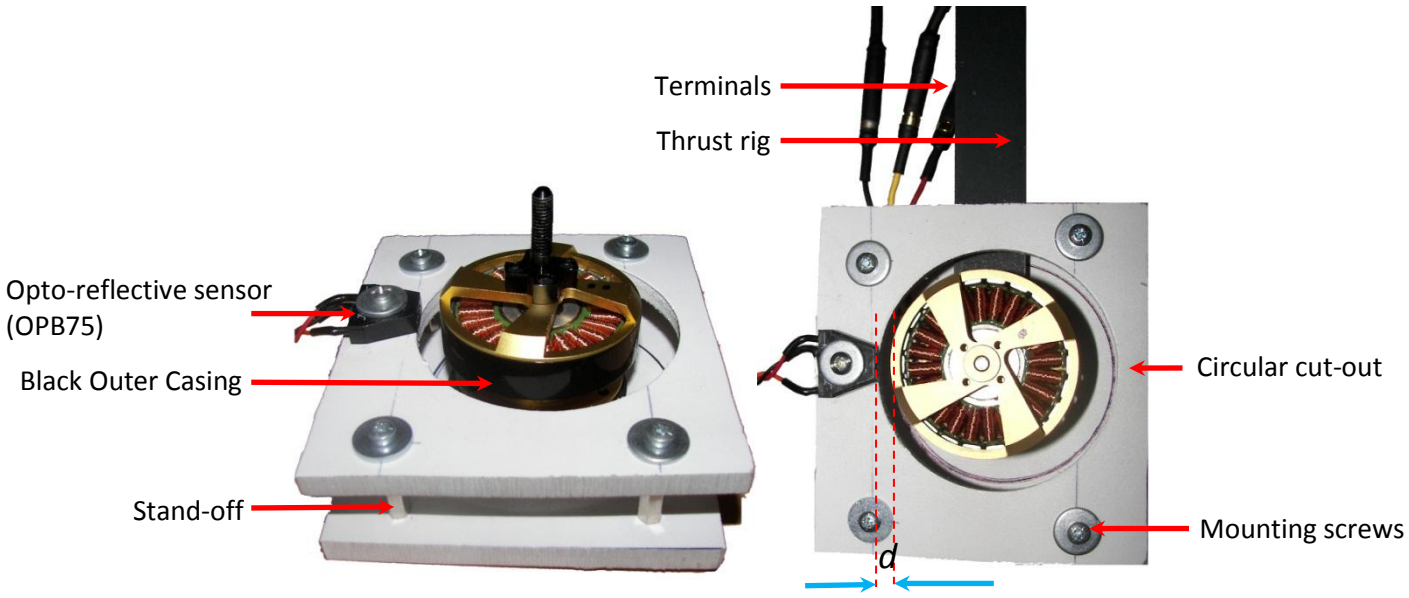

Figure 5.18: Thrust rig supporting structure for the opto-reflective sensor.

5.4.7 Sensorless Motor RPM Detection via BEMF

When the motor is spinning, the permanent magnet rotor moving past the stator coils induces an electrical potential in the coils called Back Electromotive Force (BEMF). BEMF is directly proportional to the motor speed and is determined from the motor voltage constant (KV).

The rotation rate is given by:

$$RPM = K_V(V) \tag{5.11}$$

The BEMF is given by:

$$BEMF = \frac{RPM}{K_V} \tag{5.12}$$

The cost advantage of sensing RPM through BEMF will be the elimination of the Hall position sensor. However there are several disadvantages to this method:

- A sufficient amount of BEMF must be generated by the motor
- Abrupt changes to the motor load can cause the BEMF drive loop to go out of lock
- The BEMF voltage can be measured only when the motor speed is within a limited range of the ideal commutation rate for the applied voltage
- Commutation at rates faster than the ideal rate will result in a discontinuous motor response

The K1 rpm meter uses BACK EMF to detect motor RPM. Modifications to the standard K1 meter unit setup allowed for easy integration into the current setup. Such modification include crocodile clips attached to the power line via the exposed terminals of the cutoff switch as seen in Figure 5.19.

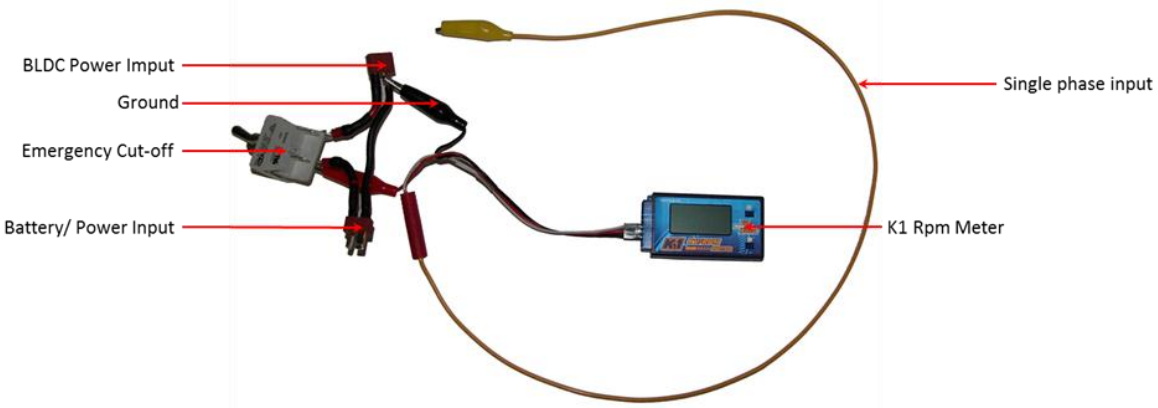

Figure 5.19: K1 RPM Meter.

5.4.8 Incremental Encoder

The third concept used a tachometer as seen in Figure 5.20 (Hengstler RS38-0/100EQ.11KB). This was used as a means of verifying the beam encoder functions as per requirements. It was powered by an external supply with a resolution of 100 steps per a revolution. Although there are losses associated with this mechanism, it allowed for verification of the Beam encoder increasing confidence in the result. The tachometer used three signal wires mainly phase1, phase 2 and index channel. The index channel attains its Boolean value after each revolution with phase A and phase B attaining its boolean value alternately with 90 degree phase changes between them as shown by Figure 5.21. The lag and lead in channels A and B denotes the direction in which rotation occurs.

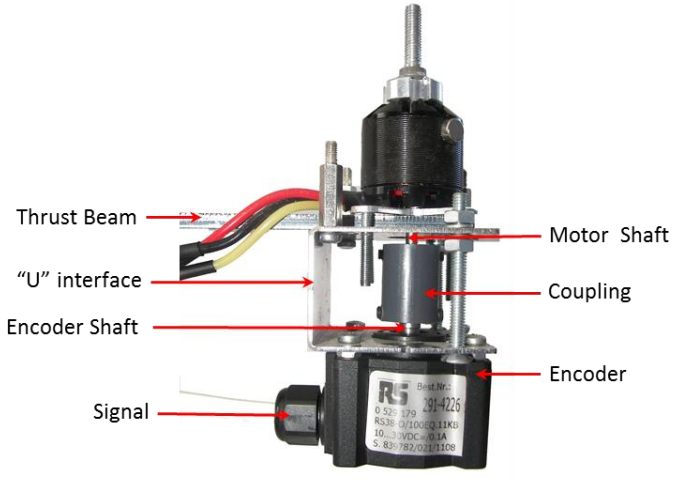

Figure 5.20: RS 291-4226 Incremental encoder with custom coupling.

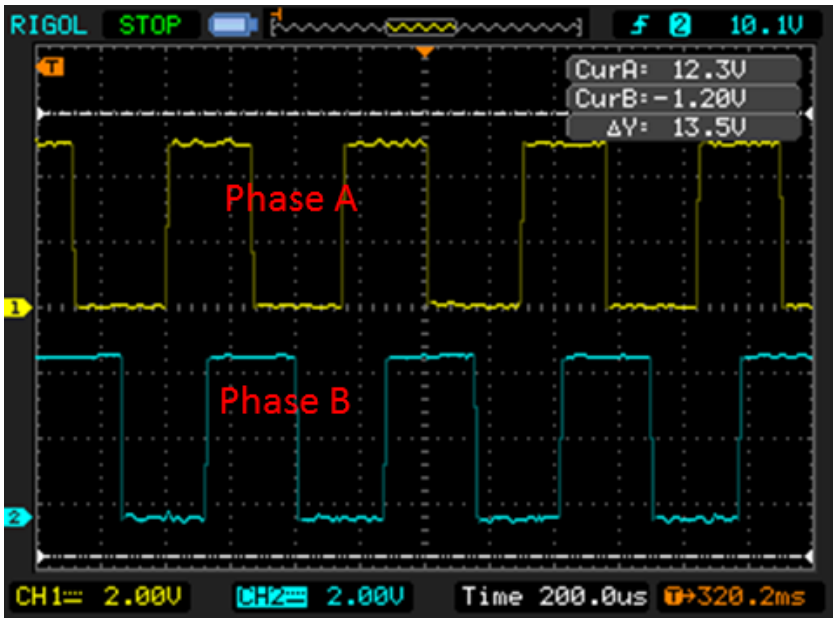

Figure 5.21: Encoding phase A and B offset by 90 degrees.

The incremental encoder benchmark testing was used in order to establish the extent of mechanical losses imposed by the encoder on the shaft of the motors. Since the incremental encoder is directly coupled to the shaft of the motor, it served as the benchmark in ascertaining the level of accuracy of the other sensors. The test was done using the Aeolian 1000KV brushless dc motor with a 9x4.5" propeller. For the first run the motor was initiated with no propeller using the outlined testing procedure as per section 3.2.6. The non-contact infrared sensor was implemented simultaneously to ensure the result produced by this sensor was consistent to that obtained from the incremental encoder.

Post calibration and verification of the infrared reflective sensor and the incremental encoder was removed and the test run redone with only the reflective rpm sensor present. Figure 5.22, Figure 5.23 and Figure 5.24 illustrate the difference in RPM and current draw prior and post the removal of the incremental encoder. This ascertained that there are losses associated with the incremental encoder however when the test was redone with a propeller the losses in RPM and current remained negligible. Figure 5.23 and Figure 5.24 illustrate that an addition of a propeller allows for losses due to the presence of the encoder to be neglected. This ascertains that the addition of a propeller imposes losses exceeding that imposed by the addition of the incremental encoder.

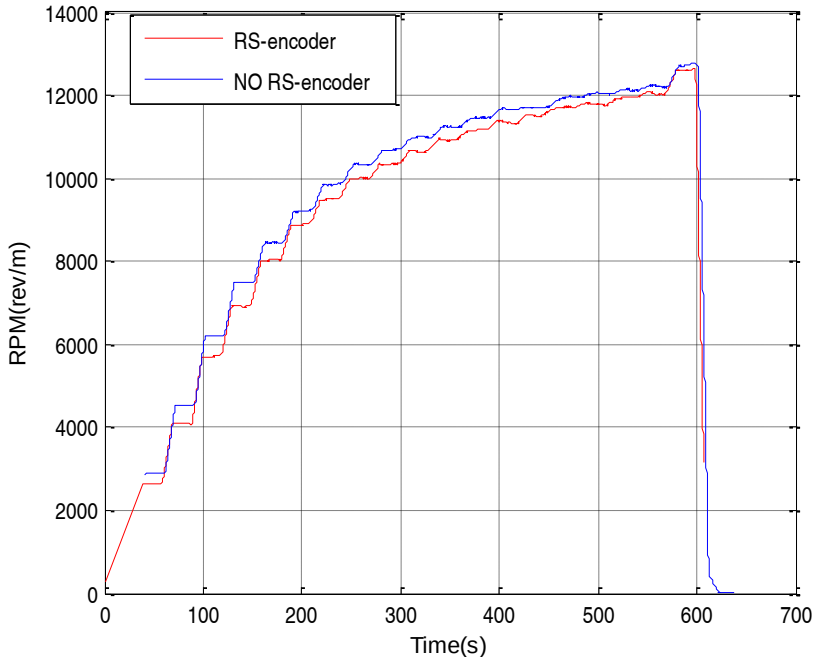

Figure 5.22: RPM comparison for uncoupled and couple encoder simulations with no blade.

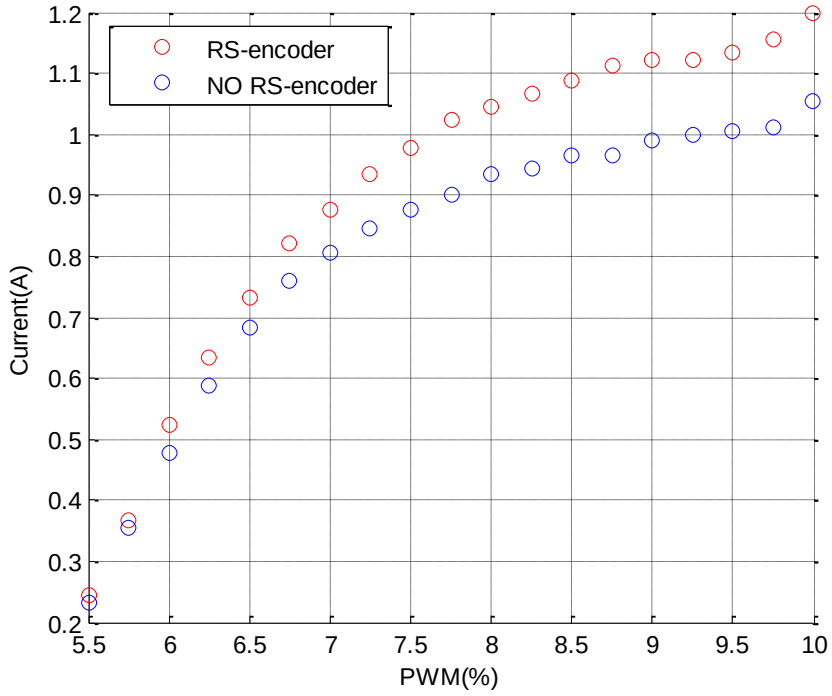

Figure 5.23: Current draw for uncoupled and coupled encoder simulations with no blade.

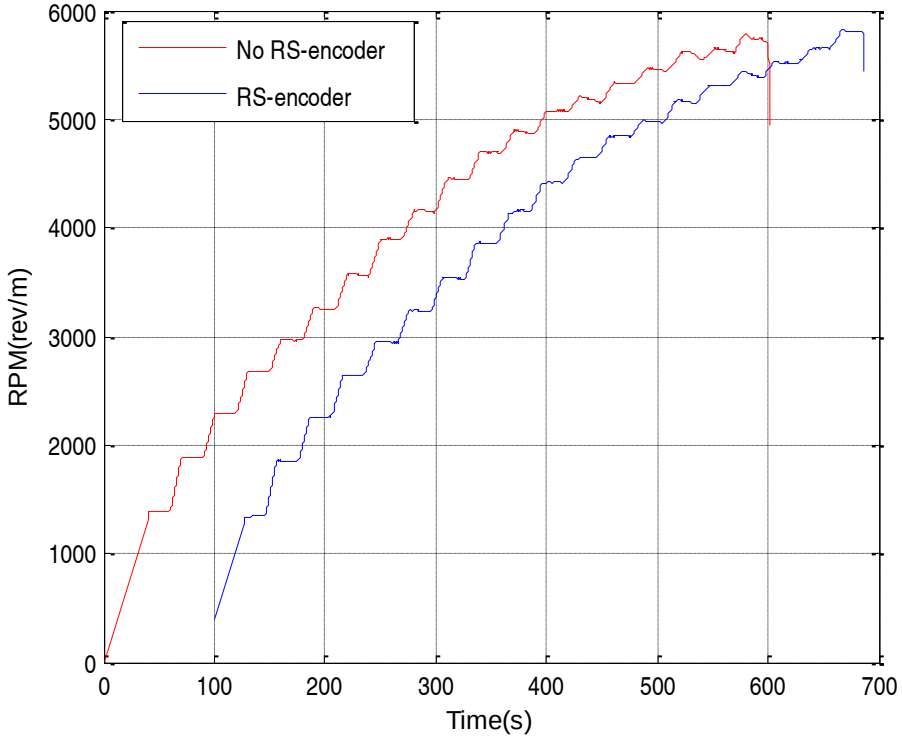

Figure 5.24: RPM for uncoupled and couple encoder simulations with 11x4.7 blade.

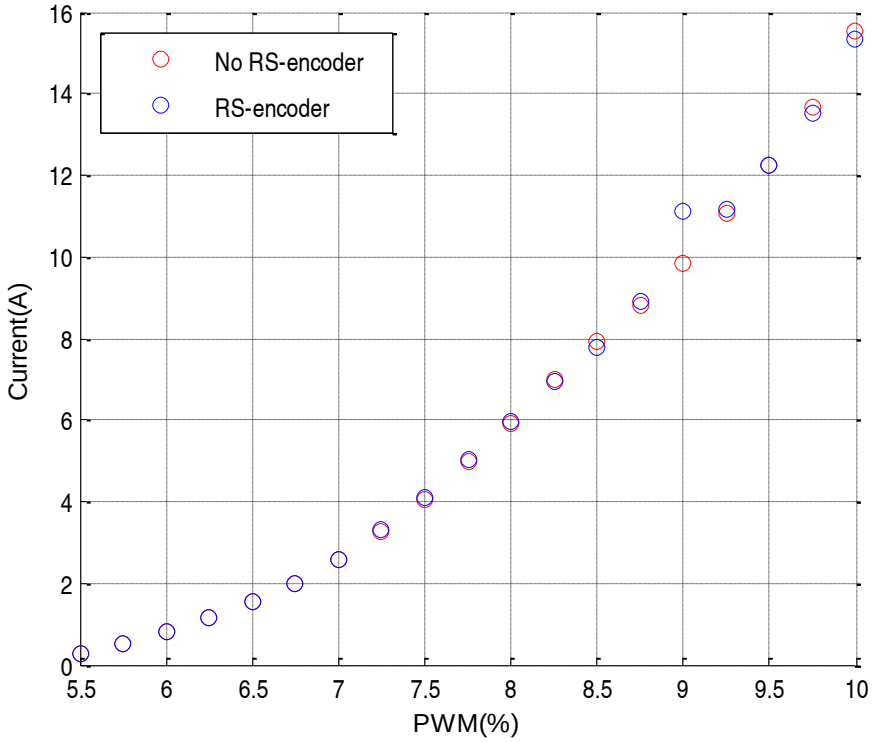

Figure 5.25: Current draw for the 11x4.7 blade.

5.4.9 Hall Sensors

The custom built hall sensor apparatus used neodium magnets mounted to the outer casing at 180^0 intervals (see Figure 5.26). The pair of magnets were epoxied to the outer casing at this interval in order to avoid rotational imbalance. The AH1751 hall sensor referred to has two operation modes Boolean 1 and 0 for the "on" ad "off" states respectively.

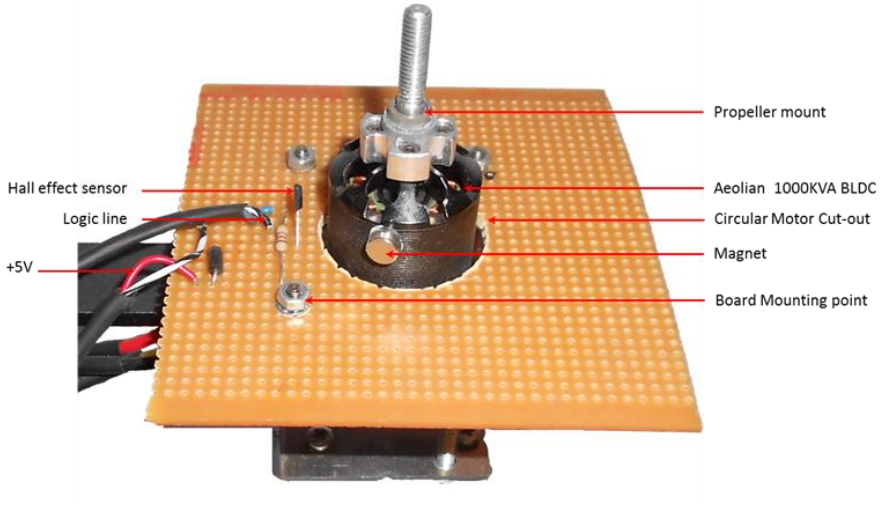

Figure 5.26: Custom built hall sensor rig.

The magnets when bonded to the casing must be bonded with the repulsive poles facing the each other. Incorrect installation of the neodium magnets as in Figure 5.27 will result in a fluctuation of RPM as can be seen in Figure 5.27. This phenomenon is purely due to the swapping of the poles.

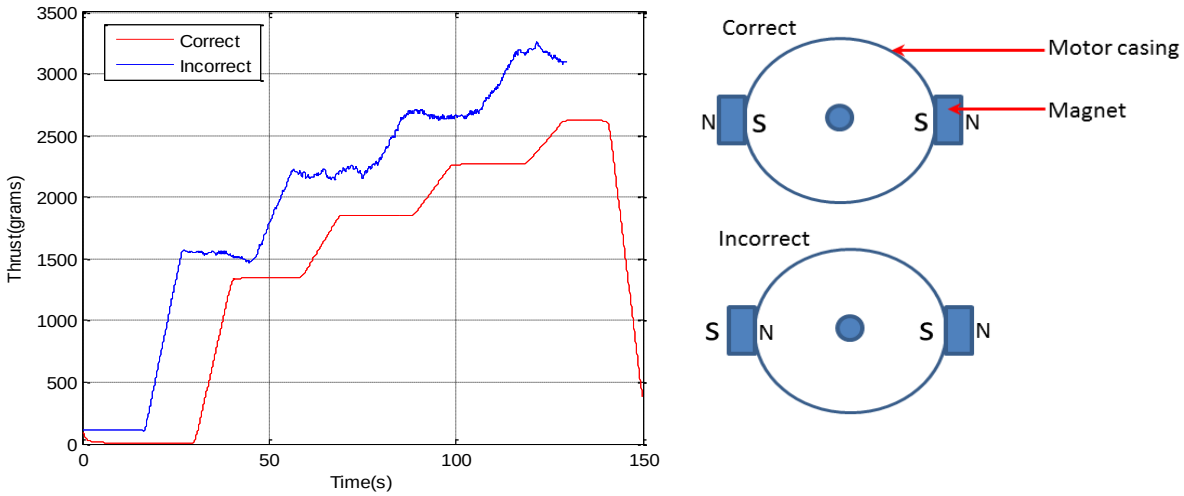

Figure 5.27: Effect of the incorrect orientation of the magnet poles.

5.5 Thrust Measurements

The physical differences in construction of BLDC motors make the performance of each motor unique. These differences affect the performance of the motor, amplifying the need for an apparatus that allows for performance specification to be extracted for a variation in propeller profiles. This need was satisfied by the construction of a custom built load cell.
The custom built load cell incorporated strain gauges mounted on the top base and bottom of the cantilever beam as seen in Figure 5.28.

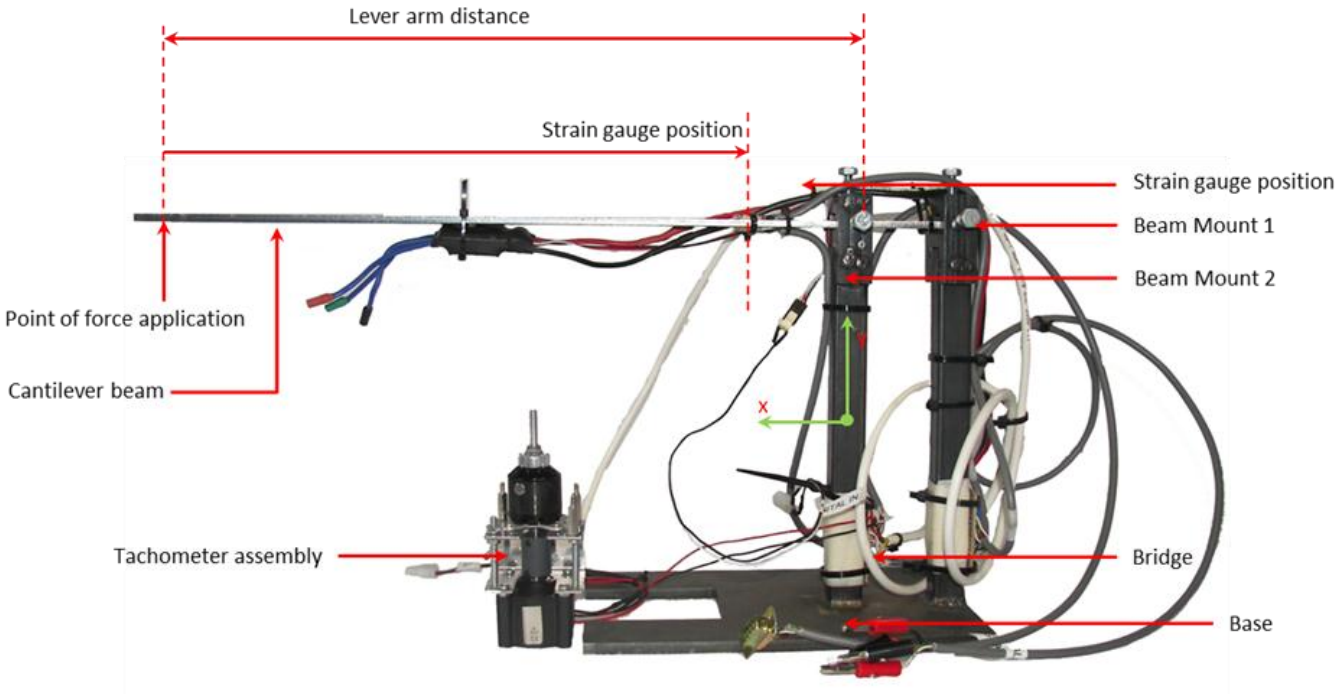

Figure 5.28: Overview of apparatus for thrust measurement.

Two vertical beam mounts were used to isolate any unnecessary motion whilst ensuring the fixed-free beam end conditions. This was further enforced by a pair of 3 hexagonal bolts serving as claps along the y and x-axis. The bolts further allowed for a variation in beam length and height. All parts were laser cut in order to maintain accuracy and were easily accessible. The base was extended to provide a counter moment and space for mounting-clamps, preventing the movement of the stand along the y-axis. A 5mm hole was created along the force application point allowing of the insertion of the rotor shaft which couples to the tachometer.

5.5.1 Strain Gage

The strain gages are bonded to the measuring loadcell with a dedicated adhesive. Strain occurring on the measuring site is transferred to the strain sensing element via the gage base as seen in Figure 5.29. For accurate measurement, the strain gage and adhesive should match the measuring material and operating conditions including temperature. The KFG-3-120-C1-11L1M2R series strain gauges used had the mechanical properties and structure as outlined in Table 6 and Figure 5.29 respectively.

Table 6: KFG-3-120-C1-11L1M2R gage mechanical properties

Series Designation	General purpose
Gage Length	3mm
Gage factor	2.1
Resistance	120Ω
Gauge Pattern	Uniaxial
Linear Expansion Coefficient	11.7
Type	Vinyl Coated
Wiring system	2 wire system

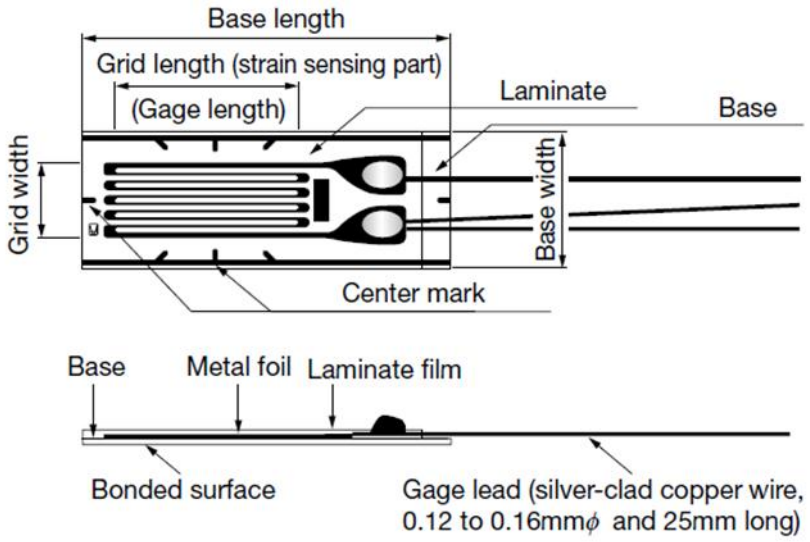

Figure 5.29: KFG series strain gauge.

5.5.1.1 Wheatstone Bridge Implementation

The Wheatstone bridge is an electrical circuit implemented to measure an unknown electrical resistance by balancing two legs of a bridge circuit, one leg of which includes the unknown component.

The two configurations that were looked at. (see Figure 5.30)

1. Active-dummy: A 2 gage setup, whereby the one gage serves as a dummy gage for temperature compensation
2. 4-active gage: A 4 gage setup connected to all four sides of the bridge ensuring large output of strain and improves temperature compensation (variations in ambient temperature) as well as eliminates strain components other than the target strain.

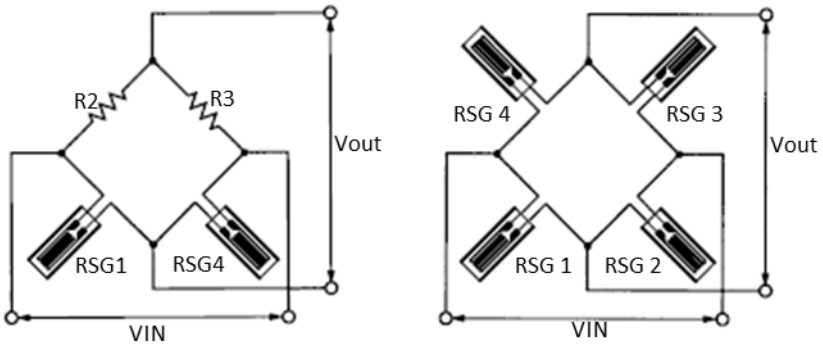

Figure 5.30: 2 and 4 gauge setup.

The initial iteration used a half bridge circuit which doubled the output from the bridge as opposed to a single gage setup (see Figure 5.31). The four gage setup produced voltage amplitudes of 4 times the output. This is shown by comparing Eq. (5.13) and (5.14).

The voltage output from a two gage setup is given by:

$$V_{out} = \frac{E}{4} K\epsilon \tag{5.13}$$

The voltage output from a four gage setup is given by: (see Figure 5.32)

$$V_{out} = EK\epsilon \tag{5.14}$$

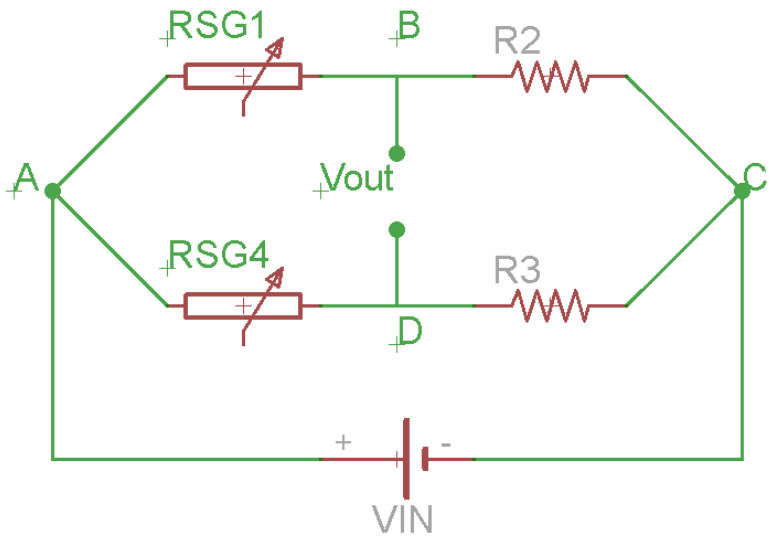

Figure 5.31: Active dummy-bridge.

$$V_{in} = V_{ABC} = V_{ADC} \tag{5.15}$$

The voltages across the bridge arms ABC and ADC are given by:

$$V_{ABC} = I_{ABC}(R_{SG1} + R_2) \tag{5.16}$$

$$V_{ADC} = I_{ADC}(R_{SG4} + R_3) \tag{5.17}$$

The Voltage across the strain gauge(RSG4) is given by:

$$V_{AD} = I_{ADC}(R_{SG4}) \tag{5.18}$$

The Voltage across the strain gauge(RSG1) is given by:

$$V_{AB} = I_{ABC}(R_{SG1}) \tag{5.19}$$

The Voltage out across the terminals are given by:

$$V_{OUT} = V_{AB} - V_{AD} \tag{5.20}$$

Using Eq. (5.18), (519) and (5.20):

$$V_{OUT} = I_{ABC}R_{SG1} - I_{ADC}R_{SG4} \tag{5.21}$$

$$V_{OUT} = \frac{V_{ABC}}{(R_{SG1} + R_2)}R_{SG1} - \frac{V_{ABC}}{(R_{SG4} + R_3)}R_{SG4} \tag{5.22}$$

The Supply voltage is equal the voltage in each arm:

$$V_{ABC} = V_{ABC} = V_{IN} \tag{5.23}$$

$$V_{OUT} = \left(\frac{(R_{SG4} + R_3)R_{SG1} - (R_{SG1} + R_2)R_{SG4}}{(R_{SG1} + R_2)(R_{SG4} + R_3)}\right)V_{IN} \tag{5.24}$$

$$V_{OUT} = \left(\frac{R_3R_{SG1} - R_2R_{SG4}}{(R_{SG1} + R_2)(R_{SG4} + R_3)}\right)V_{IN} \tag{5.25}$$

But $R_{SG1} = 120 + \Delta R$ and $R_{SG4} = 120 - \Delta R$

$$V_{OUT} = \left(\frac{R_3\big((120 + \Delta R) - (120 - \Delta R)\big)}{\big((120 + \Delta R) + R_2\big)\big((120 - \Delta R) + R_3\big)}\right)V_{IN}$$

$$V_{OUT} = \left(\frac{R_3(2\Delta R)}{(240 + \Delta R)(240 - \Delta R)}\right)V_{IN}$$

$$V_{OUT} = \left(\frac{R_3(2\Delta R)}{(240)^2 - (\Delta R)^2}\right)V_{IN} \tag{5.26}$$

Using Eq. (5.25), for a balanced bridge $V_{OUT} = 0$ therefore:

$$R_3 R_{SG1} = R_2 R_{SG4} \tag{5.27}$$

Hence from Eq. (5.27) it can be concluded that R_{SG1} and R_{SG4} must be on opposite faces of the beam to register a potential difference when a force is exerted. For trim control we can add additional potentiometers in series with R3 and R2 or both to maintain a balanced bridge at 0v. This can be seen in Eq. (5.28).

$$(R_3 + R_{pot1})R_{SG1} = (R_2 + R_{pot2})R_{SG4} \tag{5.28}$$

Similarly for a 4 gage circuit without trim, using Eq. (5.25):

$$V_{OUT} = \left(\frac{R_{SG3}R_{SG1} - R_{SG2}R_{SG4}}{(R_{SG1} + R_{SG2})(R_{SG4} + R_{SG3})}\right) V_{IN} \tag{5.29}$$

Similar to Eq. (5.27) balanced bridge $V_{OUT} = 0$ therefore:

$$R_{SG3}R_{SG1} = R_{SG2}R_{SG4} \tag{5.30}$$

With the added potentiometers in Figure 5.34 and Figure 5.35 Eq. (5.30) can be written as:

$$R_{SG1}(R_{SG3} + R_{pot2}) = R_{SG4}(R_{SG2} + R_{pot1})$$

Similarly for a 4 gage system with trim as in Figure 5.35

$$R_{SG1} + (R_{SG2} + R_{pot1}) = (R_{SG3} + R_{pot2}) + R_{SG4} \tag{5.31}$$

R_{SG1} and R_{SG3} are under tension whilst R_{SG2} and R_{SG4} are under compression

Hence $R_{SG1} = R_{SG3} = 120 + \Delta R$ and $R_{SG2} = R_{SG4} = 120 - \Delta R$

Using Eq. (5.29) the relationship between the bridge out and supply voltage for a 4 gage system can be simplified to :

$$V_{OUT} = \left(\frac{(120 + \Delta R)(120 + \Delta R) - (120 - \Delta R)(120 - \Delta R)}{\big((120 + \Delta R) + (120 - \Delta R)\big)\big((120 + \Delta R) + (120 - \Delta R)\big)} \right) V_{IN} \tag{5.32}$$

$$V_{OUT} = \left(\frac{\Delta R}{R} \right) V_{IN} \tag{5.33}$$

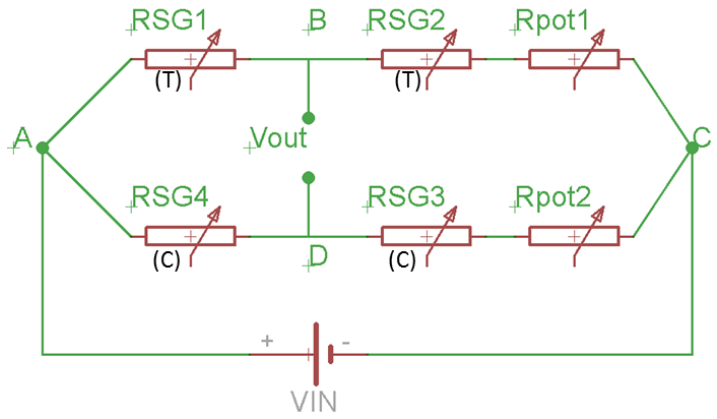

Figure 5.32: 4- gauge system with potentiometer(trim) adjustment.

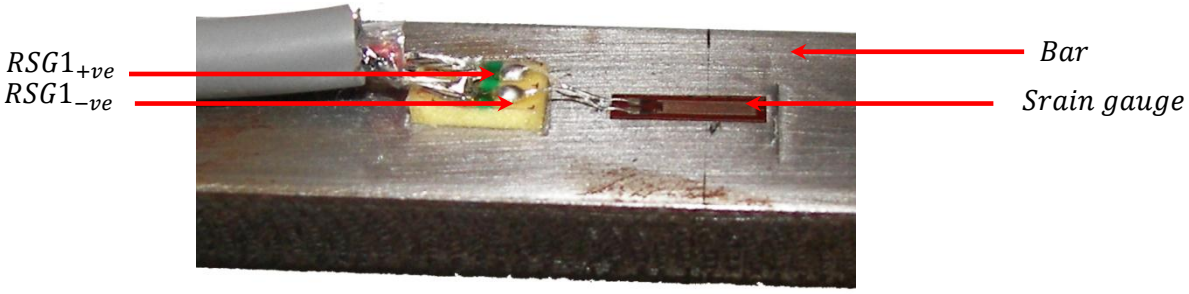

Figure 5.33: Single strain gauge (half- bridge, Top side).

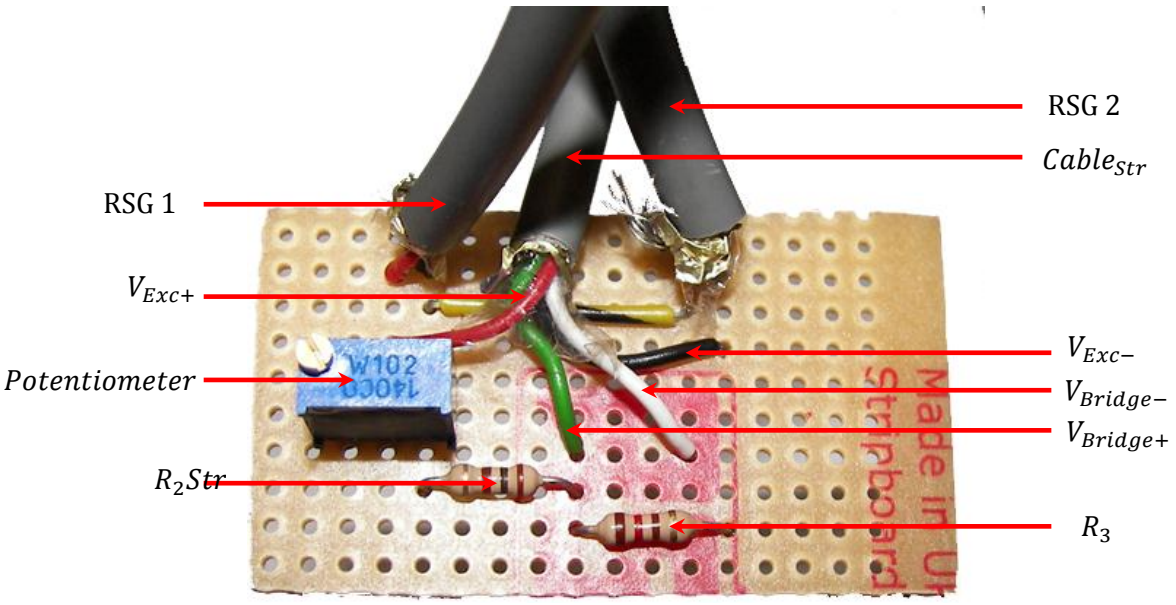

Figure 5.34: Half-Dummy-bridge circuit board.

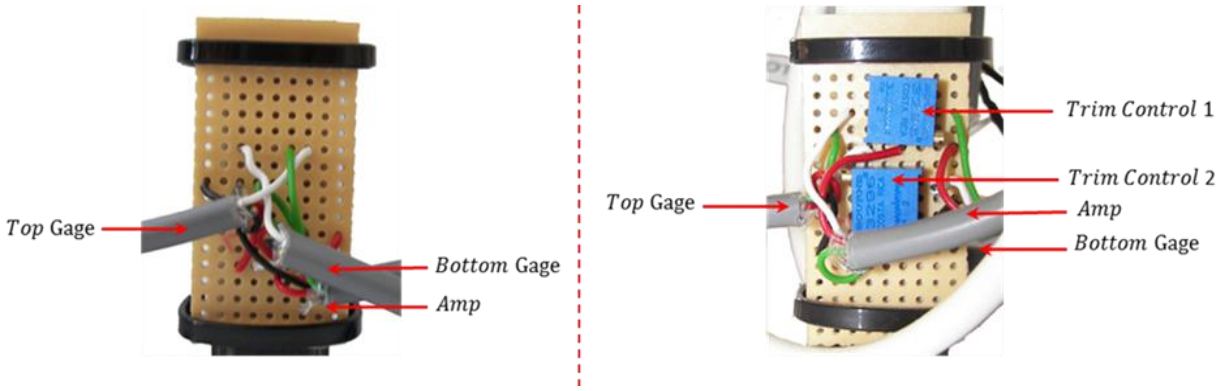

Figure 5.35: Full –Bridge circuit board with and without trim correction.

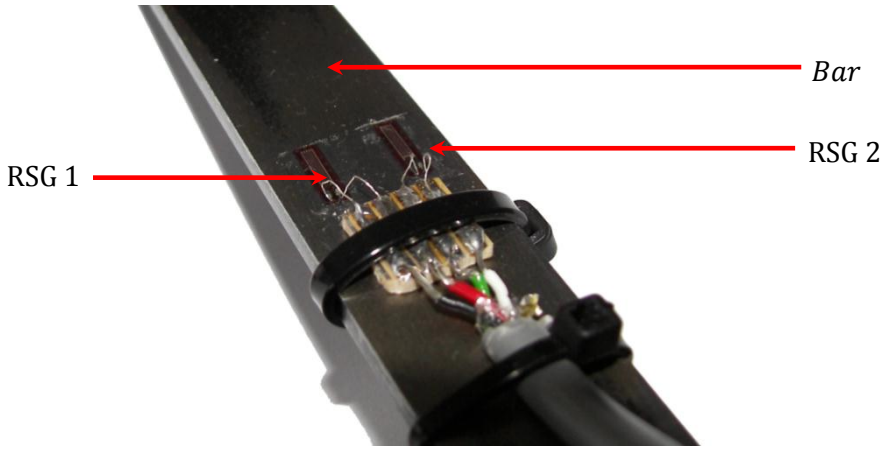

Figure 5.36: Double gauges (4-active strain gage setup, Top side).

5.5.1.2 Strain Gauge Amplifier

Bridge circuits output voltages which are small in magnitude. Small magnitude voltage ranges do not allow for adequate resolution to be achieved. This presents a large problem for calibration of the constructed apparatus. A strain gauge amplifier can be used to increase the range over which the constructed apparatus functions. A PJ dynamic strain gauge amplifier was used with a 2-12V bridge excitation (Figure 5.37). The connection to the full bridge circuit and bridge output occurs via colour coded binding posts and BNC connectors respectively. The maximum gain being permissible is 1000.

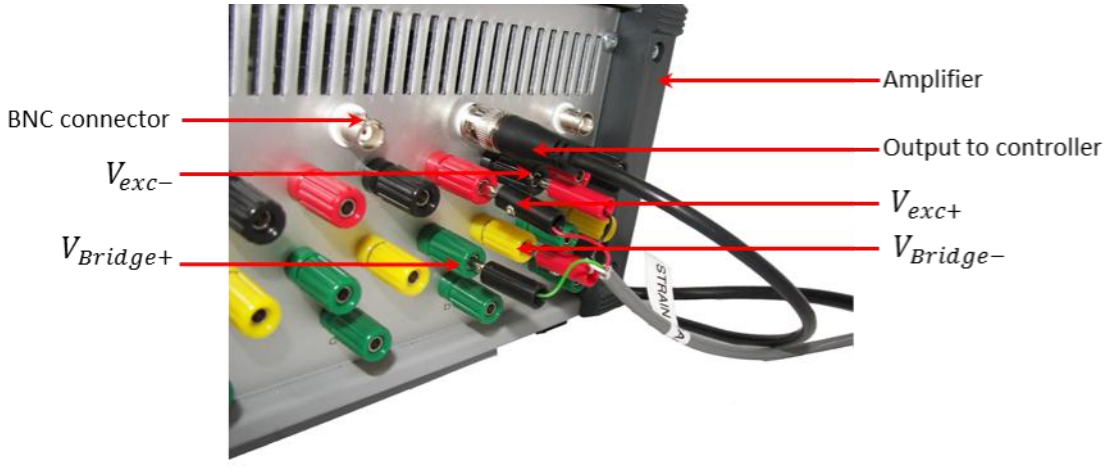

Figure 5.37: PJ Dynamic strain amplifier rear panel .

5.5.1.3 Strain Gauge Calibration

The strain gage bridge outputs a voltage value when the beam undergoes bending. However the potential difference across the junction is small in magnitude making measurement tedious due to small voltage ranges. An amplifier was used to increase the magnitude of the result. The strain gauge readings off the segment display and the ADC were calibrated using calibrated mass pieces. Mass pieces were placed at the end of the beam and the corresponding bridge amplifier output voltages were noted. The difference between the two curves were attributed to a DC offset on the amplifier. Re-calibration of the segment display corresponding to the ADC values was important however the relationship between the two were known allowing for calibration with the ADC values as these were the raw input values into the controller.

The relationship between amplifier segment display output voltages as shown in Figure 5.38 is given by:

$$y = 210.98(x) - 0.7031 \tag{5.34}$$

The relationship between amplifier ADC voltages as shown in Figure 5.38 is given by:

$$y = 231.37(x) - 531.81 \tag{5.35}$$

where:
y is the value of the mass in grams which will be translated to a thrust mass
x is the value of the amplifier reading

The thrust force is given by:

$$F_{Thrust} = yg \tag{5.36}$$

Where:
g is the gravitational acceleration

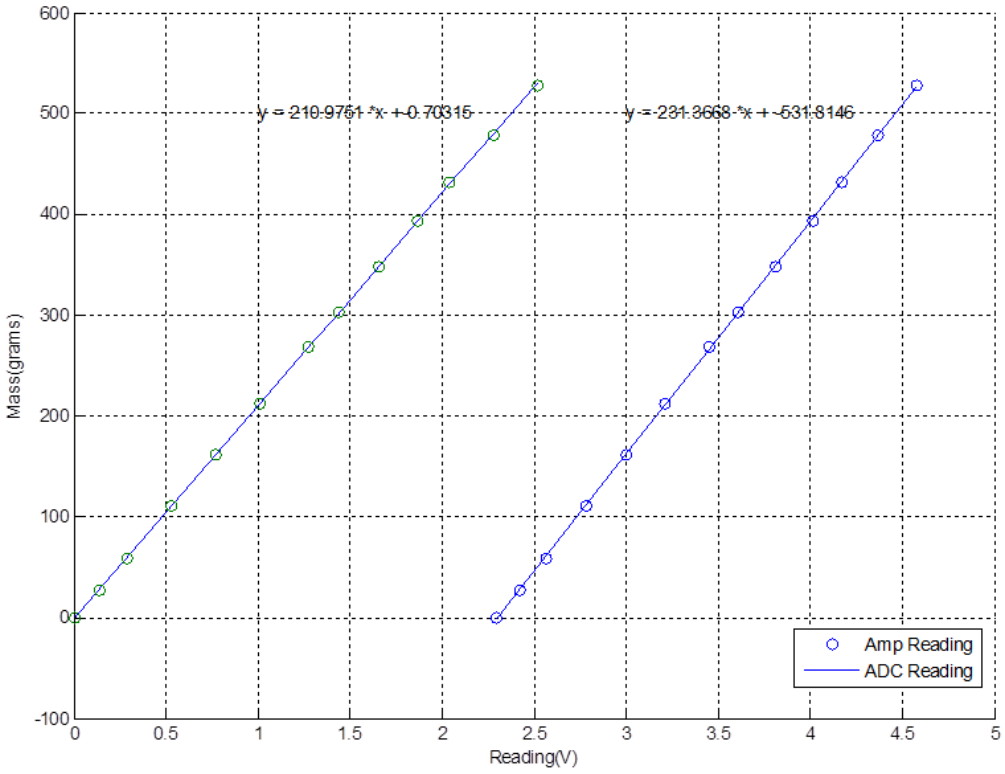

Figure 5.38: Strain gauge calibration curve.

5.5.2 Cantilever Beam Defining Equations

The cantilever beams allows for motor thrust to be calculated through the mechanical strain the beam experiences in its deflection (see Figure 5.39). The deflection of the beam creates a change in beam length which translates to a change in strain gauge length. This increases the resistance of the strain gauge pair unbalancing the bridge. A minimum of two strain gauges (2 or 4 gage system) were used as one needed to be in compression whilst the other in tension. The equation defined below extract the quantities necessary for an optimum beam geometry and bridge amplifier selection.

Strain is defined as:

$$\epsilon = \frac{\sigma}{E} = \frac{\Delta L}{L} \tag{5.37}$$

The Gauge factor of a strain gauge is defined as:

$$K = \frac{\Delta R}{R\epsilon} \tag{5.38}$$

The thrust generated by the motor creates an anti-clockwise moment on the arm as view below:

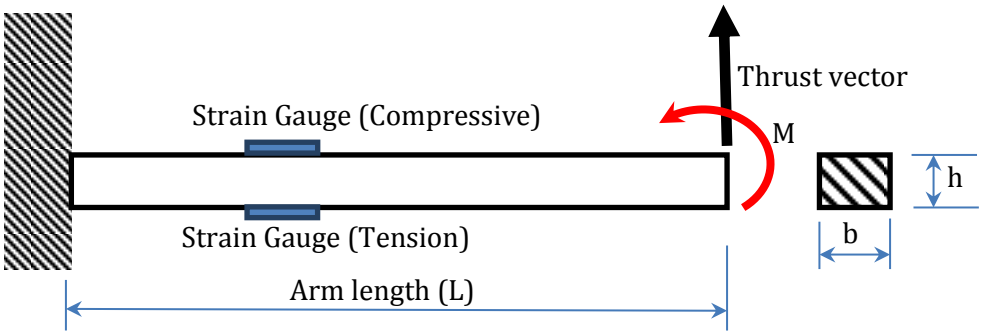

Figure 5.39: Thrust rig with gauges.

The moment generated by the motor is given by:

$$M = F_{thrust}L \tag{5.39}$$

The moment of inertia of the arm is given by:

$$I = \frac{bh^3}{12} \tag{5.40}$$

The change in resistance of the strain gauges is given by rearranging Eq. (5.38):

$$\Delta R = KR\epsilon \tag{5.41}$$

Substituting Eq. (5.41) into (5.37):

$$\Delta R = \frac{KR\sigma}{E} \tag{5.42}$$

Bending stress is defined as:

$$\sigma = \frac{My}{I} \tag{5.43}$$

Substituting Eq. (5.41) into (5.42):

$$\Delta R = \frac{KRMy}{IE} \tag{5.44}$$

Substituting Eq (5.39) into (5.44):

$$\Delta R = \frac{KRF_{thrust}Ly}{IE} \tag{5.45}$$

Maximum strain of the gauge is rated at 5%: (Refer to Appendix-A)

$$\epsilon = \frac{\Delta R}{RK} \tag{5.46}$$

As per specification: (Refer to Appendix-A)

$$K = 2 \tag{5.47}$$

Therefore the maximum change in resistance of the strain gauge can be determined from Eq. (5.39) using (5.45):

$$\Delta R = R(2)\left(\frac{5}{100}\right) \tag{5.48}$$

The strain gauge used has a resistance of 120Ω, therefore:

$$\Delta R = (120)(2)\left(\frac{5}{100}\right) \tag{5.49}$$

$$\therefore \Delta R = 12\Omega$$

The maximum length change of the resistor during applied loading must equal to 5% of the unstrained length. Since the strain gauge is attached to the bar, the bar can only increase in length by 5% of its unstrained length.

Using Eq. (5.26) the maximum voltage out of the bridge can be determined by assuming R_{SG1} to be in tension and R_{SG4} to be in compression:

$$V_{OUT} = \left(\frac{(120)\big(2(12)\big)}{(240)^2 - (12)^2}\right)V_{IN} \tag{5.50}$$

$$V_{OUT} = (0.050125)V_{IN} \tag{5.51}$$

For the 4 gage setup we use Eq. (5.33) and (5.46):

$$V_{OUT} = \left(\frac{12}{120}\right)V_{IN} = 0.1V_{IN} \tag{5.52}$$

Hence the maximum output voltage of the bridge will be 5% and 10% of the input voltage for the 2 and 4 gage setup respectively.

5.5.2.1 Cantilever Beam geometry selection

Eq. (5.33) had outlined the relationship between the bridge excitation voltage and the bridge output voltage. Eq. (5.42) established the relationship between thrust, beam geometry and variation in strain gage resistance. Combining both the equations allows for optimum beam geometry to be extracted and is shown by Eq. (5.53):

$$V_{OUT} = \left(\frac{KF_{thrust}Ly}{IE}\right)V_{IN} \tag{5.53}$$

Using the moment of inertia of the beam outlined by equation 5.40 and Table 6 for the gage factor:

$$V_{OUT} = \left(\frac{24F_{thrust}Ly}{bh^3E}\right)V_{IN} \tag{5.54}$$

Using and amplifier we add a gain term:

$$V_{OUT} = \left(\frac{12F_{thrust}L}{bh^2E}\right)V_{IN}G_{Amp} \tag{5.55}$$

Eq. (5.55) illustrates that minimizing height of the beam has the highest impact on maximizing V_{OUT}. This can be attributed to the height of the beam being a squared quantity in the denominator. For a quick and concise decision making process the following parameters were set to a constant (see Table 7). The value with the highest impact was the "h" value, minimizing the "h" value increases the V_{out} value significantly. Figure 5.40 illustrates the variation in beam height as a function of amplifier gain and voltage output.

Table 7: Fixed geometrical parameters for the thrust apparatus

Quantity	Value
$F_{thrust}(N)$	$800(g)$
b(mm)	20
E(Gpa)	200
V_{IN}(V)	11.5

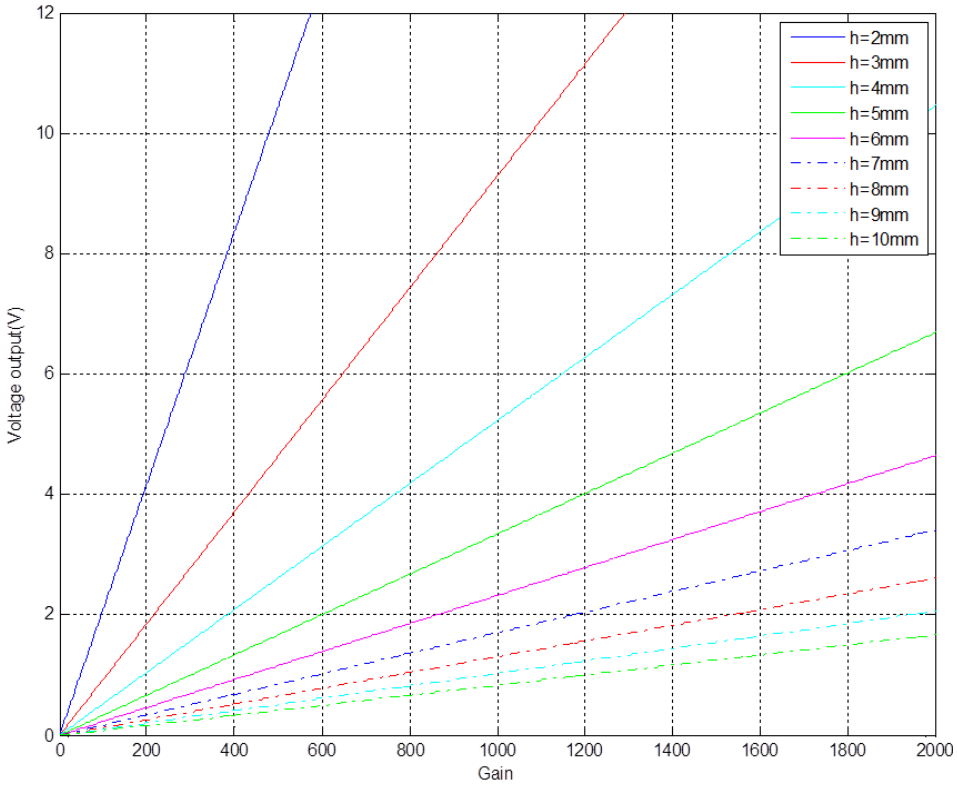

Figure 5.40: Variation in amplifier voltage output as a function of gain and beam height

The yield strength of the beam is giving by:

$$\sigma = \frac{6F_{thrust}L}{bh^2} \tag{5.56}$$

Eq. (5.56) can be plotted as a function of beam length as per Figure 5.41 and end tip mass as per Figure 5.42. The yield point of steel occurs at a σ value of 250Mpa. A safety factor of 100% was used in order to avoid failure due to yield. Beam lengths of h=2 and > 205mm cannot be used due to the safety factor being less than 1 additionally sustaining a lower end tip mass. It may also be noted as per Figure 5.40 that the higher "h" value decreases voltage sensitivity. The end tip mass consists of the motor combined with tachometer apparatus which has a mass <1kg. A value of h=3 was used when considering the above factors due to a 1.25kg tip mass carrying capability and limit beam length of 450mm whilst allowing for a good voltage sensitivity. Values of h greater than 3mm offered higher safety factors however did decrease the voltage sensitivity. Voltage sensitivity was limited by the

gain on the amplifier as described in section 5.5.1.2.

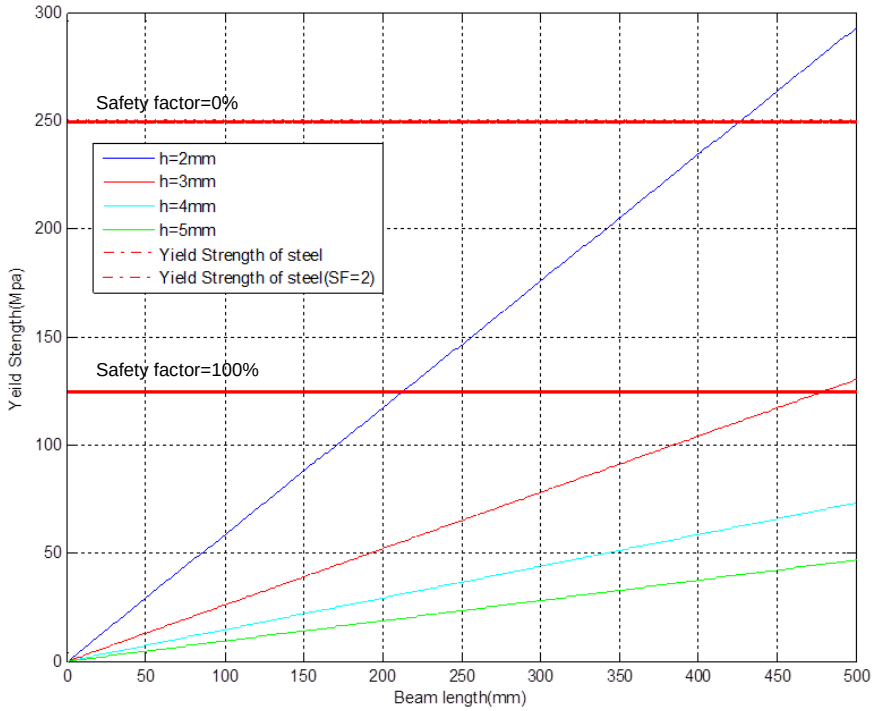

Figure 5.41: Variation in beam length with yield strength

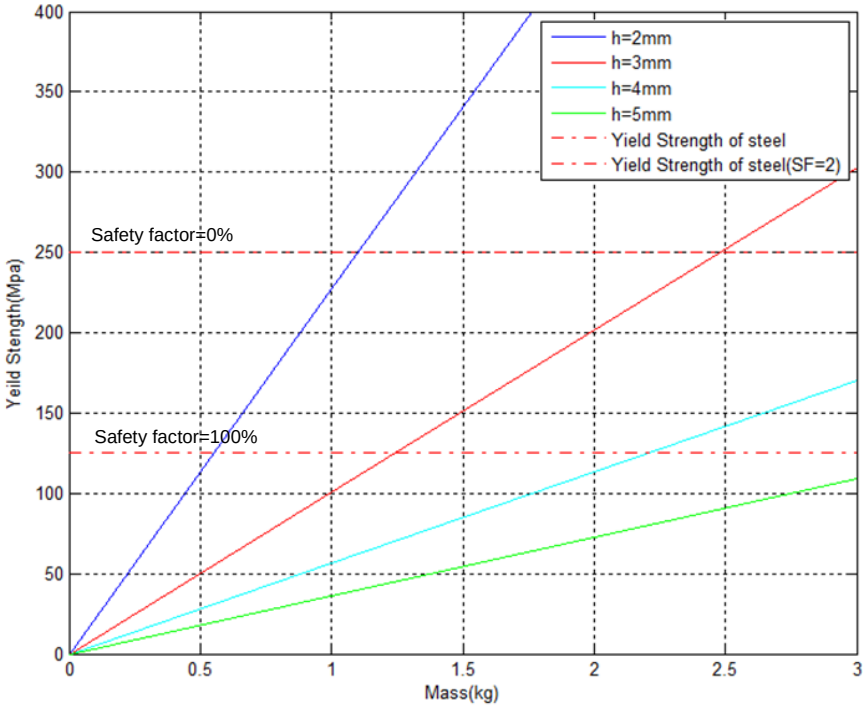

Figure 5.42: Variation in yield strengths with end tip mass

5.5.3 Motor Torque

Motor torque is measured via leverage system which when coupled to the thrust rig allows for a variation in torque with RPM to be captured. Isolation of the motor in this position allows for a single degree of freedom about the bearing axis which represents the pivot point as in Figure 5.44. The torque rig was created using the fundamental definition of torque as described by equation 5.57:

$$T = Fd \tag{5.57}$$

Torque can be calculated by the use of a lever arm combined with the component of the force perpendicular to the lever arm. The force in the case of the torque rig is generated by the rotation of the BLDC motor and drag penalty. To fully understand the construed problem moments are summed about the rotor hub as in Figure 5.43 and can be further assessed as in Figure 2.7. The electromotive force is the dominant moment creating a net resultant moment in the direction of rotation. Friction, inertia and propeller drag exert moments opposing the electromotive moment. The net moment is reacted upon by a clockwise reaction moment which is transferred to the moment arm of the torque rig (first described in section 2.5). Coupling the torque rig to the force rig decouples the moment into a perpendicular force acting a distance d_{perp} from the pivot point.

The torque rig was constructed from expanded foam sheeting due to the ease of construction (Figure 5.44). The 4 tier structure was created for added height and the cubicle construction for rigidity compensating for the added bending moment induced by the thrust force generated by the blades. The forces acting on the arm of the thrust tower are bi-planar. There exist a thrust force generated by the blades which is reacted upon by the moment generated by the clamping force on the base and the bearing support as in Figure 5.43 and Figure 5.44. The coupling of the two rigs was done via a motor mounting hole made in the bar for the purposes of thrust testing. It can be duly noted that the arm remains perpendicular to the thrust vector due to the small variations in thrust with time allowing for an accurate reading.

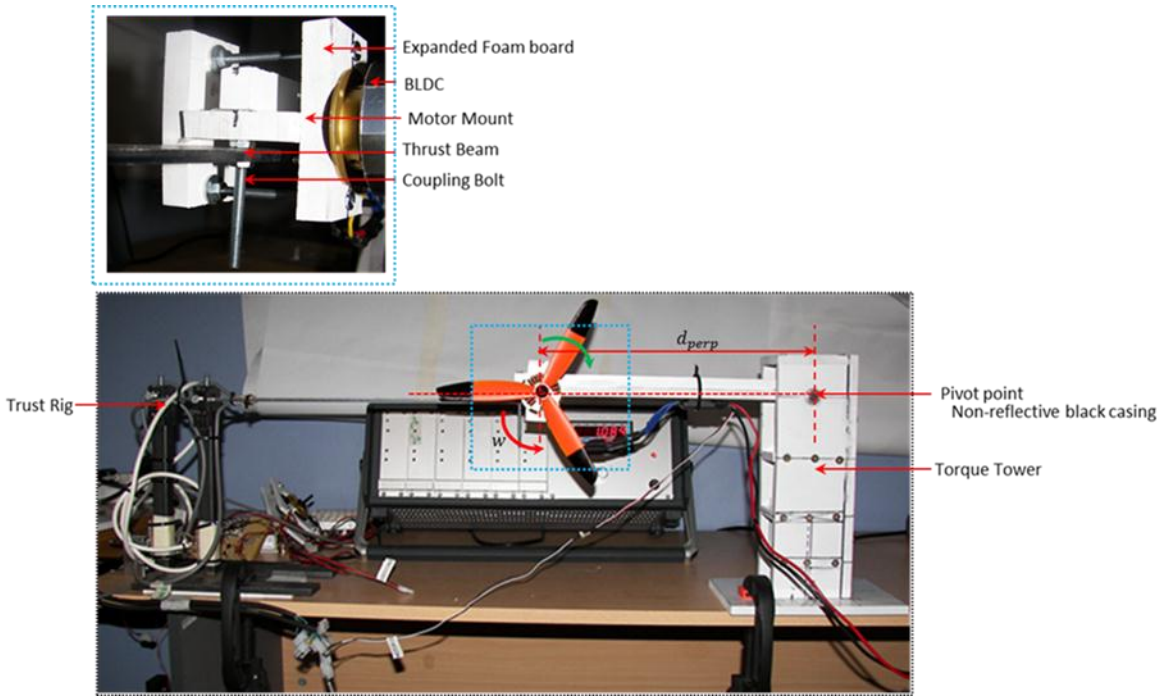

Figure 5.43: Coupling of the torque to thrust rig

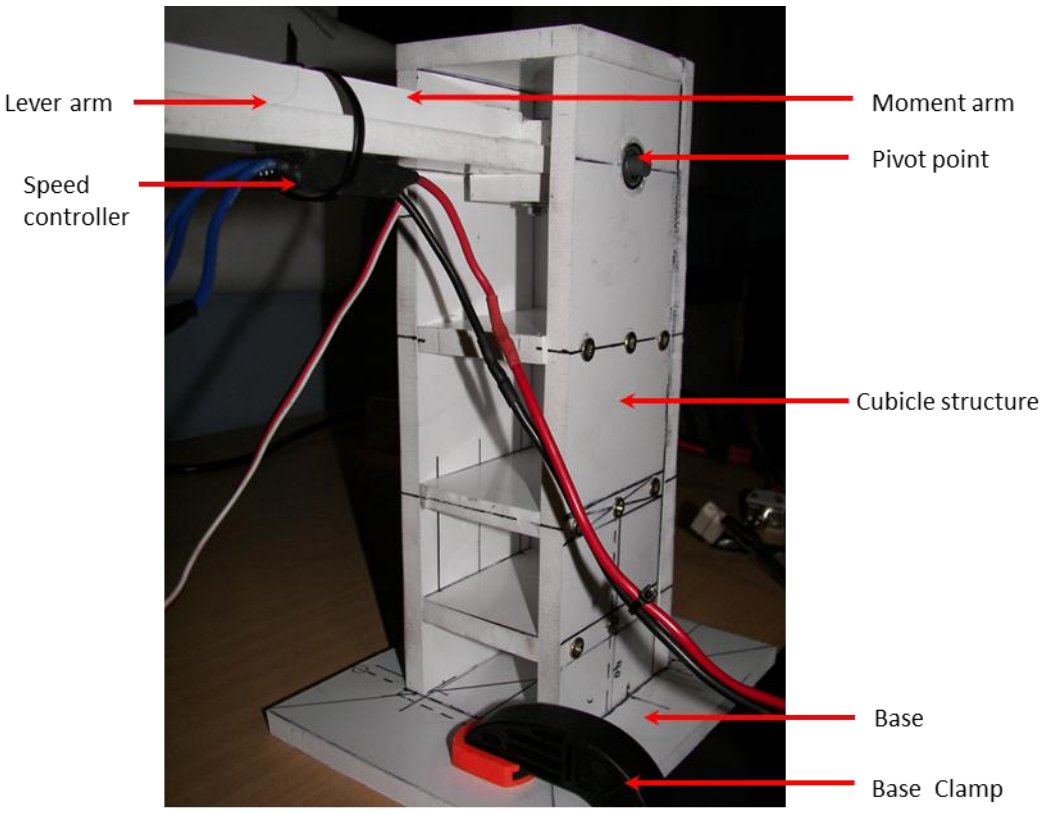

Figure 5.44: Constructed torque tower

5.5.4 Current Monitoring and Power Supply

The monitoring of current consumed by the motor is important in establishing a rough estimate on the range and endurance of the Quadrotor. Brushless DC Motor Rating is generally provided in KV. The Kilo-Volt (KV) rating in brushless motors refers to the amount of revolutions that can be achieved per a volt.

$$RPM_{OUT} = (Kv)V_{IN} \tag{5.58}$$

Capacity indicates how much power the battery pack can hold and is indicated in milliamp hours (mAh). In simpler terms, it signifies the maximum amount of current that can be drawn in an hour duration for the battery to fully discharged.

Hence the capacity of battery in circuit can be given by:

$$Capacity[hr] = \frac{Fully\ charged\ capacity[mAh]}{Current\ drawn[mA]} \tag{5.59}$$

However the current drawn varies with the RPM of the motor as demonstrated by Eq. (5.59). In order for a relationship between the current drawn and motor RPM to be established, a shunt resistor was employed as seen in Figure 5.45. This allowed for the voltage drop across the shunt resistor to be monitored and amplified through an IC Op-amp. A relationship could then be established to the RPM of the motor. The IC was used in order to amplify the voltage to that which could be used on the NI-9205 A2D module.

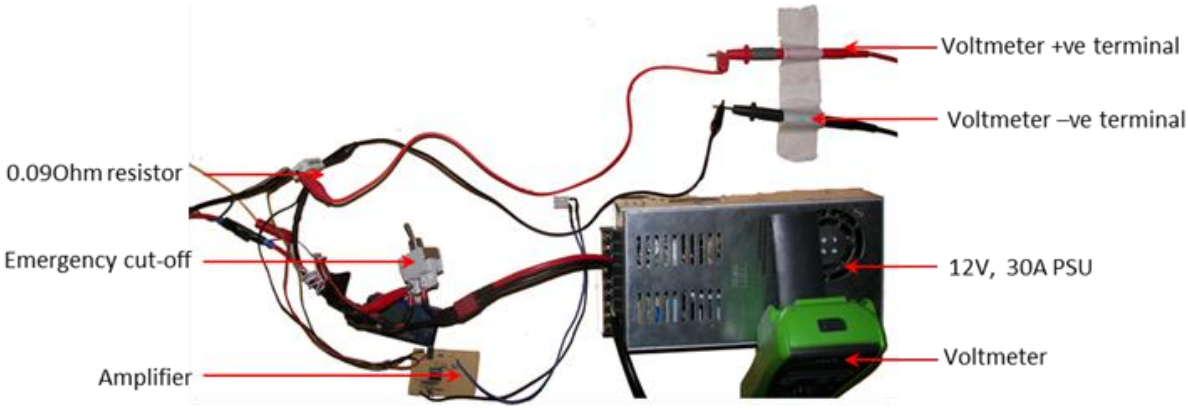

Figure 5.45: Current monitoring using a shunt resistor.

Due to the high current drawn, two Lithium polymer batteries were purchased (see Figure 5.46). These 3 cell batteries were rated at 11.1V and 4200 and 4400 mah respectively. The charger allowed for the capacity of each battery to be monitored as not to charge or drain the battery excessively after each run. The implications of the previous statements are fatal and these batteries are very volatile under those conditions and may combust.



Figure 5.46: Battery and charge.

5.6 Controller for Data Acquisition

The controller and C series modules form an important part of the data acquisition process. It allows for the data to be collected processed and analyzed. The National Instruments 9205 and 9401 are C Series module for use with NI CompactDAQ and CompactRIO chassis. The black box powerplant structure as described in section 5.1 can be viewed in Figure 5.47. It has two outputs being angular velocity and thrust one being generated by the motor and the other by the propeller motor combination. The sole input to the powerplant is the signal generated by the electronic speed controller driving the brushless dc motor.

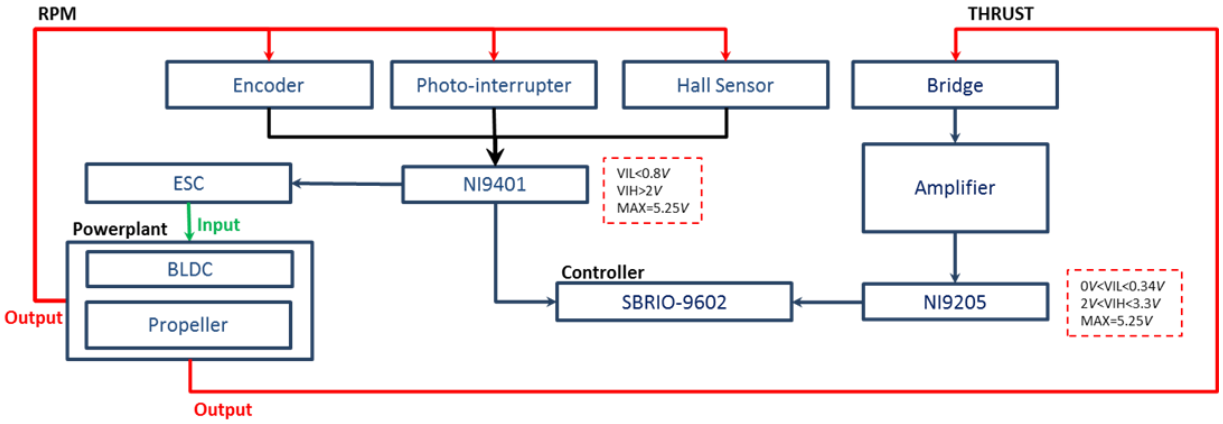

Figure 5.47: Hardware flow diagram.

5.6.1 C-Series Modules

The C-Series modules are the interface between the controller and the apparatus. They serve to condition the signal prior to it being interpreted by the controller by exposing the necessary inputs for the board. The NI 9205 C-Series module features 32 single-ended or 16 differential analog inputs, 16-bit resolution, and a maximum sampling rate of 250 kS/s. Each channel has programmable input ranges of ±200 mV, ±1, ±5, and ±10 V. The NI 9401 C-Series module is a high speed bi-directional sinking sourcing digital Input/Output with an input and output voltage range from 0-5.25v. A digital high is registered when the voltage input>2V and digital low when the voltage input<0.8v. It has a maximum clock rate of 10Mhz. Both the modules can be easily adapted to fit the SBRIO.

.

5.6.2 SBrio-9602 Main Controller

The controller allows for data acquisition, manipulation and control of hardware. The SBRIO allows for a user friendly user interface to be built via the Labview environment. It features Freescale MPC5200 real-time processor with speeds up to 400 MHz for deterministic real-time applications. The real-time processor is combined via a high-speed internal PCI bus with an onboard reconfigurable Xilinx Spartan-3 field-programmable gate array (FPGA). The FPGA is connected directly to all onboard 3.3 V digital I/O. Each onboard analog and digital I/O module has a dedicated connection to the FPGA as well. All sbRIO-96xx devices contain 110 bidirectional digital lines.

NI Single-Board RIO contain up to 32 analog inputs, four analog outputs, and 32 industrial 24 V digital inputs and digital outputs (see Figure 5.48). In addition to the built-in I/O capabilities, each NI Single- Board RIO device has three connectors for adding board-only versions of NI, third-party, or custom C Series I/O modules. The sbRIO devices accept a 19 to 30 VDC power supply and can operate within a -20 to 55 °C temperature range. With the 10/100 Mb/s Ethernet and serial ports communication with external devices and systems can be established via TCP/IP, UDP, Modbus/TCP, and serial protocols. The built-in real-time controller also features Web (HTTP) and file (FTP) servers (NI, n.d.).

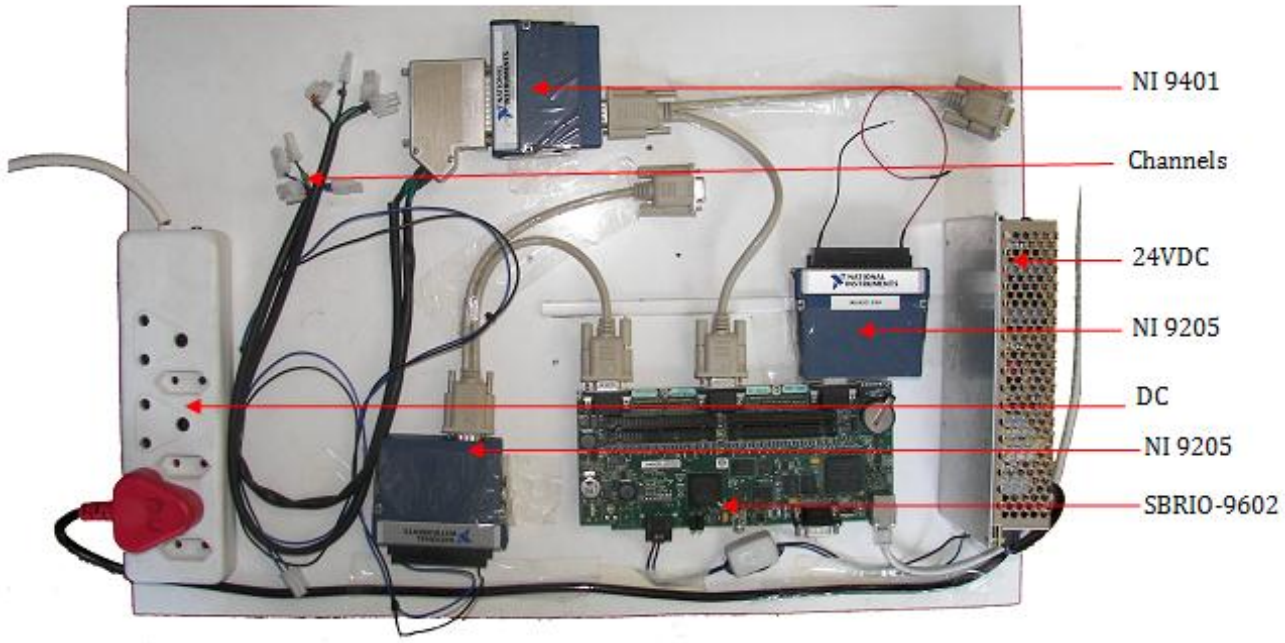

Figure 5.48: NI Controller Setup with C-series modules and PSU.

5.6.3 Labview FPGA and Real time

FPGAs can be configured to implement custom hardware functionality using prebuilt logic blocks and programmable routing resources (see Figure 5.49). This allows the user to create digital computing tasks in software and compile them down to a configuration file known as a FPGA bitstream that contains information on how the components should be wired together. FPGAs are completely reconfigurable as circuitry can attain different configurations by recompilation of the programmable resources.

FPGA chip adoption across all industries is driven by the fact that FPGAs combine the best parts of ASICs and processor-based systems. FPGAs provide hardware-timed speed and reliability, but they do not require high volumes to justify the large upfront expense of custom ASIC design. Reprogrammable silicon also has the same flexibility of software running on a processor-based system, but it is not limited by the number of processing cores available.

Unlike processors, FPGAs are truly parallel in nature, so different processing operations do not have to compete for the same resources. Each independent processing task is assigned

to a dedicated section of the chip, and can function autonomously without any influence from other logic blocks. As a result, the performance of one part of the application is not affected when you add more processing (NI, n.d.).

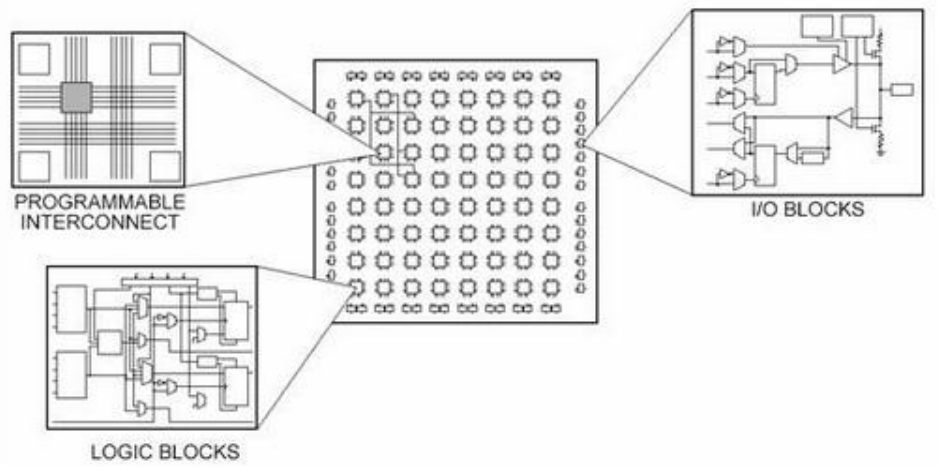

Figure 5.49: Anatomy of the FPGA (NI, n.d.).

While LabVIEW is commonly used to develop applications that run on desktop Oss such as Windows, these Oss are not optimized for running critical applications for an extended period of time. The LabVIEW Real-Time Module features real-time OS (RTOS) software that runs on NI embedded hardware devices and select third-party PC. If you selected a Real-Time architecture, you might also need a Real-Time Host VI. In this case your FPGA Host VI will be on your Real-Time controller and your will create a separate user interface or other host VI for your Windows system.

5.7 Complete Setup

Motor testing represented an important project milestone. It is essential that every monitored variable was captured with the utmost precision, accurately modelling the black box structure. This section highlights the testing procedures, difficulties and precautionary measures involved in data collection and processing. Figure 5.50 illustrates the nomenclature that will be referred to in this section.

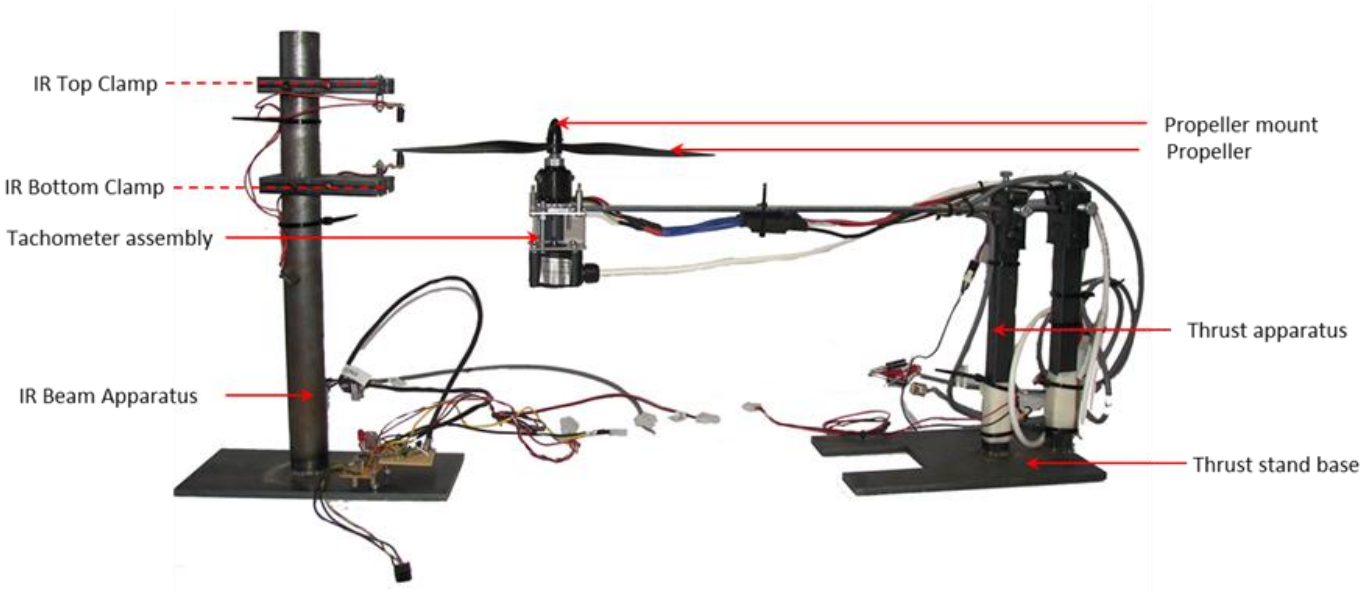

Figure 5.50: Complete setup with propeller mount, IR beam and tachometer.

5.7.1 Precautionary Measures

The presence off a rotating propeller at angular velocities ranging from 0-8000rpm is a hazard and can cause bodily harm. It is essential that the designated location for testing is absent from people or is shielded as hair line cracks on the blade profiles may be exacerbated by flutter and vibration at high blade velocities creating shrapnel. The direction of blade rotation needs to oppose the direction in which the propeller nut unscrews, tightening whilst in operation allowing for a secure mounting of the propeller.

Flutter at high speeds means that the blade tip deflects a significant vertical distance implying a greater clearance between the top and bottom infrared supporting clamps allowing for safe operation (see Figure 5.51). The 3 bolts positioned at 90 degree intervals allow for the supporting clamps to be adjusted with ease compensating for additional vertical translation of the blade.

Resonance occurs when the frequency of vibration is the same as the natural frequency of vibration of the bar. Free vibration takes place when a system oscillates under the action of forces inherent in the system itself due to initial disturbance, and when the externally applied forces are absent. The system under free vibration will vibrate at one or more of its

natural frequencies, which are properties of the dynamical system, established by its mass and stiffness distribution. The thrust apparatus has a concentrated mass at the end of the beam in the form of the tachometer assembly. Forces exerted at the beam end are a byproduct of the rotating assembly. The test software consists of a ramping function which increases the angular velocity of the motor with time at a constant rate of 0.25%PWM.

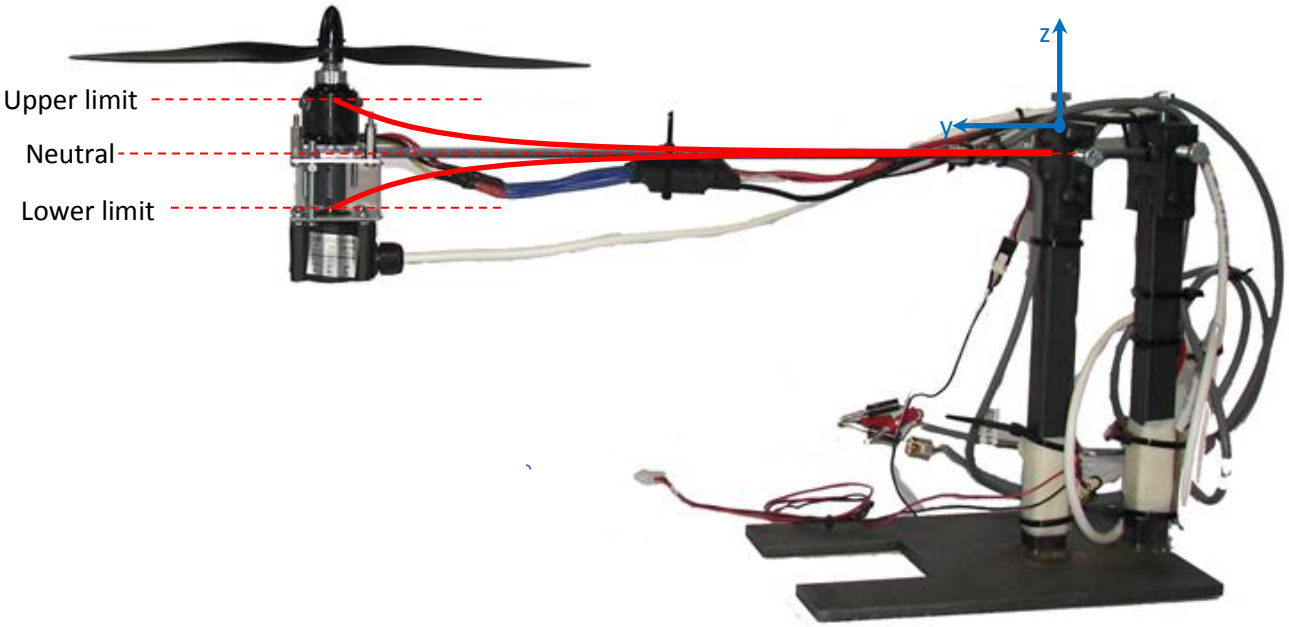

Figure 5.51: Beam deflection under resonance.

Resonance occurs when the frequency of vibration induced by the rotating assembly matches the natural frequency of the thrust stand apparatus. When this occurs, the rotating assembly has exaggerated movements along the z-axis and travels between a lower and upper limit. The range of the limits vary with assembly mass (each configuration has a different propeller and motor mass) and RPM. The thrust stand indicates resonance by rapid changes in thrust values as the strain gauge states are altered from a compressive to a tensile cyclically. This can be seen by the fluctuating thrust reading indicated in Figure 5.52. This additional travel along the z-axis must be accommodated for on the IR beam apparatus for propeller clearance. As the resonance frequency range is passed values of thrust tends to stabilize as oscillations decrease in amplitude. The trending of these oscillations form part of a tedious process as resonance varies with end tip mass.

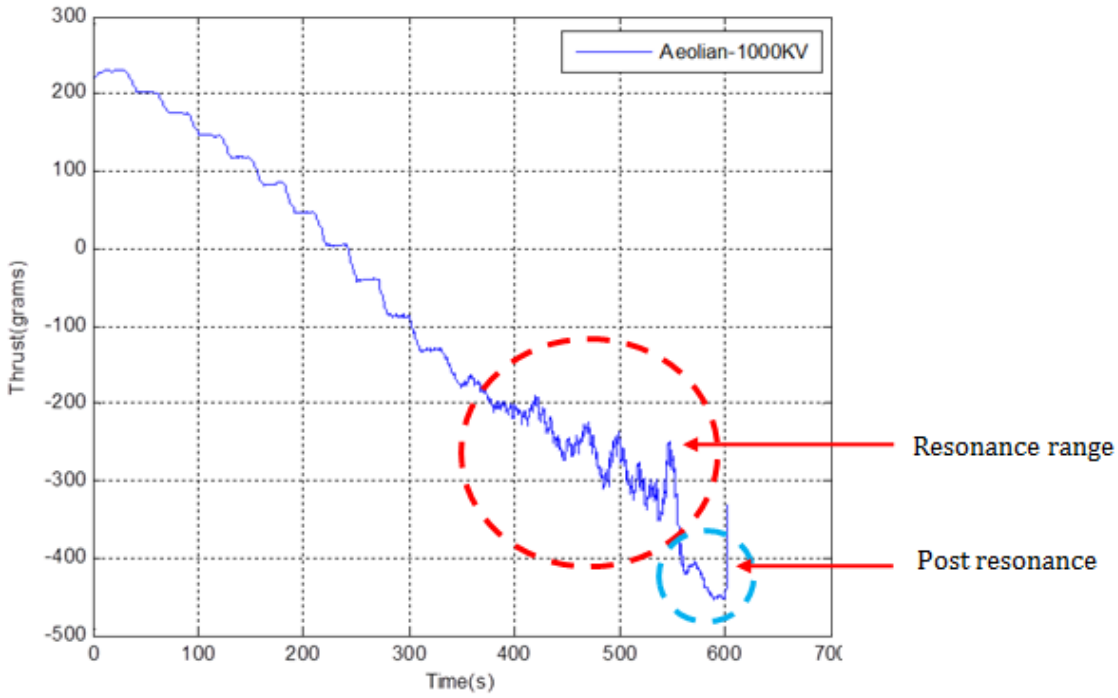

Figure 5.52: Graph of beam resonance.

The beam apparatus set uses an infrared receiver and transmitter pair, creating an invisible pathway which when crossed registers a logic low; unobstructed a logic high is registered. Figure 5.53 shows two red 10x4.5 propellers. During trial runs it was noted that the IR beam was uninterrupted by the red blades as opposed to black alternatives. It was concluded that the IR beam was not absorbed by the red plastic allowing a complete infrared pathway. The creation of black markings along 80% of the chord on opposing ends allowed for the black ink to absorb the infrared light registering an obstruction. This can be viewed in Figure 5.53, illustrative of the marked regions 1 and 2.



Figure 5.53: Marked and unmarked 10x4.5" blades.

During testing it was noted that the variation in battery capacity altered rpm and thrust readings with time. This was due to the variation in battery capacity with discharge and created another variable which hampered the study as it further complicated the motor identification phase. To eliminate this problem, a "Meanwell" high current power supply unit was purchased eliminating the need of battery charging and supplied a constant current to the motor. This was a solution that eliminated the power inconsistencies of the battery and eliminated the battery charging process.

Figure 5.54 illustrates noise produced by the encoder signal which is contradictory to the previously discussed figures. Countless runs indicated a region of isolation in noise at higher RPM values. This was attributed to blade twist as described by Figure 5.55. Figure 5.55 is broken up into 3 separate diagrams each illustrating the effect of blade twist on the angle of attack and timing diagram. The blue blade represents the first blade to cross the infrared optical path projected by the IR beam apparatus. The green following blade represents a blade under blade twist. The green blade has a decreased angle of attack creating a larger post twist length as opposed to the shorter pre-twist length. The controller triggers on a falling or rising edge(refer to section 5.4.4) as per the user specification. As the leading edge obstructs the path a flag timer is raised and raised again when the following blade obstructs the pathway. The difference between the two timing flags is the frequency that is used to calculate blade RPM and can be viewed in Figure 3.8 as t_1. The rotary encoder was used to evaluate the accuracy of the beam encoder. Figure 5.56 and Figure 5.57 conclude that the beam encoder functions accurately.

Twist in the blade at the higher RPM range allows for a significant change in this frequency creating a higher perceived RPM value as seen in Figure 5.54 and Figure 5.55. Under blade twist the angle of attack is reduced increasing the perceived length whilst generating less thrust. The blue RPM curve represents the data acquired off the photo-reflective sensor and the other represents the data acquired from the beam IR apparatus set. These were over-plotted to illustrate that the effect is purely a function of the blade behaviour.

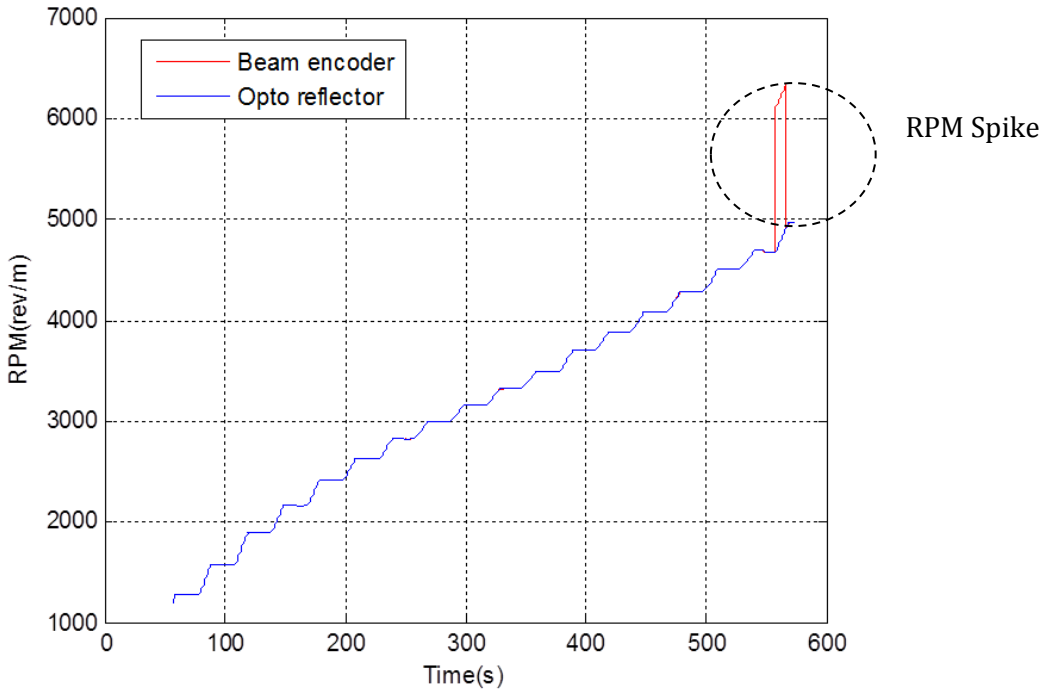

Figure 5.54: Noise on the IR beam sensor for a 9x4.7" propeller.

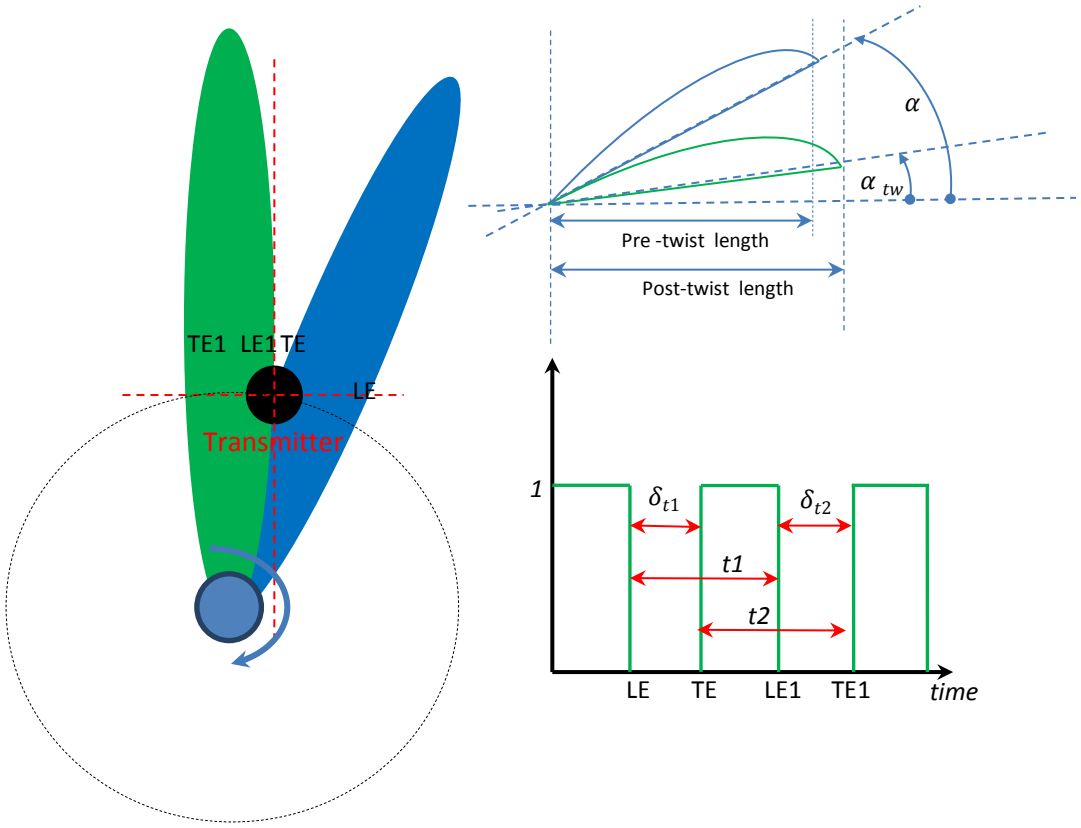

Figure 5.55: The effect of blade twist on RPM values.

5.7.2 Verification Results

Preliminary runs allowed for the functional performance verification of the constructed apparatus. This ascertains if the acquired results are correct by comparison between the three RPM sensors, allowing for an easier functional justification. Figure 5.56, Figure 5.57 and Figure 5.58 show changes in RPM with the constructed throttle function as described in section 3.2.6. The performance curves illustrate almost identical results which can be mistaken for data from one sensor being plotted repeatedly. Due to the previous statement an overlay for all 3 readings was not done culminating in 3 separate plots.

The tachometer rpm readings served as the baseline for comparison due to it being directly coupled to the motor making the confidence in this data set the highest. The difference chart using an overlay-plot of the differences between the reference curve in Figure 5.56 and that of the curves in Figure 5.57 indicated by the red and blue curves in Figure 5.59 respectively. Differences present are indicative of unique data from three different sensors. The staggered trending is an effect of a 0.25% variation in PWM single at a time interval of thirty seconds. Thrust and RPM values are allowed to reach steady state in the predetermined time however RPM fluctuations do occur. A maximum variation of 0.04% had been registered between the sensor readings. Figure 5.62 and Figure 5.63 illustrate the RPM comparison between the Opto-Relfective sensor and the IR Beam apparatus set. The maximum error is 0.2% ascertaining the function and instilling confidence in the non-contact RPM sensors results.

The thrust measurring apparatus is sensitive to changes in throttle, it is also affected by resonance. Figure 5.60 has an initial start value of 244grams which represents the mass of the trachometer assembly. The convention being, mass is registered as a a positive value whereas lift decreases mass registering a lower net value. The peak thrust value is a summation of the highest postive and negative values at steady state. The steady state value at the highest rpm averages to -440gram creating a net thrust of 684grams when combined with the initial mass of the tachometer assembly.

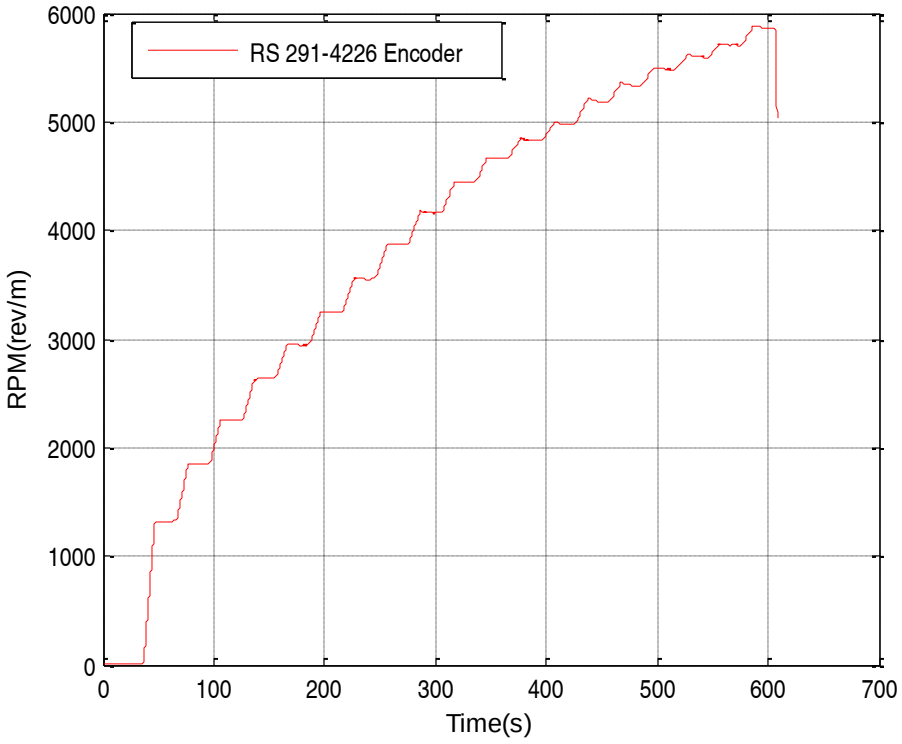

Figure 5.56: RPM detection using the RS encoder (Aeolian 1000KV).

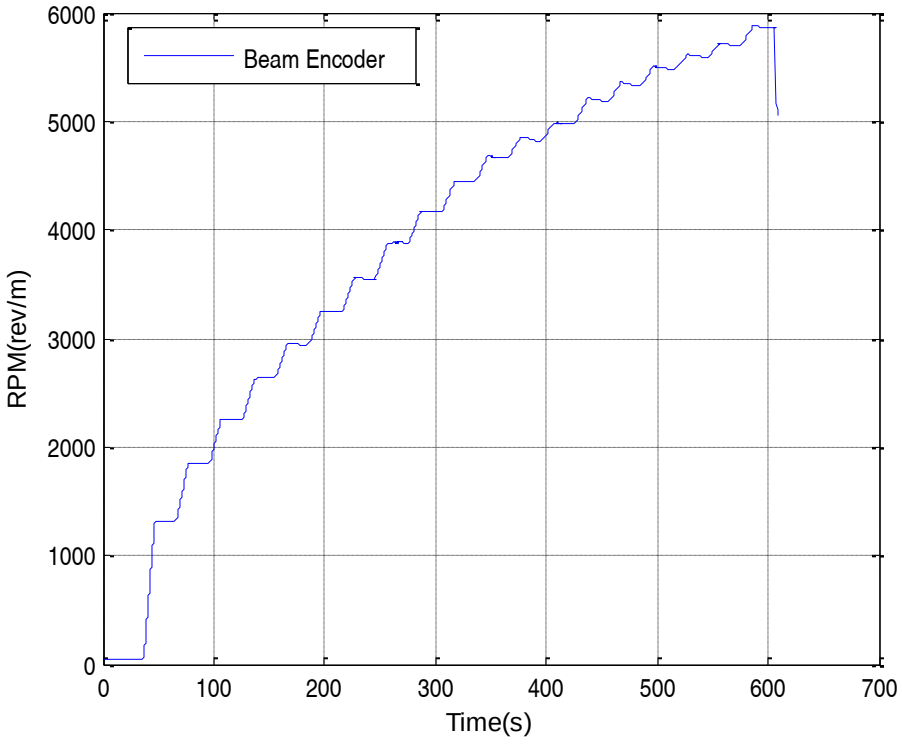

Figure 5.57: RPM detection using the IR-Beam apparatus (Aeolian 1000KV).

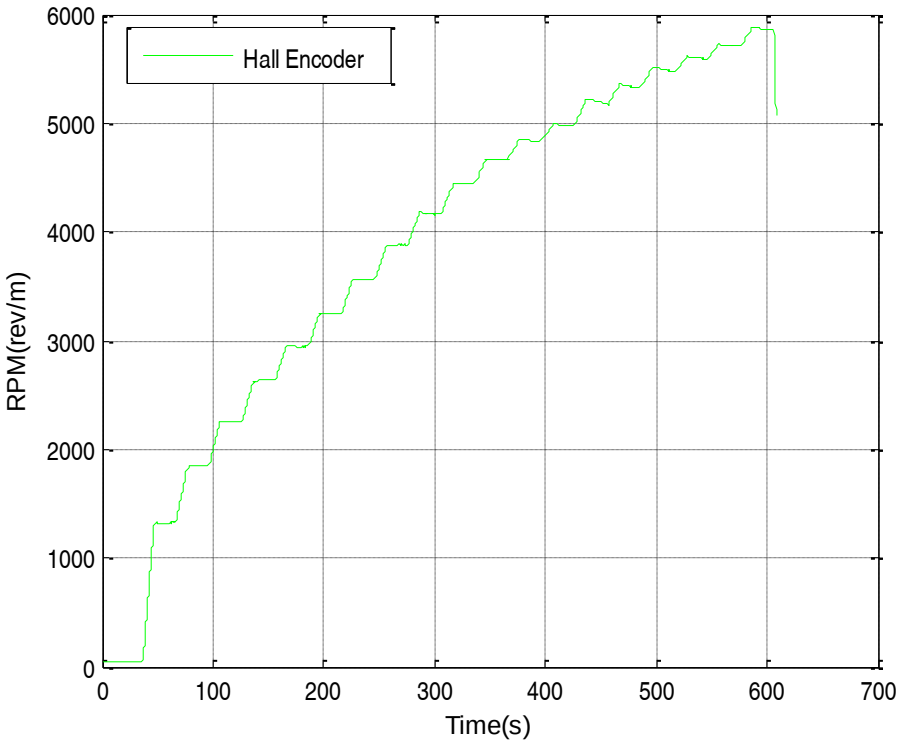

Figure 5.58: RPM detection using the Hall sensor (Aeolian 1000KV).

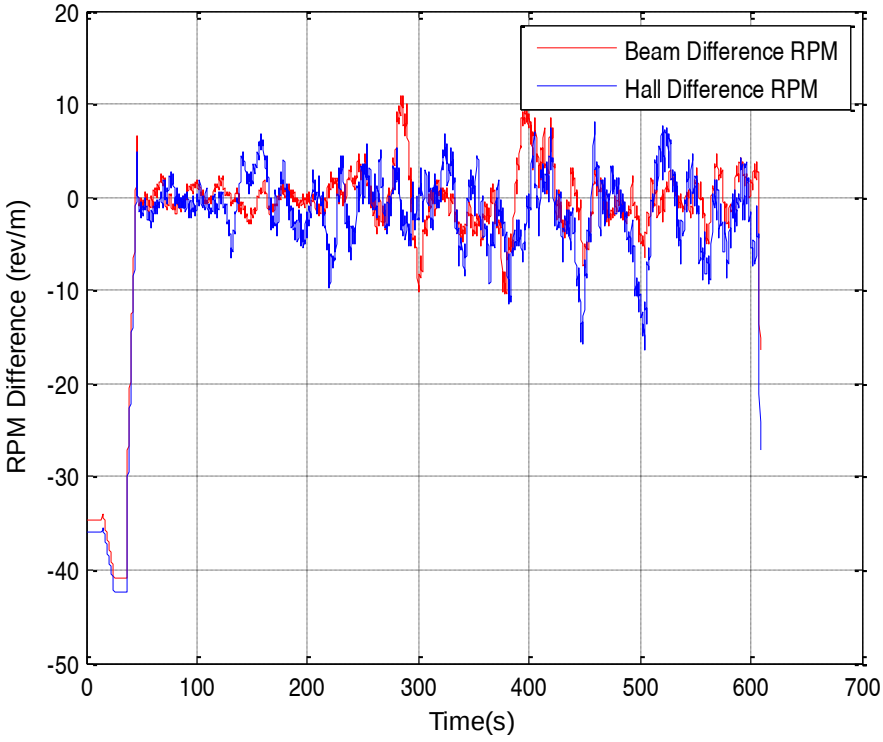

Figure 5.59: Variation in the sensor rpm's with respect to the Encoder rpm (Aeolian 1000KV).

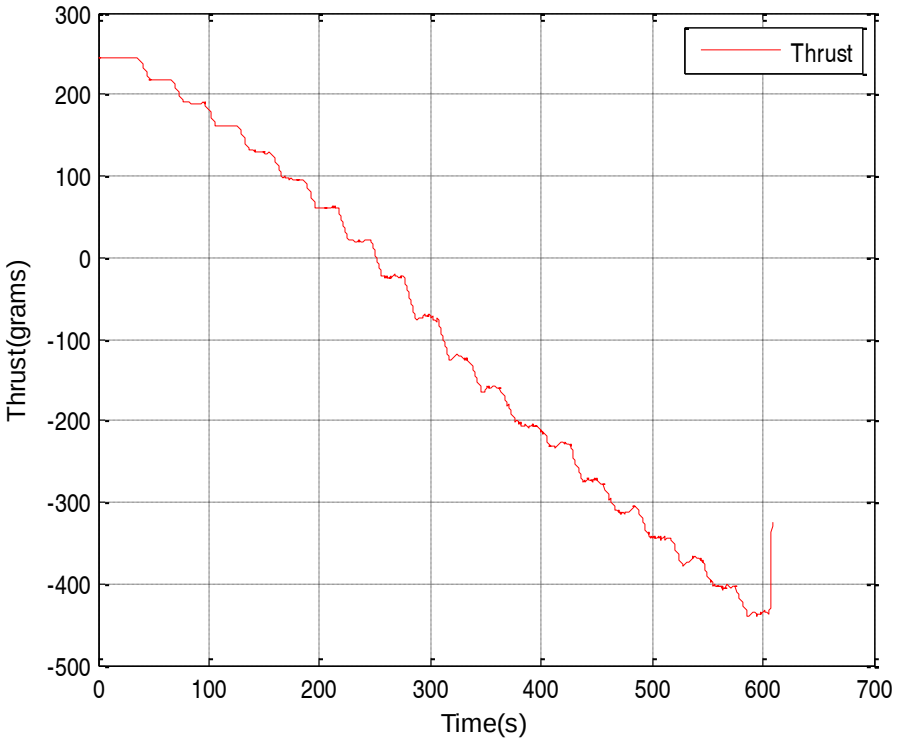

Figure 5.60: Thrust variation with PWM signal (Aeolian 1000KVA).

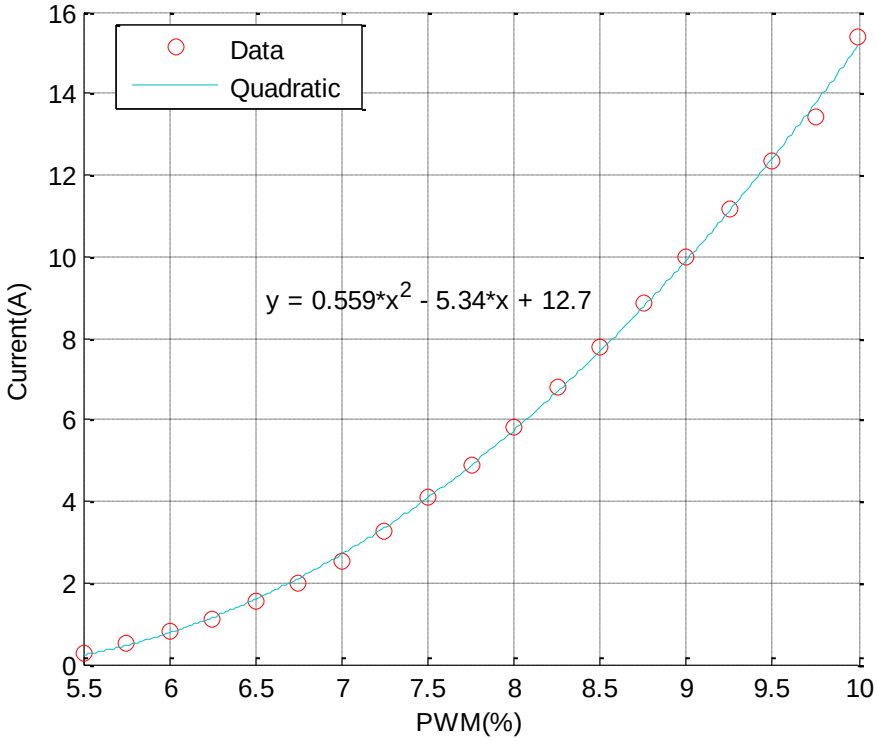

Figure 5.61: Variation in the sensor rpm's with current draw (Aeolian 1000KV).

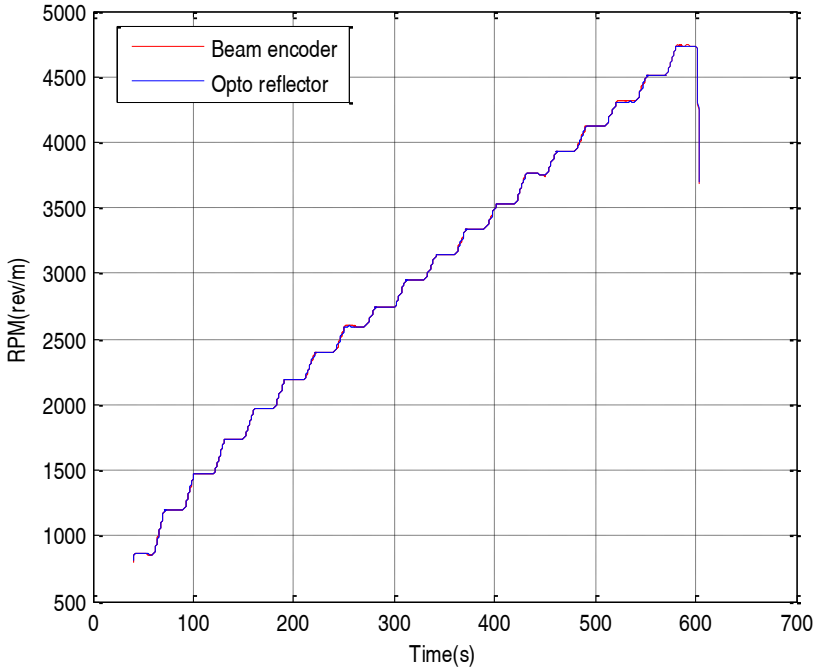

Figure 5.62: Beam IR encoder and photo-reflective encoder for 12x4.5" blade.

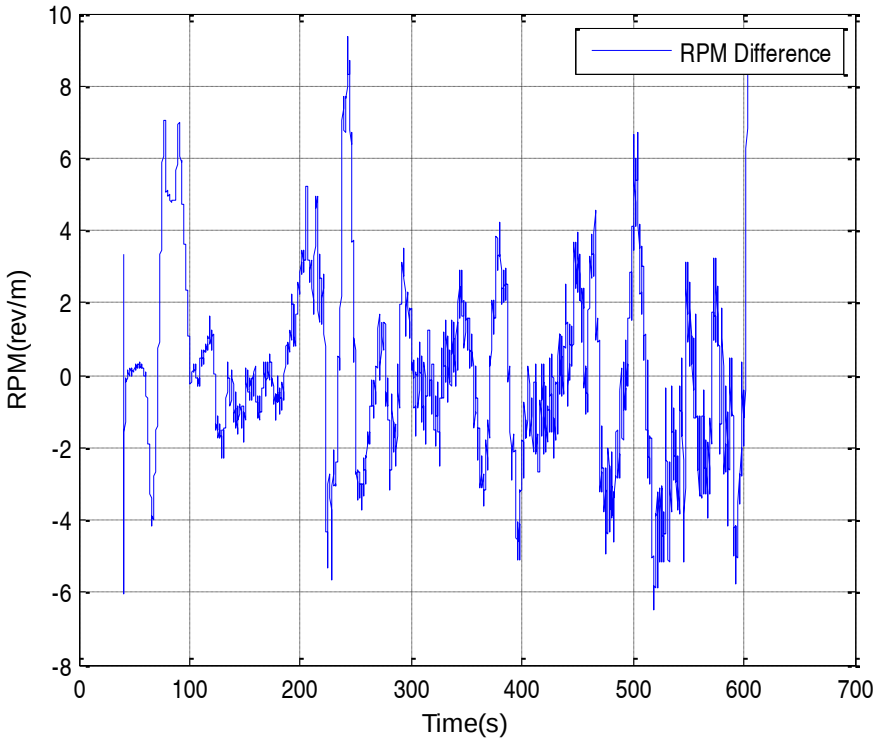

Figure 5.63: Difference in IR beam and opto-RPM apparatus for 12X4.5" blade.

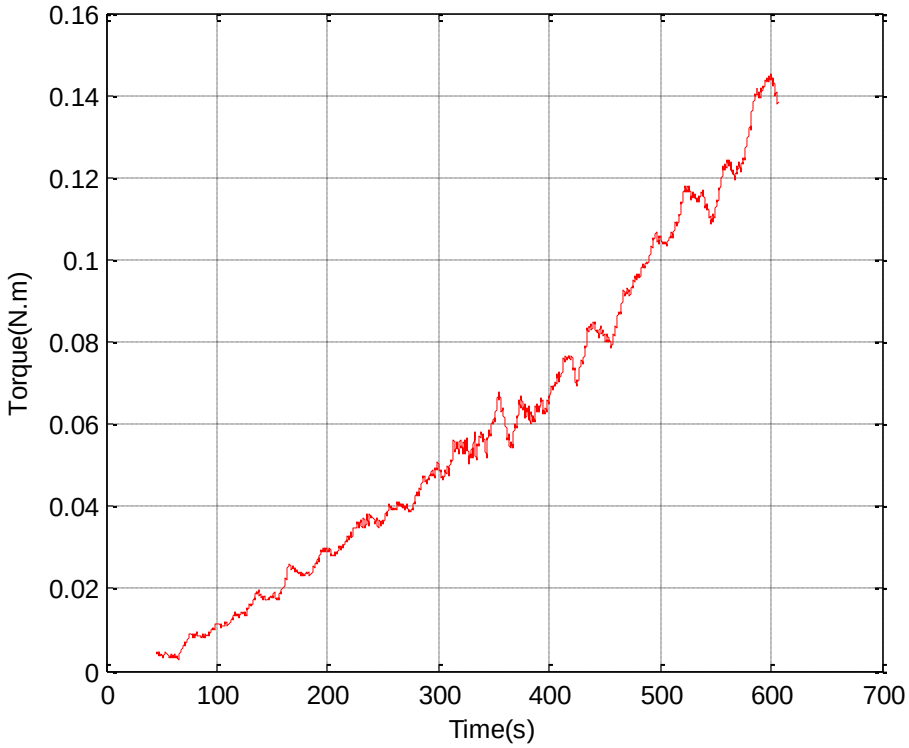

Figure 5.64: Variation in the motor torque with PWM input (11x4.7" blade).

5.7.3 Data Processing and Parameter Estimation

Data processing is needed to characterise the curves for easy integration into the mathematical model of the Quadcopter. It forms an important part of the identification process and stringent protocol must be adhered to as to maintain as much control over the manipulation of data. Data processing in itself due to the erratic nature of data is a very cumbersome process. Standardised as opposed to a manual data set processing eliminates any inconsistencies and a standardised protocol involves a set of procedures adhering consistently to specified limits. Prior to flow charting this process, a manual approach was taken in order to ascertain the difficulties involved. The manual data processing revealed the following problems and features:

- RPM values near steady state were in some cases very erratic
- Post steady state the RPM values are ramped up by a 0.25% PWM signal making the isolation and differentiation between plateaus and rises very difficult
- Large data sets of between 5000-6000 data points are tedious to process manually whilst maintaining a stringent tolerance and constant data processing method
- Constant PWM allowed for constant RPM however had no direct relation to the RPM and thrust dataset
- The acceptability of constant RPM without a tolerance factor

To combat the above difficulties an algorithm was developed specifically for the apparatus set. It uses multiple shifts in the binary table to identify features that can be isolated and processed. A very brief outline of the algorithm will be described and an overview of the algorithm can be viewed in Figure 5.80. Figure 5.58 and Figure 5.60 illustrates a typical set of RPM and thrust curves that can be obtained from the use of the constructed apparatus. Applying the first filter to the original curve allows for the difference feature between consecutive RPM values to be established as seen in Figure 5.65. The following equation is used:

$$Filter1 = RPM_{n+1} - RPM_n \tag{5.60}$$

The second filter uses a logical IF Statement. The conditions being:

$$if\ Filter1 > Threshold \tag{5.61}$$

$$Filter2 = 0$$

$$else\ Filter2 = 1$$

$$end$$

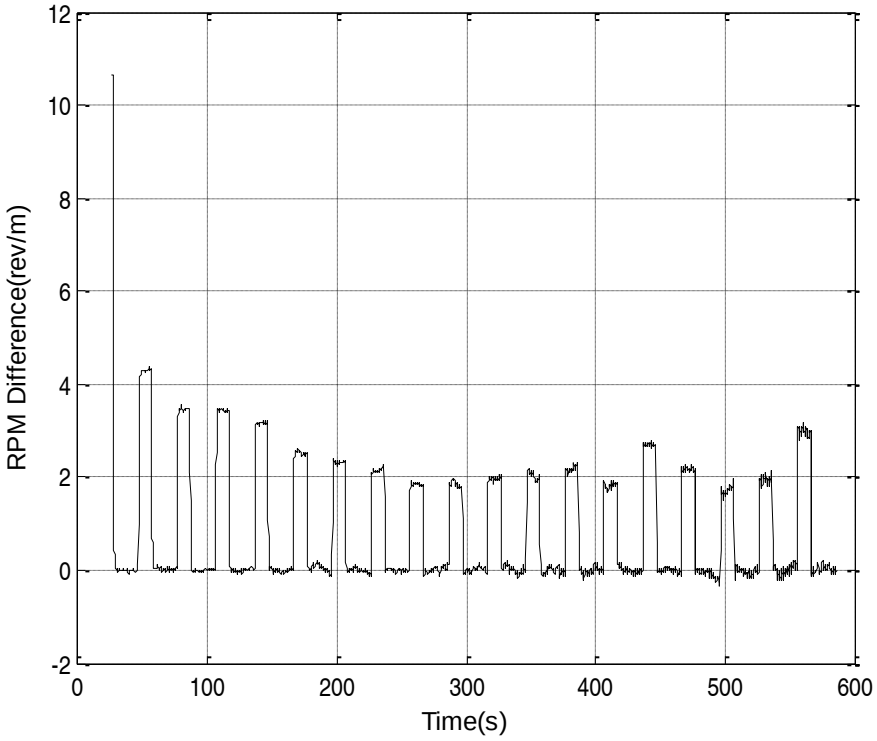

Figure 5.65: RPM difference filter applied to the RPM time curve

The threshold value represents the amplitude of the highest RPM plateau difference. The logical high allows for all the RPM ramp sectors to be masked leaving the troughs. The creation of Filter 2 is indicated by the red outline in Figure 5.66. Filter 2 however has an inherent flaw, the rising and trailing edges intersect the data points. The intersection of the walls decreases the accuracy of the algorithm as this increases the average RPM value between a rising and a falling edge. The solution to this was the creation of filter 5 which is composed of two additional filters. The two filters(Filter 3 and 4) as illustrated by the lime green and blue boundaries in Figure 5.67 allow for a tolerance band to be added to the

inside of the rising and falling edges. Tolerance bands negate the unwanted rise and fall of the difference curve achieving a higher accuracy during averaging. The bands were created by the shifting of the original matrix (Filter 2). The magnitude in shifting is a user defined offset which shifts the matrix in both directions but preserves the matrix dimension. This principle can be viewed in Figure 5.67 and Figure 5.68.

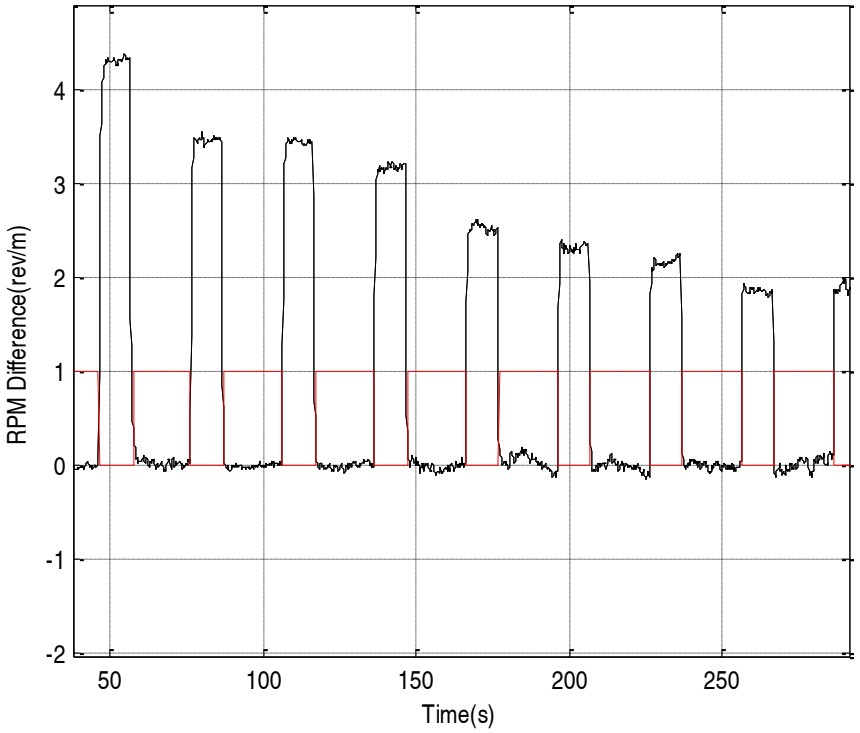

Figure 5.66: Binary filter 2 applied to the RPM difference curve.

Filter 6 allows for the location of the tolerate band initiation and termination points to be determined. Initiation and termination points were calculated using the location of -1 and+1 limits as seen in Figure 5.69 which is achieved by use of the following formulae:

$$Filter6 = Filter5_{n+1} - Filter5_n \tag{5.62}$$

Subsequently the matrix of -1 and +1 values are found using a lookup of the index values within the matrix. The index values of the filter 6 matrix allows for the location of the entries to be correlated to the original data set. This data set is then used for ascertaining the mean value between two data points. This is repeated for all 19 pairs of data. The

described process can be repeated for the thrust and time array and the subsequent results can be viewed in Figure 5.70 and Figure 5.71.

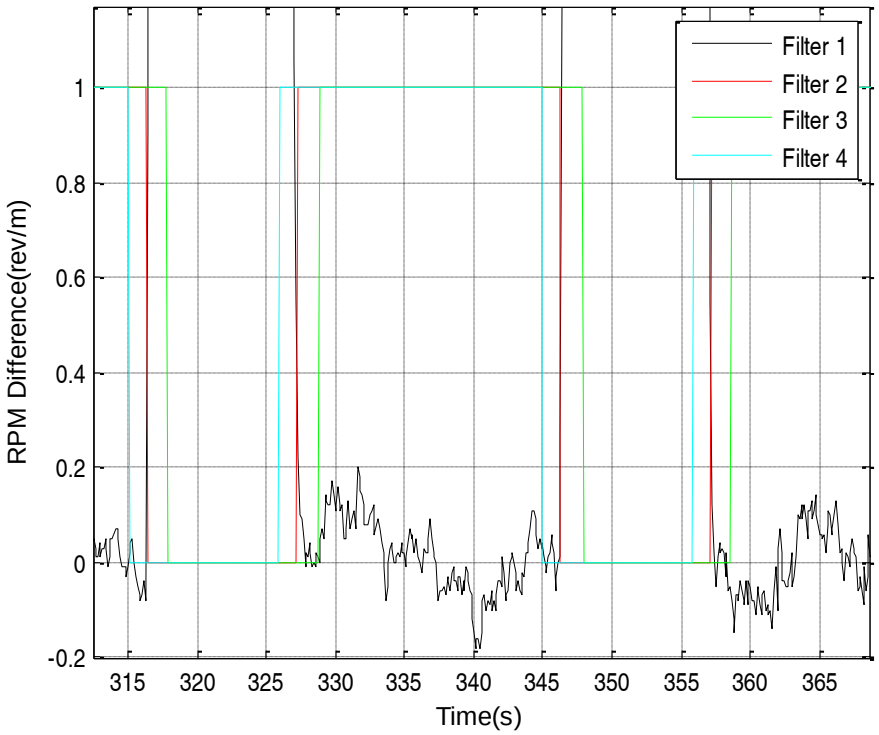

Figure 5.67: Binary filter 3 and 4 applied post difference filters.

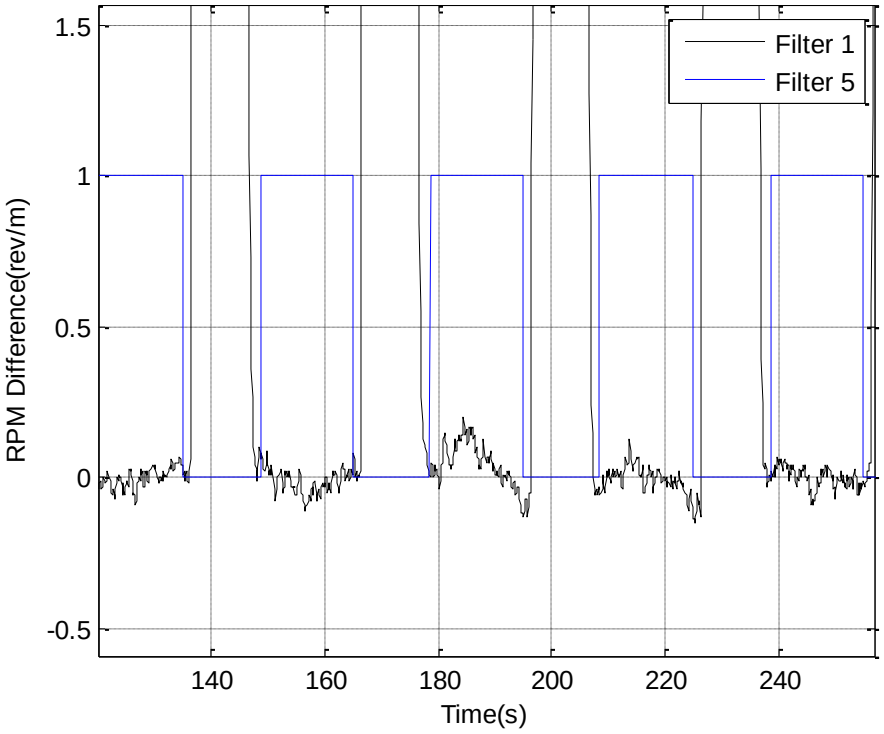

Figure 5.68: Binary filters 3 and 4 combined into a binary 5 filter.

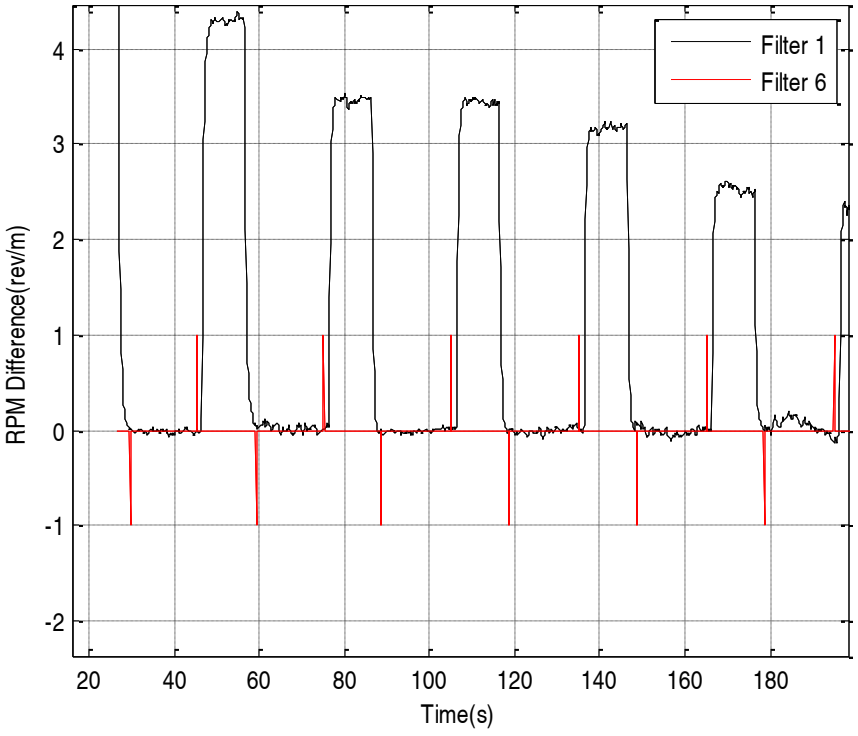

Figure 5.69: Binary Filter 6 for the isolation values (570KV-11X4.7" Prop).

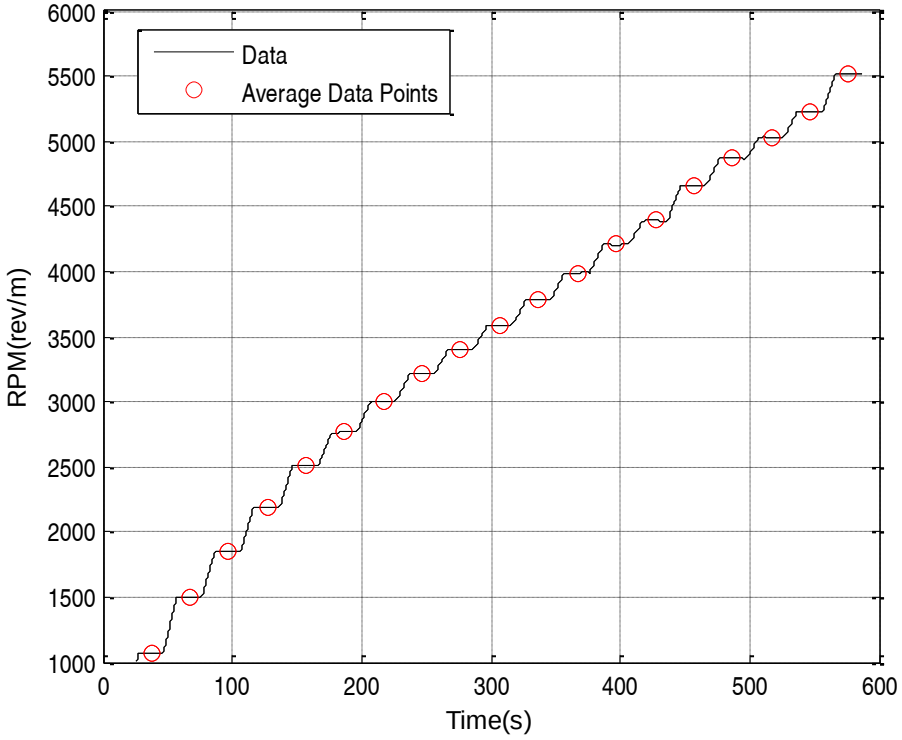

Figure 5.70: Average RPM data points for constant throttle plateau's (570KV-11X4.7" Prop).

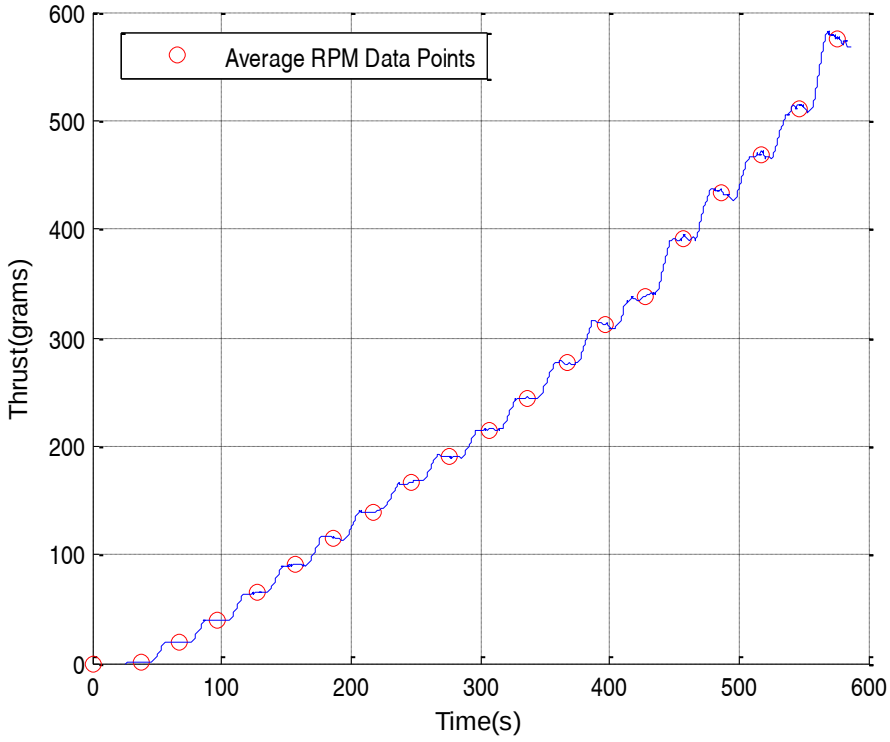

Figure 5.71: Average thrust data points for constant throttle plateau's (570KV-11X4.7" Prop).

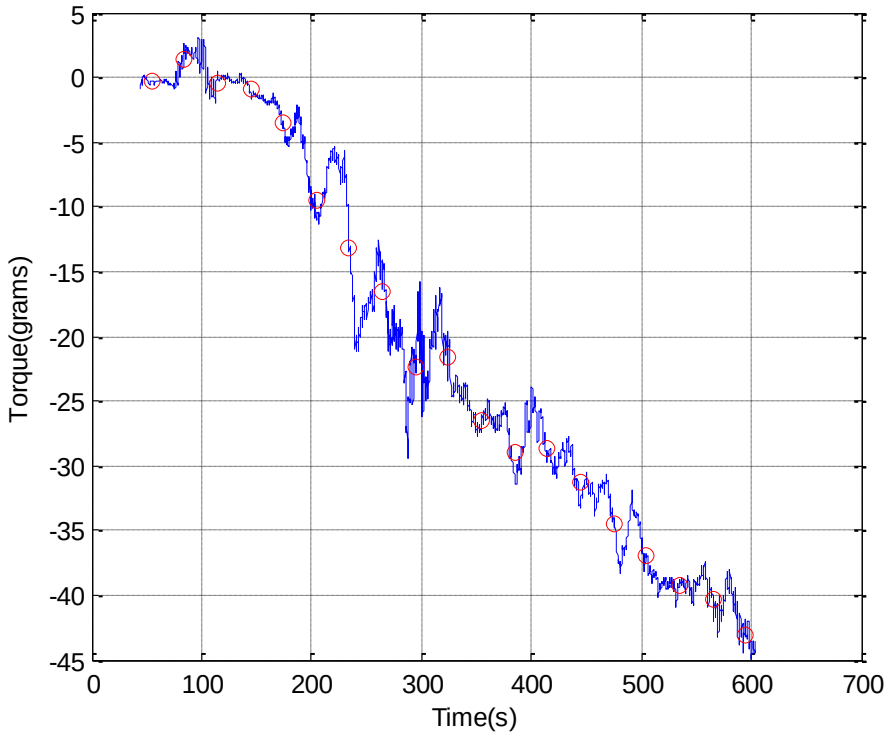

Figure 5.72: Average torque data points for constant throttle plateau's (570KV-11X4.7" Prop).

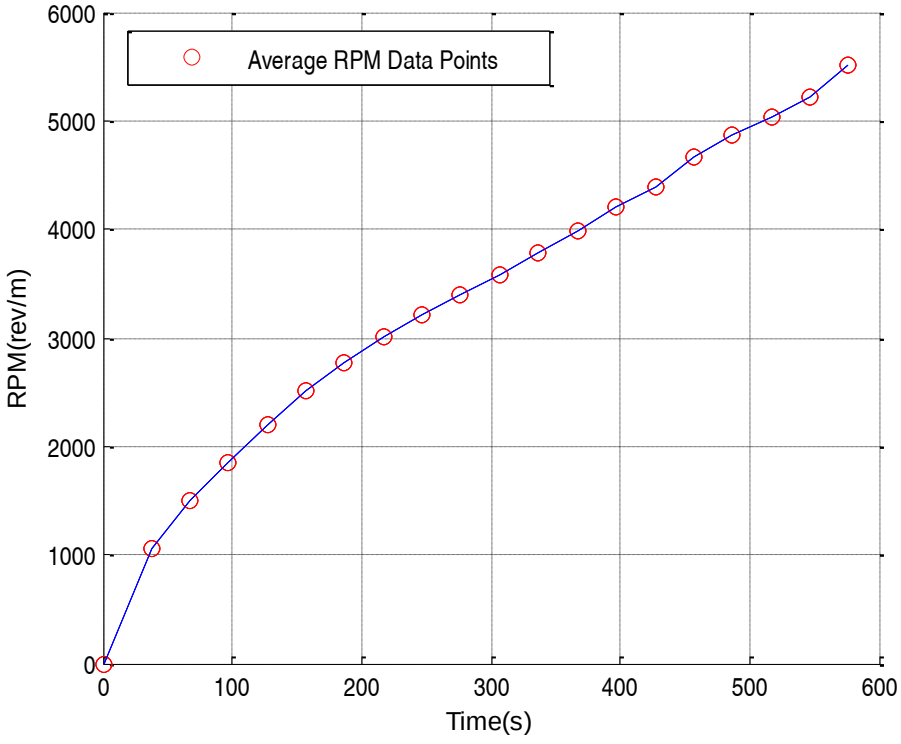

Figure 5.73: Average RPM values as a function of experimental time (570KV-11X4.7" Prop).

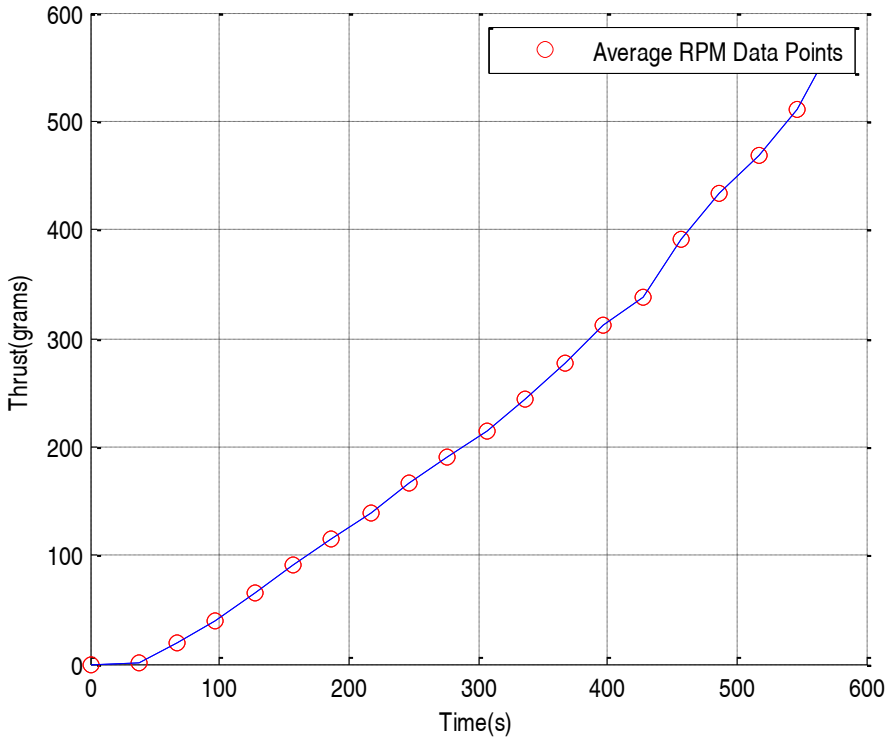

Figure 5.74: Average thrust values as a function of experimental time (570KV-11X4.7" Prop).

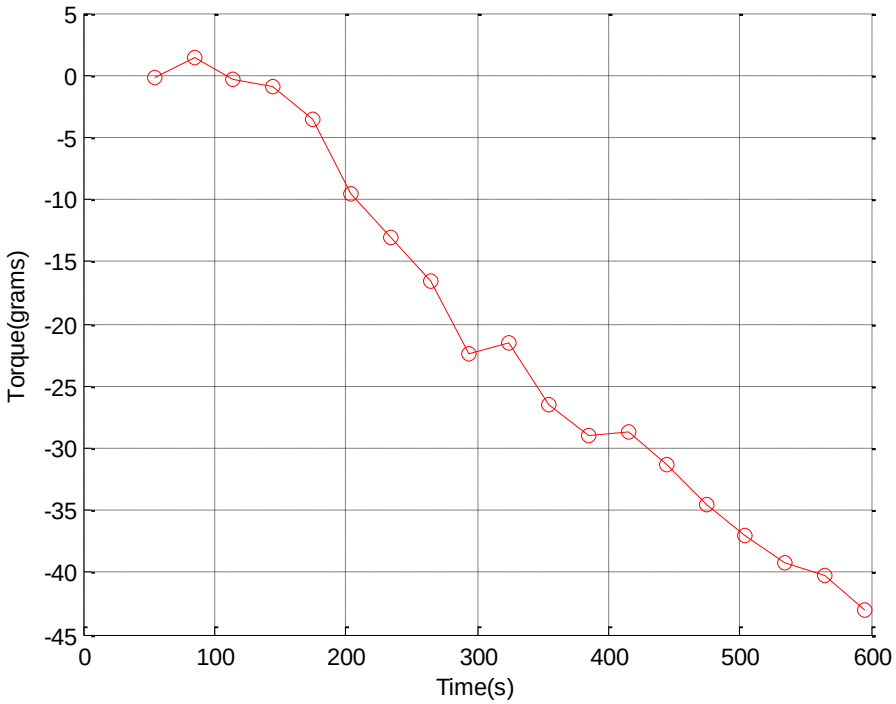

Figure 5.75: Average torque values as a function of experimental time (570KV-11X4.7" Prop).

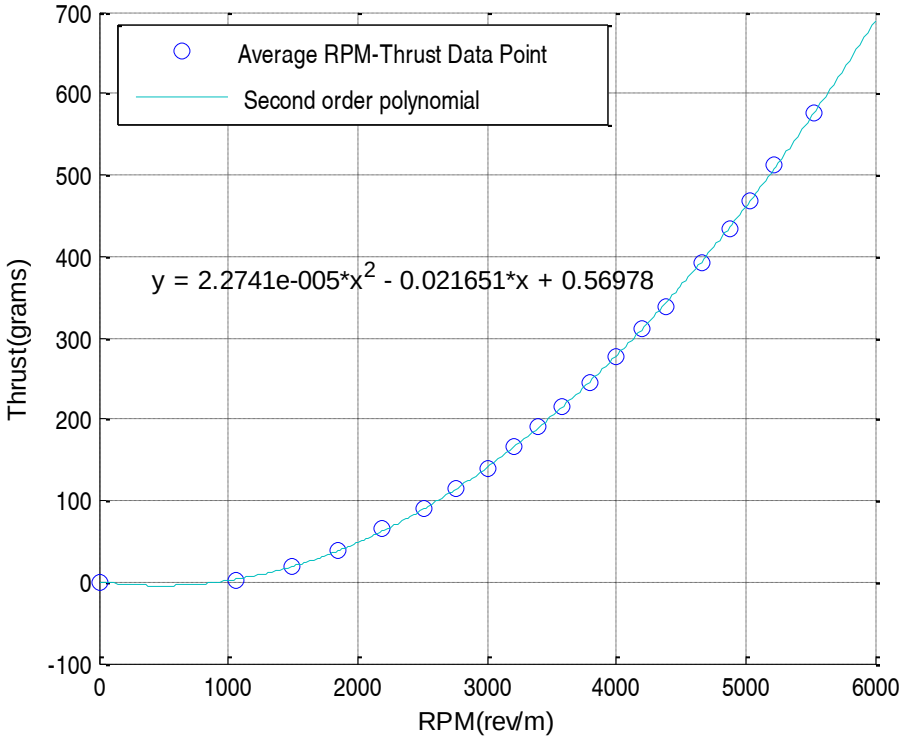

Figure 5.76: Thrust as a function of RPM for 570KV with an 11X4.7" prop.

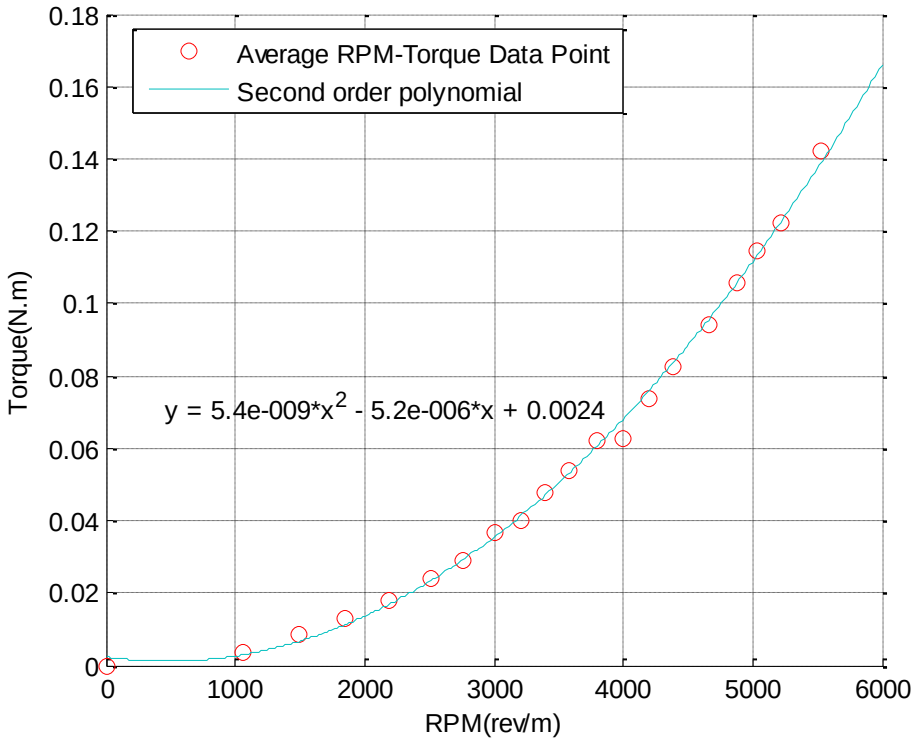

Figure 5.77: Second order polynomial for RPM vs torque for 570KV-11X4.7" prop.

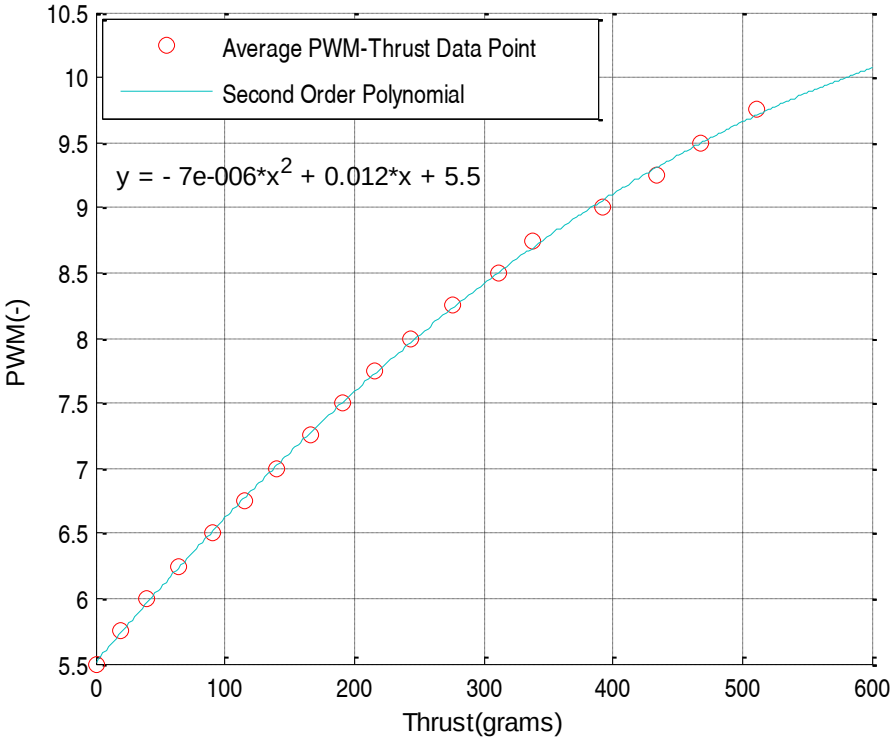

Figure 5.78: PWM vs Average Thrust for 570KV-11X4.7" prop.

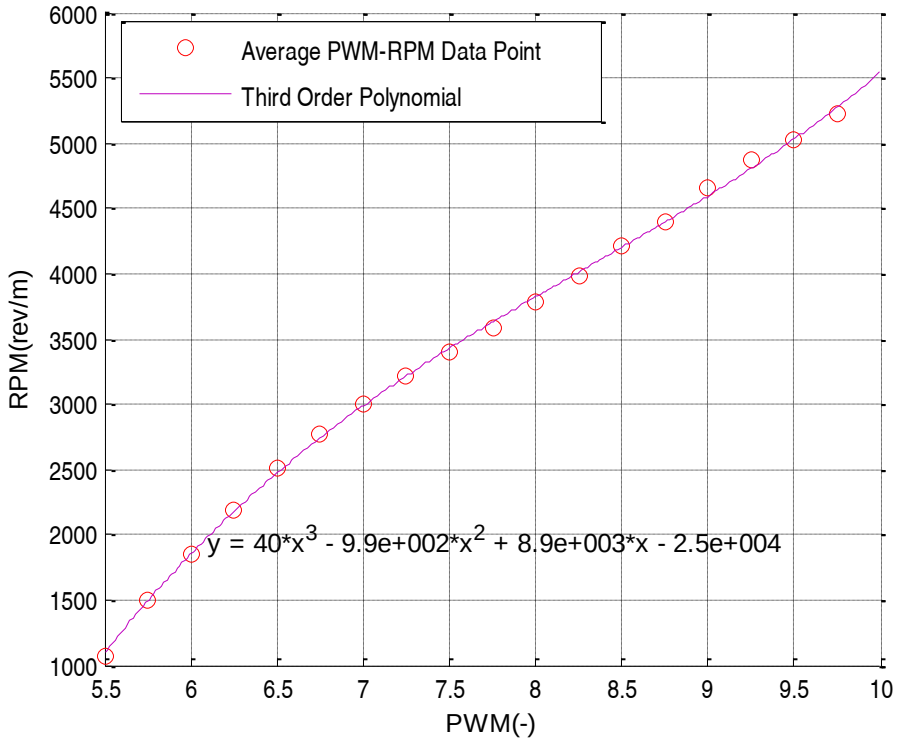

Figure 5.79: Third order polynomial for PWM vs RPM for 570KV-11X4.7" prop.

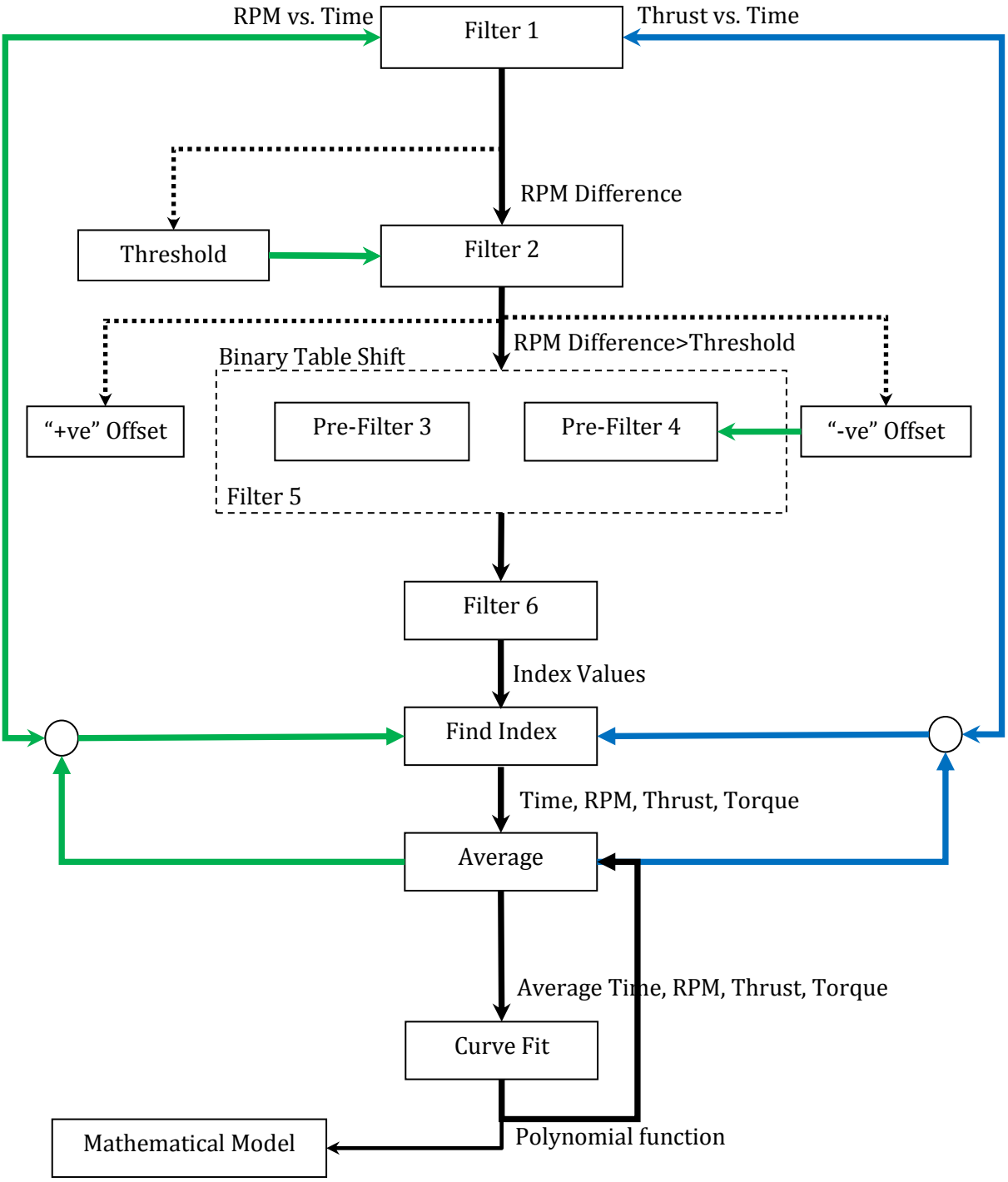

Figure 5.80: An overview of the created Binary Shift algorithm.

5.7.4 Problematic Data Patterns

The data process involved the isolation of defining features that drive the functioning of the algorithm. If the pattern that drives this system is absent as in Figure 5.85 then the basis on which the algorithm was built collapses. However factors such as threshold allow for the user to customize the features of the programming algorithm allowing for an adaptable solution. Figure 5.81 illustrates a data set where the threshold value was altered due to the erratic RPM difference pattern denoted by the red dashed circle.

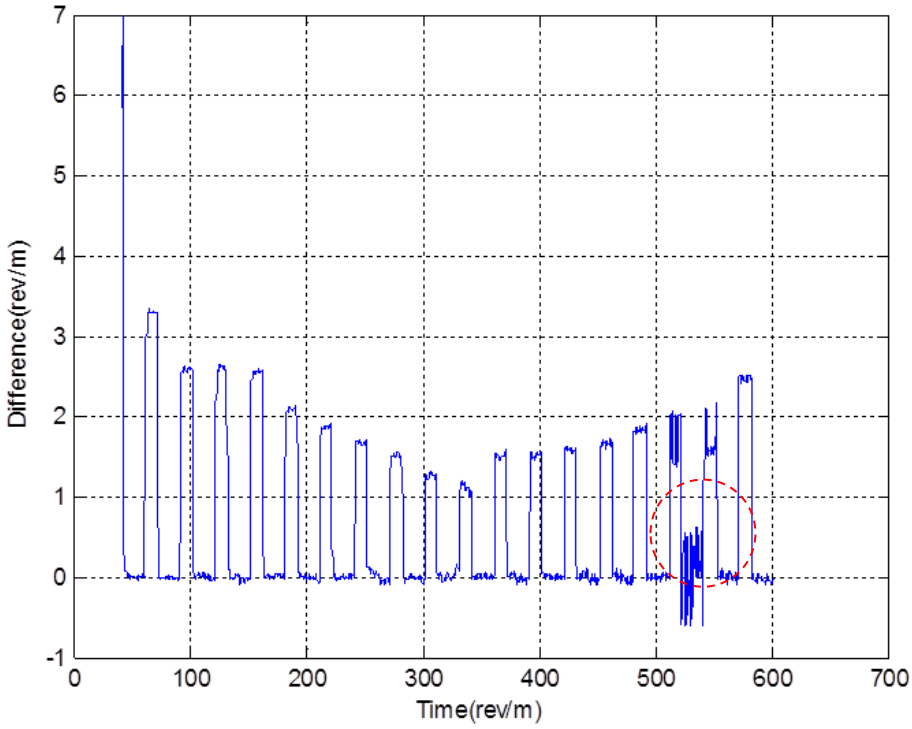

Figure 5.81: A problematic RPM difference curve data set.

Figure 5.82, Figure 5.83 and Figure 5.84 illustrate the distribution of points along each step change in RPM. A RPM tolerance band is defined as a user set quantity which classifies whether the difference signal attains a low or a high. The threshold value of 0.2 represents a lower RPM tolerance band whereas a threshold value of 1.2 represents a higher tolerance band. The distribution of points using a low tolerance band favors the lowest deviation inserting 3 red circles at a PWM value of 8 as seen in Figure 5.82. Increasing the threshold to a higher value inserts the majority of the circle at a lower threshold as seen in Figure

5.83. Using a method of trial and error with observation of the RPM difference curve and a threshold value of 0.7 allows an even distribution of circles along the scatter plot as seen in Figure 5.84.

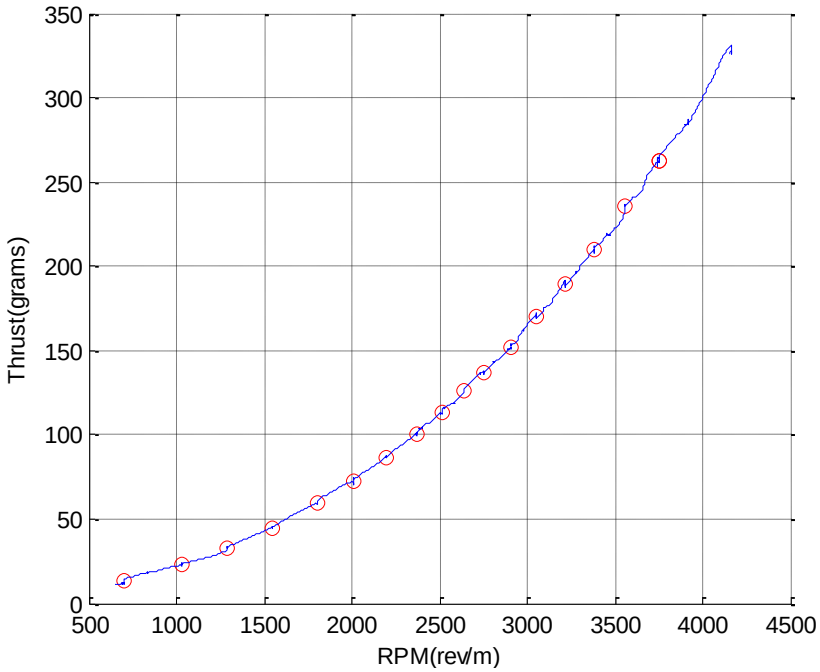

Figure 5.82: Plot of thrust vs RPM for a threshold value=0.2.

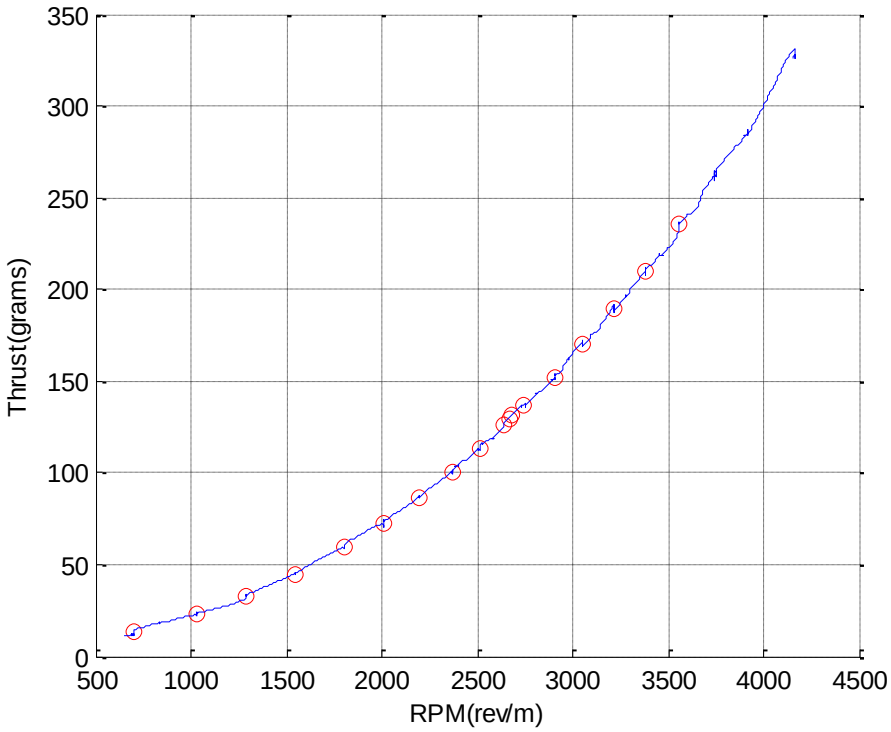

Figure 5.83: Plot of thrust vs RPM for a threshold value=1.2.

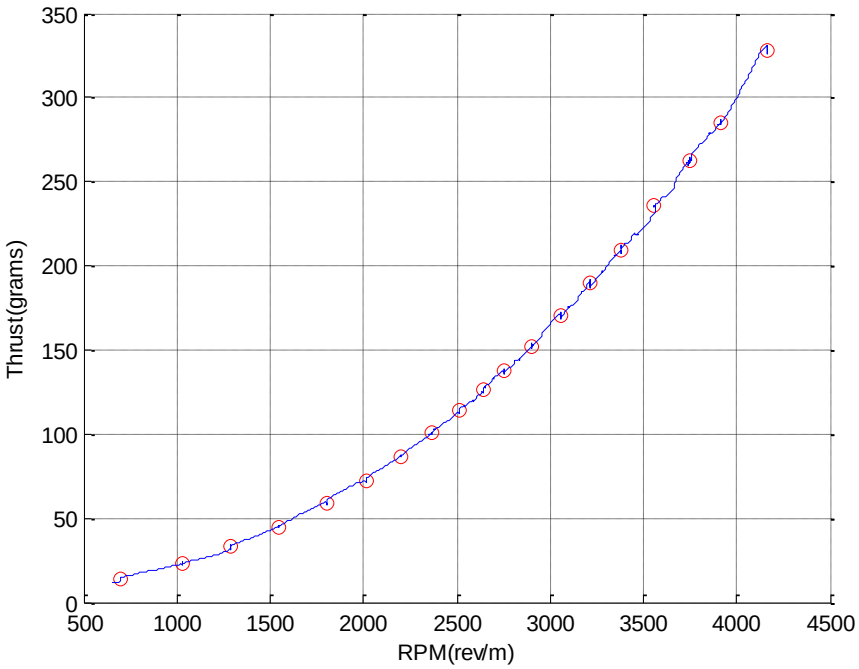

Figure 5.84: Plot of thrust vs RPM for a threshold value =0.7.

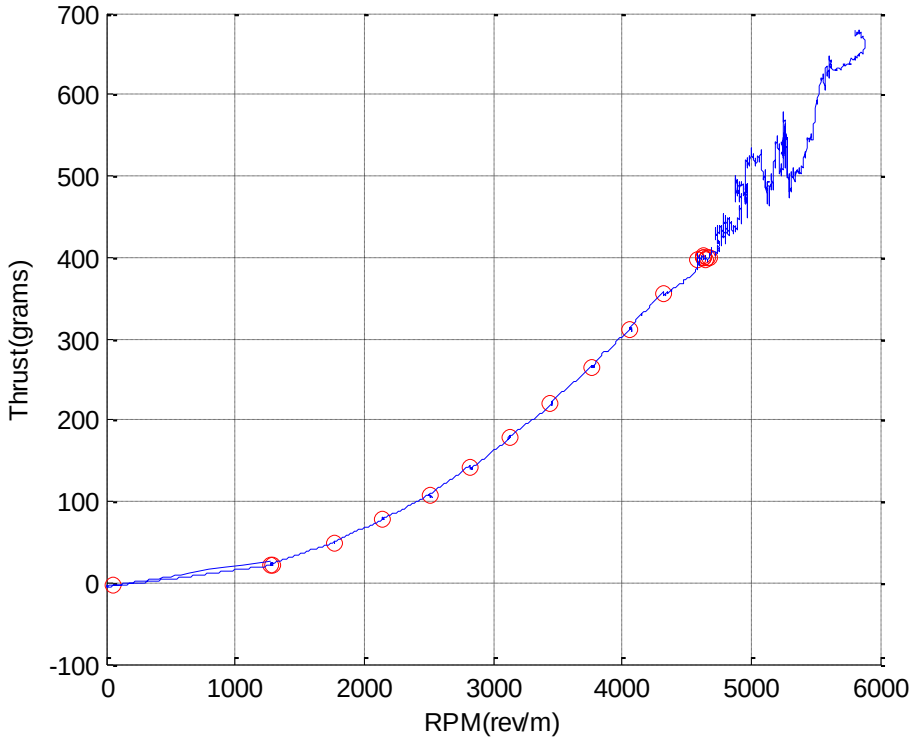

Figure 5.85 Plot of thrust vs RPM representing a data set that cannot be processed.

6. Identification Results

6.1 Motor Performance Results

Avoiding errors whilst maintaining consistency involved the collection of multiple data sets for each test run. Motor benchmarking involved the testing of 7 motors combined with 6 propeller types. The 7 motors ranged from 390KV to 1200KV. The 390KV, 490KV, 570KV and 690KV consisted of a 22 pole arrangement as opposed to the remaining 12 pole arrangement of the 850KV, 1000KV and 1250KV arrangements. The 850KV motor failed to function after two runs and was neglected from the testing schedule. The raw data that was collected for the variation in propeller type with motors are given in Appendix A. Each data set consisted of 6000 data points making the processing of these curves cumbersome. The developed algorithm allowed for the raw data points to be minimised to 19, each data point along a constant PWM step input. Figure 6.1 illustrates the reduction of data point through the data processing phase. The raw data consisted of torque, thrust, RPM and PWM all of functions of time.

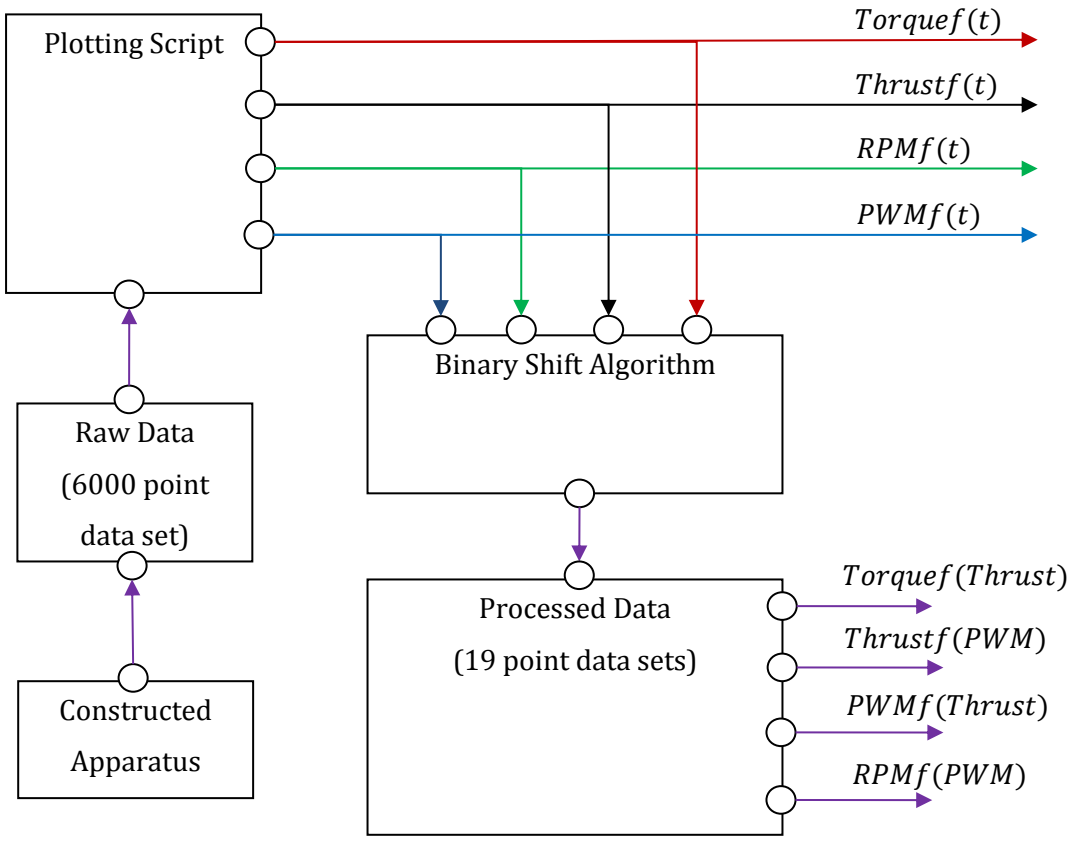

Figure 6.1: Overview the data processing and presentation process.

The two quantities that are of main interest during motor selection:

1. Current consumed by the motor
2. Maximum thrust value

The variation in the above quantities with motor and propeller type can be viewed in Figure 6.2 and Figure 6.3 respectively. The figures indicate that the smaller KV motors produce less thrust than the higher KV counterparts and also consumes less current. The highest thrust value of 675 grams was produced by the 1000KV motor combined with a 11x4.5" blade drawing 15.64 amps of current.

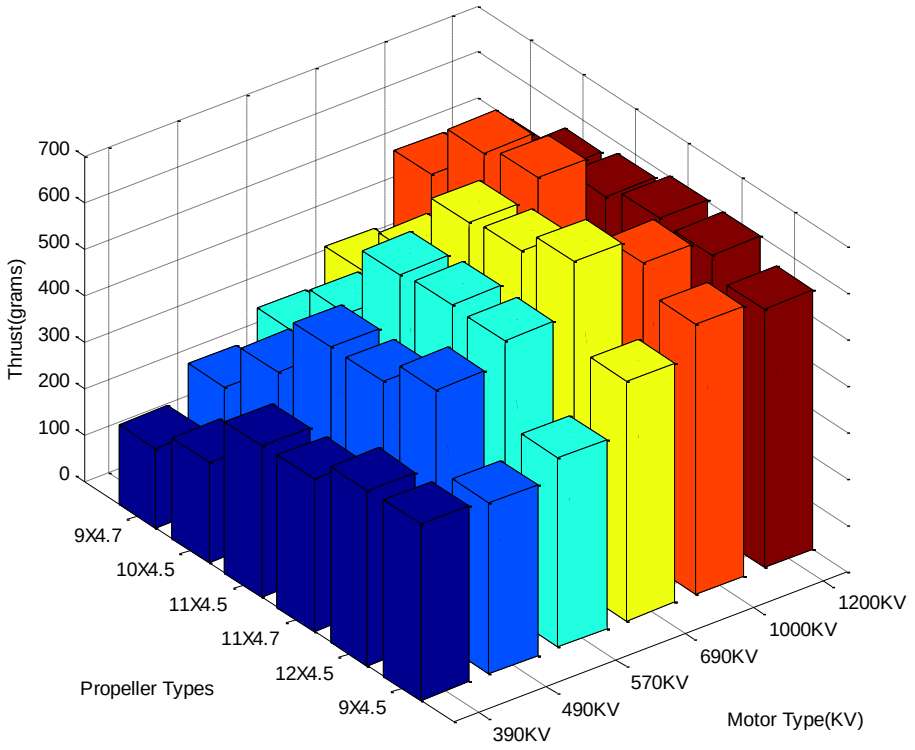

Figure 6.2: Thrust variation for all test runs.

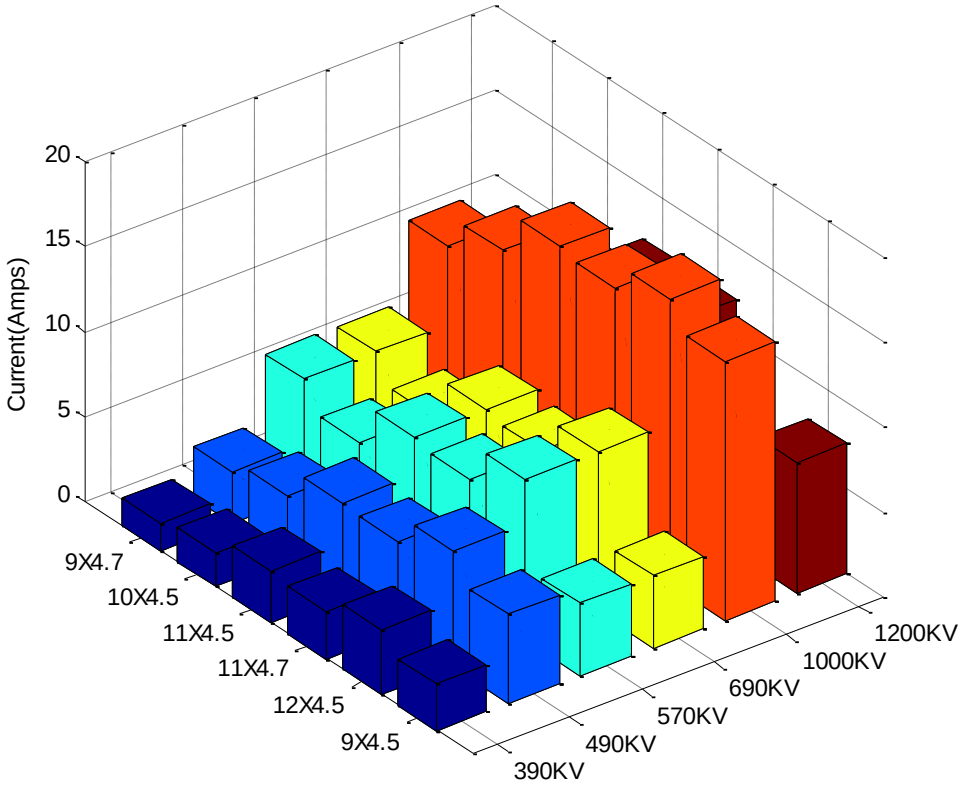

Figure 6.3: Current variation for all test runs.

The lowest thrust value of 171 grams was produced by the 390KV motor combined with a 9x4.7" blade drawing 1.61A of current. The above mentioned motors set the upper and lower limit for performance and endurance however a compromise between the two criteria are essential. A solution that satisfies both criteria can be found by studying the effect of current and thrust jointly. Figure 6.4 was created by dividing the maximum thrust produced by each motor with the current consumption at the recorded thrust value (Equation 6.1).

$$Efficiency = \frac{Max\ Thrust}{Current} \tag{6.1}$$

In a physical sense this translates to the amount of thrust produced by the motor in grams per unit amp. This can be interpreted as the efficiency of the motor, as the current drawn by the motor can be considered as an input and the thrust generated by the powerplant as an output.

Figure 6.4 illustrates the variation in the thrust per unit current with propeller and motor type. The absence of a result for the 12x4.5" propeller combination with the 1200KV motor is a result of the inability of the motor to turn the larger diameter propeller. The lower KV motors produce more torque due to the higher pole count allowing for a higher starting torque overcoming the higher inertia value of larger blade diameters. Further assessing Figure 6.4, it can be deduced that the highest conversion of current to thrust increases with the decrease in motor KV. This is represented by the higher dark blue and light blue peaks of the 390KV and 490KV motors. The 390KV motor combined with the 9x4.5" 3 blade propeller produces the highest ratio of thrust to current and would be the motor of choice but does have a limitation. The highest thrust to current ratio does not imply a higher overall thrust in the numerator of the ratio (see equation 6.1) but can imply a smaller denominator creating a larger value and in the case of the 390KV motor the maximum thrust is the lowest of all the motors. In order to overcome this problem, a proposed mass of the quadrotor(1.3kg) was used. Additionally during ascend and forward flight a resultant thrust is needed to overcome the weight of the UAV and still have the additional capacity to accelerate the craft. In order for this requirement to be met the maximum thrust needed was set to 19.62N(2g).

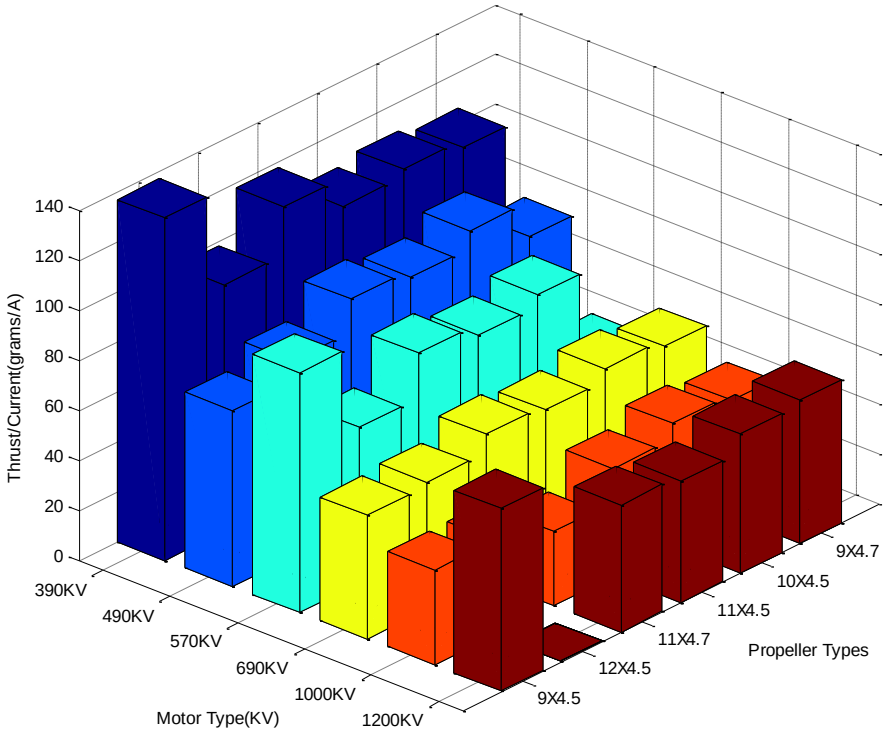

Figure 6.4: Comparative analysis of all tested motors.

Table 9 illustrates the variation of model mass as a function of motor efficiency (thrust per a unit current). Maximum model mass is the maximum mass that can be sustained in hover flight. It can be noted that irrespective of the blade type, the motor type as a function of maximum thrust was of interest to establish the grouping of data points. Hover flight as defined in section 2.9.2 constitutes force equilibrium. This implies that each point in the graph is only able to sustain hover and no residual thrust is available to provide a resultant force which is the mechanism of translation in all planes. If we multiply the y-axis by gravity this translates to the maximum thrust that can be produced by each motor. It can be noted that the 390KV and 490KV motors as opposed to the remaining motors sustain lower model masses however constitute the higher efficiencies. It can also be established that the more efficient motors are unable to sustain higher model masses whereas the lower efficiency, higher KV motors sustain larger model masses however based on the above observations, the excess energy required to create acceleration cannot be concluded. In order for this to be concluded Table 8 was created. Table 8 uses mass figures obtained from the mathematical modelling process and depicts the variation of the battery capacity with battery cell number and total model mass.

Table 8: Quadrotor total mass variation with battery capacity

Item	Total Mass of Quadrotor(kg)	Capacity(mAh)
Model mass (Excluding battery)	0.774	-
Model mass+1xBattery (1x3 cell)	1.174	4400
Model mass+2xBattery (2x3 cell)	1.574	8800
Model mass+3xBattery (3x3 cell)	1.974	13200

The resultant force for each motor was calculated using equation 2.91 with the improvement in battery capacity. This was done for all the blade types and all the motors and the results can be viewed in Appendix-A. Table 9 was used to generate the variations in the performance parameters with the battery capacity and propeller combinations using the 570KV motor. The 570 KV motor with the 11x4.7" propeller was selected due to the high efficiency and endurance as shown in Table 9 for the one, two and three battery cell setups respectively. It may be noted that the flight endurance quoted is the absolute worst case scenario as the calculations were based on the maximum thrust that can be produced by the motors at which current consumption at maximum thrust is exceeds all other values. Using Table 9 a general trend can be established that the addition of added battery cells increases flight time and decreases the surplus energy required to manoeuvre as the available thrust above sustained hover decreases.

Table 9: Variation in performance parameters with propeller and battery combinations.

	$\frac{Thrust}{Current\ Draw}$*[N/A]*	**Resultant Force*[N]***	Battery 1(4400mah)	**Flight Time*[min]***	Battery 2(8800mah)	**Flight Time*[min]***	Battery 3(13200mah)	**Flight Time*[min]***
9x4.7	0.4	0.5		9.6		19.3		28.9
10x4.5	0.8	5.0		12.6		25.2		37.8
11x4.5	0.7	11.2		8.6		17.2		25.8
11x4.7	0.8	11.6		9.0		18.0		27.0
12x4.5	0.6	11.5		7.0		14.0		21.0
9x4.5	0.9	4.5		15.5		31.1		46.6

7. Simulation Model

A six degree-of-freedom (DOF) mathematical model with the inclusion of drag was developed. The drag aspect is not very well documented and recognized in literature, and has been documented in this dissertation with the aim of specifically creating a comprehensive computer based model. The six DOF system adopted for aircraft was developed and modified to capture majority of the quadrotor system dynamics.
The main purposes of the model can be stated as:

1. The ability to perform system identification.

2. The ability to predict performance.

3. The ability to optimize the system through changes in geometry.

4. Aiding the design of the controller prior to hardware implementation.

The computer-based model realized in the Simulink environment allows for transparent graphical interfaces and various computational tools and parameters. In order for a clear and comprehensible model structure, the Simulink environment permits the main model to

be split into sub-models, further emphasizing its mathematical superiority over other GUI based applications. This interface primarily allows for the changes in aerodynamic parameters, control inputs and geometry to be done and their effect on the flight path to be viewed. The flight path is viewed via the continuous plotting of the output position co-ordinates from the simulation. Aerodynamic parameters were computed based on the geometry of the quadrotor system.

7.1 Mathematical Model Overview

The mathematical model has been broken up into the input, plant and output as seen in Figure 7.1. The input serves as actuators consisting of PWM signals where each PWM signal is individually actuated via a constant, step function or ramp function. RPM, torque and thrust are coupled functions of the PWM signal as identified in sections 6.1. The plant consists of the equations of motion of the system which determine the attitude of the vehicle when excited by the input. The output is composed of 12 quantities, the body-fixed velocities, body-fixed angular rates, angular position with respect to the earth-fixed axes and the position of the quadrotor within the earth-fixed axes. This can be realised as a 12x1 matrix. A simulation time of 10-20s was used as it remained enough time to study the flight modes. Constants linked to the model are loaded via the “CONSTANTfinal.m” which must be run prior to the Simulink model being used. An ISA (International Standard Atmosphere) model was used in order to vary the density with altitude.

7.2 Quadrotor Plant

The plant model consists of the defining equations of the systems. The relationship between RPM and input PWM as shown in Figure 5.79 is used to establish the rotational speed of the rotors at a specific PWM input. This further translates into a thrust value for each motor, which is summed and used to calculate the moment exerted by the motors. Figure 5.77 exhibits the torque exerted by the motor on the frame which can be calculated using the RPM values. The computed moments and forces are then used to calculate the angular rotation and translational rates along the body fixed axis. Using transformations these are then converted to the rates in the earth fixed frame which are then integrated to a final form

of angular displacements and position in the earth fixed axis. Figure 2.3 represents the overall process from a mathematical point of view, whereas Figure 7.2 represents the modelling process in the SIMULINK environment. The body drag is modeled using a set of "IF" statements as previously discussed in section 2.6.4.2. The computation of the drag term was developed conceptually and had been implemented for the frame drag computation (see Figure 7.3). The decision block ascertains if the velocity in the body-fixed axis is a positive or negative value orientating the drag force vector in the opposing direction to translational velocity. This ensures that the drag vector is always in the opposite direction to the aircraft velocity vector and due to this reason it is used as a positive summation term in the equations of motion.

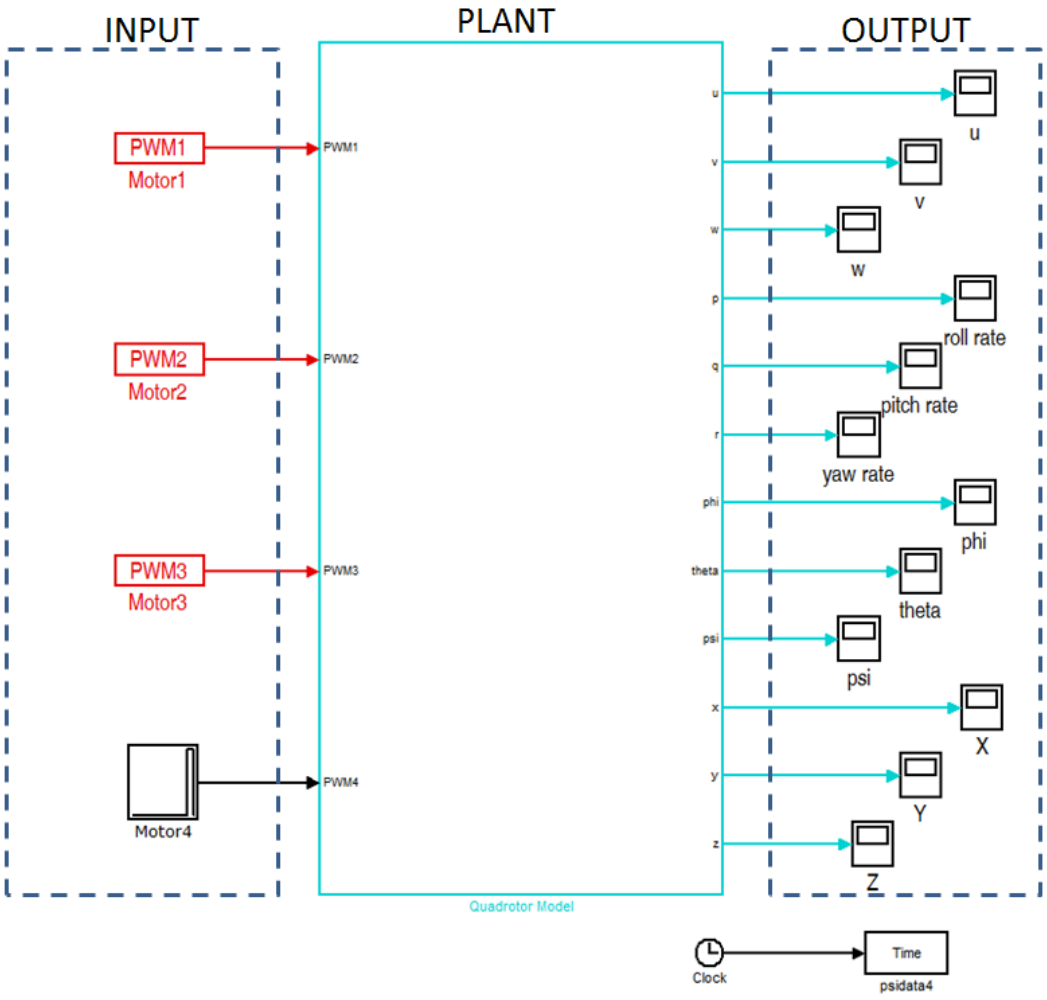

Figure 7.1: Simplified Simulink quadrotor motor representation.

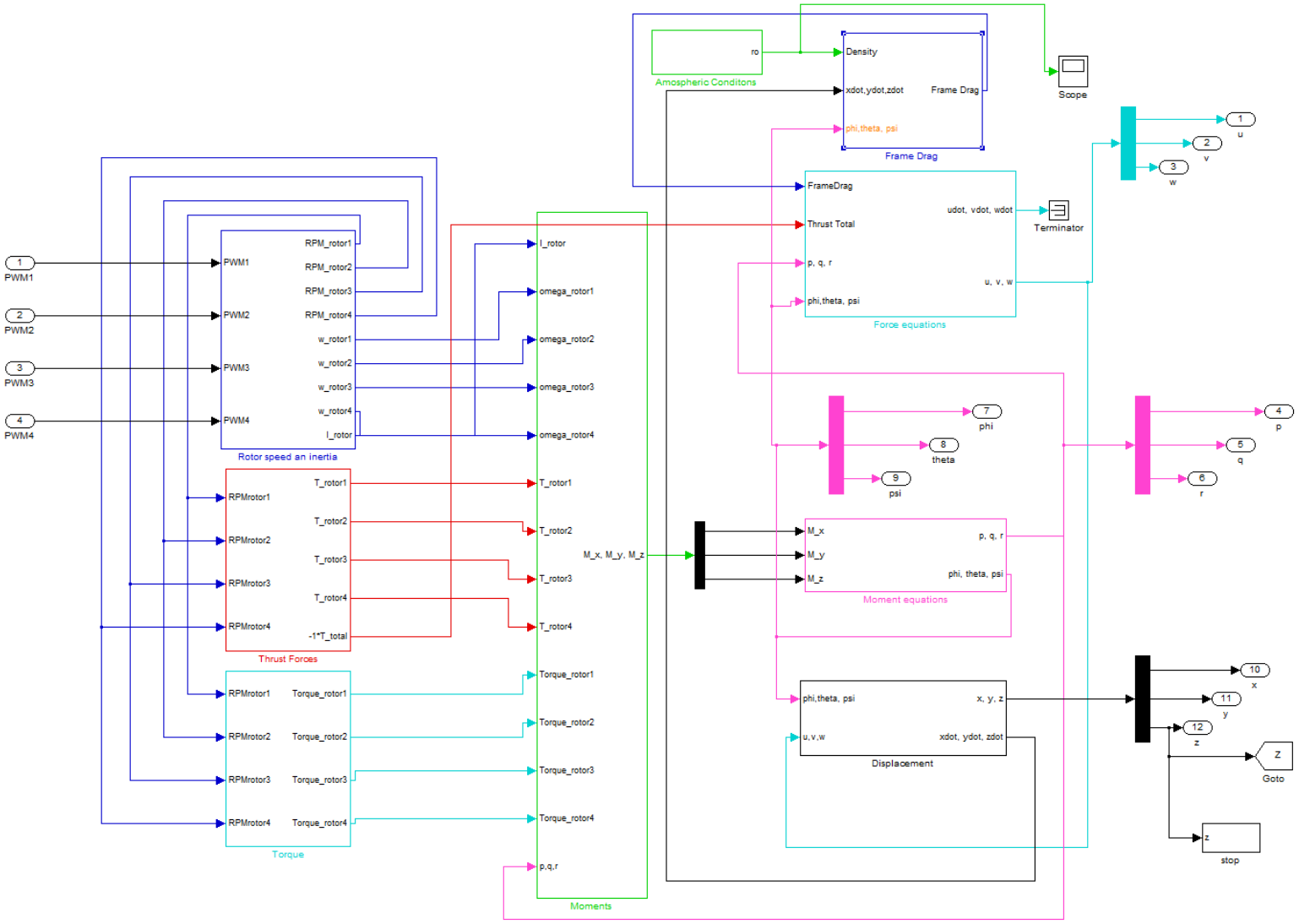

Figure 7.2: Expanded view of the plant model.

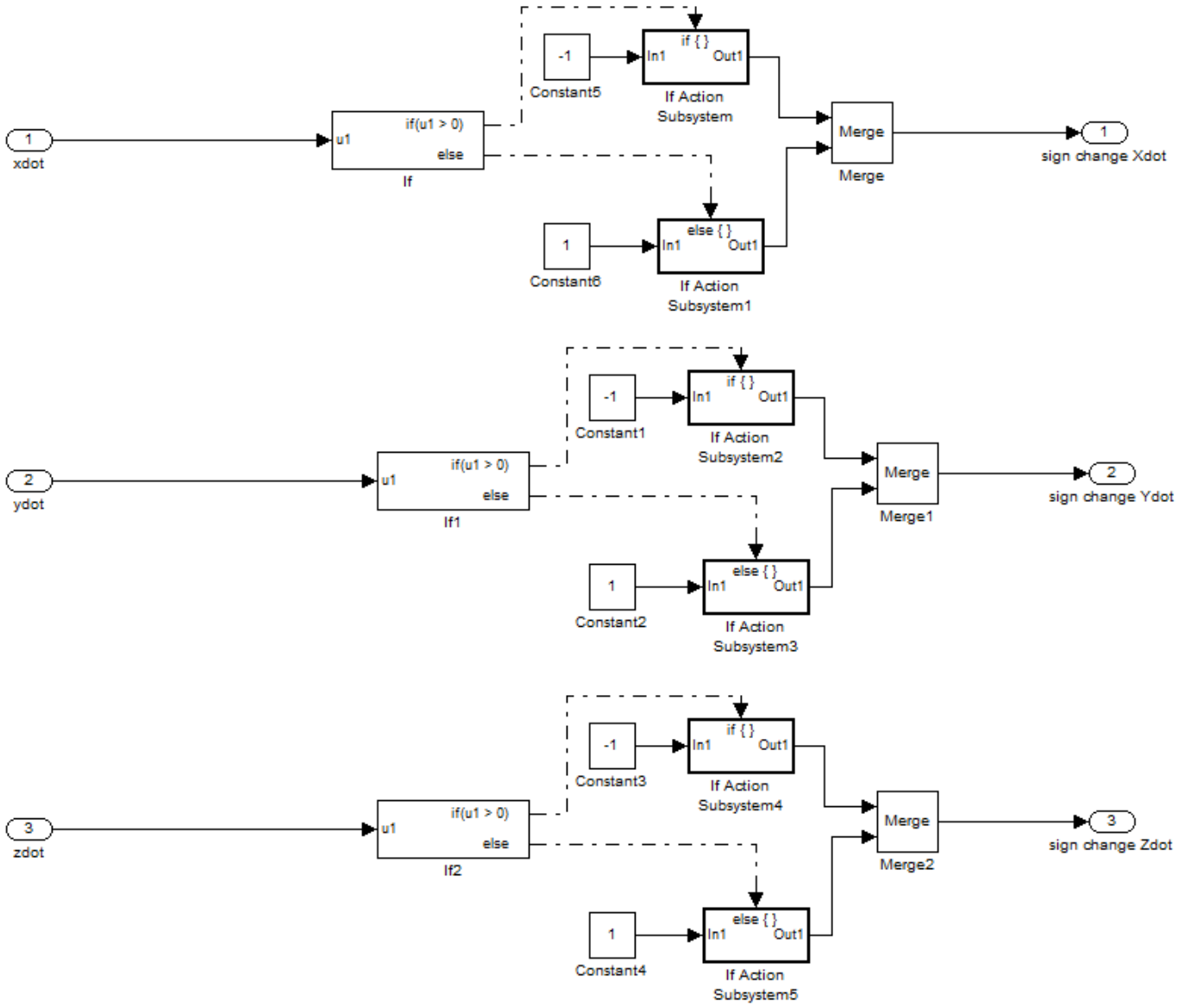

Figure 7.3: Decision blocks for the drag terms in the SIMULINK model.

7.3 Quadrotor Control Input

As specified in the MATLAB model, the state of the PWM signal plays a vital role in the quadrotor dynamics. It is for this reason that all control that will be developed in the future encompasses measuring the output then generating a stabilizing input. Rotor pairs 1 and 3,

2 and 4 with identical PWM values generate moments of equal magnitude and opposing in direction hence any variation from the null difference will induce instability. For the ascent and descent phases a constant throttle function was used, hover mode was attained using the PWM values calculated in the equilibrium analysis. The stability of the system was tested using a step input on PWM4 acting as a perturbation source (see Figure 7.4).

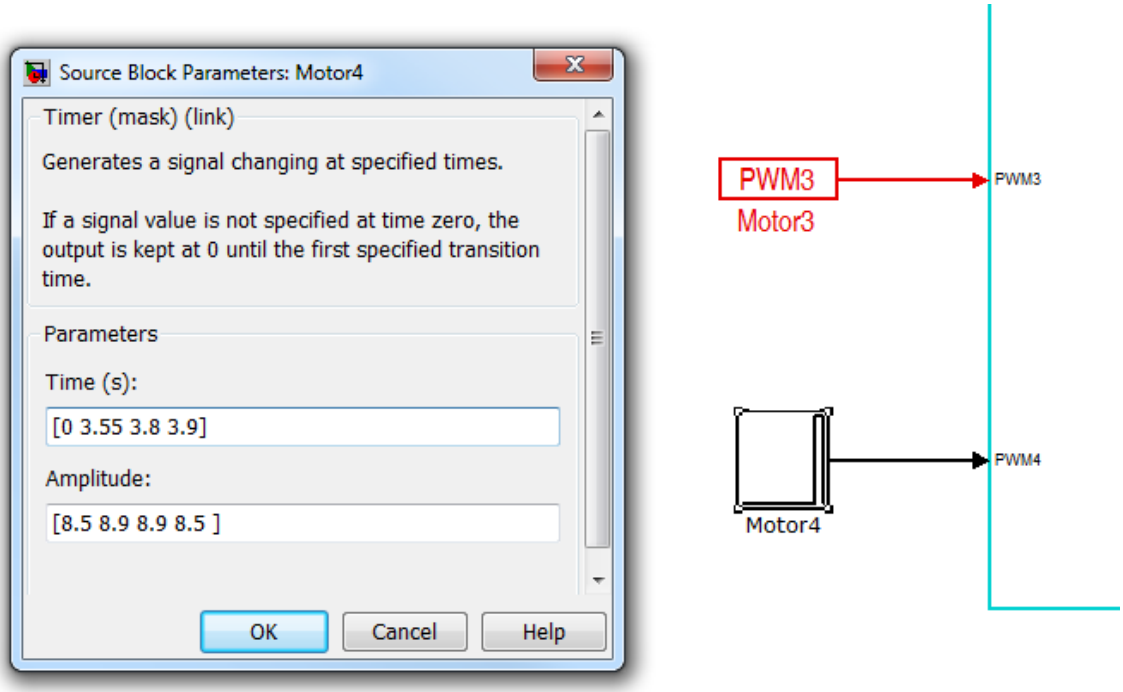

Figure 7.4: PWM actuator control as a step input (Matlab).

7.4 Simulink Results

The Simulink model used 4 different control inputs to generate 4 modes of flight (see Figure 2.16). Each mode exciting the vehicle dyanmics making for a quantifiable analysis on which stabilty can be jugdged. The state of the PWM signals, displacements, velocities and trajectories serve as visual reperesentation of essential telemetry that can be used to determine atitude.

7.4.1 Take-off/ Ascent Phase

The first control input consisted of a constant PWM mode in the ascent phase. To initiate a take off sequence the motors need to receive a PWM signal higher in magnitude than that at the equilibrium phase. A PWM signal of 8.5 was generated on each motor channel as seen in Figure 7.5. During the take off phase the quadrotor climbs 63m in 20s at a PWM input of 8.5 with the body fixed and earth fixed axis being aligned. The resultant force is a function of the thrust, weight of the quadrotor and drag force A null resultant force is the effect of the drag vector against the motion of the quadrotor which can be seen in Figure 7.7, where the translational velocity plateau's to a value of 4m/s implying a constant velocity. Angular rates and displacements (seen in Figure 7.8 and Figure 7.9) are null due to a balance in moments generated by each pair of thrust forces and a singular resultant force along the z-axis of the earth. Figure 7.10 illustrates the take-off trajectory on the earth fixed axis. These results ascertain the functioning of the model with emphasis being placed on themdrag component in each direction. Take-off was initiated from sea level.

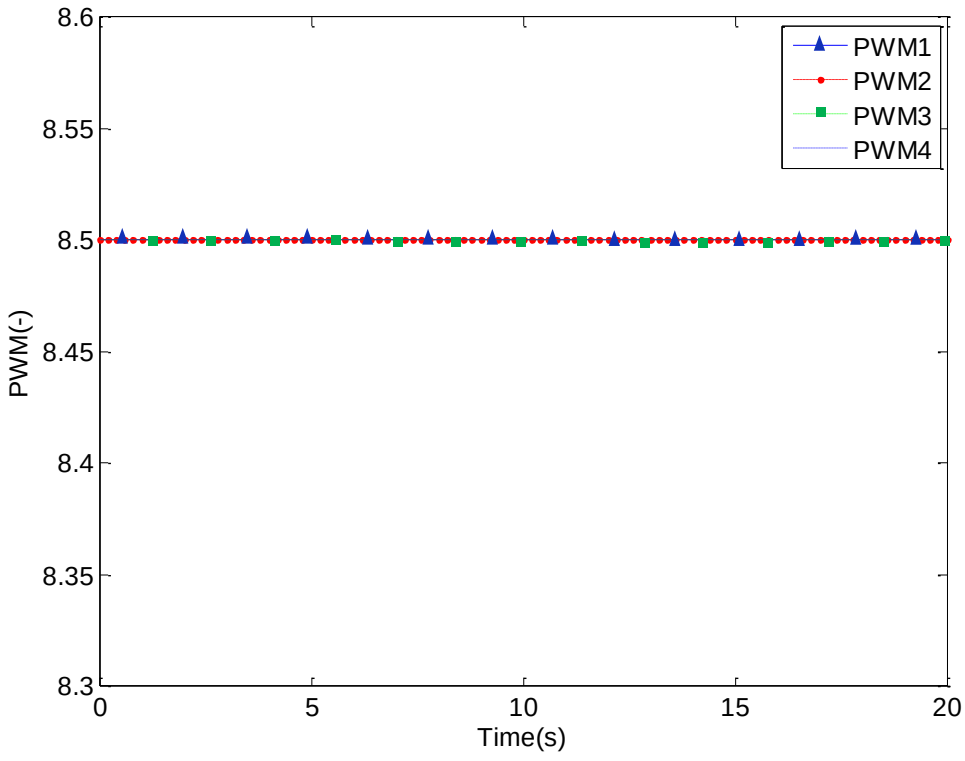

Figure 7.5: PWM signal for all motors during the ascent phase.

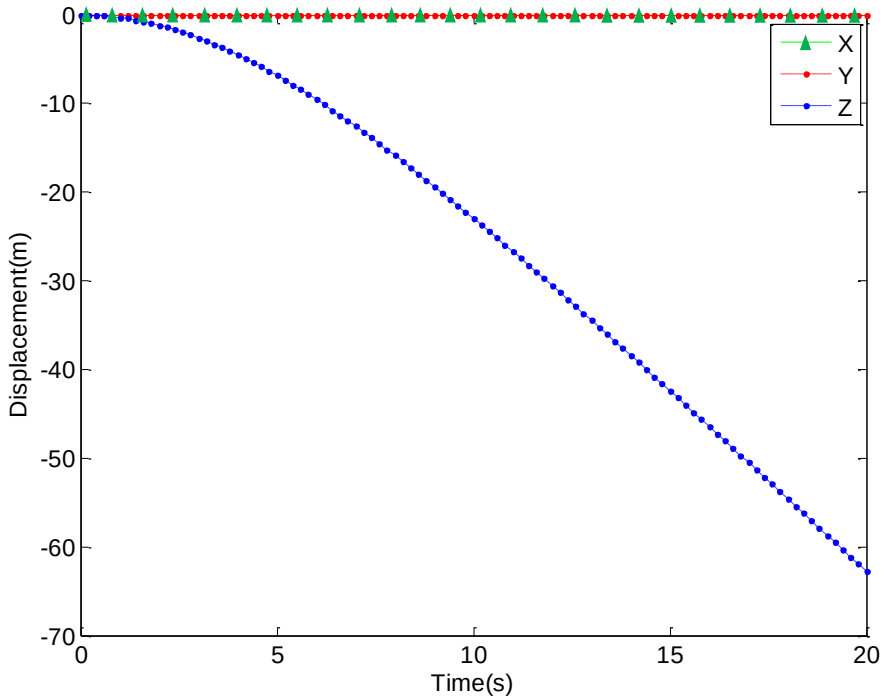

Figure 7.6: Variation in displacement with time during the ascent phase.

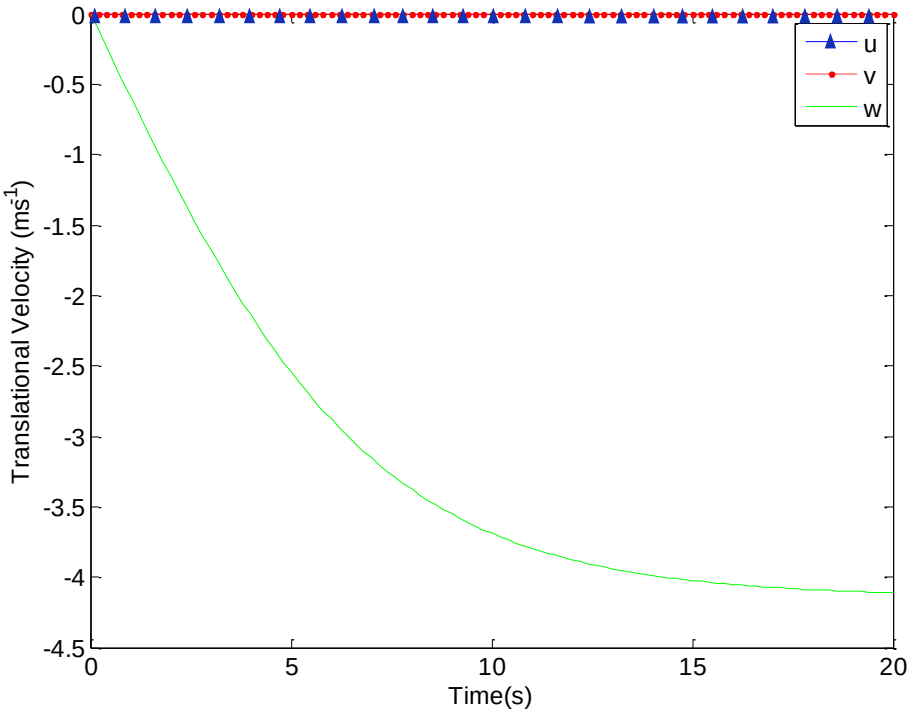

Figure 7.7: Variation in translational velocity with time during the ascent phase.

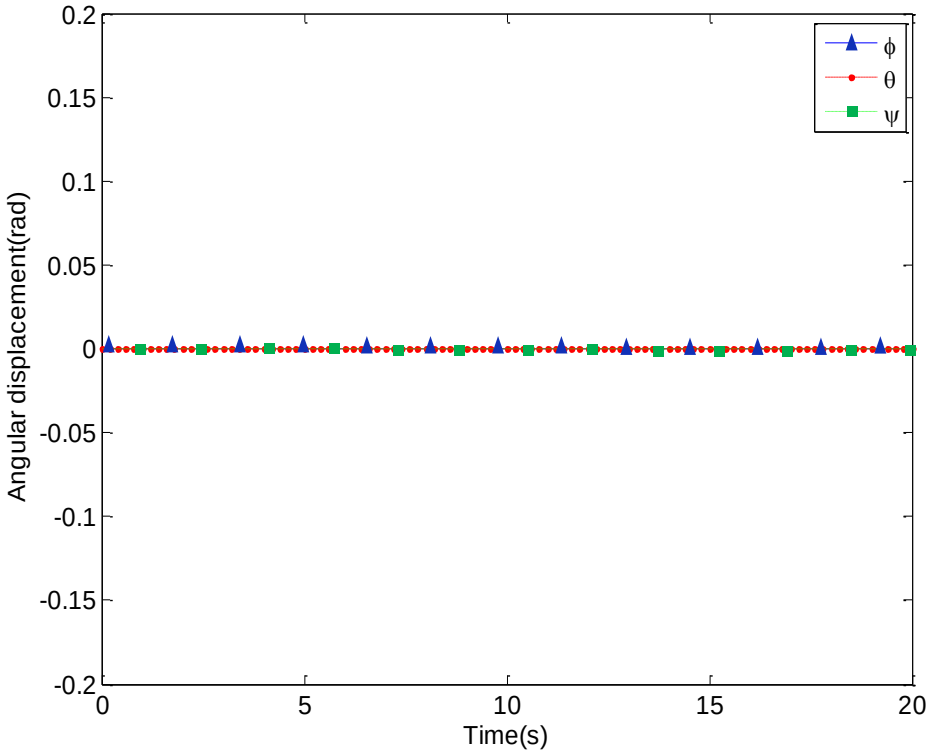

Figure 7.8: Variation in angular displacements with time during the ascent phase.

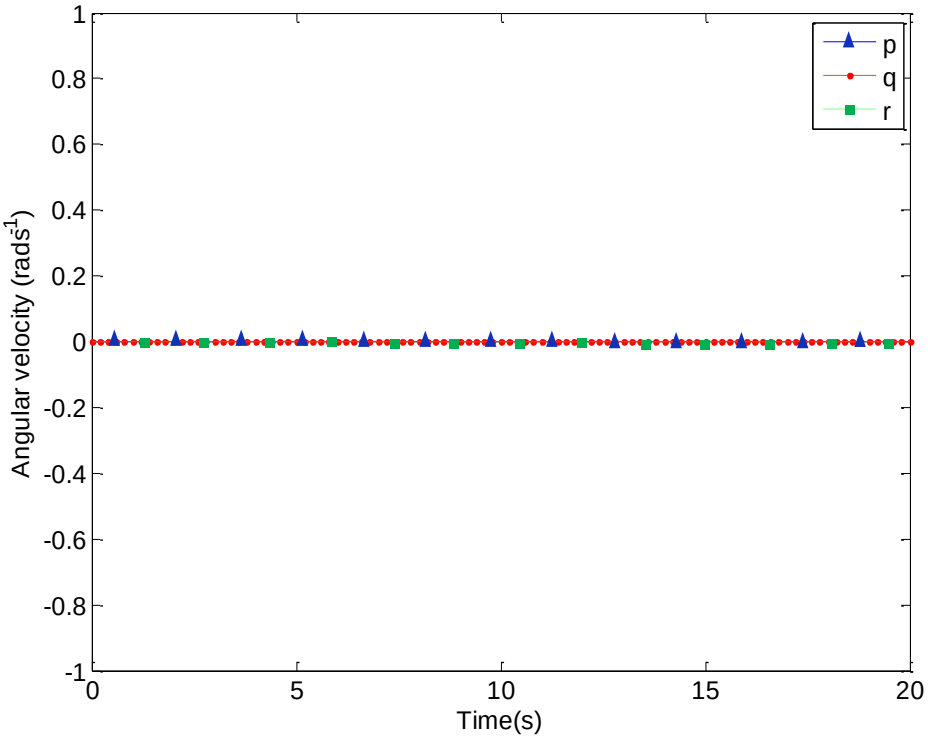

Figure 7.9: Variation in angular velocity with time during the ascent phase.

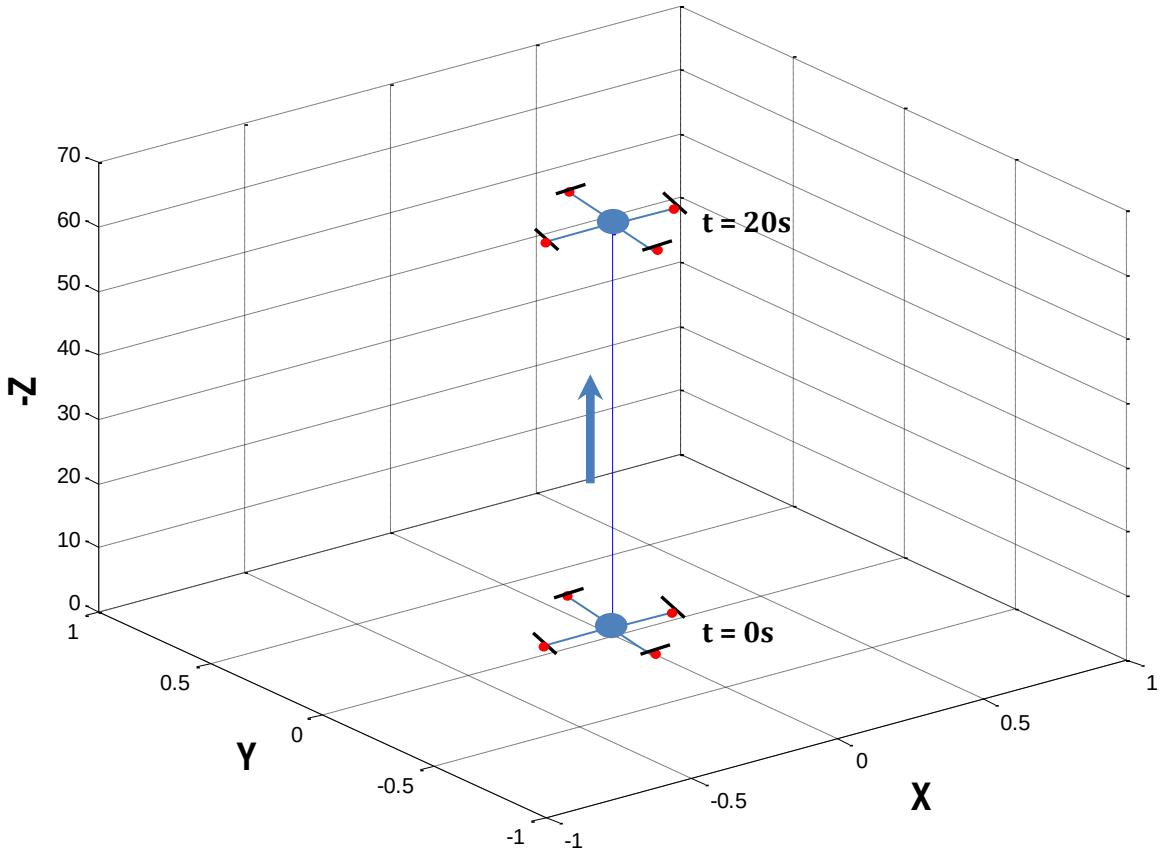

Figure 7.10: Trajectory plot during the ascent phase from base.

7.4.2 Hover Phase

The hover phase follows the take-off phase and involves the quadrotor holding its altitude. Figure 7.12 is illustrative of this as there is no variation in the X, Y and Z coordinates with time. The position of the quadrotor with time remains at the coordinate achieved post take-off as previously illustrated in Figure 7.10. This requires the equilibrium PWM signal to be generated by each motor. The resultant force in the body-fixed frame is null implying an equilibrium condition. Angular and translational rates are zero. Control is not essential at this phase of the mission due to the absence of dynamic environmental conditions which generate a resultant force on the body frame.

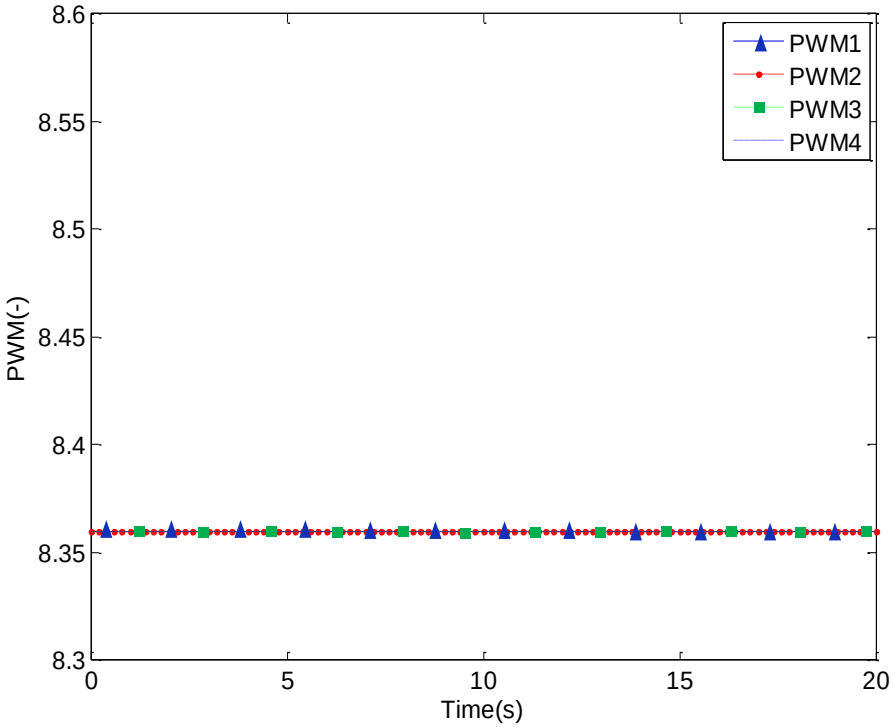

Figure 7.11: PWM signal for all motors during the hover phase.

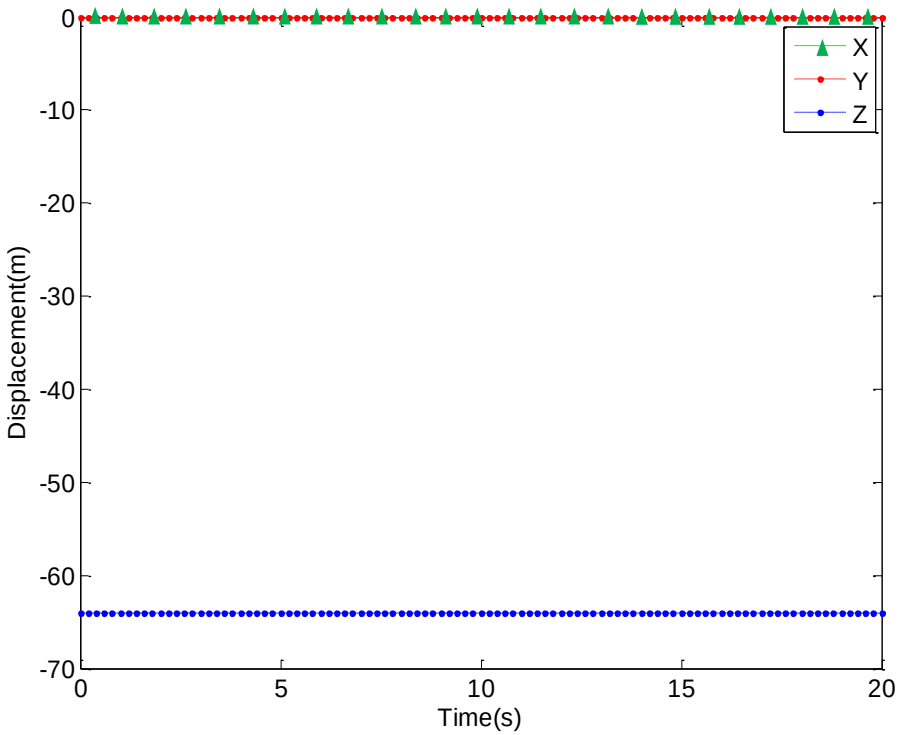

Figure 7.12: Variation in displacement with time during the hover phase.

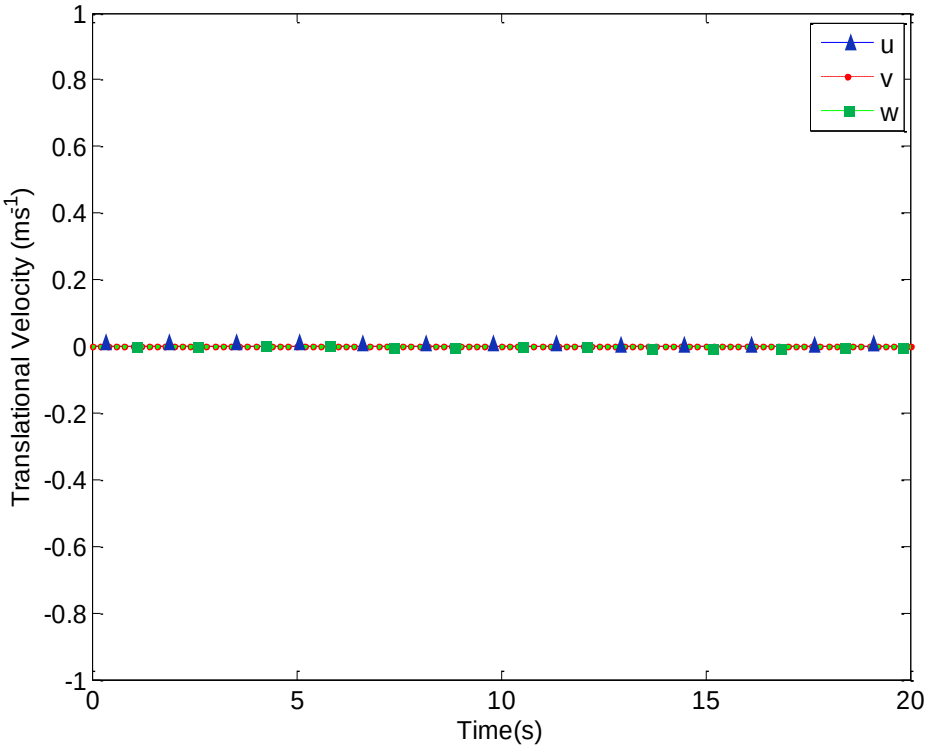

Figure 7.13: Variation in the translational velocity with time in the hover phase.

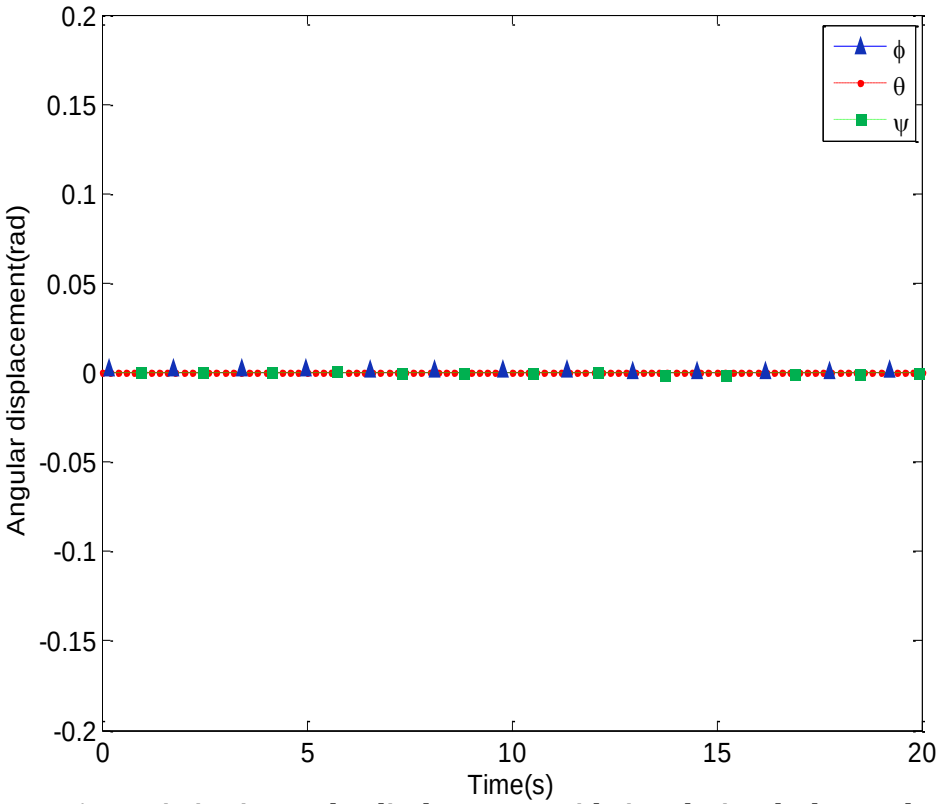

Figure 7.14: Variation in angular displacements with time during the hover phase.

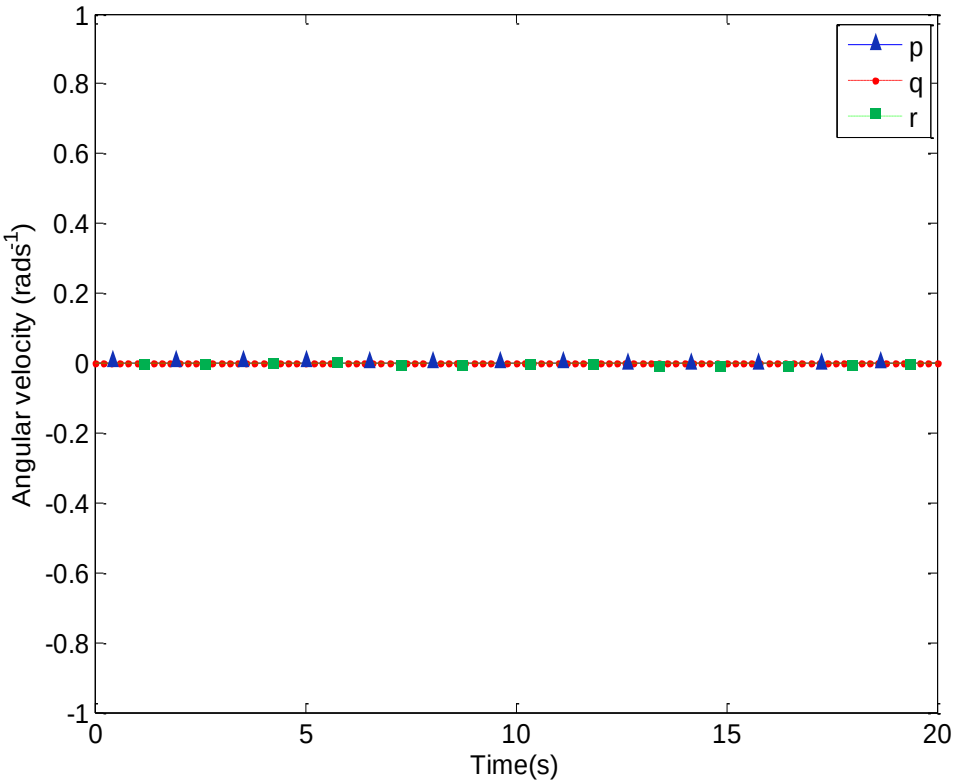

Figure 7.15: Variation in angular velocity with time during the hover phase.

7.4.3 Mode Excitation Phase

The mathematical model of the quadorotor system as descirbed in section 2.6 consists of second order differential equations creating a challenging stability analysis. Figure 7.16 illustrates the the system being excited by the generation of three constant PWM signals and a fourth ramp/step function. The simulation is intiated at an altitude of 63 meters with a simulation end condition of 0 meters above sea level. The step function initially holds a PWM value of 8.5 which is then increased to a value of PWM=8.51 for 0.15 second after which it returns to the intial value of PWM=8.5. It can be noted by observing Figure 7.18 that the pulsed PWM signal sent to motor 4 creates a rolling moment. This increases the pitch angle as in Figure 7.19 changing altitude and increasing the translational velocity. The change in PWM signal on rotor 4 induces an additional yawing moment as seen in Figure 7.19 and Figure 7.20 changing the *X* coordinate with time resulting a curved flight path as seen in Figure 7.21.

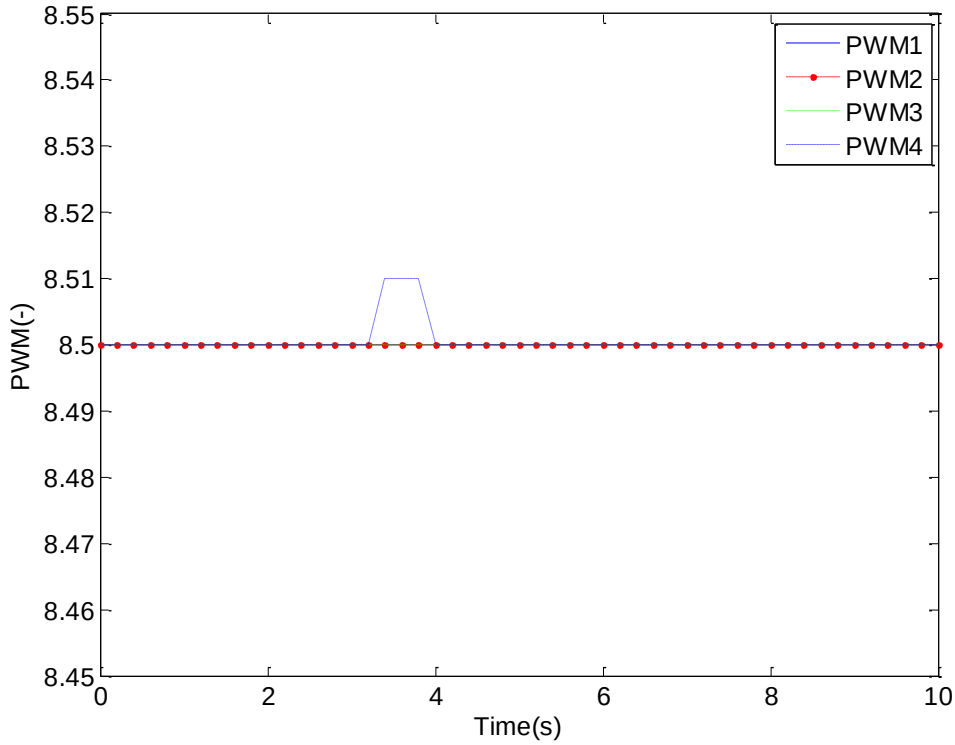

Figure 7.16: PWM signal for all motors during a signal perturbation on motor 4.

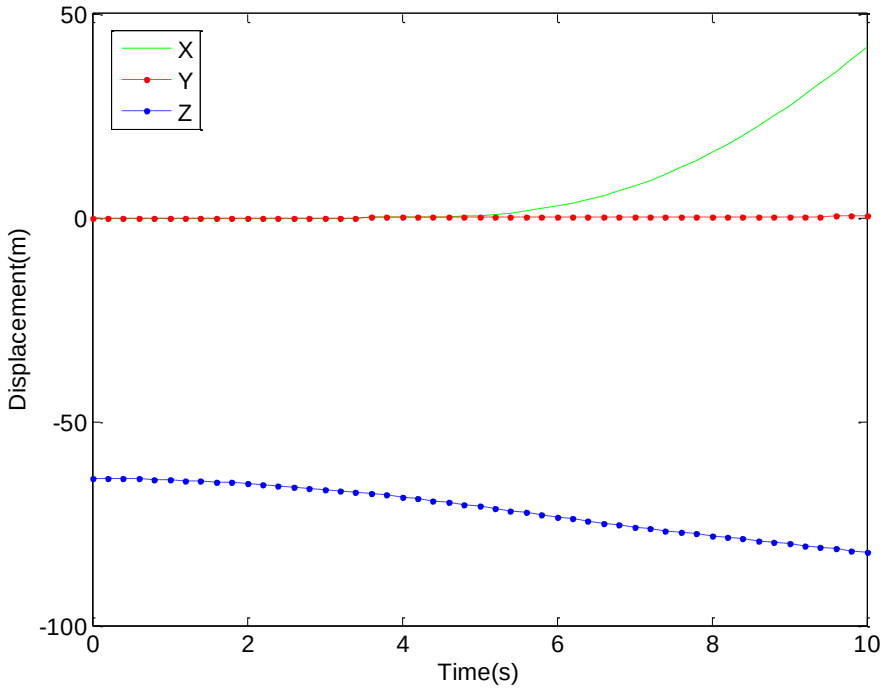

Figure 7.17: Variation in the displacement with time in the excitation phase.

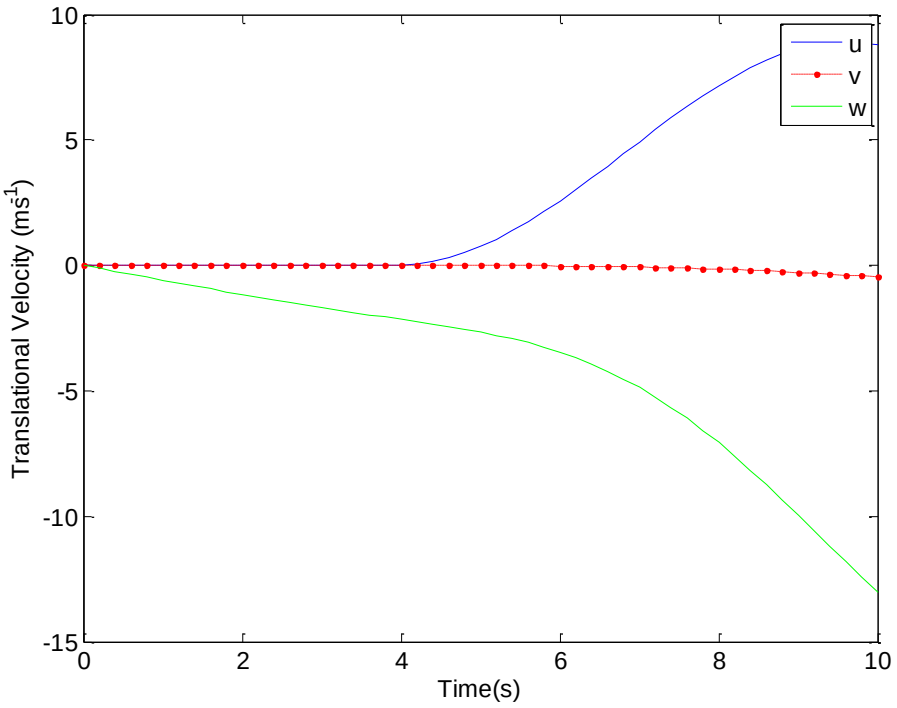

Figure 7.18: Variation in the linear velocity with time in the excitation phase.

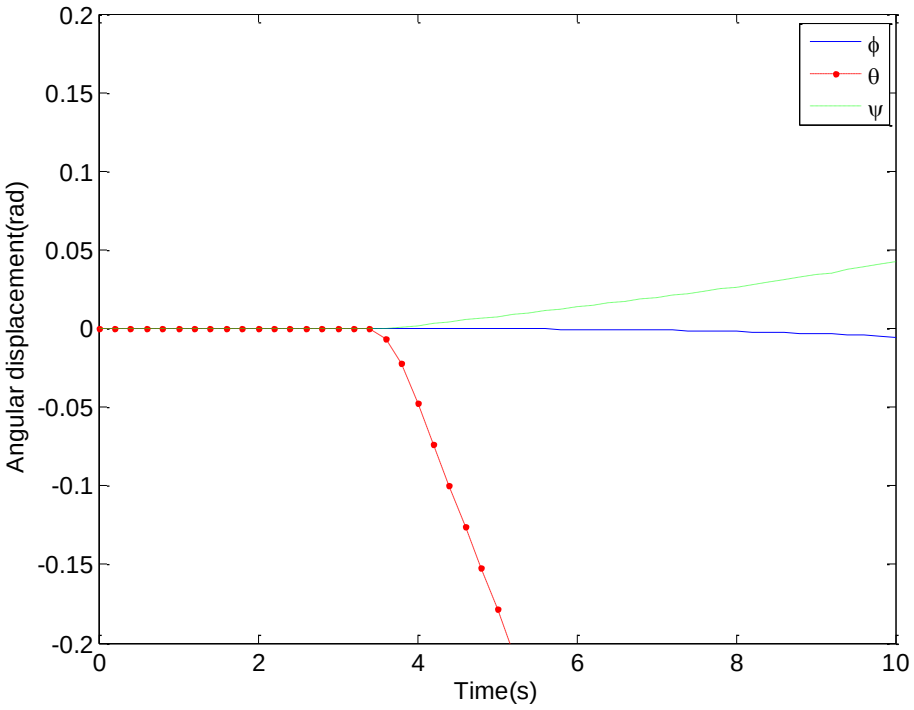

Figure 7.19: Variation in the angular displacement with time in the excitation phase.

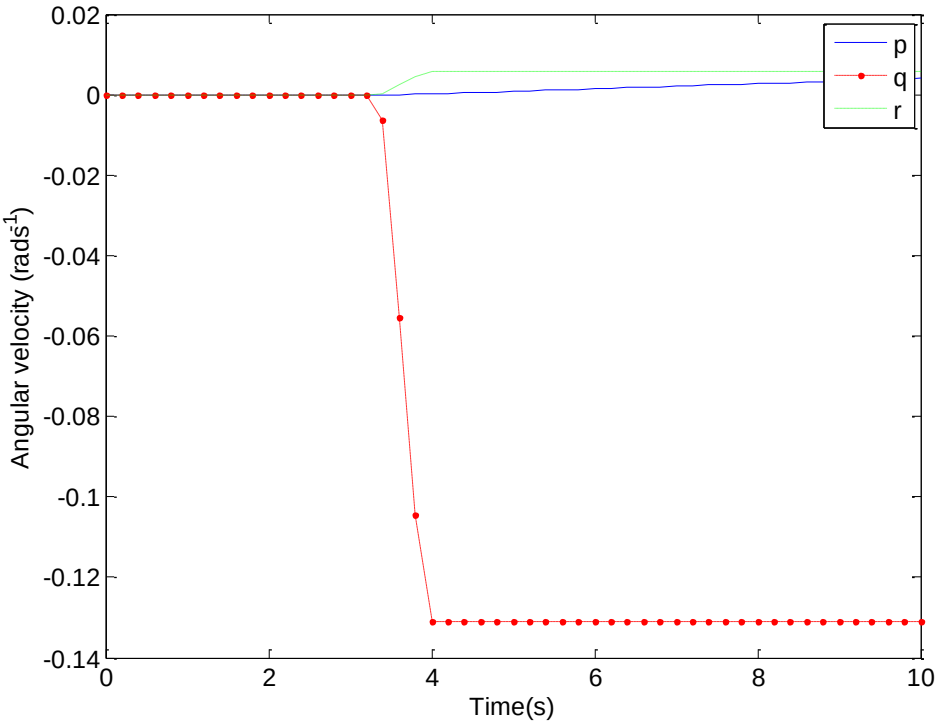

Figure 7.20: Variation in the linear velocity with time in the excitation phase.

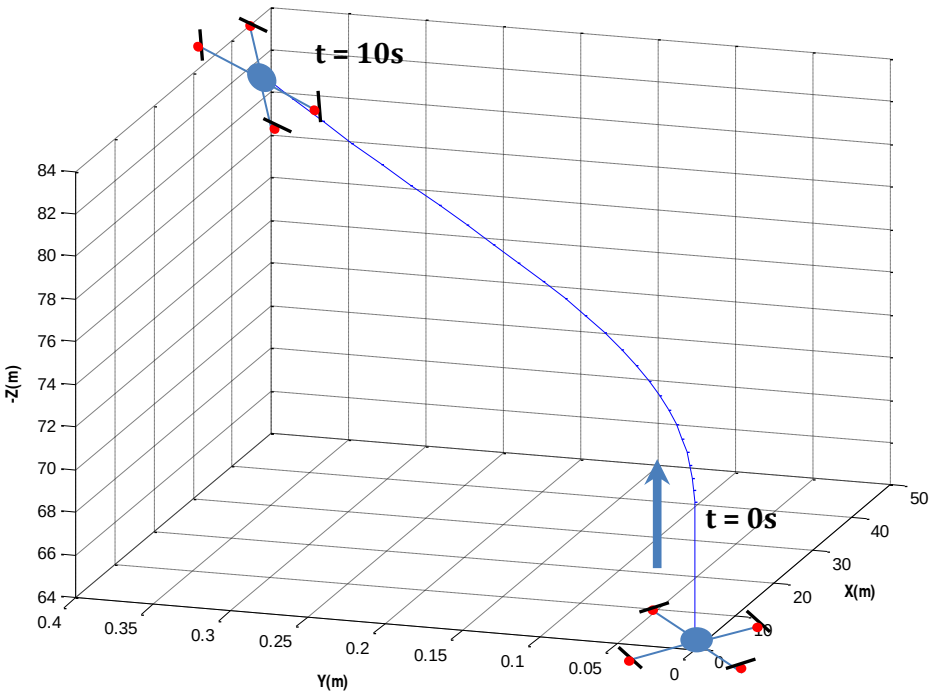

Figure 7.21: Trajectory plot during the excitation phase.

7.4.4 Landing/ Descent Phase

The final phase of the mission profile consists of the descent phase. This phase is similar to the ascent phase in that the PWM signals generated for the motors are constant however at a PWM signal lower than that required to maintain hover (see Figure 7.22). The PWM signal supplied for the purposes of testing was set to a value that allowed for a steady landing. During this phase the displacement occurs only along the earth-fixed Z-axis and due to the drag vector the displacement and velocity vector varies non linearly with time (see Figure 7.23 and Figure 7.24). During this phase level flight must be maintained which can be seen by the null angular displacement and velocity curves with time (see Figure 7.25 and Figure 7.26). The trajectory during this phase can be viewed in Figure 7.27. It can be noted that lower PWM signal implies a smaller descent velocity and longer decent duration from its initial position.

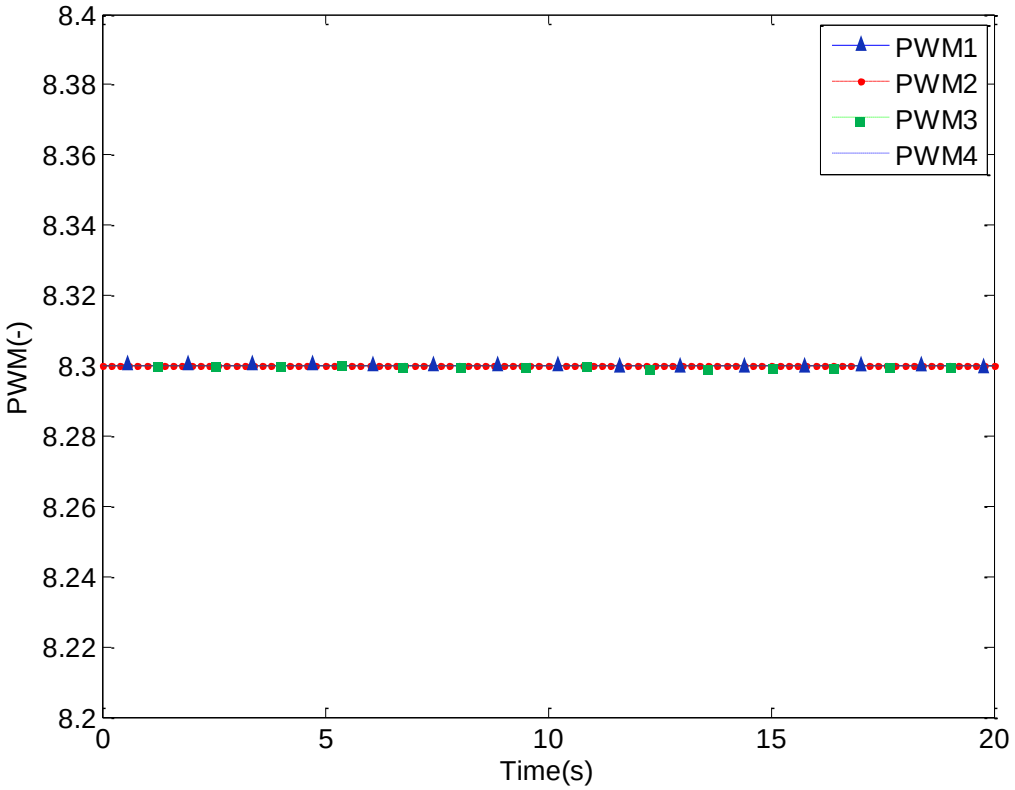

Figure 7.22: PWM input for the landing phase of the mission.

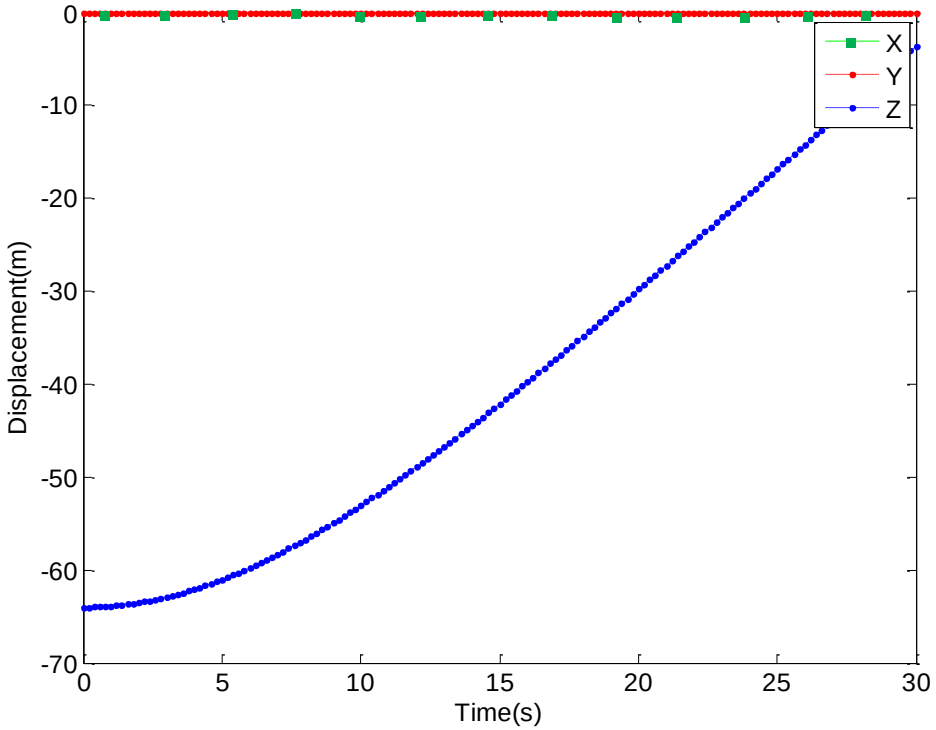

Figure 7.23: Variation in displacement with time during the descent phase.

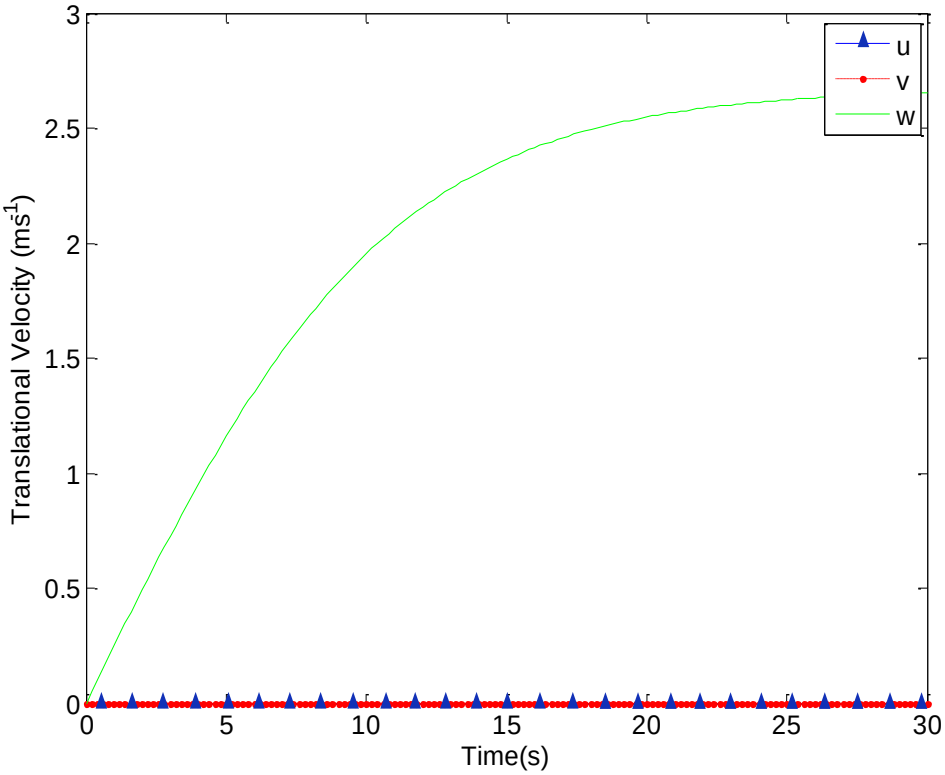

Figure 7.24: Variation in translational velocity with time during the descent phase.

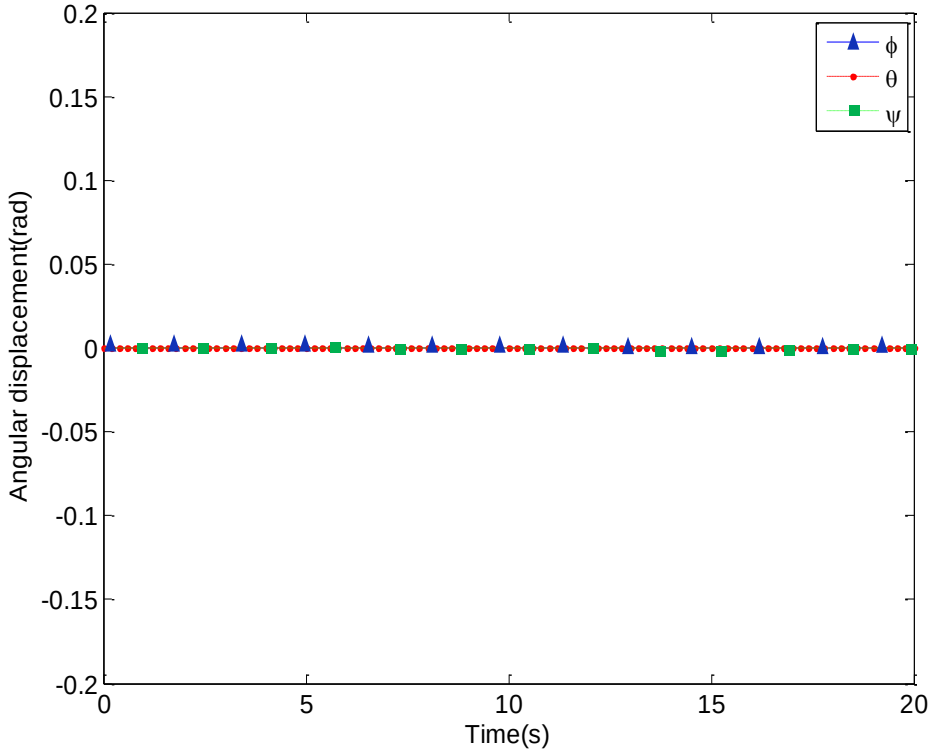

Figure 7.25: Variation in angular displacements with time during the descent phase.

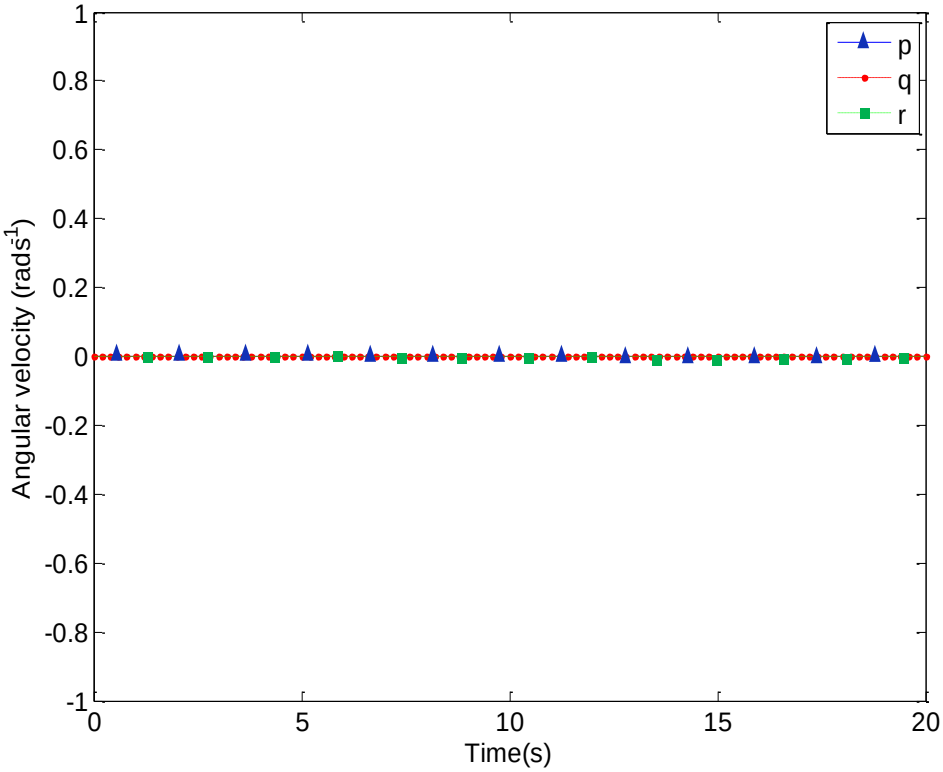

Figure 7.26: Variation in angular velocity with time during the descent phase.

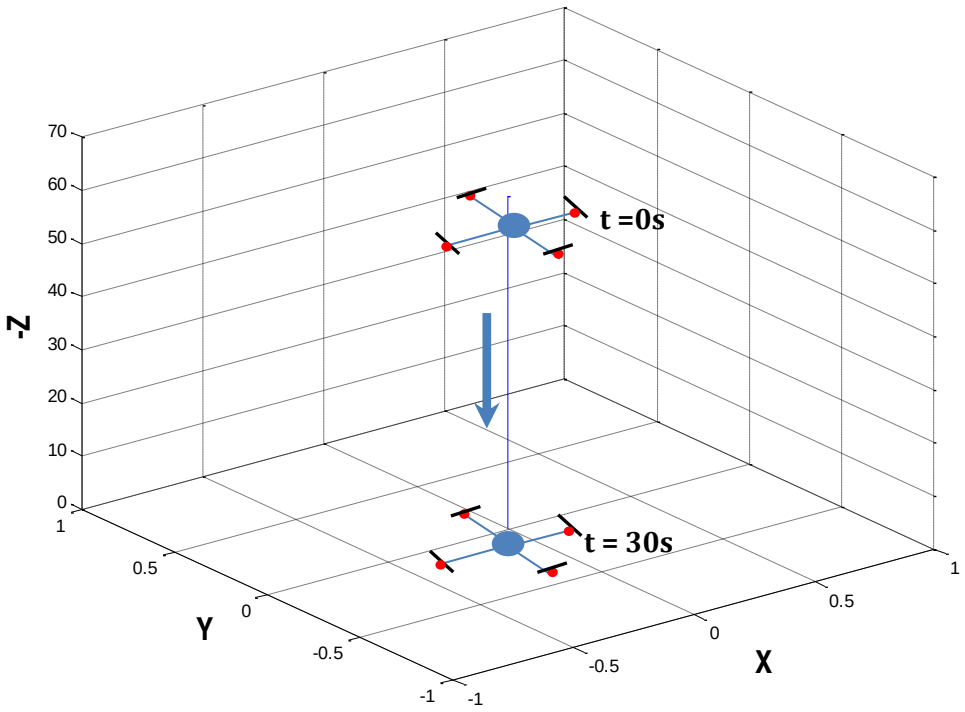

Figure 7.27: Trajectory plot during the descent phase.

8. Summary, Conclusion and Future Work

8.1 Summary

8.1.1 Test Rig Implementation

The concept of the black box structure applied to the powerplant had been successfully achieved through the use of the constructed test rig and a target pattern binary shift algorithm. The constructed test rig allowed for the functional performance verification of the motors in terms of measured variables such as thrust, torque, RPM and PWM. Simultaneous measurement of the variables instilled a higher level of confidence in the data due to a marginal error in RPM readings of 0.04%. Thrust values were achieved through the calibration of a custom built load cell which through amplification provided thrust values for 36 motor and propeller combinations. The characterisation of torque was problematic due to the low level of resolution and erratic nature and remains an area to be further improved. Characterisation of the curves via the devised algorithm was successfully achieved as relationships between torque, thrust and RPM were quantified in terms of the input PWM signal. This forms an important part of the identification process by adhering to a stringent set of data manipulation protocols set out by the algorithm ensuring consistency.

The consistent data acquiring and sorting nature of the constructed apparatus make the rig ideal for future testing of new propeller-motor combinations.

8.1.2 Data Acquisition Results

The results of the data acquisition process had two main interests, that being the maximum thrust produced by a motor for the least amount of current and if the maximum allowable take-off weight with the chosen setup accommodates the simulation model mass. The 390KV motor combined with the 9x4.5", 3 blade propeller produces the highest ratio of thrust to current but limitations imposed on the required model mass eliminated this setup. The 570 KV motor with the 11x4.7" propeller was selected due to the high efficiency and overhead to accommodate larger simulation model masses.

8.1.3 Inertial Measurement Unit and AHRS

The AHRS system was successfully implemented in the "C code" environment and validated via the construction of the rotation rig. The rig ascertained that an individual axis could be isolated and used for future controller testing. The Sparkfun unit provided an AHRS platform through the use of the ATMEGA-328 which performed all the on-board processing. Future integration of this system into the Labview interface will require the porting of the software into the Labview environment so that all the processing is performed aboard the National Instruments hardware module.

8.1.4 Mathematical Modelling

The mathematical modelling was realised using the graphical user interface of the Matlab environment. The initial model testing used the ascent, descent and hover phases as forms of model validation. The requisite PWM signal to attain hover on all the motors was calculated using an equilibrium analysis. For a given model mass the corresponding equilibrium PWM value varies. Any value of PWM above and below the equilibrium value generates the corresponding ascent and descent phases respectively. The perturbation phase consisted of a step input of PWM on a single motor whilst maintaining a constant but equal in magnitude PWM value on the remaining motors. The plotted trajectory in response

to the input conformed to predictions of a pitching and rolling action. The mathematical model included the effects of body drag which was approximated as a spherical hub. The effects of the drag vector can be seen when the translational velocity vector asymptotes to 4.4m/s. If the drag vector was absent then the object would accelerate to the velocity value beyond that reached for equilibrium with the drag vector present. It remains the aim of future work to further address this issue, adding realism to the mathematical modelling process.

8.2 Conclusion

- The developed data processing algorithm worked as intended identifying trends in torque, thrust, RPM, and PWM.
- The 570KV motor with 11x4.7" propeller combination was shown to be the most efficient providing a flight time of 9, 18 and 27min for the single, bi and tri cell arrangements respectively.
- Higher blade diameters require a larger torque at start-up and produce a decreased maximum RPM value.
- An increase in the voltage rating of the motor decreases the efficiency of the motor.
- The 6-DOF system was found to be effective in simulating flight trajectories with dynamic inputs.
- The drag force encountered had been accurately modelled for the ascent and decent phases.
- Dynamic disturbance in the form of wind were neglected from the model due to the lack of wind tunnel test data.
- The mathematical model worked as intended, predicting flight performance for all the construed phases in the mission profile.

8.3 Future Work

8.3.1 Quadrotor Construction

Future work of the project will encompass the complete design and build of the quadrotor UAV with geometrical design features such as arm length and chassis geometry extracted from the mathematical model. A complete stress analysis will need to tbe conducted on the conceived chassis establishing areas prone to fatigue loading. Resonance was established to be one of the main design considerations noted by the rapid changes in displacement of the test beam and will be a design critieria. The preliminary design as shown in Figure 8.1 was built in order to facilitate a design space for the avionics and wiring and is a necessary pre-requisite.



Figure 8.1: Quadrotor UAV preliminary design.

Figure 8.2 illustrates the conceptual cage built for the housing and protection of the avionics during flight. A SBRIO 9606 will be used due to the experience gathered in Labview FPGA, powerful processing and easy integration. A three tier structure was selected due to a perceived greater structural intergrity. Carbon fibre sheeting, tubing and an alluminium supports was selected due to the inherent strength under loading. Provision for an increased battery capacity was made increasing the predicted endurance of the aircraft.

Currenlty the perceived flight time with a single 4400mah battery stands at 13.2min at a average consumption of 20A. Once constructed the performance can be verfifed.

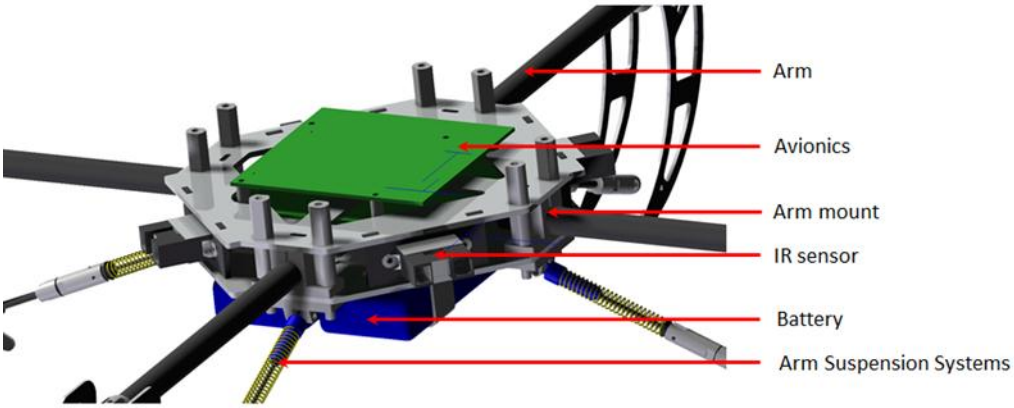

Figure 8.2: Avionics integration into proposed chassis.

8.3.2 Sensors

The current IMU board developed by Sparkfun will need to be redesigned for the use on the avionics board. The DCM algorith will need to be implemented on a newly constructed IMU board for interfacing with a GPS unit and barometric pressure sensor increasing the accuracy of the algorithm due to the redundant heading vector calculation by the magnetometer and GPS unit. Flight obstacle avoidance in the form of LIDAR and SONAR system will need to be integrated into the model. It is essetial than the implemented AHRS system be ported to the Labview environment for easy integration.

8.3.3 Control Systems

Dynamic control is critical to unmanned aerial vehicle (UAV) flight. The quadorotot relies on changing rotor thrusts for manoeuvering hence the method and means of rotor speed control is of great interest. Hobby brushless DC motors have been used with generic speed controllers however a newer form of vector speed control will be implemented with the aim of a more effiecient commutaution process. Control systems in the form of general PID to Neural Networks will need to employed in order to stabilise the quadrotor in flight. This remains an important area that needs to be covered.

8.3.4 Wind Tunnel Test Data

The absence of wind tunnel test data for the purposes of quadrotor simulation makes drag estimation a tedious process. It remains an area that has not been explored and will be explored in the future. A custom built load cell will need to be built in order for the drag forces to be captured inside the wind tunnel facilities adding a dynamic to the simulation that is missing in documented models.

The above recommendation will allow for the completeness of the project. The main aim of past and future work will be to have a functional test unit for data gathering at a cost effective price.

9. References

Analog Devices, 2009. *Small Low Power, 3 Axis Accelerometer,* s.l.: s.n.

Ascending Technologies, n.d. Ascending Technologies, viewed 11 Spetember 2012, from http://www.asctec.de/uav-applications/research/products/asctec-hummingbird.

Bristeau, P. J., Martin, P., Salaun, E. & Petit, N., 2009. *The Role of Propeller Aerodynamics in the Model of Quadrotor UAV.* Hungary, Proceeedings of the European Control Conference.

Brown, W., 2002. *Brushless DC Motor Contorl Made Easy,* s.l.: s.n.

Cybertechnology, n.d. CyberTechnology, viewed 21 August 2012, from http://www.cybertechuav.com.au/-Overview,85-.html.

David Schmidt, M., 2011. *Simulation and Control of a Quadorotr Unmanned Vehicle,* s.l.: University of Kentucky.

Devantech, n.d. Using the I2C Bus, viewed 5 July 2012, fromat http://www.robot-electronics.co.uk/acatalog/I2C_Tutorial.html.

DiCesare, A., Gustafson, K. & Lindenfelzer, P., 2008. *Design Optimization of a Quad-Rotor Capable of Autonomous Flight,* s.l.: Worcester Polytechnic Institute.

Domingues, J., 2009. *Quadrotor prototype,* Lisbon: University of Lisbon.

Etkin, B. & Duff Reid, L., 1996. *Dynamics of Fight.* s.l.:John Wiley and Sons.

Finkpeterson, C. et al., 2008. *Autonomous Hovering with a Quadrotor Helicopter,* s.l.: Aalrborg University.

Vachtsevanos, G., Ludington, B., Reimann, J., AntsaklisP. & Valavanis, K., 2007. *Modeling and Control of Unmanned Aerial Vehicles-Current Status and Future Directions.* South Florida, Workshop on Modeling and Control of Complex Systems.

Hoffmann, G.M., Huang, H. ,Waslander, S. L. & Tomlin, C.J., 2007. *Quadrotor Helicopter Flight Dynamics and Control:Theory and Experiment.* South Carolina, AIAA Guidance, Navigation and Control Conference and Exhibit.

Huang, G., Hoffman, G., Waslander, S. & Tomlin, C., 2008. *Aerodymanics and Control of Autonomous Quadrotor Helicopters in Aggressive Maneuvering,* California: s.n.

Innovations, D., n.d. Draganflyer X4-P, viewed 21 August 2012, from http://www.draganfly.com/uav-helicopter/draganflyer-x4p.

Invensense, n.d. ITG-3200 Integrated Triple-Axis Digital-Output Gyroscope, viewed 9 August 2012 from http://invensense.com/mems/gyro/itg3200.html.

Konvalin, C., n.d. Motion/Velocity/Displacement, viewed 18 July 2012 from http://www.sensorsmag.com/sensors/motion-velocity-displacement/compensating-tilt-hard-iron-and-soft-iron-effects-6475.

Li, L., 2008. *Strutural Design of Composite Rotor Blades with Consideration of Manufacturabikty, Durability, and Manufacturuing uncertainies.,* s.l.: Georgia Institute of Technology.

Mary, C., Crisitiana Totu, L. & Konge Kolbaek, S., 2010. *Modelling and Control of Autonomous Quad-Rotor,* Denmark: Faculty of Engineering, Science and Medicine University of Aalborg.

Microdrone, n.d. Microdrone Products, viewed 12 August 2012 from http://www.microdrones.com/products/products.php.

NI, n.d. FPGA Fundamentals, viewed 4 May 2012 from http://www.ni.com/white-paper/6983/en.

Oliveira, M. D. L. C. d., 2011. *Modeling, Identification and Cotrol of a Quadrotor Aircraft.* Prague, Czech Technical University.

Pounds, P., Mahony, R. & Gresham, J., 2004. *Towards Dynamically-Favourable Quad-Rotor Aerial Robots,* Brisbane: CSIRO ICT Centre.

Paradigm, B., n.d. Introduction to SPI and I^2C protocols viewed 2 July 2012 from http://www.byteparadigm.com/kb/article/AA-00255/.

Pounds, P., Mahony, R. & Corke, P., 2007. System Identification and Control of an Aerobot Drive System.

Rawashdeh, O. A., Chul Yang, H., AbouSleiman, R. D. & Sababha, B. H., 2009. *Microraptor: A low cost autonomous quadrotor system.* California, ASME 2009.

Raza, S. A. & Gueaieb, W., 2010. Intelligent Flight Control of an Autonomous Quadrotor. *Motion Control .*

Rimestad, M. et al., 2008. *Autonomous Hovering with a Quadrotor Helicopter,* s.l.: Aalborg university, Department of electronic systems.

Roy, B. & M Pradeep, A., n.d. *Introduction to Aersopace Propulsion,* Bombay: s.n.

S. Bouabdallah and R. Siegwart, 2007. *Full Control of a Quadrotor.* San Diego, CA, USA, s.n.

Craciunas, S.S., Kirsch, C.M., Rock, H. & Trummer, R., 2008. *The JAviator: A High-Payload Quadrotor UAV with High-Level Programming Capabilities.* Honolulu, Hawaii, AIAA Guidance, Navigation and Control Conference and Exhibit.

Salih, A., Moghavvemi, M., Mohammed, H. & Gaeid, K. S., 2010. Flight PID controller design for a UAV quadrotor.

ST Electronics, 2010. *LIS3DH-Mems didtal output motion sensor,* s.l.: s.n.

Stanculeanu, I. & Borangiu, T., 2011. *Quadrotor Black-Box System Identification.* Venice, Italy, World Academy of Science, Engineering and Technology.

Premelamni, W., & Bizard, P., 2009. *Direction Cosine Matrix IMU: Theory,* s.l.: W. Premelamni and P. Bizard.

Wacker, G., 2001. Requirements for the Certification of Rotor Blades.

Appendix A – Raw Data

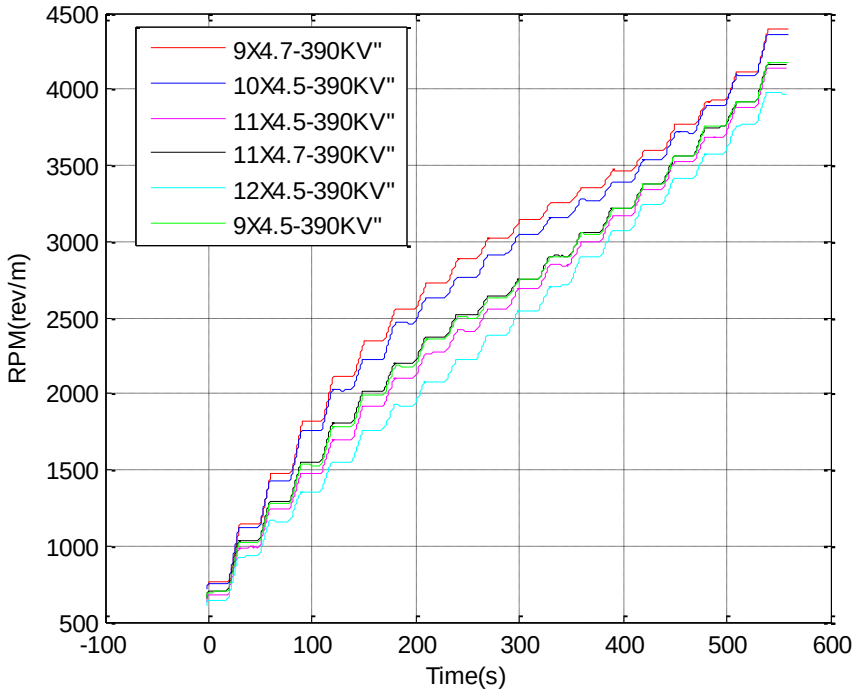

Figure A.1: Propeller raw data curves for a 390KV motor.

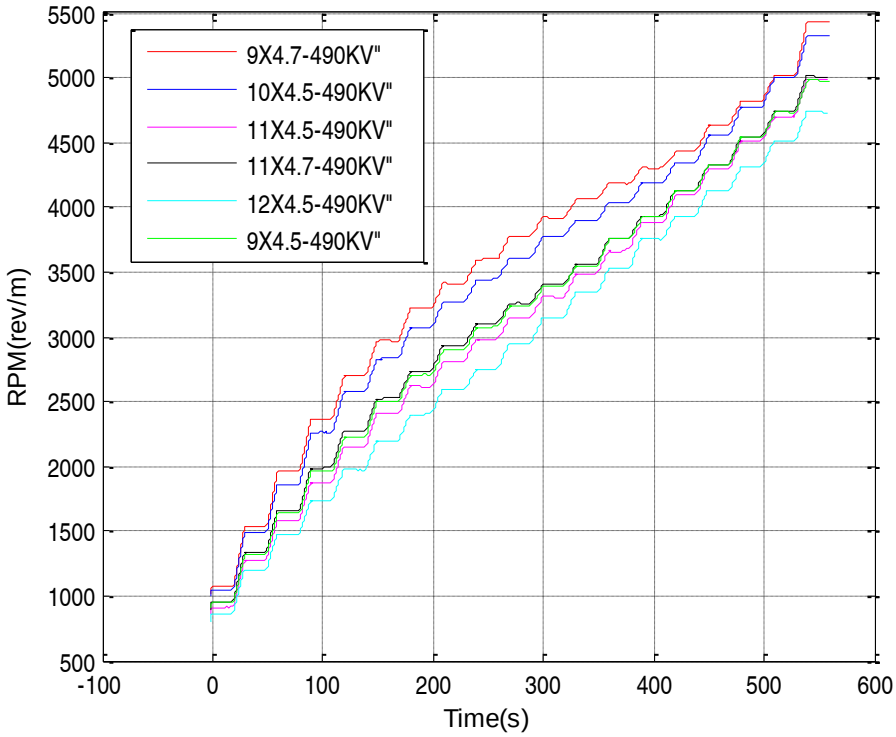

Figure A.2: Popeller raw data curves for a 490KV motor.

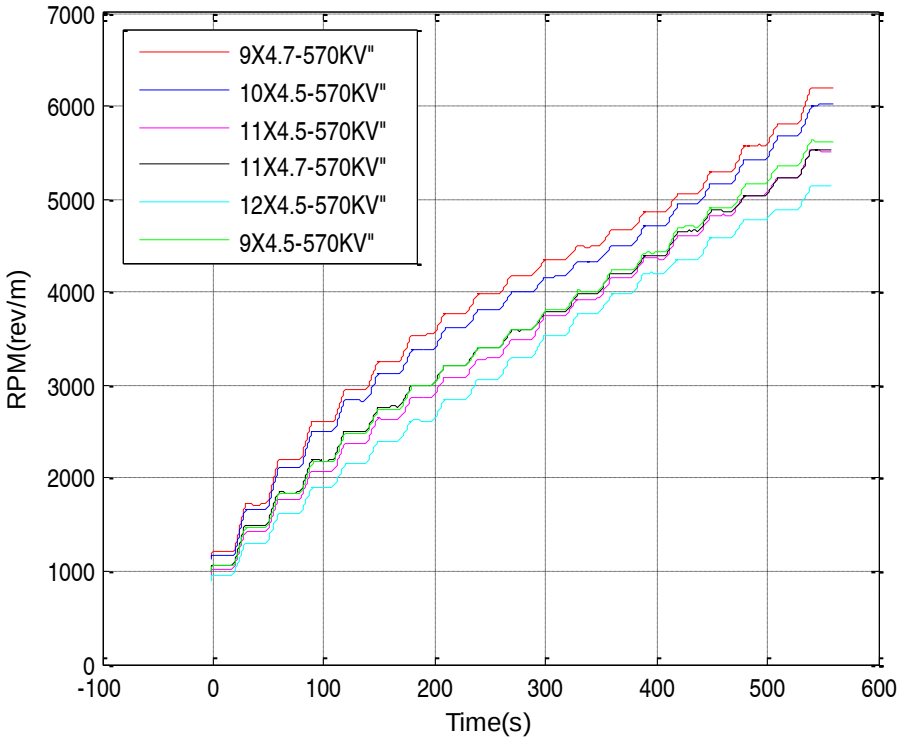

Figure A.3: Propeller raw data curves for a 570KV motor.

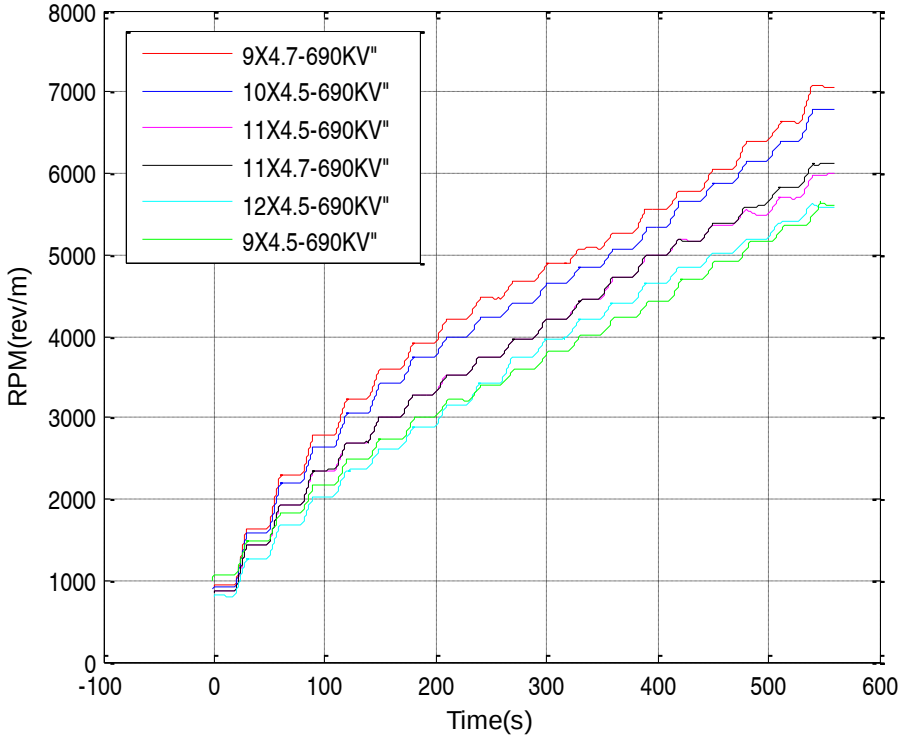

Figure A.4: Propeller raw data curves for a 690KV motor.

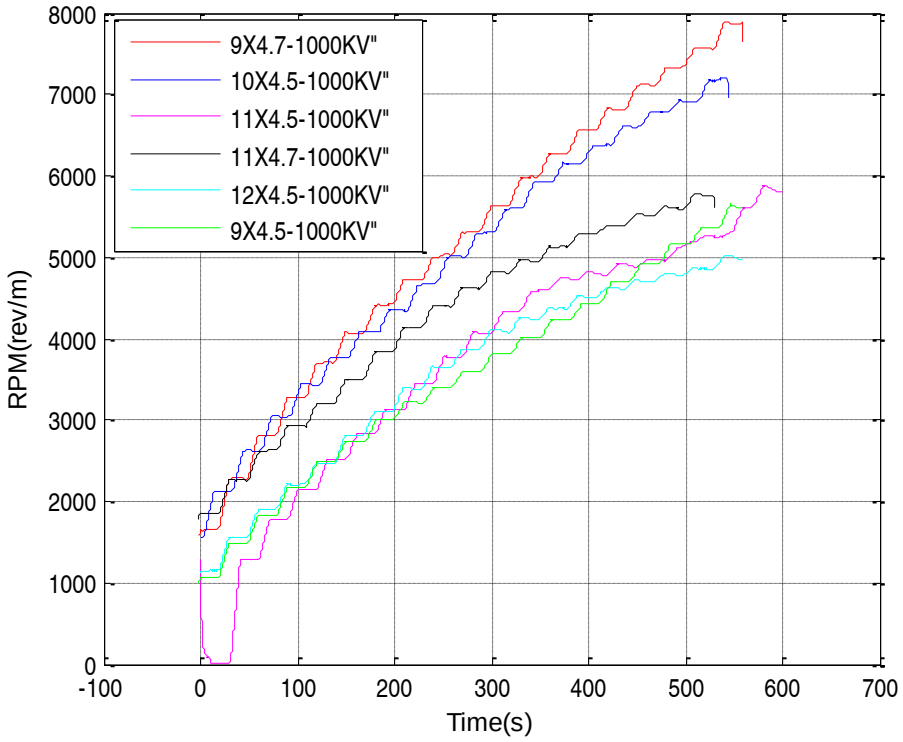

Figure A.5: Propeller raw data curves for a 1000KV motor.

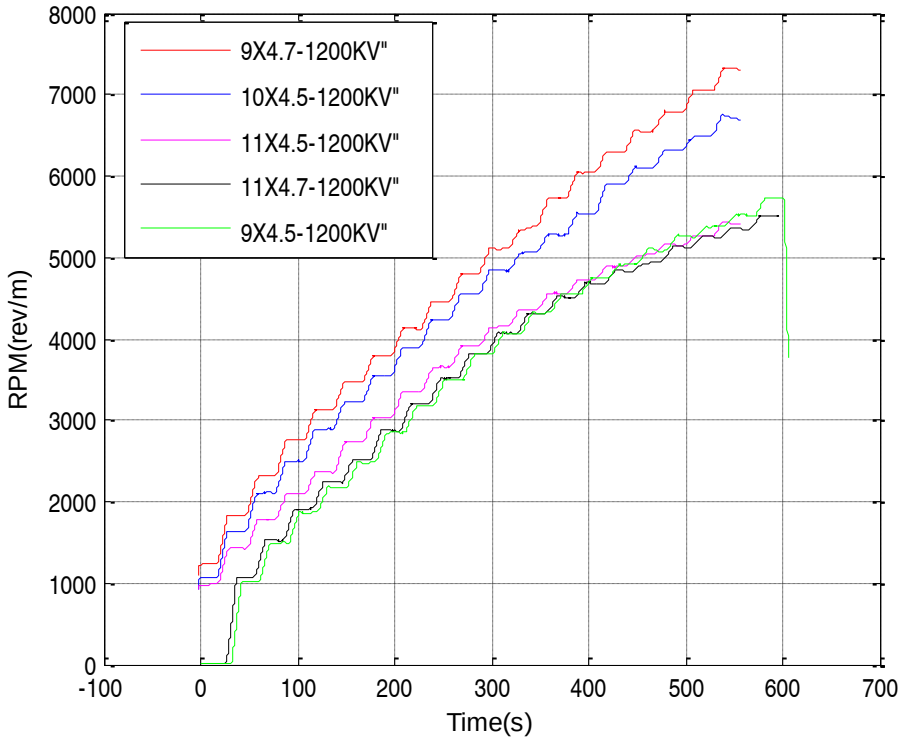

Figure A.6: Propeller raw data curves for a 1200KV motor.

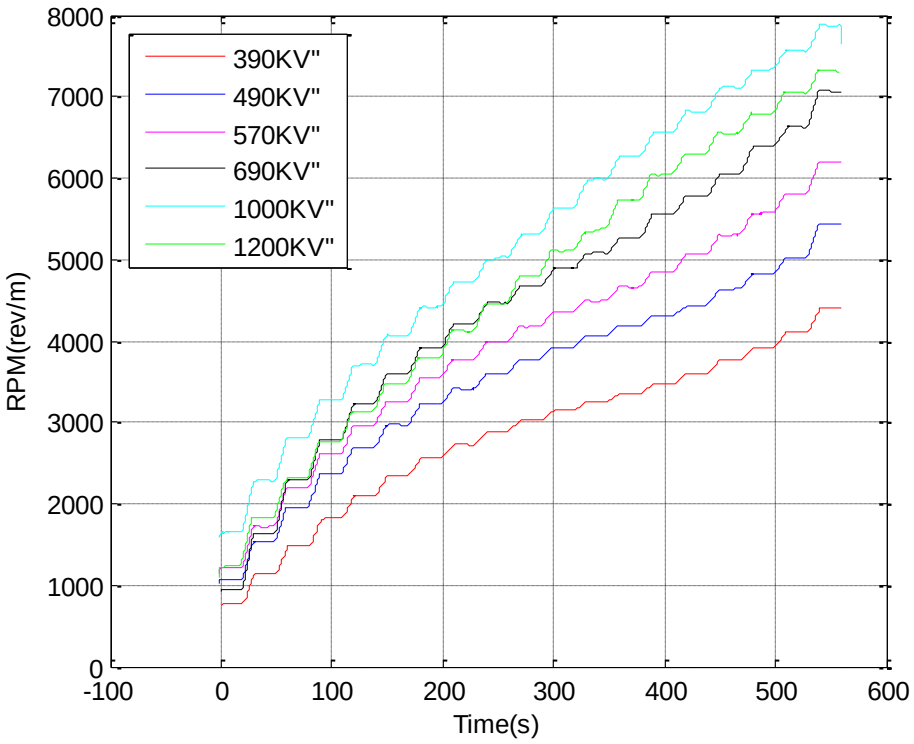

Figure A.7: Variation in RPM for 9x4.7" propeller with different motor combinations.

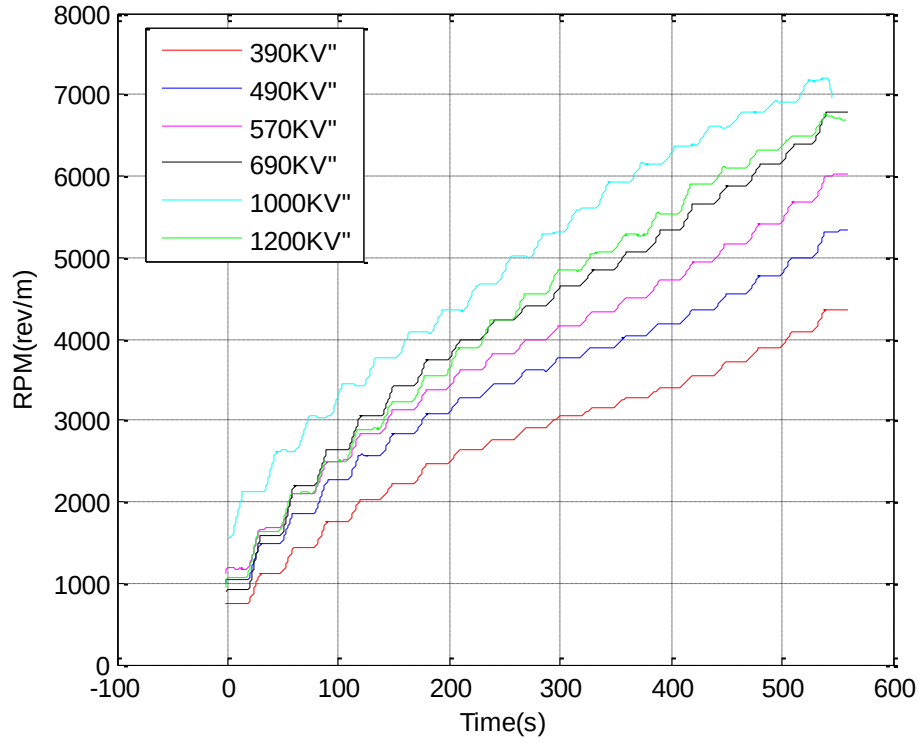

Figure A.8: Variation in RPM for 10x4.5" propeller with different motor combinations.

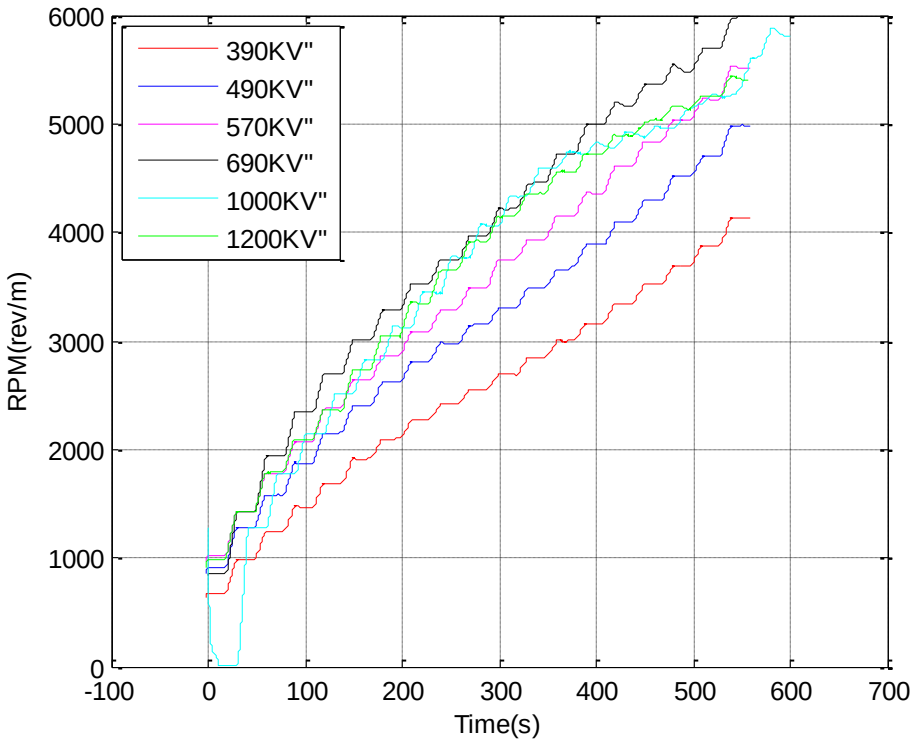

Figure A.9: Variation in RPM for 11x4.5" propeller with different motor combinations.

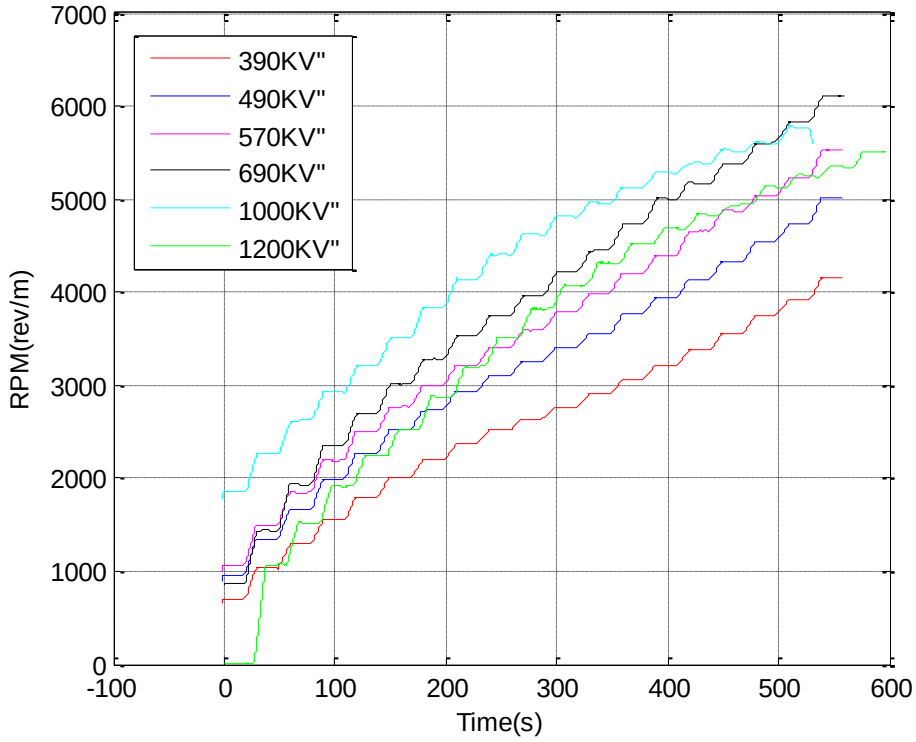

Figure A.10: Variation in RPM for 11x4.7" propeller with different motor combinations.

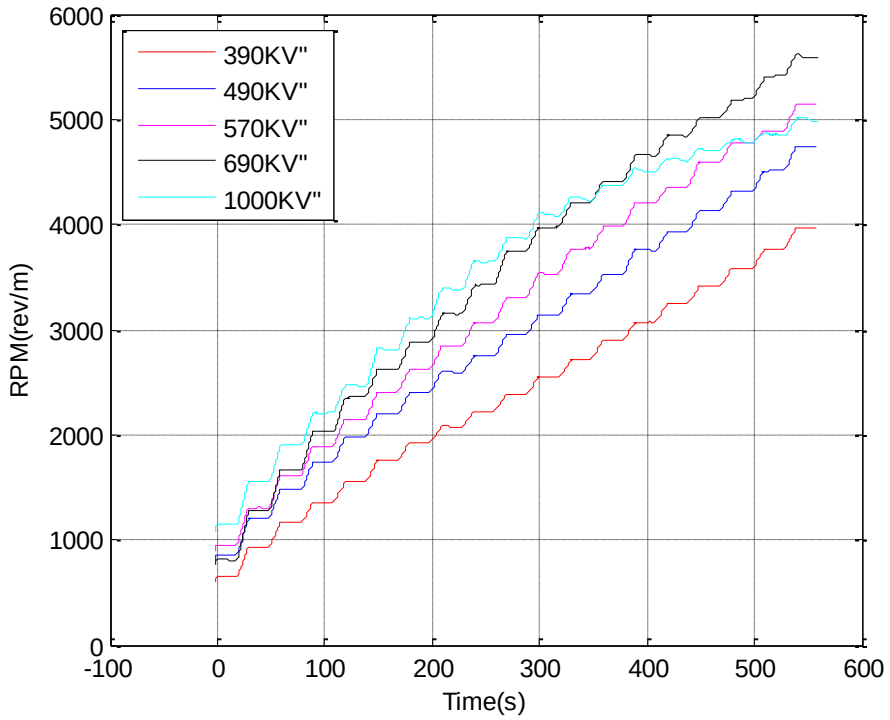

Figure A.11: Variation in RPM for 12x4.5" propeller with different motor combinations.

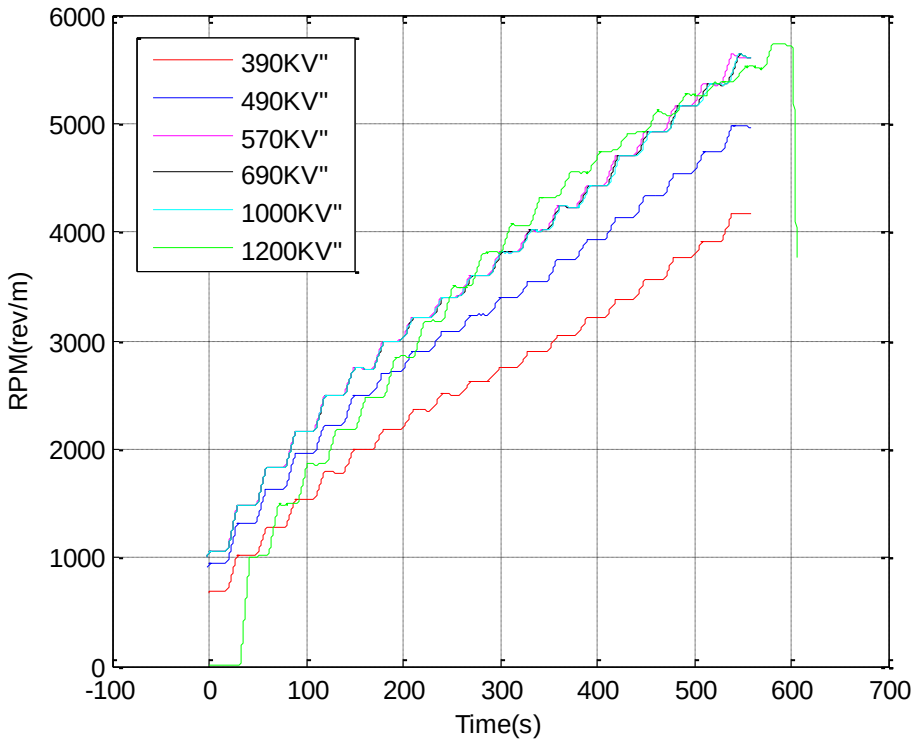

Figure A.12: Variation in RPM for 9x4.5" tri-blade propeller with different motor combinations

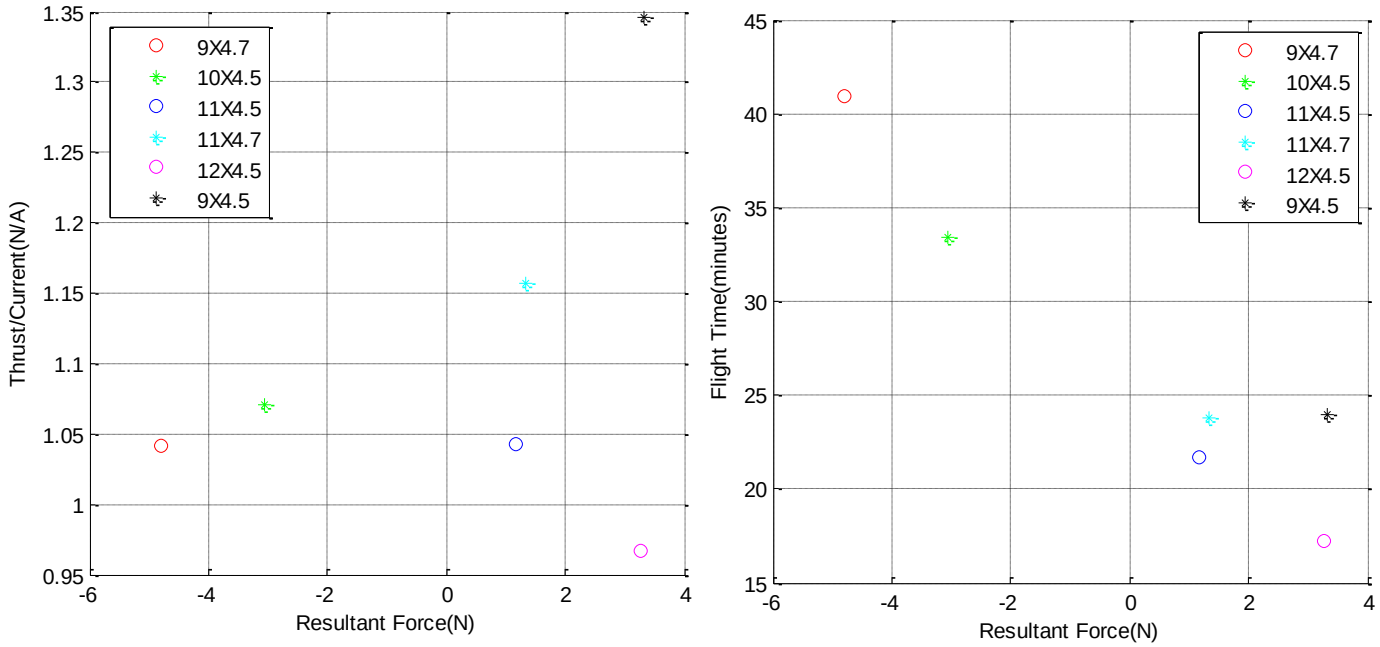

Figure A.13: Flight time and efficiency vs. resultant force for 390KV with a single battery.

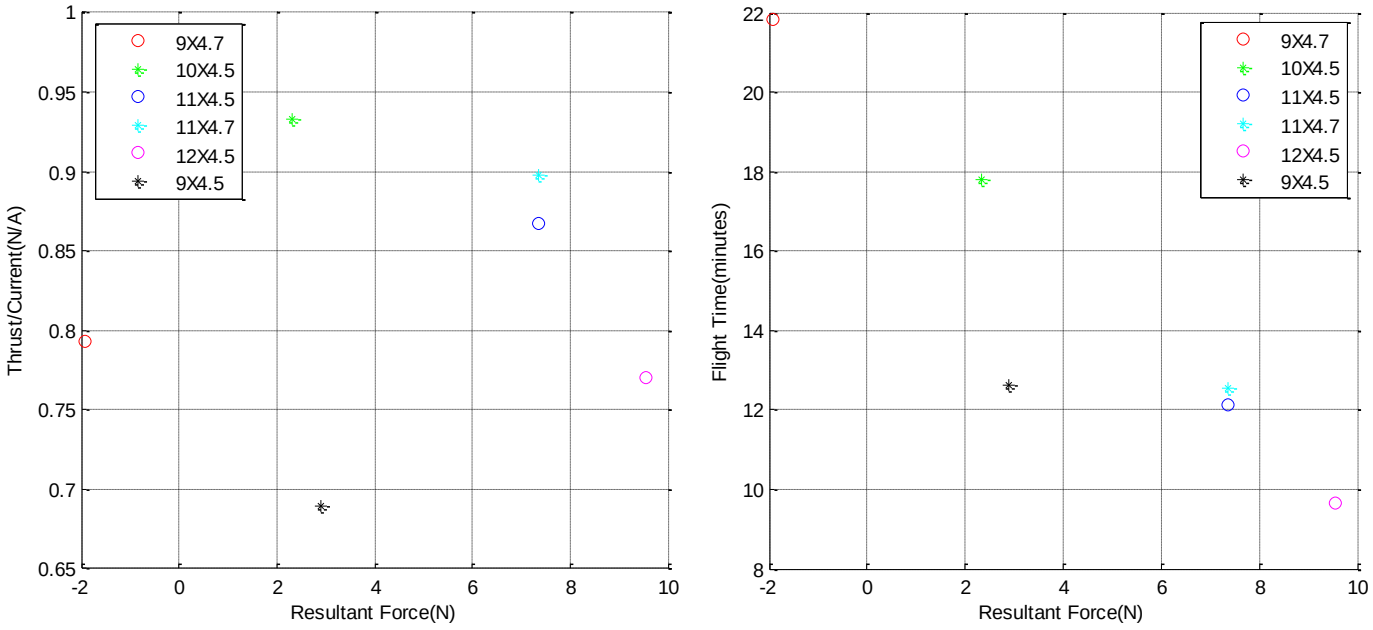

Figure A.14: Flight time and efficiency vs. resultant force for 490KV with a single battery.

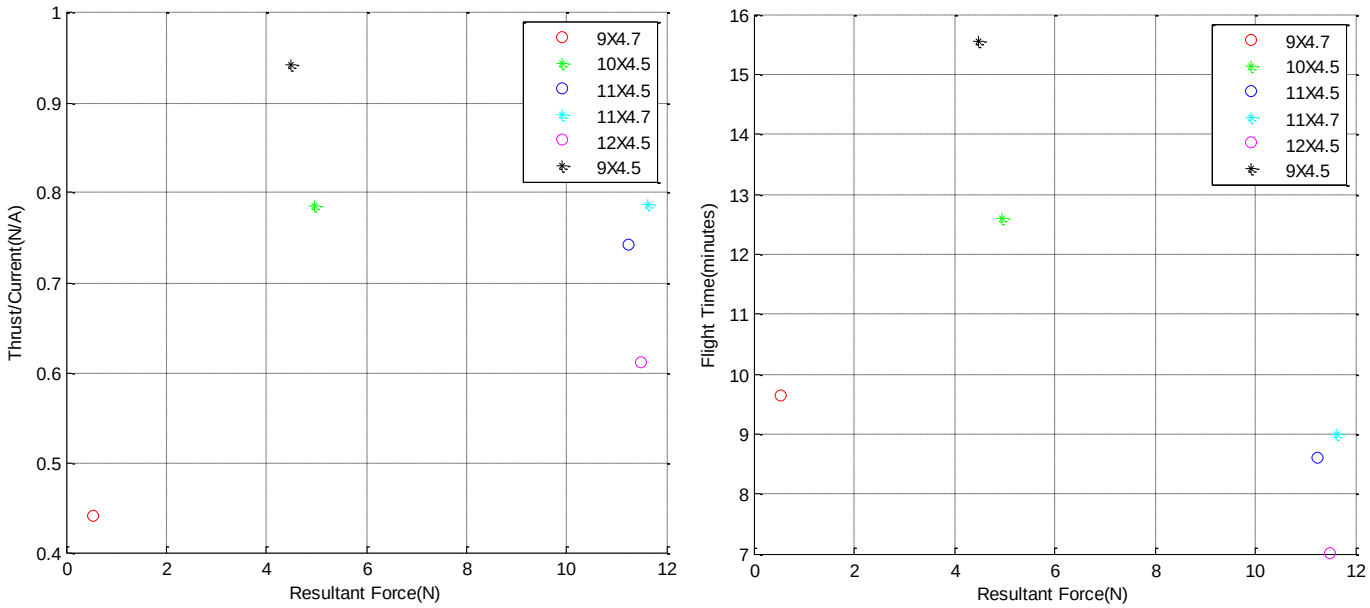

Figure A.15: Flight time and efficiency vs. resultant force for 570KV with a single battery.

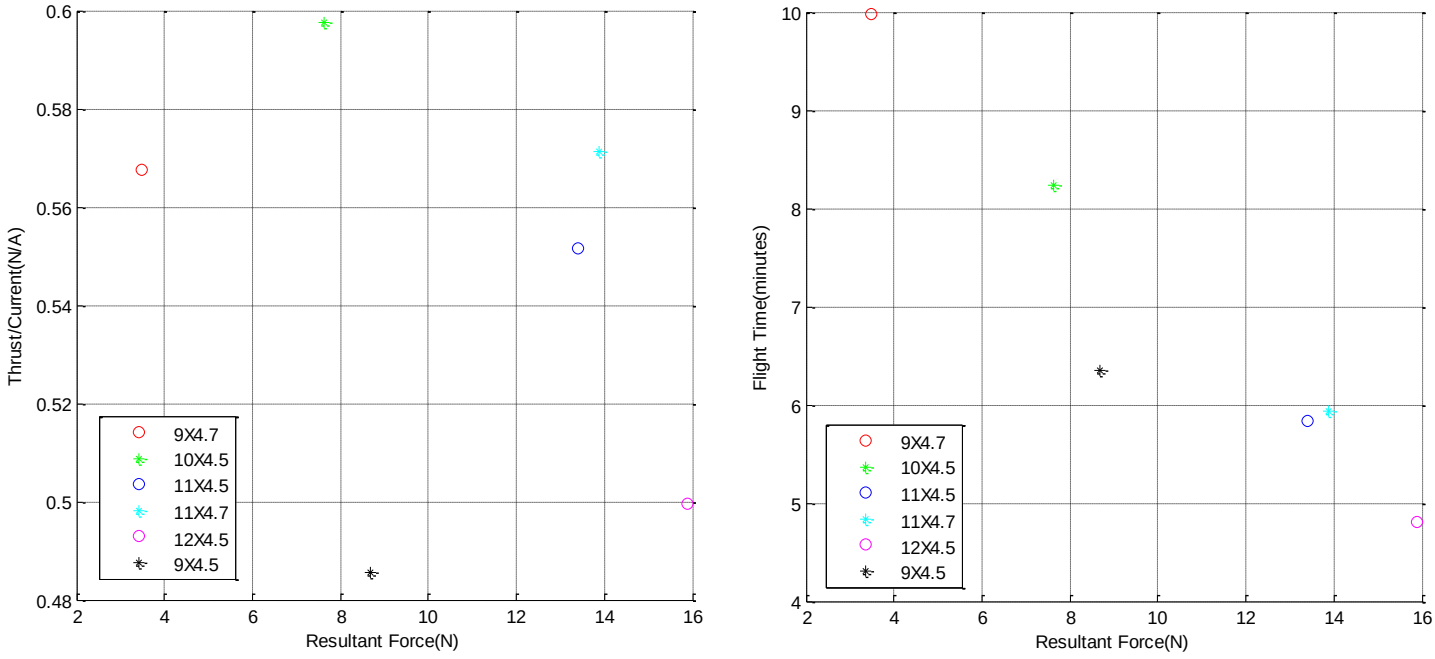

Figure A.16: Flight time and efficiency vs. resultant force for 690KV with a single battery.

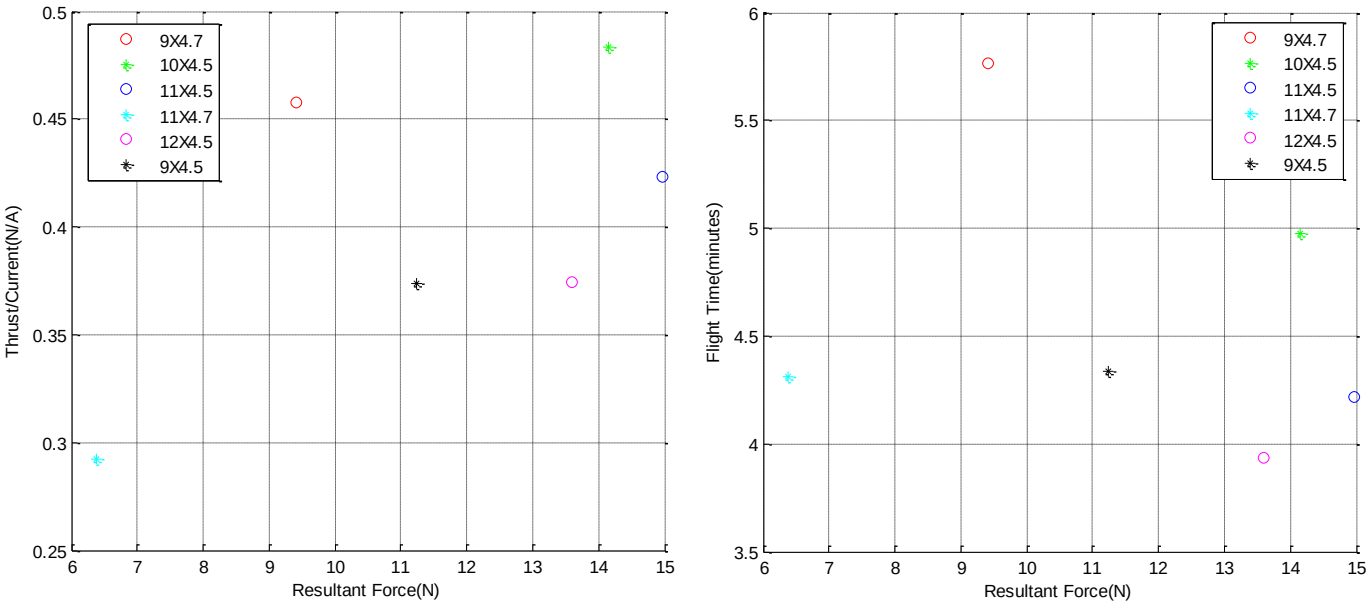

Figure A.17: Flight time and efficiency vs. resultant force for 1000KV with a single battery.

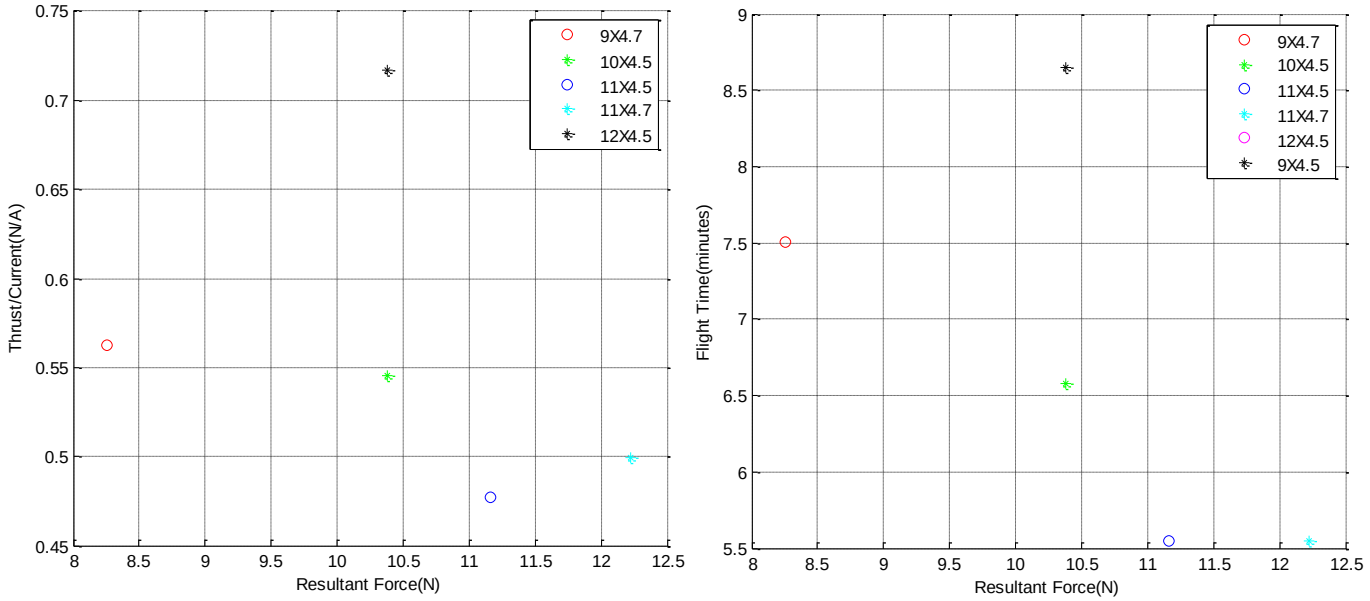

Figure A.18: Flight time and efficiency vs. resultant force for 1200KV with a single battery.

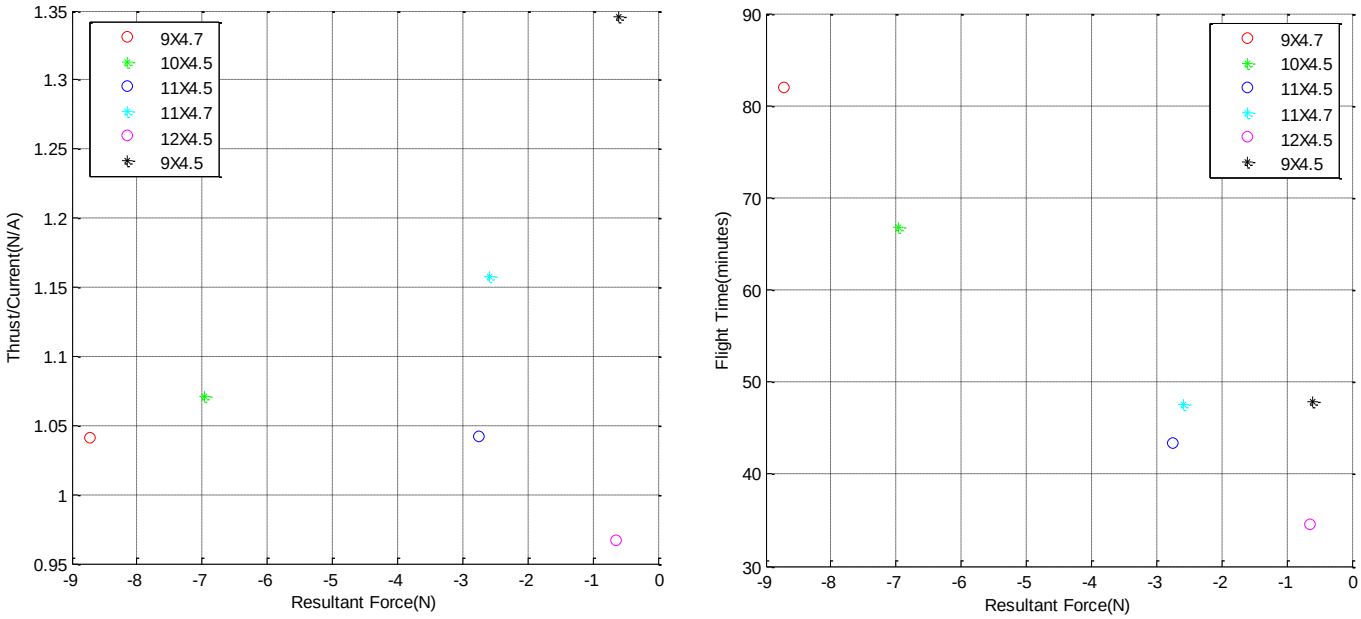

Figure A.19: Flight time and efficiency vs. resultant force for 390KV with a dual battery.

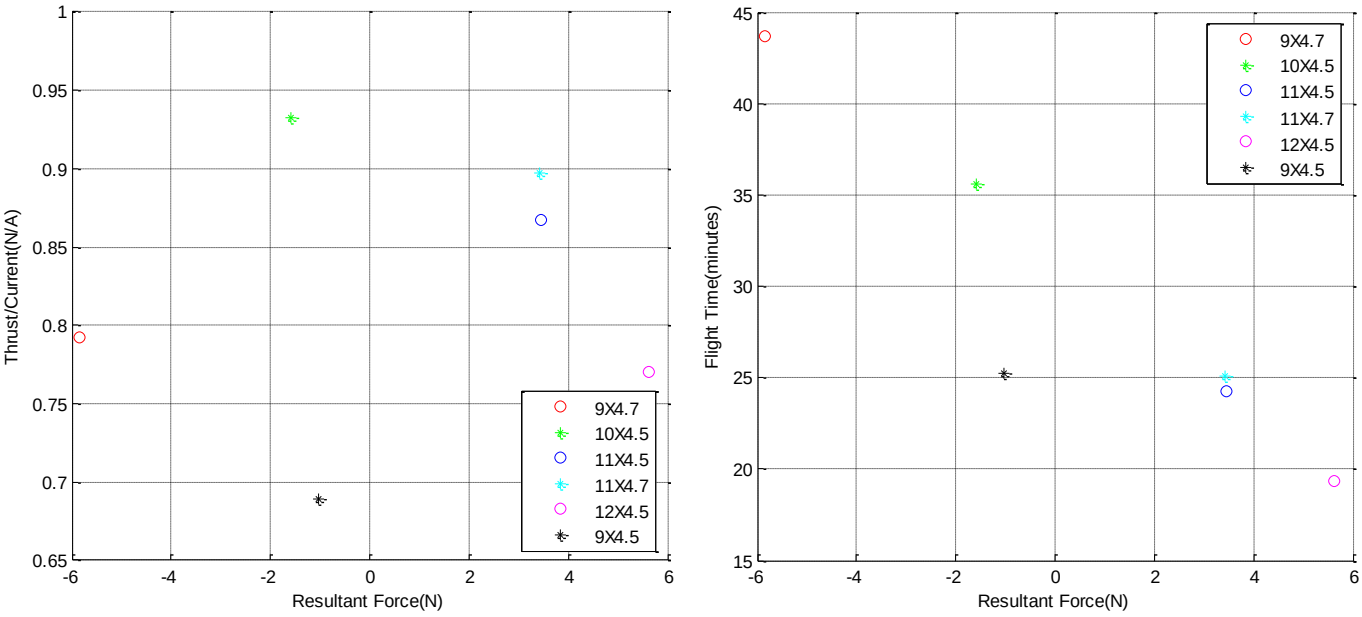

Figure A.20: Flight time and efficiency vs. resultant force for 490KV with a dual battery.

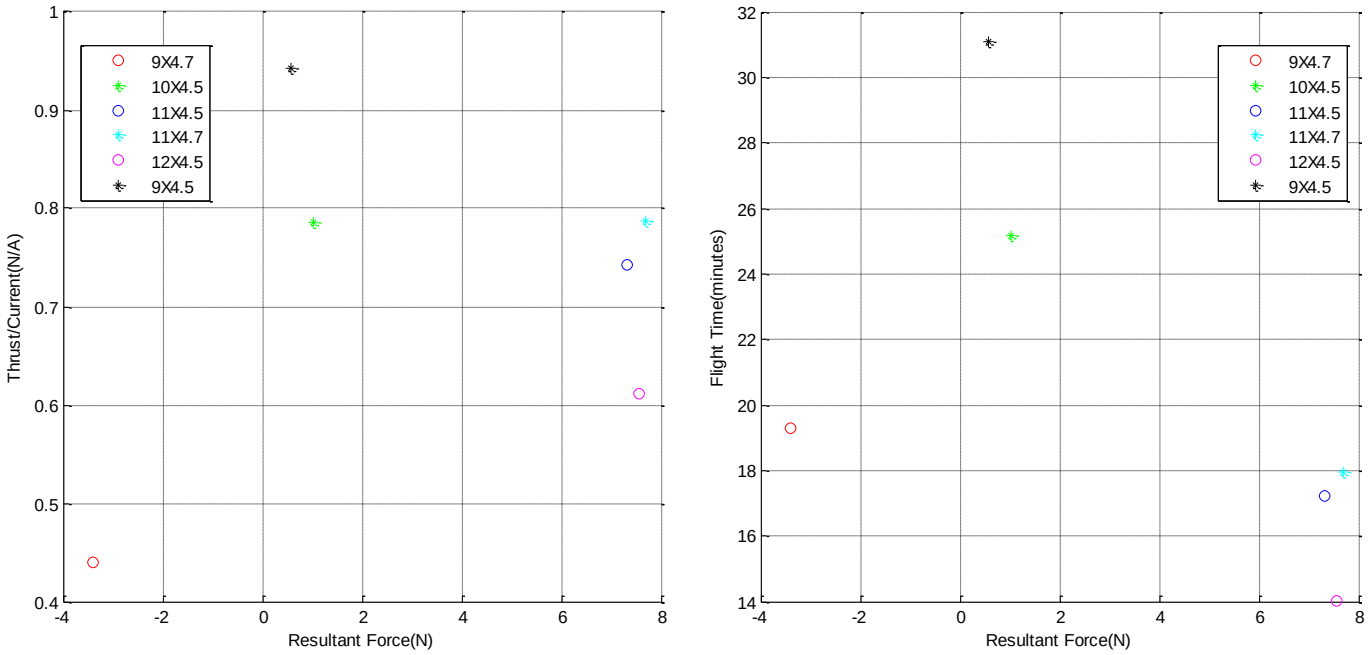

Figure A.21: Flight time and efficiency vs. resultant force for 570KV with a dual battery.

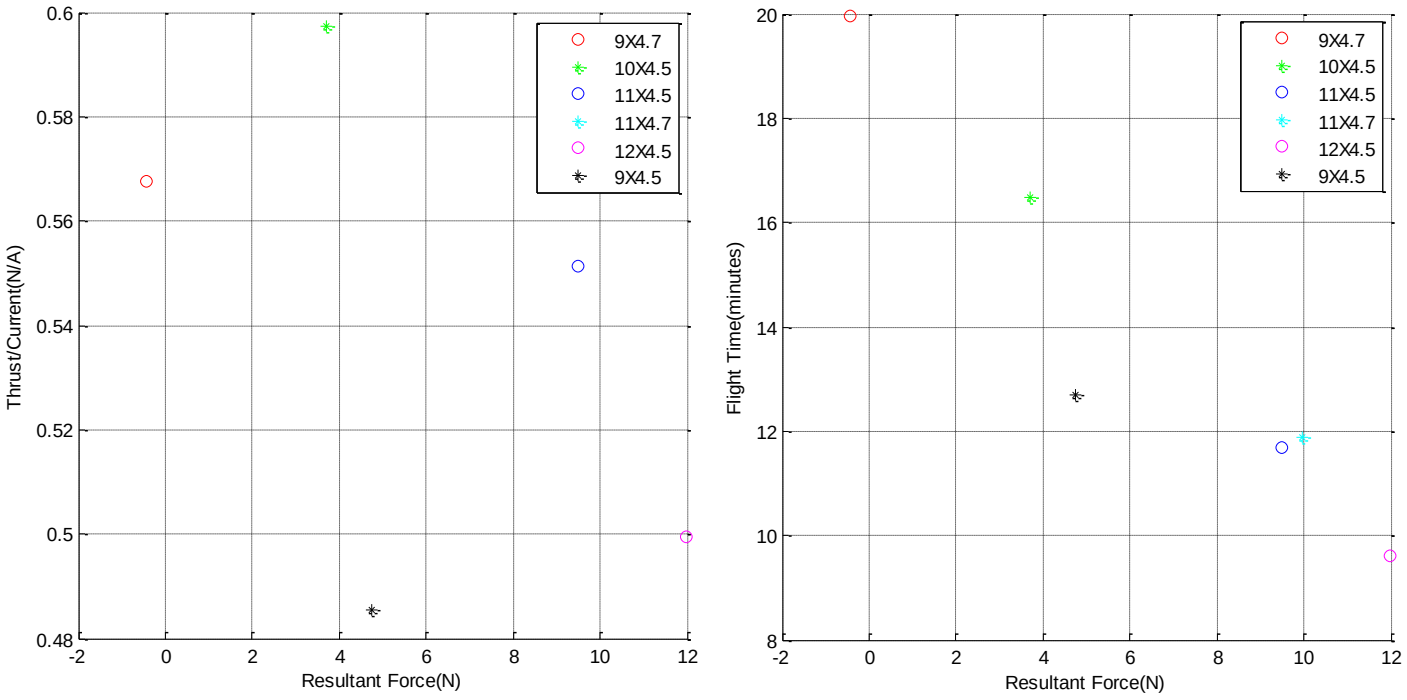

Figure A.22: Flight time and efficiency vs. resultant force for 690KV with a dual battery.

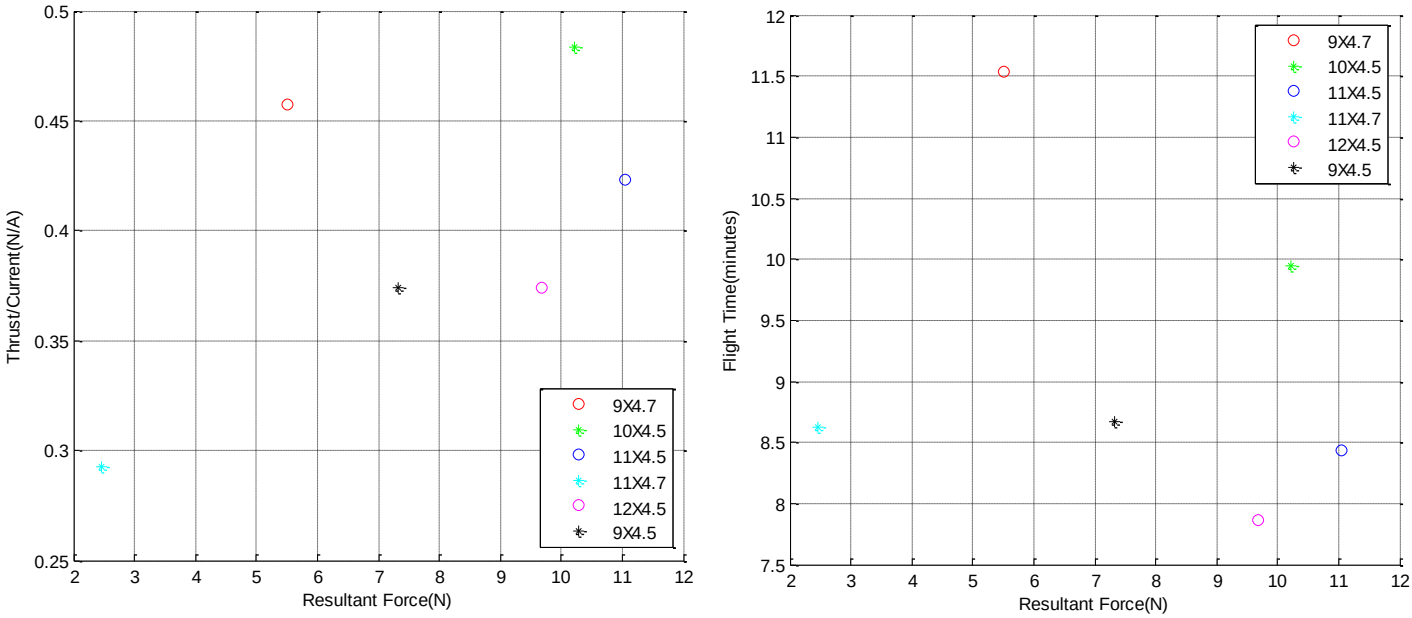

Figure A.23: Flight time and efficiency vs. resultant force for 1000KV with a dual battery.

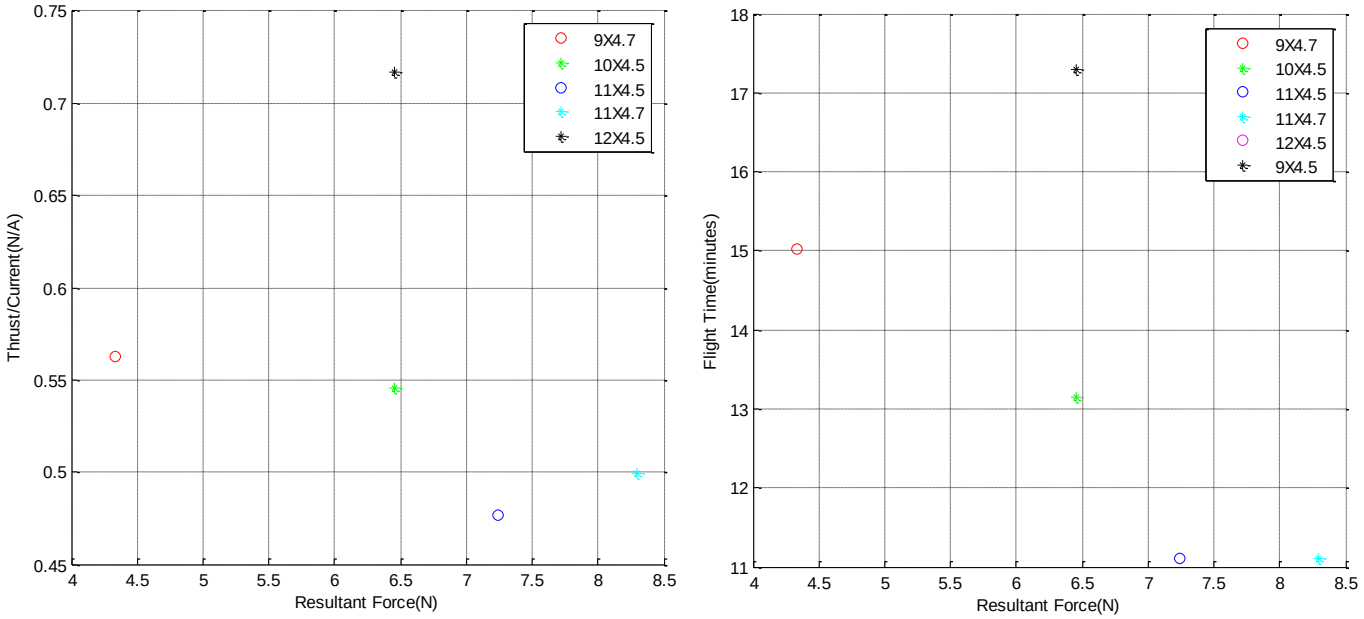

Figure A.24: Flight time and efficiency vs. resultant force for 1200KV with a dual battery.

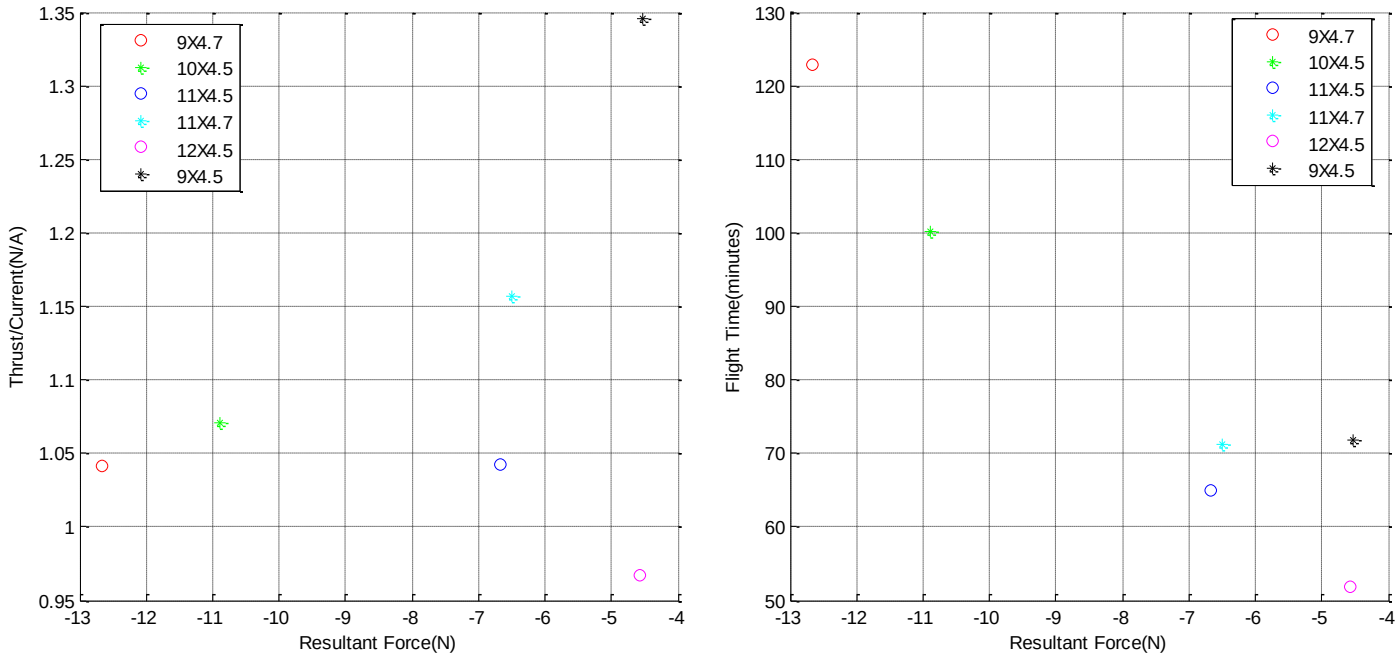

Figure A.25: Flight time and efficiency vs. resultant force for 390KV with a tri-battery.

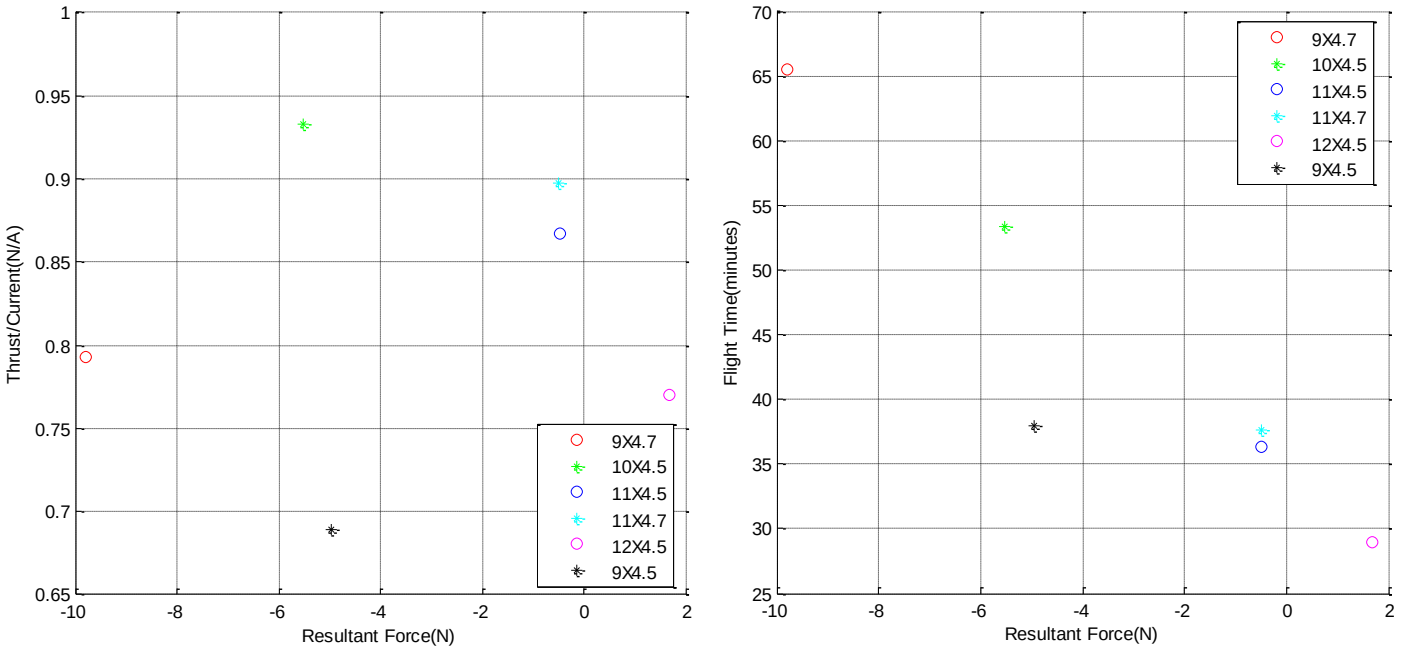

Figure A.26: Flight time and efficiency vs. resultant force for 490KV with a tri-battery.

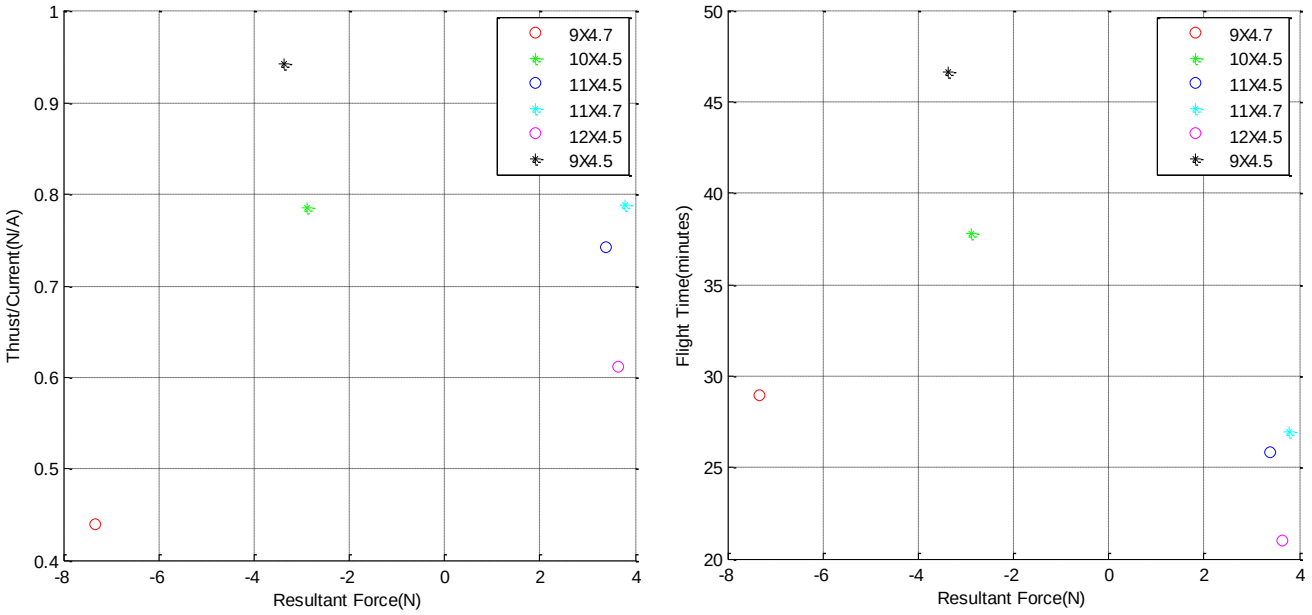

Figure A.27: Flight time and efficiency vs. resultant force for 570KV with a tri-battery.

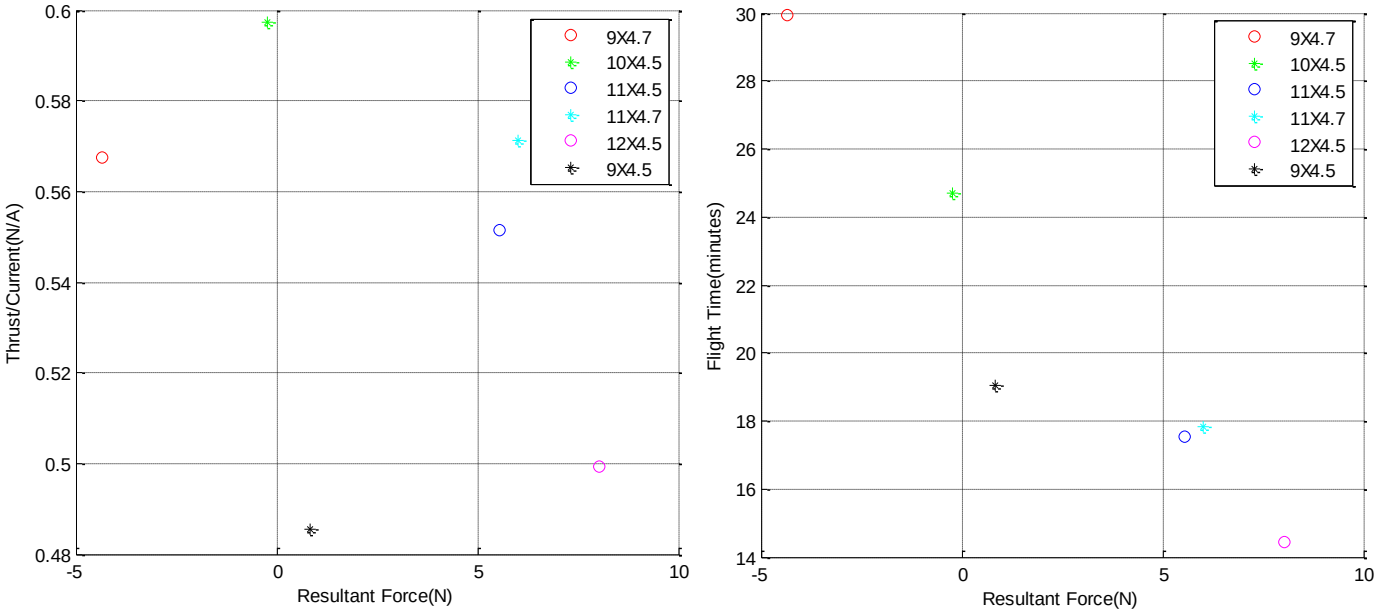

Figure A.28: Flight time and efficiency vs. resultant force for 690KV with a tri-battery.

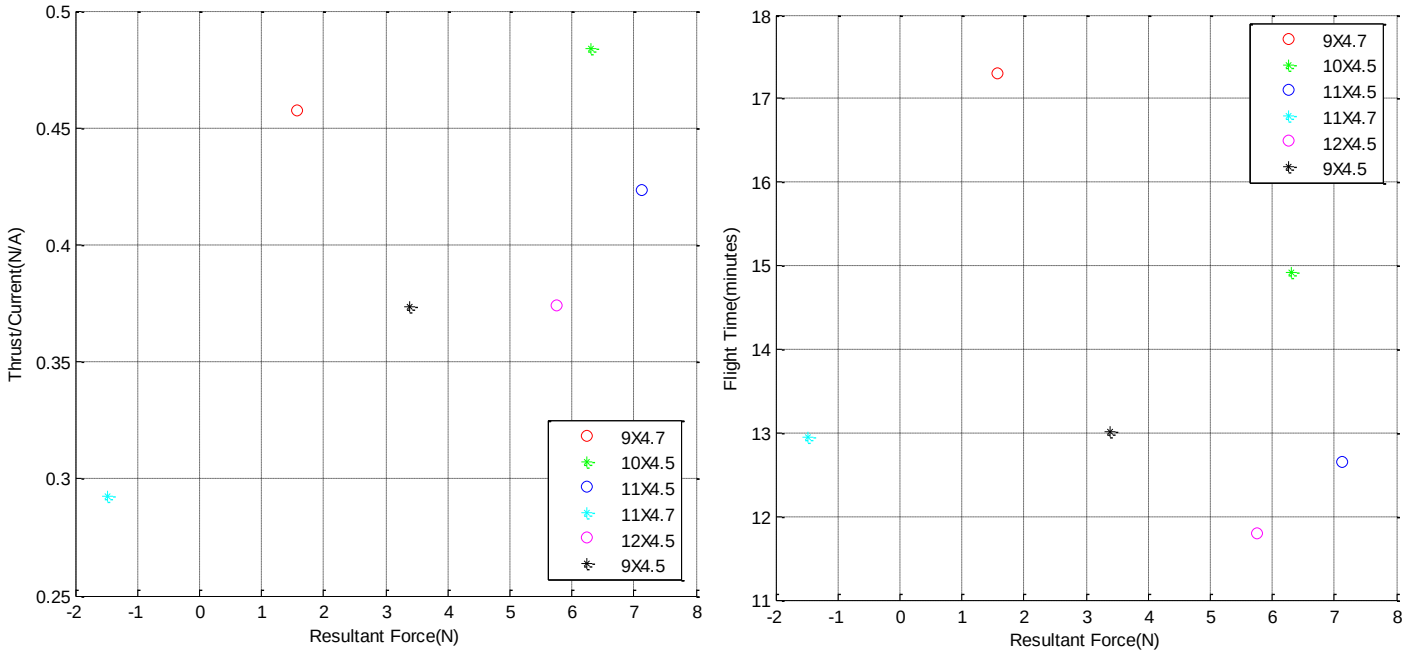

Figure A.29: Flight time and efficiency vs. resultant force for 1000KV with a tri-battery.

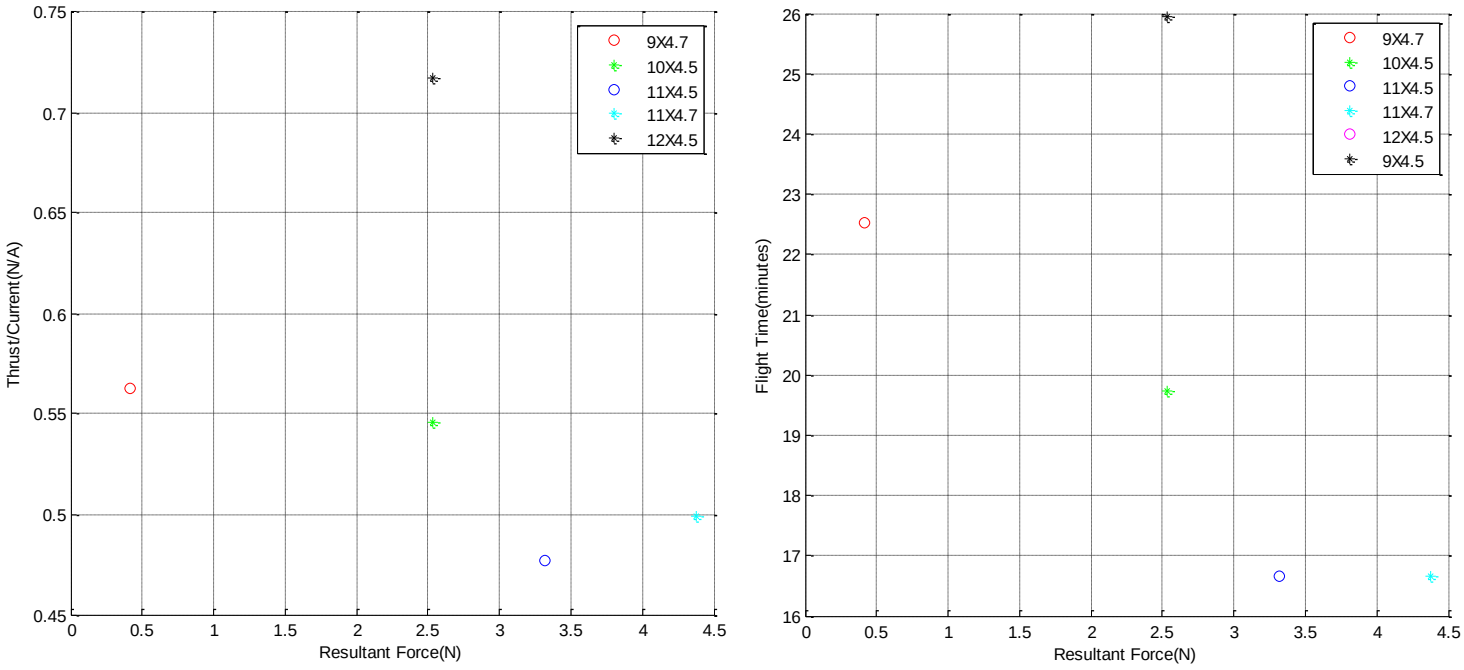

Figure A.30: Flight time and efficiency vs. resultant force for 1200KV with a tri-battery.

Appendix B – Strain Gauge

	SG SERIES	KFG SERIES
Foil strain gages are constructed by embedding a foil measuring element into a carrier. Foil measuring grid Carrier Substrate thickness Cover thickness Connection dimensions in (mm) [in]	 Constantan foil 5 µm thick Polyimide 50 µm 25 µm Solder pads or ribbon leads (30 long x.05 thick x 3 wide) [1.2 long x .002 thick x .012 wide]	 Constantan foil 6 µm thick Kapton 15 µm 9 µm 27 AWG strand polyvinyl insulation (1 x 2) [.04 x .08]
Nominal resistance Resistance tolerance per package Gage factor (µΩ/µ/µΩ) (actual value printed on each package) Gage factor tolerance per package	Stated in "to order" box 0.5% Approximately 2.0 1.0%	120 ±0.4 ohms 03% 2.10 ±10% 1.0%
Thermal Properties Reference temperature Service temperature: Static measurements Dynamic measurements Temperature characteristics: Steel Aluminum Uncompensated Temperature compensated range Tolerance of temp. compensation	 23°C/73°F -30 to 250°C (-22 to 482°F) -30 to 300°C (-22 to 572°F) 11 ppm°C (6.1 ppm°F) 23 ppm°C (12.8 ppm°F) ±20 ppm°C (±11.1 ppm°F) -5 to 120°C (5 to 248°F) 1 ppm°C (0.5 ppm°F)	 23°C/73°F -20 to 100°C (-4 to 212°F) -20 to 100°C (-4 to 212°F) 10.8 ppm°C (6 ppm°F) — — 10 to 80°C (50 to 176°F) 1 ppm°C (0.5 ppm°F)
Mechanical Properties Maximum strain Hysteresis Fatigue (at ±1500 µϵ) Smallest bending radius Transverse sensitivity	 3% or 30,000 µϵ Negligible > 10,000,000 cycles 3 mm (⅛ inch) —	 5% or 50,000 µϵ Negligible > 10,000,000 cycles 3 mm (⅛ inch) Stated on each package

Figure B.1: Strain Gauge Technical specifications

Appendix C – Encoder and ESC

Mechanical data

Mounting	square flange*
Shaft diameter	6 mm
Absolute max. shaft load	radial 30 N (6.5 lbs), axial 15 N (3.3 lbs)
Max. speed	10,000 RPM
Torque	≤ 0.2 Ncm
Protection class housing/ball bearing	IP 50/40
Operating temperature	-10 ... +60 °C
Storage temperature	-25 ... +85 °C
Vibration performance (IEC 68-2-6)	100 m/s^2 (10 ... 2000 Hz)
Shock resistance (IEC 68-2-27)	1000 m/s^2 (6 ms)
Connection	cable radial
Housing	glassfibre reinforced plastics
Weight	60 g approx.
Bearing life	1 x 10^{10} revolutions (typ.) at 35% of full rated shaft load 1 x 10^9 revolutions (typ.) at 75% of full rated shaft load 1 x 10^8 revolutions (typ.) at 100% of full rated shaft load e.g. 30,000 h at 6,000 RPM with a 2 lb radial load

* use threads M3 for fastening

Figure C.1: Mechanical Data of Incremental Shaft encoder

Electrical data

General design		as per DIN VDE 0160, protection class III, contamination level 2, overvoltage class II			
Power consumption		5V/40 mA, 24V/30 mA (10...30 V), 10V/60 mA (10...30V)			
Supply voltage U_B (SELV)		5 V DC ±10%			10...30 VDC
Output circuit[1]		PP	PP	RS422	PP
Code letter		K	D	R, T	K
Output load [mA]		±10	±30	±30	±30
Output voltage [V]	High	≥2.5	≥2.5	≥2.5	U_B-3
	Low	≤0.5	≤0.5	≤0.5	≤2
Pulse rise time [ns]		250	100	100	2000
Max. pulse frequency [kHz]		300	300	300	200
Reverse polarity protection		yes	no	no	yes
Short-circuit protection		yes	1 channel	1 channel	yes
Pulse duty factor		1 : 1			
Pulse width error		± 25° electrical			
Phase shift		90° (distance from Channel A to B is at least 0.45 µs, at 300 kHz)			
Pulse shape		rectangular			
Alarm output		Open Collector, NPN (with U_B=5 VDC: max. 5 mA, 24 V; with U_B=10...30 VDC: max. 5 mA, 32 V)			

[1] PP=Push-pull; RS422=Line driver

Figure C.2: Electical Data of Incremental Shaft encoder

Connection diagram

Colour (PVC)	Output RS 422 (T)	RS 422 (R)	Push-pull (K, D)
white	Channel A	Channel A	Channel A
white/brown	Channel $\overline{A}$	Channel $\overline{A}$	
green	Channel B	Channel B	Channel B
green/brown	Channel $\overline{B}$	Channel $\overline{B}$	
yellow	Channel N	Channel N	Channel N
yellow/brown	Channel $\overline{N}$	Channel $\overline{N}$	
yellow/black	Sense GND	$\overline{Alarm}$	$\overline{Alarm}$
yellow/red	Sense V_{cc}	Sense V_{cc}	
red	5 V DC	5 V DC	5/10...30 V DC
black	GND	GND	GND

Figure C.3: Connection Diagram of Incremental Shaft encoder

Ordering data (see identification plate)

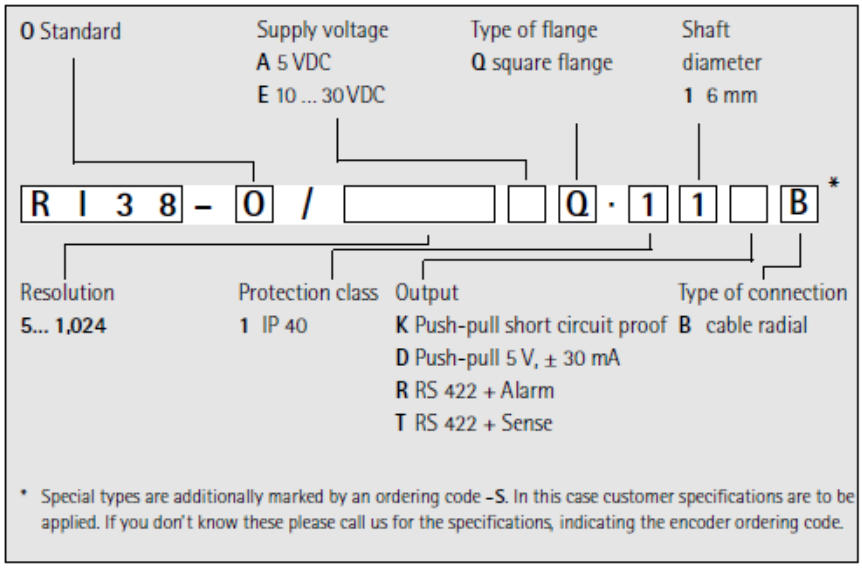

Figure C.4: Ordering Data of Incremental Shaft encoder

Using ESC

Normal Startup Procedure

Move throttle stick to the bottom position (full Off throttle) → Switch on the transmitter →Connect battery pack to ESC → System detects the Min throttle signal, makes a long "beep" sound → System detects battery voltage and makes several short "**beep-**" sounds, which denotes the number of battery cells → when self-test is finished → "♪123" tone should be emitted →ready for start.

Set Throttle Range (Throttle range should be setup when a new transmitter is being used)

Push the throttle stick to the top position (full On throttle) → switch on the transmitter →Connect battery pack to ESC → System detects the Max throttle signal, and makes two "**beep-**" sounds, which denotes that Max throttle has been confirmed and saved → Pull the throttle stick to the bottom position within 5 seconds(program mode will be entered if you wait for 6 seconds) →System detects the Min throttle signal, makes a long "**beep-**" sound → System detects battery voltage and makes several short "**beep-**" sounds, which denotes the number of battery cells →when self-test is finished → "♪123" tone should be emitted → Ready for start.

If the system doesn't detect the throttle signal, it will make "**beep-**" sounds continuously without stopping.

Any fault in self- test, it will make 20 very short "**beep-**" sounds.

Protection

A. Low voltage protection: When power voltage is lower than the cutoff threshold, ESC will reduce output power or cut off. Read the "Configurable parameter" for more information.

B. Throttle signal lost protection: The ESC will reduce output power to 20% if throttle signal lost for 1 second, the output power will recover if signal is detected.

C. Over heat protection: when the temperature of ESC is over 110℃,the ESC will reduce output power, the min output power can be reduced to 35%. The output power will raise after temperature gets low.

D. Self-test: ESC will start self-test when power on.. If self-test fail, ESC will continuously emit 20 short "**beep-**" tones.

Wiring Diagram

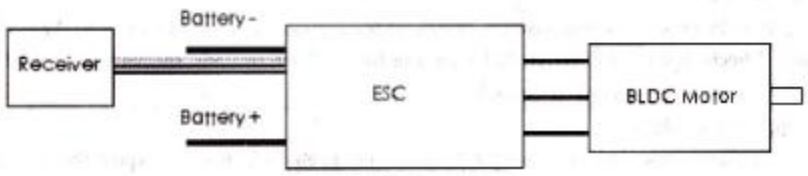

Figure C.5: Start-up and throttle range procedures for ESC arming

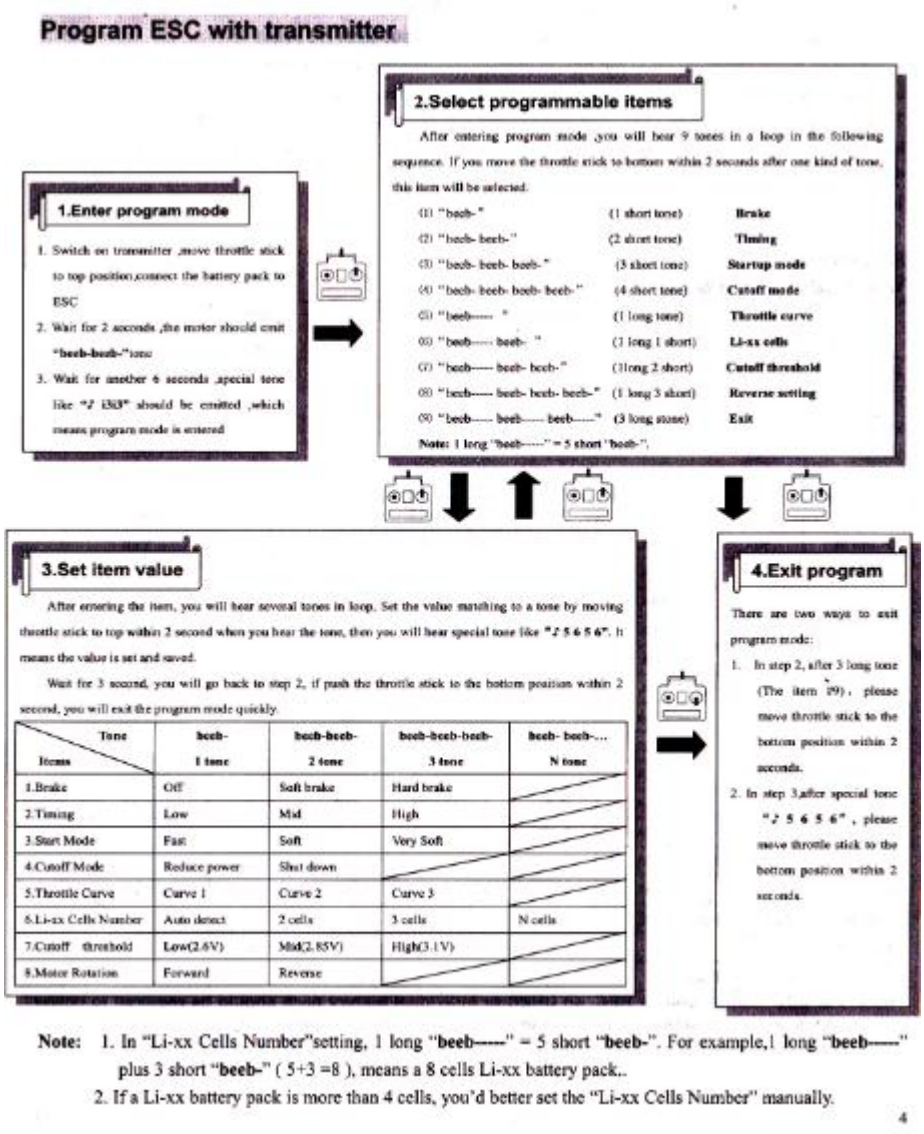

Figure C.6: Programming ESC with the transmitter

Appendix D – Transformations and Moment of Inertia

D.1 Transformation in 2 dimensions

The 2-dimension transformation will be typical of the Quadrotor during a yaw maneuver as seen in Figure D.1. Figure D.1 illustrates a plan view of the vehicle in the earth fixed axis represented by a red coordinate system and a green coordinate system represented by the body fixed axis. Initially both coordinates are aligned then rotated with respect to the inertial according to the right hand rule.

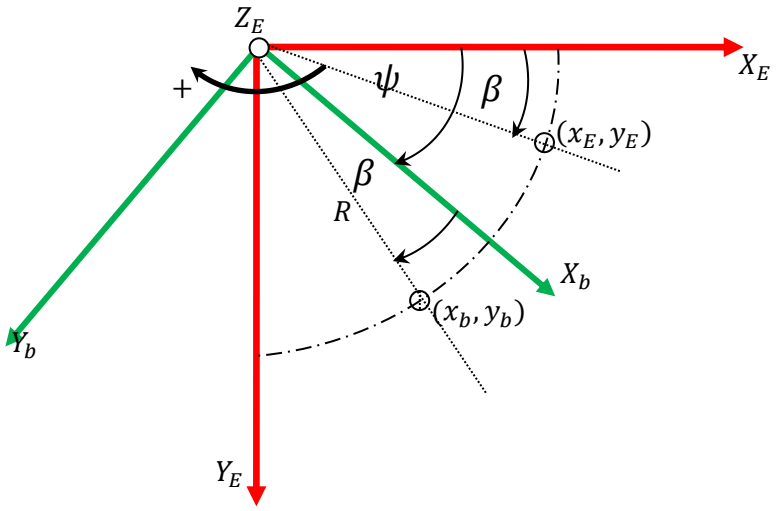

Figure D.1: Plan view of the vehicle during a clockwise (+ve) yaw rotation

The axis(X_E-Y_E) are rotated through an angle of β to their new position (X_b-Y_b):

$$x_E = R\cos\beta \tag{D.1}$$

$$y_E = R\sin\beta \tag{D.2}$$

Transforming the new coordinate to the old coordinate system:

$$x_b = R\cos(\psi + \beta) \tag{D.3}$$

$$y_b = Rsin(\psi + \beta) \tag{D.4}$$

Expanding the previous equations:

$$x_b = R\big(cos(\psi)cos(\beta) - sin(\psi)sin(\beta)\big) \tag{D.5}$$

$$y_b = R\big(sin(\psi)cos(\beta) + cos(\psi)sin(\beta)\big) \tag{D.6}$$

Now using equation D.3 and D.4:

$$x_b = x_0 cos(\psi) - y_0 sin(\psi) \tag{D.7}$$

$$y_b = x_0 sin(\psi) + y_0 cos(\psi) \tag{D.8}$$

In Matrix form:

$$\begin{bmatrix} x_b \\ y_b \end{bmatrix} = \begin{bmatrix} cos(\psi) & -sin(\psi) \\ sin(\psi) & cos(\psi) \end{bmatrix} \begin{bmatrix} x_E \\ y_E \end{bmatrix} \tag{D.9}$$

Hence the transformation matrix is given by:

$$\mathbb{T}_{Eb_\psi} = \begin{bmatrix} cos(\psi) & -sin(\psi) \\ sin(\psi) & cos(\psi) \end{bmatrix} \tag{D.10}$$

Any vector having undergone a yaw rotation can be transformed to the body fixed axis in 2-dimension using the following equation:

$$X_B = \mathbb{T}_{Eb} X_E \tag{D.11}$$

Similarly the 2-D transformation matrix for a pitch maneuver can be extracted from Figure D.2.

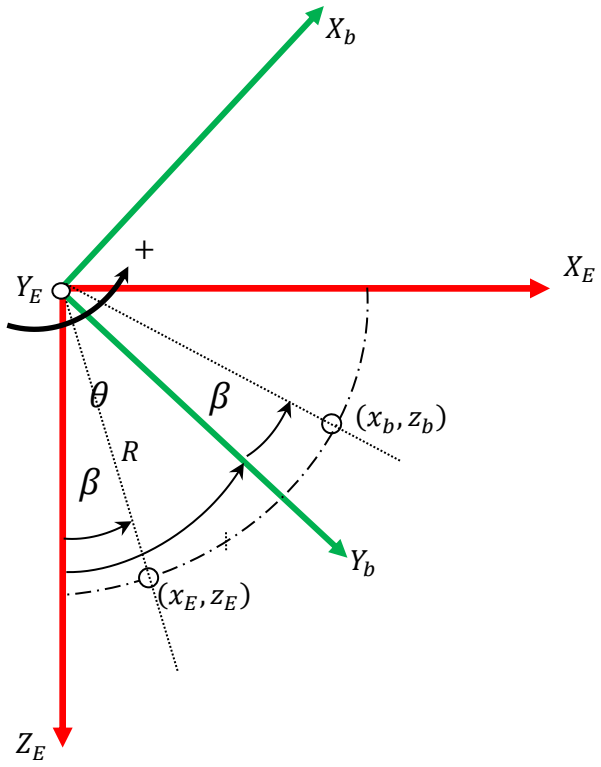

Figure D.2: A +ve pitch rotation of a coordinate system in 3-D

$$\begin{bmatrix} x_b \\ z_b \end{bmatrix} = \begin{bmatrix} cos(\theta) & sin(\theta) \\ -sin(\theta) & cos(\theta) \end{bmatrix} \begin{bmatrix} x_E \\ z_E \end{bmatrix} \tag{D.12}$$

Hence the transformation matrix is given by:

$$\mathbb{T}_{Eb_\theta} = \begin{bmatrix} cos(\theta) & sin(\theta) \\ -sin(\theta) & cos(\theta) \end{bmatrix} \tag{D.13}$$

Similarly the 2-D transformation matrix for a roll maneuver can be extracted from Figure D.3.

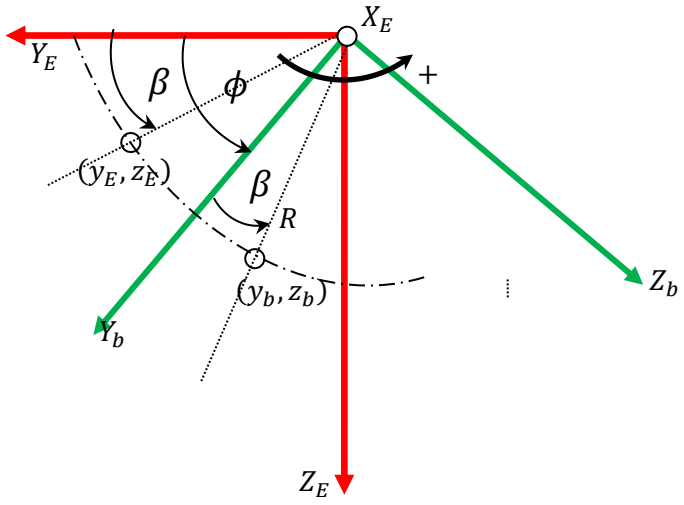

Figure D.3: A +ve roll rotation of a coordinate system in 3-D

$$\begin{bmatrix} y_b \\ z_b \end{bmatrix} = \begin{bmatrix} cos(\phi) & -sin(\phi) \\ sin(\phi) & cos(\phi) \end{bmatrix} \begin{bmatrix} y_E \\ z_E \end{bmatrix} \tag{D.14}$$

Hence the transformation matrix is given by:

$$\mathbb{T}_{Eb_\phi} = \begin{bmatrix} cos(\phi) & -sin(\phi) \\ sin(\phi) & cos(\phi) \end{bmatrix} \tag{D.15}$$

D.2 Transformation in 3 dimensions:

The yaw maneuver performed in 2-dimension as in section 0 will now be recreated in the 3-dimension field of transformation. The yaw axis of the body (green) is aligned with the earth fixed axis.(red)

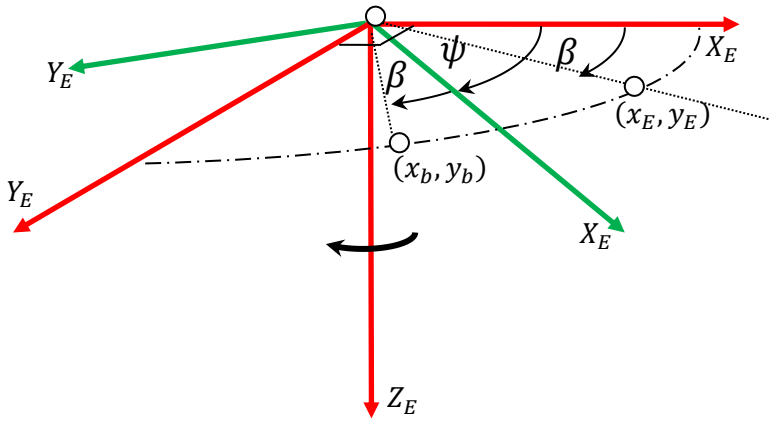

Figure D.4: A +ve yaw rotation of a coordinate system in 3-D

The axis(X_0-Y_0-Z_0) are rotated through an angle of β to their new position (X_1-Y_1-Z_1):

$$x_b = R\cos\beta \tag{D.16}$$

$$y_b = R\sin\beta \tag{D.17}$$

$$z_b = z_b$$

Transforming the new coordinate to the old coordinate system:

$$x_E = R\cos(\psi + \beta) + 0 \tag{D.19}$$

$$y_E = R\sin(\psi + \beta) + 0 \tag{D.20}$$

$$z_1 = 0 + 0 + z_0 \tag{D.21}$$

Expanding:

$$x_E = R\big(cos(\psi)cos(\beta) - sin(\psi)sin(\beta)\big) + 0 \tag{D.22}$$

$$y_E = R\big(sin(\psi)cos(\beta) + cos(\psi)sin(\beta)\big) + 0 \tag{D.23}$$

Now using equation 2.61 and 2.62:

$$x_E = x_b cos(\psi) - y_b sin(\psi) + 0 \tag{D.24}$$

$$y_b = x_E sin(\psi) + y_E cos(\psi) + 0 \tag{D.25}$$

In Matrix form:

$$\begin{bmatrix} x_b \\ y_b \\ z_b \end{bmatrix} = \begin{bmatrix} cos(\psi) & 0 & sin(\theta) \\ sin(\psi) & cos(\psi) & 0 \\ 0 & 0 & 1 \end{bmatrix} \begin{bmatrix} x_E \\ y_E \\ z_E \end{bmatrix} \tag{D.26}$$

$$\mathbb{T}_{Eb_\psi} = \begin{bmatrix} cos(\psi) & -sin(\psi) & 0 \\ sin(\psi) & cos(\psi) & 0 \\ 0 & 0 & 1 \end{bmatrix} \tag{D.27}$$

Performing a transformation about the y-axis using equation D.13 and a similar approach to that employed in Figure D.4.

In Matrix form:

$$\begin{bmatrix} x_b \\ y_b \\ z_b \end{bmatrix} = \begin{bmatrix} cos(\theta) & 0 & sin(\theta) \\ 0 & 1 & 0 \\ -sin(\theta) & 0 & cos(\theta) \end{bmatrix} \begin{bmatrix} x_E \\ y_E \\ z_E \end{bmatrix} \tag{D.28}$$

$$\mathbb{T}_{Eb_\theta} = \begin{bmatrix} cos(\theta) & 0 & sin(\theta) \\ 0 & 1 & 0 \\ -sin(\theta) & 0 & cos(\theta) \end{bmatrix} \tag{D.29}$$

Similarly for a transformation about the x—axis in 3 dimension using equation D.15:

In Matrix form:

$$\begin{bmatrix} x_b \\ y_b \\ z_b \end{bmatrix} = \begin{bmatrix} 1 & 0 & 0 \\ 0 & cos(\phi) & -sin(\phi) \\ 0 & sin(\phi) & cos(\phi) \end{bmatrix} \begin{bmatrix} x_E \\ y_E \\ z_E \end{bmatrix} \tag{D.29}$$

$$\mathbb{T}_{Eb_\phi} = \begin{bmatrix} 1 & 0 & 0 \\ 0 & cos(\phi) & -sin(\phi) \\ 0 & sin(\phi) & cos(\phi) \end{bmatrix} \tag{D.30}$$

D.3 Moment of Inertia:

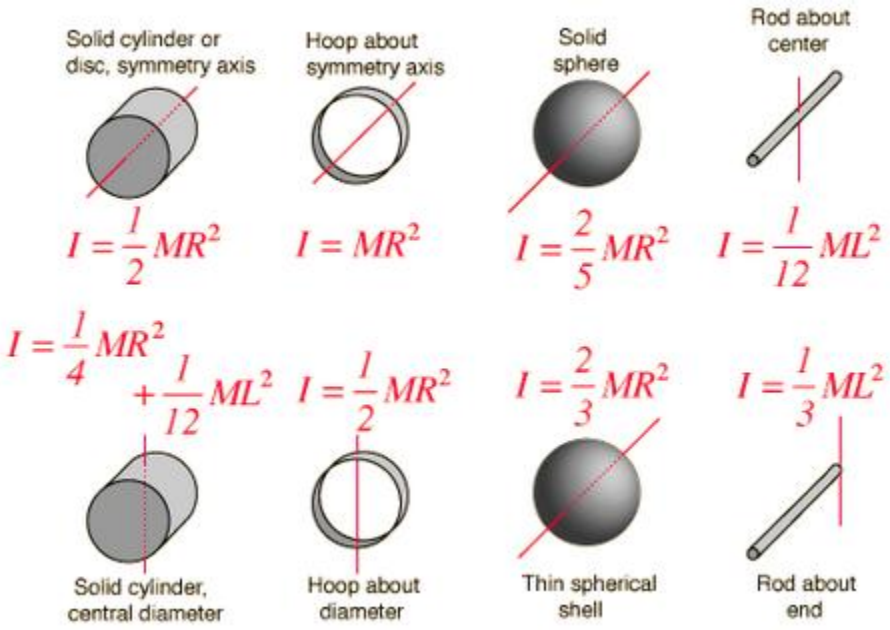

Appendix E- IMU Flow and Coding structure

E.1 IMU User Command Setup

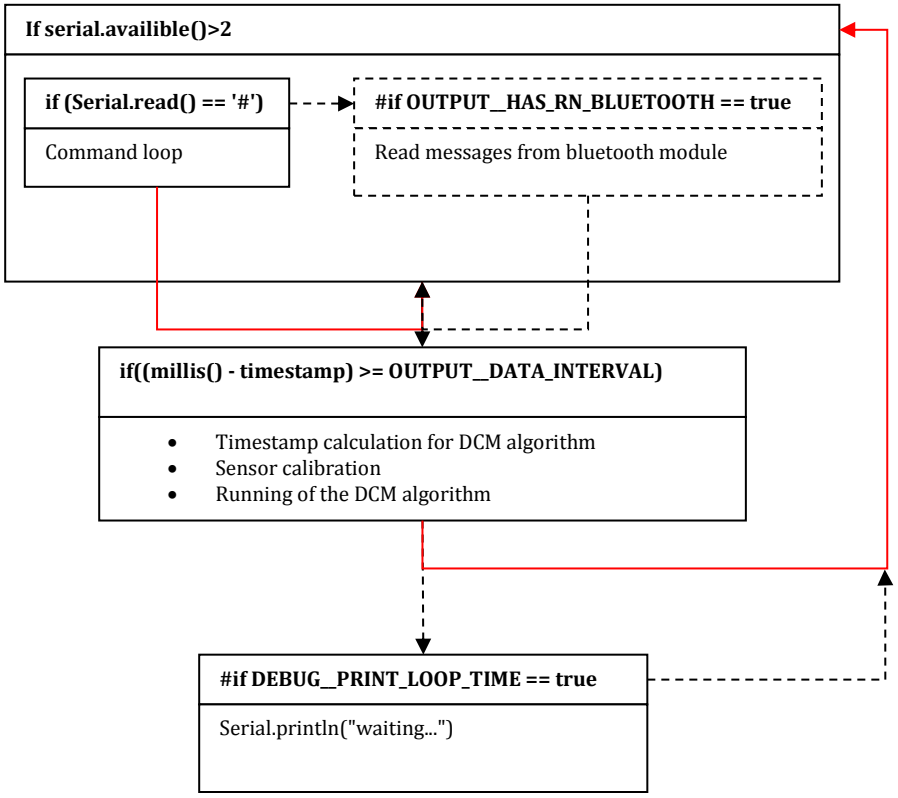

Figure E.1: Main Setup Flow chart

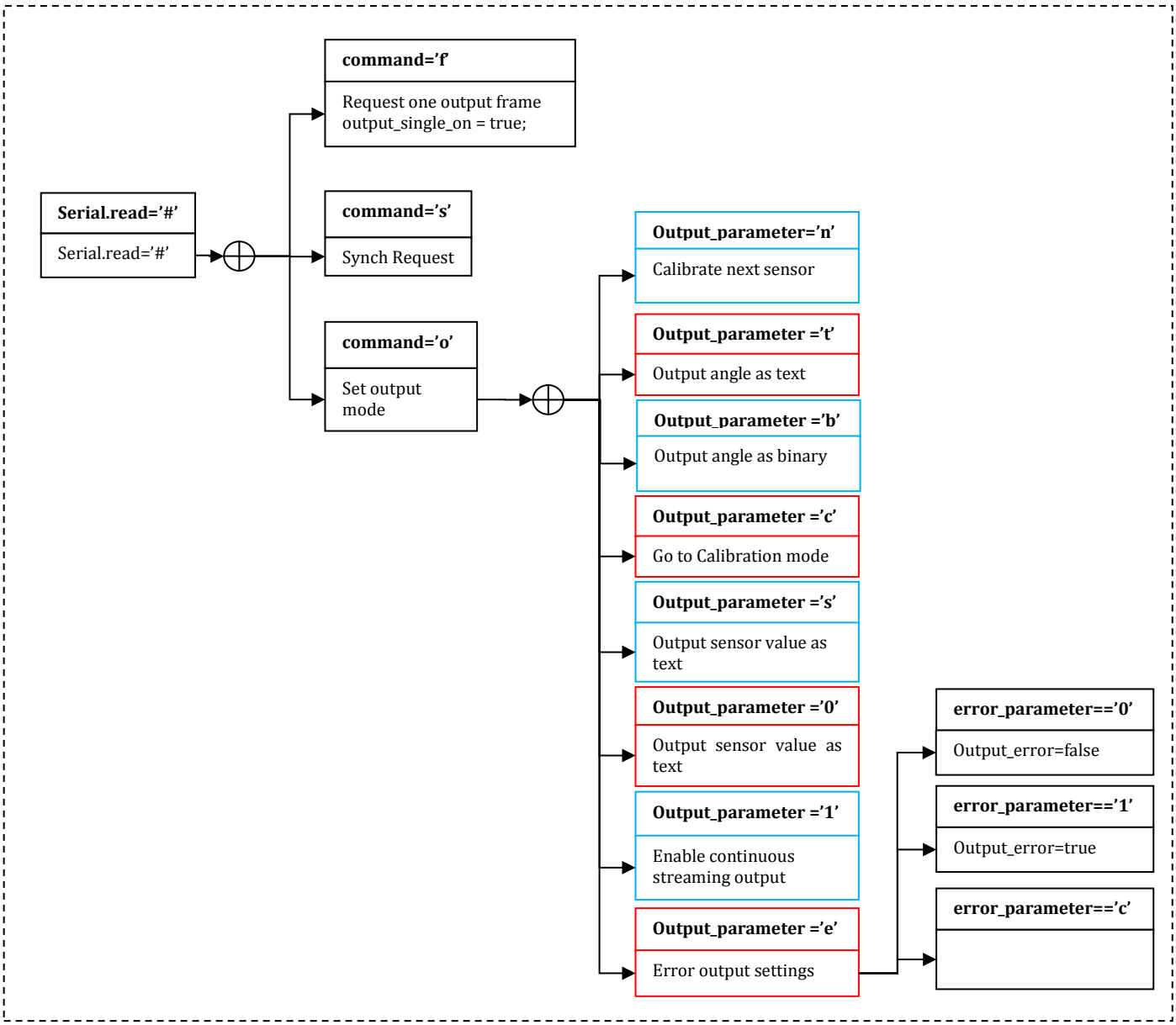

Figure E.2: Control messages from the user

E.2 Coding structure

The offsets of the sensors are given by:

$$AN[select] - AN_OFFSET[select] \tag{E.1}$$

The offsets are stored in the following arrays: (9dof constant)

$$AN_OFFSET[6] = \{0,0,0,0,0,0\} \tag{E.2}$$

The 3 ADC filtered sets of data for the gyro's are stored in the following array: (9 dof constant)

$$AN[6] = \{0,0,0,0,0,0\} \tag{E.3}$$

Matrix Multiplication Function:

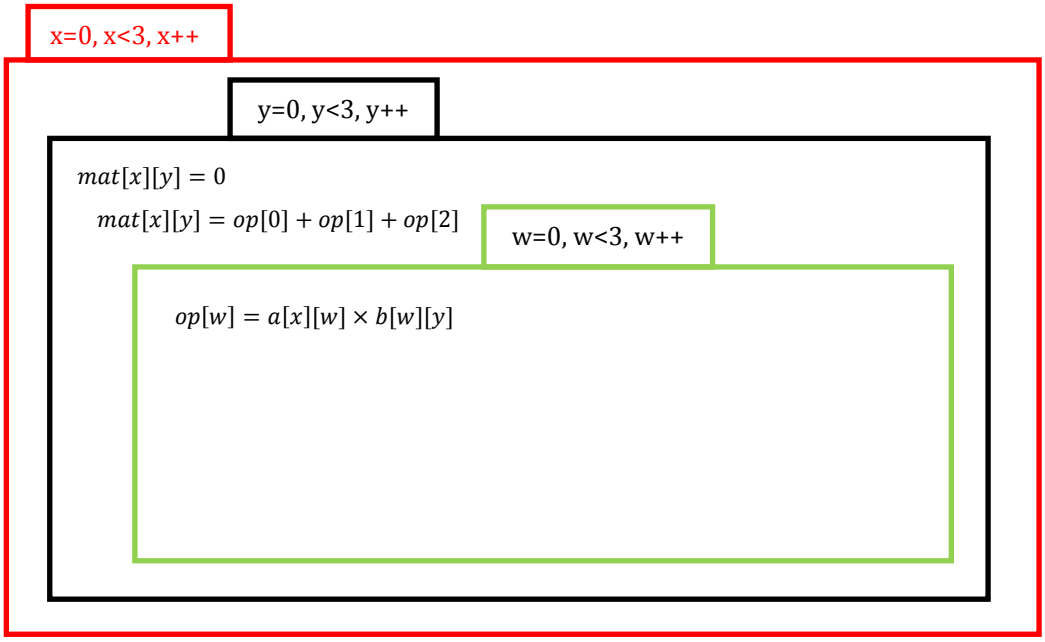

The above function describes three loops the inner most loop will need to complete in order to progress to the outer most loop for the next iteration cycle.

The matrix produced is indexed in the following way:

$$a=\begin{bmatrix}0,0 & 0,1 & 0,2\\ 1,0 & 1,1 & 1,2\\ 2,0 & 2,1 & 2,2\end{bmatrix}, b=\begin{bmatrix}0,0 & 0,1 & 0,2\\ 1,0 & 1,1 & 1,2\\ 2,0 & 2,1 & 2,2\end{bmatrix}, c=\begin{bmatrix}0,0 & 0,1 & 0,2\\ 1,0 & 1,1 & 1,2\\ 2,0 & 2,1 & 2,2\end{bmatrix} \quad \text{(E.4)}$$

Assuming we carry out the multiplication of $axb = c$

$$\therefore c=\begin{bmatrix}a[0,0]\times b[0,0]+a[0,1]\times b[1,0]+a[0,2]\times b[2,0] & \dots & \dots\\ a[1,0]\times b[0,0]+a[1,1]\times b[1,0]+a[1,2]\times b[2,0] & \dots & \dots\\ \dots & \dots & \dots\end{bmatrix} \quad \text{(E.5)}$$

Euler angles are calculated using raw data from the ADC: [No drift correction]

The ADC gains are set by the Gyro gains:

$$Gyro_Gain_X = 0.92 \quad \text{(E.6)}$$

$$Gyro_Gain_Y = 0.92 \quad \text{(E.7)}$$

$$Gyro_Gain_Z = 0.92 \quad \text{(E.8)}$$

These ADC values can be scaled by:

$$Gyro_Vector[0] = Gyro_Scaled_X(read_adc(0)) \quad \text{(E.9)}$$

$$Gyro_Vector[1] = Gyro_Scaled_Y(read_adc(1)) \quad \text{(E.10)}$$

$$Gyro_Vector[2] = Gyro_Scaled_Z(read_adc(2)) \quad \text{(E.11)}$$

The scaling values are given by the equations below where the values of x has been set by the equations above:

$$Gyro_Scaled_X(x) = x * ToRad(Gyro_Gain_X) \tag{E.12}$$

$$Gyro_Scaled_Y(x) = x * ToRad(Gyro_Gain_Y) \tag{E.13}$$

$$Gyro_Scaled_Z(x) = x * ToRad(Gyro_Gain_Z) \tag{E.14}$$

$$Update_Matrix = \begin{bmatrix} 0 & -G_{Dt} * Omega_Vector[2] & G_{Dt} * Omega_Vector[2] \\ G_{Dt} * Omega_Vector[2] & 0 & -G_{Dt} * Omega_Vector[0] \\ -G_{Dt} * Omega_Vector[1] & G_{Dt} * Omega_Vector[0] & 0 \end{bmatrix} \tag{E.15}$$

$$\begin{bmatrix} Omega_{Vector[0]} \\ Omega_{Vector[1]} \\ Omega_{Vector[2]} \end{bmatrix} = \begin{vmatrix} w_x \\ w_y \\ w_z \end{vmatrix} \tag{E.16}$$